ÉCOLE POLYTECHNIQUE DE BRUXELLES
UNIVERSITÉ LIBRE DE BRUXELLES

LIÈGE université

Optimal Architectures for Mechatronic System Design

A Pole-Zero Distance Approach

Thesis presented by Dimitri PIRON

in fulfilment of the requirements of the PhD Degree in Engineering Sciences and Technology ("Docteur en Sciences de l'Ingénieur et Technologie")

Academic year 2024-2025

Supervisor: Professor Arnaud DERAEMAEKER
Université libre de Bruxelles
Co-supervisor: Professor Christophe COLLETTE
Université de Liège

Thesis jury:

Université libre de Bruxelles:
Prof. Patrick HENDRICK (Chair)
Prof. Thierry J. MASSART (Member)
Prof. Arnaud DERAEMAEKER (Supervisor)
Université de Liège:
Prof. Gaetan KERSCHEN (Member)
Prof. Pierre DUYSINX (Member)
Prof. Christophe COLLETTE (Supervisor)
Università di Genova:
Prof. Marta BERARDENGO (Member)

fnrs LA LIBERTÉ DE CHERCHER

“ Soldiers! Don’t give yourselves to brutes [...]
Don’t give yourselves to these unnatural men,
machine men with machine minds and machine hearts!
You are not machines! You are not cattle! You are men!
You have the love of humanity in your hearts! [...]
Soldiers! Don’t fight for slavery! Fight for liberty! ”

Charlie Chaplin, 1940
The Great Dictator

À Sacha & Maxime

Abstract

The proper positioning of transducers in active damping of structures is fundamentally important. Their placement directly influences several critical aspects: closed-loop stability, overall performance and the robustness of the system with respect to uncertainties (inaccuracies of the model, ageing of the transducers, misplacement). The importance of this placement concern is reflected by the numerous optimal placement criteria developed over the past decades. Depending on the application, the different criteria provide a cost function that determines the most effective transducer locations. However, identifying the optimal positions based on those criteria necessitates the use of search algorithms, as evaluating the cost function across all possible configurations is infeasible. Among the available methods, genetic algorithms (also called evolutionary algorithms) represent an attractive solution as they do not require prior knowledge and are capable of identifying the global optimum even in the presence of numerous local ones. Nonetheless, these algorithms typically require an extensive number of evaluations to converge towards a solution. Because of the possible prohibitive convergence duration, optimization of large and/or complex structures are not commonly implemented.

This doctoral thesis investigates the potential of replacing the genetic algorithms by non-evolutionary ones, reducing consequently the computational effort required to obtain the optimal placement of transducers. In this regard, a new pole-zero distance criterion is introduced for single-input-single-output (SISO) systems, as well as for multiple-input-multiple-outputs (MIMO) ones. This criterion is based on the maximization of the pole-zero distance of the mode(s) to be damped, which has a direct link with the maximum achievable damping ratio once in closed-loop. Such well-established link in SISO system is extended and experimentally demonstrated for MIMO ones.

It is shown that this pole-zero distance criterion allows the extraction, based on a limited number of evaluations, of a configuration that exhibits high damping and strong robustness. It consequently provides a suitable starting position for a non-evolutionary algorithm, which converges extremely fast compared to the genetic ones. This new method is applied to multiple examples, including industrial structures. Its effectiveness is numerically demonstrated in terms of computational effort required to find the solution, as well as the performance and robustness of the optimal position. Finally, the reliability of numerical models is discussed, and some recommendations are provided to reduce potential inaccuracies.

Remerciements

La réalisation d'une thèse de doctorat est un ouvrage extrêmement solitaire, mais à la fois collaboratif. Cet oxymore reflète la nature paradoxale d'un tel projet.

La recherche scientifique, c'est essayer des choses, explorer, se questionner, sans jamais savoir si au bout du compte cela va aboutir. Certes, les directions empruntées sont éclairées mais ces dernières ne garantissent malheureusement pas un résultat probant. Or le travail de doctorat doit, *in fine*, aboutir à la rédaction d'une thèse assez étoffée pour justifier quatre années de recherches. Inévitablement, des questionnements voire des doutes apparaissent, et la solitude surgit. C'est dans ces moments de tension que le caractère collaboratif joue un rôle central.

Faisant suite à cet aspect collaboratif, je tiens à exprimer ma sincère et profonde gratitude envers mes deux superviseurs : Christophe Collette et Arnaud Deraemaeker. Ce fut en effet un réel plaisir de partager ces quatre années de recherche à leurs côtés, à la fois d'un point de vue scientifique mais également humain. J'ai pu établir un lien fort avec eux, chacun apportant une dynamique unique propre à leurs personnalités respectives. Une chose est sûre : mon passage à leurs côtés aura marqué mon parcours professionnel et personnel.

Bien d'autres personnes ont collaboré, de près ou de loin, à la réalisation de ma thèse. Je tiens bien sûr à remercier mon comité d'accompagnement ainsi que mon jury, chaque membre ayant contribué à challenger mes résultats dans l'optique positive d'améliorer mon travail.

Un grand merci également à tous les chercheurs (doctorants, post-doctorants) et techniciens croisés au fil des années. Les nombreuses interactions que j'ai pu avoir (scientifiques mais également humaines) ont contribué à l'aboutissement de ce travail. Je tiens particulièrement à remercier Vicente Lafarga, Jennifer Watchi, Cédric Dumoulin, Ahmad Paknejad, Loìc Amez-Droz, Shashank Pathak, Arun Narayanan et Gilles Vanhooren.

Evidemment, un merci particulier à mes amis et à ma famille, qui m'ont soutenu tout au long de ce parcours. Merci à mes enfants, Sacha et Maxime, d'être un véritable rayon de soleil dans ma vie (même si je dois l'avouer, ils sont parfois fatigants !).

Enfin, je tiens à adresser un remerciement tout particulier à Samira, pour m'avoir soutenu, encouragé et... encore soutenu. La finalisation fût longue, mais nous y sommes arrivés.

The research presented in this manuscript has been possible thanks to the Fonds de la recherche scientifique (FRS-FNRS) through a FRIA grant given to Dimitri Piron.

Contents

Contents xi

List of Figures xiii

List of Tables xvii

Acronyms xix

Notations and operators xxi

Introduction 1
References . . . 7

1 Poles and transmission zeros 11
1.1 Introduction . . . 11
1.2 Reminder on principles of system dynamics . . . 12
1.2.1 The single-degree-of-freedom system . . . 12
1.2.2 The effects of active control on the system dynamics . . . 14
1.2.3 Multiple-degree-of-freedom system . . . 15
1.2.4 State-space representation . . . 17
1.2.5 Modal decomposition and truncation . . . 18
1.3 Zeros in single input single output systems . . . 21
1.3.1 Zeros in SISO collocated system . . . 23
1.3.2 Zeros in SISO non-collocated system . . . 24
1.4 Computation of the zero value in SISO systems . . . 26
1.4.1 The analytical zero approximation for collocated systems . . . 26
1.5 Zeros in multiple inputs multiple outputs systems . . . 30
1.5.1 Computation of the TZs in collocated MIMO systems . . . 30
1.5.2 Properties of the TZs in collocated MIMO systems . . . 32
1.6 Conclusion . . . 34
References . . . 34

2 The pole-zero distance as a mean to evaluate damping 37
2.1 Introduction . . . 37
2.1.1 Link between pole-zero distance and damping in SISO systems . . . 38
2.1.2 Motivation and chapter outline . . . 39
2.2 Link between PZ distance and damping in MIMO systems . . . 39
2.2.1 Numerical validation of the MIMO extension . . . 41
2.3 Experimental validation of the link in MIMO systems . . . 45
2.4 Conclusion . . . 52
References . . . 53

3 Introduction of the pole-zero distance criterion **55**
3.1 Introduction . . . 55
3.2 Literature review on optimal placement criteria . . . 56
3.2.1 Criterion in open-loop configuration . . . 56
3.2.2 Criterion in closed-loop configuration . . . 59
3.3 The proposed PZ distance criterion . . . 61
3.4 Discussion and numerical validation of the PZ distance criterion . . . 64
3.4.1 Application to a SISO system . . . 64
3.4.2 Application to a MIMO system . . . 71
3.5 Conclusion . . . 76
References . . . 77

4 The pole-zero distance criterion for fast transducer placement optimization **81**
4.1 Introduction . . . 81
4.2 Genetic algorithms and gradient descent convergence . . . 83
4.3 On the use of the PZ distance criterion to apply a non-evolutionary algorithm 85
4.3.1 Numerical validation of the proposed approach . . . 87
4.4 Conclusion . . . 95
References . . . 96

5 Application of the optimization method to industrial structures **99**
5.1 Introduction . . . 99
5.2 Wing of a Boeing 777-200ER . . . 100
5.2.1 Description of the model . . . 101
5.2.2 Application of the optimization method . . . 104
5.2.3 Conclusion . . . 111
5.3 Wafer gripper from ASML . . . 111
5.3.1 Description of the model . . . 113
5.3.2 Application of the optimization method . . . 114
5.3.3 Conclusion . . . 118
5.4 Reliability of the FE models and methodology for model matching . . . 119
5.4.1 Discussion on the reliability of the FE model . . . 119
5.4.2 Matching of the piezoelectric patch . . . 121
5.4.3 Matching of the structural properties . . . 128
5.4.4 Matching of the boundary conditions . . . 130
5.4.5 Final comparison and conclusion . . . 131
5.5 Conclusion . . . 132
References . . . 133

6 Conclusions **135**
Perspectives for future research . . . 136
Publications associated with this thesis . . . 139

A Analysis of the beam and shell elements **143**
A.1 Description of the beam elements . . . 143
A.2 Description of the multi-layer shell elements . . . 143
A.3 On the use of shell elements for piezoelectric patch modelling . . . 145

B Analysis of the search algorithms **147**
B.1 Analysis of the Genetic algorithm from Matlab . . . 147
B.2 Analysis of the *'fminsearch'* algorithm from Matlab . . . 148

List of Figures

1.1 Representation of a fundamental sDoF system 12
1.2 Effect of the damping ratio on the free response of a sDoF submitted to an initial displacement 13
1.3 Bode plot of a sDoF system 14
1.4 Block diagram of a system with a feedback controller 15
1.5 Root locus obtained with the demonstration active damping system 16
1.6 Illustration of the modal decomposition of a transfer function 19
1.7 Illustration of the modal truncation 20
1.8 Effect of the SA position on the zero frequency 22
1.9 Evolution of the zeros as a function of a collocated SA pair position along a cantilever beam 23
1.10 First three mode shapes of a cantilever beam 24
1.11 Illustration of the phenomena that can appear when non-collocated pair is used: zeros migration and pole-zero flipping 25
1.12 Numerical systems used to assess the proposed analytical approximation of the zero 28
1.13 Maximum relative errors of the proposed zero approximation on two systems 29
1.14 Open-loop response of a simple MIMO system 32
1.15 Response of a simple MIMO system when zero input directions are applied 33

2.1 Graphical illustration of the link between the PZ distance and the maximum reachable damping ratio 38
2.2 Illustration of the hypothesis on the root locus for the MIMO extension of direct link with damping 40
2.3 Representation of the two structural systems used for the numerical validation 42
2.4 Root locus obtained with an identical decentralised DVF controller for two MIMO configurations 44
2.5 Maximum reachable damping ratio as a function of the normalised pole-TZ distance obtained with numerical simulations 45
2.6 MFC patch array used for the experimental validation of the MIMO extension 45
2.7 Experimental system used to validate the MIMO extension 46
2.8 Maximum reachable damping ratio as a function of the normalised pole-TZ from the experimentally extracted model 48
2.9 Illustration (top view) of the four configurations that have been experimentally tested 49
2.10 Illustration of the control scheme used for the experimental validation . . . 49
2.11 Comparison between the simulated and the experimental closed-loop poles convergence for the experimental validation of the MIMO extension 50
2.12 Comparison between the experimental and the simulated loop gain functions 51

3.1 Illustration of the current trade-off between performance and computational cost for the optimal placement criteria . . . 61
3.3 Illustration of the loss of controllability and root locus reshaping due to adjacent zero . . . 63
3.4 Graphical representation of the three PZ distance criterion factors . . . 63
3.5 Numerical cantilever beam used to validate the PZ distance criterion in SISO systems . . . 64
3.6 Normalized PZ distance criterion obtained on the cantilever beam for modes 1, 2 and 3 . . . 65
3.7 Normalized PZ distance criterion obtained on the cantilever beam for modes 1 & 2 and modes 2 & 3 . . . 65
3.8 Normalised Gramian and normalised spatial H_2 criteria obtained on the cantilever beam for modes 1, 2 and 3 . . . 66
3.9 Gramian criterion as function of the modal amplitude obtained on the cantilever beam for modes 1, 2 and 3 . . . 67
3.10 PZ criterion as function of the modal amplitude obtained on the cantilever beam for modes 1, 2 and 3 . . . 67
3.11 PZ distance as function of the modal amplitude obtained on the cantilever beam for the second mode . . . 68
3.12 Root locus obtained at a position that presents a large PZ distance but a small modal amplitude for the second mode . . . 69
3.13 Damping ratios in closed-loop obtained with three open-loop criteria on a cantilever beam for single mode damping . . . 70
3.14 Damping ratios in closed-loop obtained with three open-loop criteria on a cantilever beam for multi-modal damping . . . 70
3.15 Frequency response functions obtained with three open-loop criteria on a cantilever beam for multi-modal damping . . . 71
3.16 Numerical cantilever beam used to validate the PZ distance criterion with MIMO systems . . . 72
3.17 Modal amplitudes of modes 4, 5 & 6 obtained with the MIMO cantilever beam . . . 72
3.18 Normalized PZ distance criterion obtained on the MIMO cantilever beam for the simultaneous damping of modes 4, 5 & 6 . . . 74
3.19 Strain map of modes 4, 5 & 6 obtained with the MIMO cantilever beam . . . 75
3.20 PZ distance as function of the strain obtained on the cantilever beam for modes 4, 5 and 6 . . . 76
3.21 Root locus obtained at the positions that maximises the PZ distance and the strain for the fourth mode . . . 77

4.1 Illustration of the convergence process of a GA . . . 83
4.2 Illustration of the convergence process of the gradient descent algorithm . . . 84
4.3 Illustration of the identification method for establishing the limited positions to be evaluated by the PZ distance criterion on a simply supported beam . . . 86
4.4 Flowchart of the proposed optimization method . . . 87
4.5 Numerical cantilever beam used to validate the proposed approach . . . 88
4.6 Graphical representation of the limited positions to be evaluated by the PZ distance criterion . . . 88
4.7 Comparison of the number of evaluations and the performance obtained with the PZ, the Gramian and the GA approaches on the cantilever beam . . . 91
4.8 Comparison of the damping convergence of the first bending mode of the beam between the direct search algorithm and the GA . . . 92

4.9 Convergence of the direct search algorithm for the first bending mode of the cantilever beam (focus on the parameters) . . . 93
4.10 Convergence of the genetic algorithm for the first bending mode of the cantilever beam (focus on the parameters) . . . 93
4.11 Sensitivity analysis of the SA pair misplacement with respect to the optimal positions . . . 94
4.12 Maximum reachable modal damping along the longitudinal axis of the cantilever beam for the second bending mode . . . 95

5.1 Picture of a Boeing 777-200ER that proceeds to its take-off . . . 100
5.2 Illustration of the numerical wing of the Boeing 777-200ER used to validate the proposed approach . . . 102
5.3 First four mode shapes of the Boeing 777-200ER wing (bending and torsion) 103
5.4 Limited positions on the wing of the Boeing 777-200ER to be evaluated by the PZ distance criterion . . . 104
5.5 Comparison of the damping convergence of the first three modes of the wing with the PZ distance criterion and the modal amplitude methods . . . 106
5.6 Comparison of the convergence for multi-modal damping of modes 1 & 2 on the wing with the PZ distance criterion and the modal amplitude methods 107
5.7 Convergence of the *'fminsearch'* algorithm for the first mode of the wing (focus on the parameters) . . . 108
5.8 Sensitivity analysis of the SA pair misplacement with respect to the optimal positions on the Boeing 777-200ER wing . . . 109
5.9 Illustration of a silicon wafer and a thin wafer gripper . . . 112
5.10 Experimental setup of the ASML wafer gripper available at the Department of Precision and Microsystems Engineering . . . 112
5.11 Illustration of the numerical ASML wafer gripper model and its high mesh density used to perform the optimal placement optimization . . . 113
5.12 First two natural frequencies of the wafer gripper and illustration of their related mode shapes . . . 114
5.13 Visualization of the limited configurations on the ASML wafer gripper to be evaluated by the PZ distance criterion . . . 115
5.14 Convergence of the *'fminsearch'* algorithm for the multi-modal damping of modes 1 & 2 performed on the ASML wafer gripper (focus on the damping values) . . . 116
5.15 Convergence of the *'fminsearch'* algorithm for the multi-modal damping of modes 1 & 2 on the ASML wafer gripper model (focus on the parameters) . 117
5.16 Illustration of the original MIMO configuration on the ASML wafer gripper model (experimental setup) and the optimised one based on the PZ distance approach. . . . 119
5.17 Comparison between the experimental response and the FE prediction obtained on a cantilever beam with five pairs of MFC piezoelectric patches . . 121
5.18 Illustration of a piezoelectric stack and the general shape of the impedance curve of a piezoelectric transducer . . . 123
5.19 Illustration of the matching procedure for the piezoelectric patch on a MFC example . . . 125
5.21 Illustration of the matching procedure for the piezoelectric patch on a MFC example with step 7 (zero frequency adjustment) and final comparison between the experimental response of the MFC patch and its tuned model . . 126
5.22 Consistency analysis on the 10 MFC piezoelectric patches . . . 128

5.23 Visual comparison between the original FE model response of a cantilever beam with piezoelectric patches, its experimental response and the tuned FE model response based on the proposed model matching procedure . . . 132

A.1 General layout of a MFC patch 144
A.2 Illustration of the multilayer principle in SDT 144
A.3 Illustration of the localised deformation in the vicinity of a piezoelectric patch when actuated and visualization of the induced transverse strain . . . 145

B.1 Visual illustration of the mechanisms to update the simplex 151

List of Tables

1.1 Numerical values used for the demonstration active damping system 16
1.2 Maximum relative error and processing time to compute 600 SA positions with three different methods 28

3.1 Damping ratios in closed-loop obtained with the PZ distance criterion on the MIMO beam for multi-modal damping 73

4.1 Parameter settings used for the implementation of the GA 90
4.2 Normalised optimal positions obtained with the PZ, the Gramian and the GA approaches on the cantilever beam 90

5.1 First four natural frequencies of the Boeing 777-200ER wing and the type of each related mode shape 103
5.2 Modal damping results obtained for the first mode of the wing when the lead control law parameters are tuned at the optimal position derived with the proposed approach 110
5.3 Comparison of the convergence outcomes when two different lead control laws are implemented for the convergence of the first mode of the wing . . . 111
5.4 Comparison of the MIMO closed-loop performance on the ASML wafer gripper obtained with the original configuration from the experimental setup and the optimised one based on the PZ distance approach 118
5.5 Comparison between the original and the tuned values of the MFC parameters based on the piezoelectric matching procedure 127
5.6 Comparison of the first three resonance frequencies of a beam between the experimental setup and its FE model (structural properties matching procedure) 129
5.7 Comparison of the first three resonance frequencies of a beam between the experimental setup and its FE model (boundary conditions matching) . . . 131
5.8 Comparison between the original and the tuned values of the cantilever beam parameters based on the boundary conditions matching procedure . . 131

B.2 Remaining parameter settings used for the implementation of the GA . . . 148
B.3 Parameter settings implemented in the *'fminsearch'* algorithm for the validation of the proposed method on the cantilever beam 151
B.4 Parameter settings implemented in the *'fminsearch'* algorithm for the validation of the proposed method on the wing of the Boeing 777-200ER 151
B.5 Parameter settings implemented in the *'fminsearch'* algorithm for the validation of the proposed method on the wafer gripper 152

Acronyms

3D 3-dimensional.

CRM Common Research Model.

DVF direct velocity feedback.
DoF degree of freedom.

FE finite element.

GA genetic algorithm.

HAC high authority controller.

IFF integral force feedback.

LAC low authority controller.

MFC macrof fiber composites.
MIMO multiple inputs multiple outputs.

ODE ordinary differential equation.

PPF positive position feedback.
PZ pole-zero.
PZT lead zirconate titanate ceramic material.

SA sensor and actuator.
SDT Structural Dynamics Toolbox.
SISO single input single output.

TZ transmission zero.

sDoF single-degree-of-freedom.

Notations and operators

$\{\,.\,\}$	Vector notation.
$\lceil\,.\,\rceil$	Ceiling function.
$[\,.\,]$	Matrix notation.
$.^H$	Complex-conjugate transpose operator.
$.^T$	Transpose operator.
0_{ab}	$a \times b$ zero matrix.
I_N	$n \times n$ identity matrix.
$tr(\,.\,)$	Trace operator.
$\lvert\,.\,\rvert$	Modulus operator of a complex number.

Introduction

The vibrations of an elastic structure appear when a deviation of its structural equilibrium state arises due to external and/or internal dynamic loadings. When such dynamic disturbances match the natural frequencies of the system, the resonance phenomenon occurs which translates to a significant magnification of the system response. The presence of such unwanted vibrations and resonance phenomena is a critical concern in numerous industrial applications. They can indeed alter the stability, the reliability and the efficiency of the affected system at different degrees of severity. Consequently, the appearance of spurious vibrations on systems as well as their related consequences have been widely studied for the past decades in the industrial sector.

The loss of comfort for the end user is an effect that is often encountered on a daily basis due to undesirable vibrations and their resulting parasitic noise. For example, the transport industry is highly concerned with reducing the level of noise produced during operation, e.g. in the automotive [1, 2] or in the rail sector [3, 4].

Operational errors are another type of effect induced by vibrations that prevent the system from properly and/or efficiently work. Satellites are well-known to be subjected to micro-vibration problems that can, among others, degrade their attitude stability capability [5, 6] or alter the quality of the images captured from orbit. This is reflected in Figure 1a [7] where the comparison between the same image captured with or without the presence of vibrations is highlighted. Several other examples exist, such as the different works conducted to ensure high quality from imaging systems [8, 9] or the efforts implemented by the semiconductor industry to engrave the computer chips even smaller and faster by reducing the vibration levels, as done in [10, 11]. Fundamental research equipments are part of another representative field that is highly concerned by operational errors. Indeed, the exploration of the universe and the experimental study of physical phenomena usually require large structures that are extremely sensitive to the presence of unwanted vibrations. For example, the Laser Interferometer Gravitational-Wave Observatory that aims to sense the cosmic gravitational waves is composed by a 4 km long detector that is sensitive to ground motion. Many studies are consequently performed to reduce the level of vibrations of such equipment [12] or to improve the performance of the involved sensors [13].

The third and most severe effect of spurious vibrations concerns the appearance of structural damages to the system. Those damages can result from excessive resonance amplification leading to large deformation of the structure, which generates too high internal stress levels with respect to the material limit. An emblematic example illustrating this effect is the collapse of the Tacoma Narrows bridge in 1940 which has been captured during its failure and shown in Figure 1b [14]. This famous failure was indeed, among others, due to such internal resonance effects [15]. Internal damages can also occur from fatigue phenomena, i.e. when the initiation and the propagation of cracks appear in the system due to cyclic loading even though the stress level inside the material is below the ultimate strength value. Such a failure is illustrated in [16] where the fatigue after only three years

of service of a helical gear from a bus gearbox is studied. Consequently, to comply with the safety regulations and avoid massive field returns during the warranty period because of early failures, manufacturers must ensure that their systems present enough resilience to cyclic vibrations.

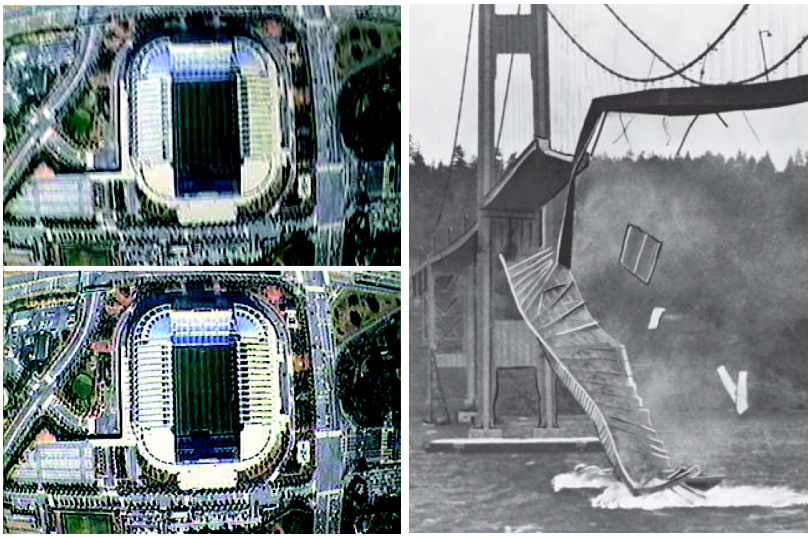

(a) Operational error [7] (b) Failure from resonance [14]

Figure 1: Illustration of detrimental effects due to vibrations: (a) same image captured by a satellite with and without vibrations, (b) failure of the Tacoma Narrows bridge.

Vibration alleviation

Specific precautions need to be taken during the design phase to avoid that the severity of the detrimental effects reaches a defined threshold on the considered system. When the level of vibration is still problematic despite the implemented design precautions (e.g. due to the limitation of the possible solutions during the conception phase or a poor modelling of the system with respect to its real-life behaviour), additional actions are required to mitigate the vibrations and to ensure that the requirements of the product are met. Different techniques exist and the choice of the most adequate depends on many parameters, including the sources of disturbances, the damping objectives or the operating conditions. The three most common ones can be identified as stiffening (an increase of the overall stiffness of the system to shift the resonance frequencies out of the dynamic loading frequency band), isolation (the decoupling of the disturbance with respect to the sensitive part(s) of the system) and damping (a reduction of the resonance(s) amplification by dissipating the vibrational energy or by applying counteracting forces) [17].

Mitigation by damping

Nowadays, for technical, economical and environmental requirements, large and lightweight structures are preferred for reaching high performance. Unfortunately, this translates to systems that present small internal damping. For example, the aerospace sector challenges the development of monolithic sub-structures instead of assembled ones as done in the past, which inevitably lowers the damping [18]. This thesis is concerned with industrial systems that encounter vibration problems because of small internal damping.

The reduction of the resonance effect by damping can be achieved passively, actively or by a combination of both approaches . Passive damping is performed with systems that dissipate the vibrational energy. This dissipation can be performed by transferring the vibration energy towards another secondary structure as done with dynamic vibration absorbers. The mass of the absorber is tuned to resonate at a specific frequency and starts to oscillate when a corresponding disturbance appears, which reduces the overall vibration [19]. Passive damping can also be performed by converting the mechanical vibrating energy into another form, e.g. in electrical energy by using piezoelectric transducers. This energy can then be dissipated in heat through a tuned electrical circuit [20] or harvested for low consumption appliances [21]. Although passive damping systems are simple and present low cost to be implemented, the damping performance is limited by the system properties. Moreover, their effectiveness strongly depends on the proper modelling of the system dynamics. Indeed, they usually present a narrow operating frequency bandwidth which should match the targeted resonance to properly work. Finally, a modification of the system properties (e.g. due to ageing or due to high-temperature sensitivity) can alter the damping efficiency over time.

In active damping, the strategy consists of using transducers that directly measure and act on the system dynamics: a controller unit receives the signal from the sensor(s) and delivers, using a defined control law, the interpreted signal(s) to the actuator(s). Unlike with the passive method, active damping requires an external power source to supply energy to the controller unit, to the actuator(s) and possibly to the sensor(s) as well. A schematic representation of a typical active damping architecture is given in Figure 2. Although the active damping strategy increases the control performance compared to the passive approach, it is (1) more complex (integration of the transducers on the system, defining and tuning of the control law, wiring of the feedback loop) and (2) more expensive to implement (costs for the transducers, the controller unit, the power supply, the signal conditioner if any).

Hybrid damping consists of combining the passive and the active methods to benefit from the advantages of both systems. It can cover a larger frequency bandwidth, reduce the power consumption or increase the reliability of the control unit by having redundancy. Nevertheless, those benefits come at the expense of a more complex architecture [22].

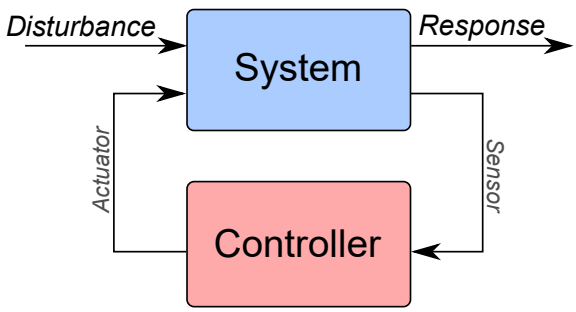

Figure 2: Schematic representation of an active control loop.

During the conception of the damping control architecture, the appropriate number of transducers to use and their suitable positioning on the system to be controlled is a well-established concern. A poor choice of their locations can indeed deteriorate the performance of the control architecture by inducing a lack of controllability and/or observability, i.e. the ability of the control architecture to modify/observe the dynamics of the system. For active damping, it can lead in the worst case to stability concerns when the transducers

are non-collocated, i.e. when the sensor and the actuator are not placed in the vicinity of each other [23]. The interest in optimal transducers placement strategies is highlighted by the numerous types of research that have been performed during the past decades and by the availability of several technical reviews that analyse the different optimal placement techniques, for example in [24–26].

Optimal positioning of the transducer

The problem of mathematical optimization consists in finding the values of the involved parameter(s) that either maximize or minimize a defined objective function. In the context of optimal positioning of the transducer, the objective function is commonly called the placement criterion. The major difficulty related to the optimal transducer placement is that the obtained positioning solution highly depends on the criterion used to perform the optimization, impacting therefore the performance of the controlled structure. Hence, the selection of the placement criterion to use among all the ones that are available in the literature is of major importance. When considering active damping, although the transducers are part of a closed-loop architecture, their optimal placement can be performed either in open-loop or closed-loop configurations.

Open-loop criterion

The open-loop optimization is focusing on the plant open-loop model only, i.e. the dynamics of the control that will be used afterwards is not considered in the optimization process. Because the transducers must be positioned in a place that ensures authority over the structure, a vast majority of the open-loop criteria is based on maximizing the controllability and/or the observability of the transducers. This concept was first introduced in 1992 by Hac et al. [27], who proposed the Gramian controllability and observability that allow to scale the level of authority of the transducers over the targeted modes. This led to an innovative cost function which has then been widely used in other studies by slightly modifying the criterion or by adding some constraints to the optimization (e.g. for the optimization of the location of piezoelectric sensors and actuators on a simply supported beam [28], for the positioning of piezoelectric patches on plates [29, 30] or for the piezoelectric positioning on a large flexible structure [31]). Another emblematic open-loop optimization concept relies on the maximization of the H_2 norm, i.e. the amplitude of vibration the input can induce at the output [32]. Several studies based on this H_2 norm have been conducted, for example its extension to the spatial H_2 norm by Moheimani [33]. This spatial extension allows to compute the norm over a domain of interest instead of just a location. Another example is the addition of constraints to the H_2 cost function in order to reduce the risk of destabilization at high frequencies as done in [34].

Although the open-loop criteria are rather simple to implement and do not require large computational efforts, they present a major drawback. Indeed, they do not account for the additional dynamics brought by the controller in the system as they only focus on open-loop optimization. Considering that a strong interaction between this extra dynamics and the one from the plant is highly probable, performing the placement optimization in open-loop can lead to sub-optimal solutions, as demonstrated for instance by Devasia et al. [35]. To overcome this notable inconvenience, the optimal placement study can be performed in closed-loop configurations.

Closed-loop criterion

The optimal placement of the transducers in closed-loop configuration adds to the optimization process the control law and optimizes therefore the control parameters simultaneously with the position of the transducers. Such closed-loop optimization was already developed in 1983 by Schulz et al. [36] in which the criterion was based on the maximization of the energy dissipated through the controller. Dhingra and Lee adapted this criterion a few years later to ease its calculation by removing the dependence on the initial conditions [37]. Cost functions based on the maximization of the damping emerged as well, such as the work from Kang et al. dealing with the optimization of piezoelectric placement and gain values with a state feedback controller [38]. Recently, even more advanced controllers have been used in closed-loop placement optimizations. For example, several positioning criteria have been developed based on the use of a linear–quadratic regulator [39–41], i.e. a modern controller that tries to minimise the control effort and the deviation of the system with respect to its targeted state.

Although including the control law in the optimization process certainly improves the performance compared to the one obtained with open-loop optimizations, the computational costs related to the evaluation of the criterion drastically increase. Indeed, the optimization has to be performed by combining the position of the transducer(s) and the parameter(s) of the control law. Moreover, modern controllers usually require a strong knowledge of the system dynamics, which is often not fully available and presents inaccuracies. It is therefore clear that a real trade-off exists between the achievable performance obtained with the selected optimization criterion and the computational time required for its evaluation.

Optimization algorithms

Whether the chosen placement criterion is in an open or closed-loop configuration, the implementation of a search algorithm is usually considered to obtain the optimal solution. The aim of such an algorithm is to converge towards the best solution without computing all possible combinations. A full analysis can indeed be prohibitive when the evaluation of the objective function is expensive in terms of computational time and/or when too many combinations are possible. The genetic search algorithms are often considered in the literature for optimal positioning studies. Inspired by the process of natural selection, those stochastic algorithms do not need prior knowledge, they can solve linear and non-linear problems and they can find the global optimum despite the presence of multiple local ones [42]. They are consequently well suited for the optimization of transducer placement.

Nevertheless, a major drawback inherent to such a search algorithm is that it requires numerous iterations to properly converge. Extremely long computational time may therefore be required for a large and/or complex structure for which each evaluation of the cost function can be very demanding in terms of computational effort. In addition, a proper tuning of the algorithm parameters is required to achieve a satisfying convergence, which may necessitate several attempts before obtaining an acceptable solution. Consequently, and because of the highly possible prohibitive convergence duration, the optimization of transducer(s) position for real industrial applications is unfortunately not commonly implemented.

Contribution of the thesis

As reported, the use of transducer placement optimization for industrial systems faces two major obstacles. First, the trade-off that exists between the performance that can be obtained with the placement criterion and its related computational time. Secondly, the quasi-mandatory use of a genetic search algorithm to perform the convergence and obtain the solution, which requires a tremendous number of evaluations. When high-performance and complex structures are targeted, the combination of those two aspects clearly results in an extremely long computational time (up to several days or weeks), which is not conceivable in the industrial sector.

The aim of this doctoral thesis is to develop innovative solutions that will grant to conduct optimal transducer placement with limited computational cost. For this purpose, a novel placement criterion for maximizing the damping has been developed. This criterion targets collocated systems and is based on the maximization of the distance between the poles and the zeros that are respectively the resonance frequencies and the frequencies for which a non-zero harmonic input leads to a zero output. This distance has indeed a direct link with the maximum achievable damping ratio once in closed-loop when a low authority controller is applied on a system with a single collocated pair. The advantage of this new criterion relies consequently on its fast open-loop evaluation and its efficient closed-loop prediction. Different aspects have been pursued in connection with this new criterion which led to those 5 main original contributions:

- The development and introduction of the innovative open-loop pole-zero distance criterion for maximizing the structural damping.
- The numerical validation of the pole-zero distance criterion by its comparison to other open-loop criteria. This validation focuses on the performance (damping) and the robustness to misplacement of the optimal solutions.
- The introduction of a new placement optimization approach which does not require the use of a genetic algorithm but employs a non-evolutionary approach instead. This approach is made possible thanks to the use of the pole-zero distance criterion that provides an efficient and reliable starting point for the search algorithm.
- The development of an analytic approximation of the zero values. The advantage of this approximation is the possibility to compute the zeros of multiple transducer positions at once using simple arithmetic operations.
- The extension of the link between the pole-zero distance and the damping in collocated single input single output systems to multiple inputs multiple outputs ones. This extension is numerically demonstrated and experimentally validated.

To present those contributions in detail, this thesis is organised in three parts. The first one, composed of Chapters 1 and 2, focuses on the link between pole-zero distance and maximum damping for collocated architectures. Chapter 1 recalls the important notions about structural dynamics that are used throughout the manuscript. It first provides the fundamentals of control theory and analyses the mathematical and physical meanings of the zeros. Subsequently, an analytical approximation for fast calculation of the zeros is introduced. The concept of direct link between pole-zero distance and maximum reachable damping is then analysed in Chapter 2. This well-established link in system equiped with a single pair of collocated transducers pair is first reviewed. The extension of the link for multiple pairs is then mathematically and numerically proved with two systems: a cantilever beam and a simply supported plate. Ultimately, this link is experimentally

validated on a cantilever beam.

The second part is constituted of Chapters 3 and 4 and is concerned with the introduction of the new pole-zero distance criterion. Chapter 3 starts with a brief review of the different placement criteria available in the literature. The pole-zero distance criterion is then introduced and its effectiveness is illustrated with numerical systems by comparing the performance with other open-loop criteria. Afterwards, Chapter 4 addresses the use of optimization algorithms when performing transducer placement optimizations. It first outlines the long processing time inherent to genetic search algorithms that are widely employed in optimal placement studies. A remedy is to use a non-evolutionary algorithm, which is possible with the proposed pole-zero distance criterion that provides a efficient and reliable starting point. This approach is consequently numerically applied on a cantilever beam.

The last part of the thesis consists of Chapter 5. It presents the application of the proposed method to two industrial systems: (1) the wing of a Boeing 777-200ER and (2) a wafer gripper from ASML, a Dutch company specialised in the development and manufacturing of photolithography machines used to produce computer chips [43]. After the application of the method on those two structures, a discussion on the reliability of the numerical models is conducted. It is demonstrated that matching a simple cantilever beam model with respect to its equivalent experimental setup can already be a challenge. Based on those observations, the importance of robustness when designing an active control strategy is then discussed.

Finally, conclusions regarding the presented research and the associated contributions are drawn in Chapter 6. Ultimately, comments about the possible extension of the work for future studies are given as well.

References

[1] K. C. Panda. "Dealing with Noise and Vibration in Automotive Industry". In: *Procedia Engineering* 144 (2016), pp. 1167–1174. DOI: 10.1016/j.proeng.2016.05.092.

[2] D. J. O'Boy. "Automotive wheel and tyre design for suppression of acoustic cavity noise through the incorporation of passive resonators". In: *Journal of Sound and Vibration* 467 (2020), p. 15037. DOI: 10.1016/j.jsv.2019.115037.

[3] C. Collette. "Rail corrugation mitigation via a dynamic vibration absorber mounted on driven wheel sets of metro vehicles". In: *Third International Conference on Advanced Computational Methods in Engineering*. 2005.

[4] D. Thompson, C. Jones, T. Waters, and D. Farrington. "A tuned damping device for reducing noise from railway track". In: *Applied acoustics* 68.1 (2007), pp. 43–57. DOI: 10.1016/j.apacoust.2006.05.001.

[5] C. Peng, X. Zhou, T. Wei, and Y. Ren. "High precision synchronous vibration suppression for a MSFW subject to phase lag influence". In: *Mechanical Systems and Signal Processing* 120 (2019), pp. 408–421. DOI: 10.1016/j.ymssp.2018.10.017.

[6] C. Liua, X. Jing, S. Daley, and F. Li. "Recent advances in micro-vibration isolation". In: *Mechanical Systems and Signal Processing* 56–57 (2015), pp. 55–80. DOI: 10.1016/j.ymssp.2014.10.007.

[7] D.-O. Lee, L.-H. Kang, and J.-H. Han. "Active vibration isolation demonstration system using the piezoelectric unimorph with mechanically pre-stressed substrate". In: *Journal of Intelligent Material Systems and Structures* 22.13 (2011), pp. 1399–1409. DOI: 10.1177/1045389X11411215.

[8] S. Kuiper and G. Schitter. "Active damping of a piezoelectric tube scanner using self-sensing piezo actuation". In: *Mechatronics* 20.6 (2010), pp. 656–665. DOI: 10.1016/j.mechatronics.2010.07.003.

[9] M. Smrz, R. Bastaits, and A. Preumont. "Active damping of the camera support mast of a Cherenkov Gamma-ray telescope". In: *Nuclear Instruments and Methods in Physics Research Section A: Accelerators, Spectrometers, Detectors and Associated Equipment* 635.1 (2011), pp. 44–52. DOI: 10.1016/j.nima.2011.01.092.

[10] W. Aribowo, T. Yamashita, K. Terashima, Y. Masui, T. Saeki, T. Kamigaki, and H. Kawamura. "Vibration control of semiconductor wafer transfer robot by building an integrated tool of parameter identification and input shaping". In: *IFAC Proceedings Volumes* 44.1 (2011), pp. 14367–14373. DOI: 10.3182/20110828-6-IT-1002.02675.

[11] W. Tao, M. Zhang, M. Liu, and X. Yun. "Residual vibration analysis and suppression for SCARA robot arm in semiconductor manufacturing". In: *2006 IEEE/RSJ International Conference on Intelligent Robots and Systems*. IEEE. 2006, pp. 5153–5158. DOI: 10.1109/IROS.2006.282610.

[12] G. Zhao, B. Ding, J. Watchi, A. Deraemaeker, and C. Collette. "Experimental study on active seismic isolation using interferometric inertial sensors". In: *Mechanical Systems and Signal Processing* 145 (2020), p. 106959. DOI: 10.1016/j.ymssp.2020.106959.

[13] B. Ding, G. Zhao, J. Watchi, A. Sider, and C. Collette. "An interferometric inertial sensor for low-frequency seismic isolation". In: *Sensors and Actuators A: Physical* 335 (2022), p. 113398.

[14] D. W. Olson, S. F. Wolf, and J. M. Hook. "The tacoma narrows bridge collapse". In: *Physics today* 68.11 (2015), pp. 64–65.

[15] K. Billah and R. Scanlan. "Resonance, Tacoma Narrows Bridge failure, and undergraduate physics textbooks". In: *American Journal of Physics* 59 (1991), pp. 118–124. DOI: 10.1119/1.16590.

[16] O. Asi. "Fatigue failure of a helical gear in a gearbox". In: *Engineering failure analysis* 13.7 (2006), pp. 1116–1125. DOI: 10.1016/j.engfailanal.2005.07.020.

[17] A. Preumont. *Vibration Control of Active Structure, An Introduction*. Thrid Edition. Springer, 2011. DOI: 10.1007/978-94-007-2033-6.

[18] A. Paknejad. "Passive and Active Strategies for Vibration Control of Lightly Damped Structures". PhD thesis. Université Libre de Bruxelles, Ecole polytechnique de Bruxelles, 2021.

[19] V. Steffen Jr and D. Rade. "Dynamic vibration absorber". In: *Encyclopedia of Vibration* (2001), pp. 9–26. DOI: 10.1006/rwvb.2001.0176.

[20] J. Gripp and D. Rade. "Vibration and noise control using shunted piezoelectric transducers: A review". In: *Mechanical Systems and Signal Processing* 112 (2018), pp. 359–383. DOI: 10.1016/j.ymssp.2018.04.041.

[21] D. Spreemann and Y. Manoli. *Electromagnetic vibration energy harvesting devices: Architectures, design, modeling and optimization*. Vol. 35. Springer, 2012.

[22] A. M. Baz. *Active and passive vibration damping*. John Wiley & Sons, 2019.

[23] D. K. Miu. *Mechatronics: electromechanics and contromechanics*. Springer Science & Business Media, 1993.

[24] M. I. Frecker. "Recent advances in optimization of smart structures and actuators". In: *Journal of Intelligent Material Systems and Structures* 14.4-5 (2003), pp. 207–216. DOI: 10.1177/1045389X03031062.

[25] V. Gupta, M. Sharma, and N. Thakur. "Optimization Criteria for Optimal Placement of Piezoelectric Sensors and Actuators on a Smart Structure: A Technical Review". In: *Journal of Intelligent Material Systems and Structures* 21.12 (2010), pp. 1147–1156. DOI: 10.1177/1045389X10381659.

[26] K. Morris and S. Yang. "Comparison of actuator placement criteria for control of structures". In: *Journal of Sound and Vibration* 353 (2015), pp. 1–18. DOI: 10.1016/j.jsv.2015.05.002.

[27] A. Hac and L. Liu. "Sensor And Actuator Location In Motion Control Of Flexible Structures". In: *Journal of Sound and Vibration* 167.2 (1992), pp. 239–261. DOI: 10.1006/jsvi.1993.1333.

[28] I. Bruant and L. Proslier. "Optimal Location of Actuators and Sensors in Active Vibration Control". In: *Journal of Intelligent Material Systems and Structures* 16.3 (2005), pp. 197–206. DOI: 10.1177/1045389X05047989.

[29] A. Sadri, J. Wright, and R. Wynne. "Modelling and optimal placement of piezoelectric actuators in isotropic plates using genetic algorithms". In: *Smart Materials and Structures* 8 (1999), pp. 490–498. DOI: 10.1088/0964-1726/8/4/306.

[30] F. Peng, A. Ng, and Y.-R. Hu. "Actuator Placement Optimization and Adaptive Vibration Control of Plate Smart Structures". In: *Journal of Intelligent Material Systems and Structures* 16.3 (2005), pp. 263–271. DOI: 10.1177/1045389X05050105.

[31] K. Lim. "Method for optimal actuator and sensor placement for large flexible structures". In: *Journal of Guidance, Control, and Dynamics* 15.1 (1992), pp. 49–57. DOI: 10.2514/3.20800.

[32] W. Gawronski. *Advanced Structural Dynamics and Active Control of Structures*. Mechanical Engineering Series. Springer-Verlag New York, 2004. DOI: 10.1007/978-0-387-72133-0.

[33] S. Moheimani and T. Ryall. "Considerations on placement of piezoceramic actuators that are used in structural vibration control". In: *38th IEEE Conference on Decision and Control*. Vol. 2. 1999, pp. 1118–1123. DOI: 10.1109/CDC.1999.830077.

[34] W. Liu, Z. Hou, and M. Demetriou. "A computational scheme for the optimal sensor/actuator placement of flexible structures using spatial H_2 measures". In: *Mechanical Systems and Signal Processing* 20.4 (2006), pp. 881–895. DOI: 10.1016/j.ymssp.2005.08.030.

[35] S. Devasia, T. Meressi, B. Paden, and E. Bayo. "Piezoelectric actuator design for vibration suppression - Placement and sizing". In: *Journal of Guidance, Control, and Dynamics* 16.5 (1993), pp. 859–864. DOI: 10.2514/3.21093.

[36] G. Schulz and G. Heimbold. "Dislocated actuator/sensor positioning and feedback design for flexible structures". In: *Journal of Guidance, Control, and Dynamics* 6.5 (1983), pp. 361–367. DOI: 10.2514/3.19843.

[37] A. Dhingra and B. Lee. "Optimal Placement Of Actuators In Actively Controlled Structures". In: *Engineering Optimization* 23.2 (1994), pp. 99–118. DOI: 10.1080/03052159408941347.

[38] Y. Kang, H. Park, W. Hwang, and K. Han. "Optimum Placement of Piezoelectric Sensor/Actuator for Vibration Control of Laminated Beams". In: *AIAA Journal* 34.9 (1996), pp. 1921–1926. DOI: 10.2514/3.13326.

[39] K. Bendine, F. Boukhoulda, and M. Haddag B. andNouari. "Active vibration control of composite plate with optimal placement of piezoelectric patches". In: *Mechanics of Advanced Materials and Structures* 26.4 (2017), pp. 341–349. DOI: 10.1080/15376494.2017.1387324.

[40] A. Daraji and J. Hale. "Reduction of structural weight, costs and complexity of a control system in the active vibration reduction of flexible structures". In: *Smart Materials and Structures* 23.9 (2014), p. 095013. DOI: 10.1088/0964-1726/23/9/095013.

[41] K. R. Kumar and S. Narayanan. "The optimal location of piezoelectric actuators and sensors for vibration control of plates". In: *Smart Materials and Structures* 16.6 (2007), pp. 2680–2691. DOI: 10.1088/0964-1726/16/6/073.

[42] M. Mitchell. *An Introduction to Genetic Algorithms*. MIT Press, 1998.

[43] *ASML Holding N.V.* URL: https://www.asml.com/en.

Chapter 1

Poles and transmission zeros

Abstract

This chapter presents important notions that will be used throughout this thesis. It first properly defines the concept of pole and damping from the mathematical point of view and provides physical illustration of their crucial impact on system dynamics. The representation of physical systems via mathematical models is studied, including their possible truncation. The zeros of a system that presents one pair of transducers is then extensively studied, which clearly demonstrates their importance in the dynamical behaviour of structures. Emphasis is put on the different properties of the zeros and how to compute them. Because of the computational complexity observed to obtain their values, a analytical approximation is introduced. It is numerically demonstrated that the approximation is extremely efficient in terms of computational cost and provides enough accuracy to be used as a first efficient estimation of the zeros when needed. Finally, the zeros of systems with multiple transducer pairs are investigated and their specific properties are analysed.

1.1 Introduction

The poles of a mechanical system are an important element when implementing active or passive control solutions. They indeed define the stability of a system and govern its response when it is subjected to external disturbances. The poles also determine how the system can follow a defined command and how fast it can react to a change of set point.

Conversely, the zeros are often neglected in dynamic studies. Yet, the zeros of a dynamic system were already discussed in 1965 in [1] and properly defined for the first time by Rosenbrock in 1970 when considering multi-variable systems [2]. As for the poles, the zeros of a system play a crucial role in its behaviour and in the achievable performance of any implemented control architecture. They correspond to the frequencies at which the response of the system equals zero when a non-zero harmonic loading is applied. This explains why the zeros are often refereed as blocking or absorbed frequencies.

This first chapter presents the concepts of poles and zeros in structural dynamics and is organized as follows. Theoretical reminders on system dynamics are given in Section 1.2. The zero frequencies of systems with one single pair of transducers are extensively studied in Section 1.3 and the different methods for calculating them are reviewed in Section 1.4. The important sensitivity of the computational effort with respect to the system complexity is raised, which leads to the introduction of a new analytical approximation. The zeros of systems with multiple pairs of transducers are then studied in Section 1.5. It

is demonstrated that for such systems, there is a relationship between the zero frequencies and the applied inputs to ensure the absence of response. Finally, conclusions on the importance of the zeros in system dynamics are drawn in Section 1.6.

1.2 Reminder on principles of system dynamics

This section reminds important fundamentals on system dynamics that are used throughout this thesis. Section 1.2.1 recalls the response of a single-degree-of-freedom (sDoF) system and introduces, mathematically and physically, the concept of pole and damping ratio. The effect of an active control architecture on the dynamics of a sDoF system is studied in Section 1.2.2. Section 1.2.3 presents the multiple-degrees-of-freedom systems while Section 1.2.4 introduces the state-space representation of such systems. Finally, the concept of modal decomposition and frequency truncation are developed in Section 1.2.5.

1.2.1 The single-degree-of-freedom system

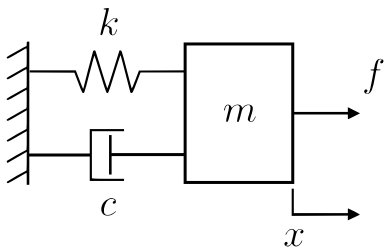

Figure 1.1: Representation of a fundamental sDoF system.

The basic notions of system dynamics can be addressed by first considering a sDoF system as shown in Figure 1.1. Composed of a mass m connected to a fixed reference through a linear spring of stiffness k and a linear viscous damper of damping constant c, such a simple structure can handily describe the concept of pole, system response and resonance. By considering the external force f acting on the mass and its induced displacement x defined in the same direction, the equation of motion is obtained using Newton's second law, which gives:

$$m\ddot{x} + c\dot{x} + kx = f \tag{1.1}$$

The resonance phenomenon of a system is purely intrinsic, i.e. it only depends on its physical properties and it is not impacted by the type nor position of the disturbance applied on the system. It is consequently studied in a free-vibration configuration which consists of cancelling the right hand side of Equation 1.1. The resulting homogeneous differential equation can be solved by assuming that its solution has the form $x = e^{st}$, where t is the time and s is an unknown constant called the pole of the system. Due to this assumption, the differential equation simplifies into the following algebraic characteristic equation:

$$ms^2 + cs + k = 0 \tag{1.2}$$

The solution of Equation 1.2 can be obtained without further difficulty:

$$s_{1,2} = -\frac{c}{2m} \pm \frac{\sqrt{c^2 - 4km}}{2m} \tag{1.3}$$

When considering practical cases, the damping constant c is small with respect to the stiffness value k [3]. Mathematically, this reads that $c^2 < 4km$, which leads to the complex solutions of s. In such a case, the solutions of s can be expressed by:

$$s_{1,2} = -\xi\omega_n \pm j\omega_d \tag{1.4}$$

where the natural frequency ω_n, the damping ratio ξ and the damped natural frequency ω_d are defined according to:

$$\omega_n^2 = \frac{k}{m}, \qquad \xi\omega_n = \frac{c}{2m}, \qquad \omega_d = \omega_n\sqrt{1-\xi^2} \tag{1.5}$$

Considering the response of the system in absence of external force and using the obtained solution of s given by Equation 1.4, the general solution of the equation of motion expressed by Equation 1.1 is:

$$x(t) = e^{-\xi\omega_n t}(A\,cos(\omega_d t) + B\,sin(\omega_d t)) \tag{1.6}$$

where A and B depend upon the initial displacement and velocity conditions. The analysis of this free response provides valuable insight regarding the role of the damping ratio ξ in system dynamics. Indeed, the motion of the mass decays following a decreasing exponential envelope, which is a function of the damping ratio and the natural frequency of the system. Hence, the time required to dissipate the oscillations induced by any external initial conditions is highly impacted by the internal damping coefficient of the system. This is highlighted by Figure 1.2 that illustrates, for an initial imposed displacement x_0, the free response of a sDoF system with two different damping coefficients ξ.

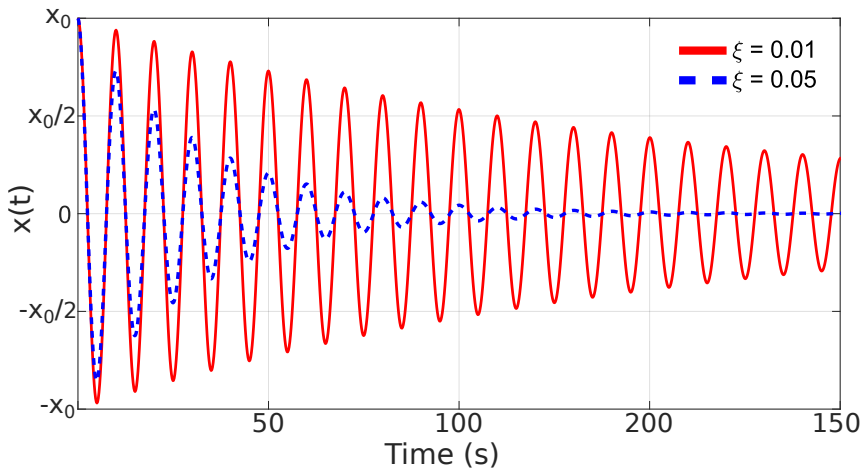

Figure 1.2: Effect of the damping ratio on the free response of a sDoF submitted to an initial displacement x_0.

The effect of the damping remains significant when the external force f is retained. If f is assumed to be harmonic at an angular frequency ω such that $f(t) = Fe^{j\omega t}$ where F is a complex amplitude, the structure will present a harmonic behaviour at the same frequency due to the linearity property. Hence, the response of the system can be expressed as $x(t) = Xe^{j\omega t}$ where X is another complex amplitude. Injecting those two harmonic signals within Equation 1.1 provides the following governing equation:

$$(-m\omega^2 + jc\omega + k)Xe^{j\omega t} = Fe^{j\omega t} \tag{1.7}$$

By using the definitions of the natural frequency and the damping ratio introduced in Equation 1.5, the ratio between the output displacement X and the input force F, called the compliance of the system, is expressed by:

$$G(\omega) = \frac{X}{F} = \frac{1}{k}\left(\frac{1}{1-(\omega/\omega_n)^2 + 2j\xi(\omega/\omega_n)}\right) \tag{1.8}$$

The compliance characterizes the complex response of the mass m when the external force f is a harmonic unitary force at frequency ω. Due to its complex nature, it allows to provide information on the magnitude of the response as well as on its phase, i.e. the lead or the lag of one signal with respect to the other. The compliance is consequently often graphically illustrated by a Bode diagram where both the magnitude and the phase are plotted with respect to ω. Such a representation is illustrated in Figure 1.3, which allows to clearly observe the dynamic amplification due to the resonance of the system in the vicinity of the natural frequency ω_n. Moreover, the magnitude of this amplification is expressed by $1/(2\xi)$ for small value of ξ. The amplification is therefore strongly affected by the damping ratio ξ: a bigger value will further mitigate this resonance phenomenon.

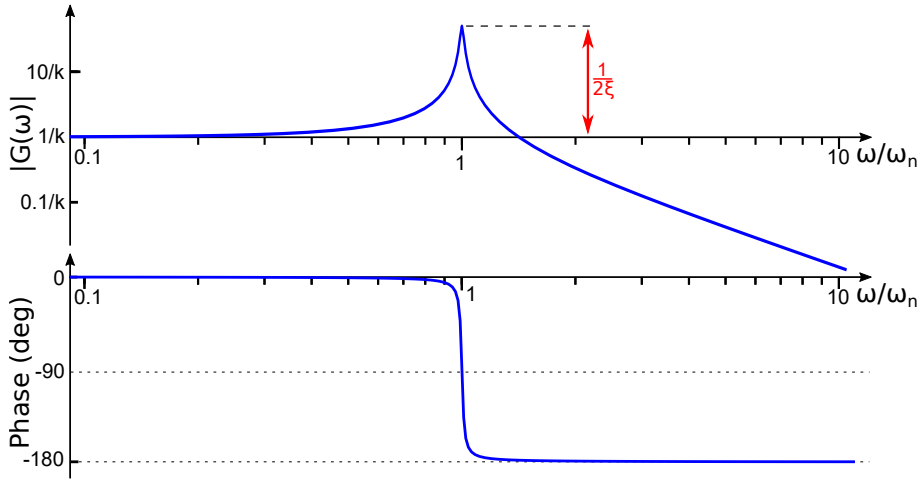

Figure 1.3: Bode plot of a sDoF system.

As it can be noticed, the phase of $G(\omega)$ is zero before resonance while it switches to $-180°$ after its appearance. This physically indicates that both the external disturbance and the system response are in phase before the resonance frequency but once the frequency of the disturbance is higher than ω_n, the response is in opposition of phase with respect to the excitation.

The two observations made with Equations 1.6 and 1.8 highlight that whether the sDoF system is facing a perturbation from some imposed initial conditions or from an external harmonic force, the induced structural vibrations are better mitigated when the damping ratio ξ is higher. Nevertheless, large and lightweight structures such as satellites and other space structures usually present truly low values, i.e. $\xi \simeq 0.001 - 0.005$ [4]. If the system presents too low structural damping, an active control architecture can be applied on it to modify its dynamics and reduce the resonance amplification.

1.2.2 The effects of active control on the system dynamics

The active damping strategy aims to attenuate the dynamic amplification from the resonance phenomenon in the vicinity of the natural frequency. Mathematically, the attenuation of the resonance amplification has to be done by increasing the real part of the

system pole. Consequently, the active damping architecture acts on the system dynamics in order to steer the pole towards the left hand side of the complex plane. Practically, this pole relocation is achieved by the use of a feedback loop: a predefined control law interprets the vibratory state of the system based on the sensor(s) signal. The resulting conditioned signal is then fed to the actuator(s) to apply the counteracting force(s). A schematic representation of such a feedback controller is presented in Figure 1.4 where an ideal actuator and an ideal sensor are considered, i.e. their own dynamics are not represented.

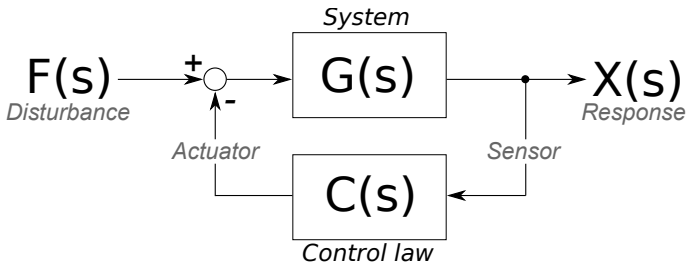

Figure 1.4: Block diagram of a system with a feedback controller and ideal transducers.

The addition of a feedback controller as depicted in Figure 1.4 leads to a modification of the system dynamics. This new dynamics is usually expressed by the closed-loop transfer function $T(s)$ defined by the ratio between the output and the input signals. The general form of such a feedback architecture is given by Equation 1.9 [5] where $G(s)$ is the open-loop transfer function of the system to be controlled and $C(s)$ is the transfer function of the controller. Although it is clear that the value of the closed-loop pole differs from the open-loop one, its position in the complex plane and the possible increase of its real part strongly depend on the selected control law $C(s)$.

$$T(s) = \frac{\text{Out}}{\text{In}} = \frac{G(s)}{1 + C(s)G(s)} \tag{1.9}$$

To illustrate the effect of active damping on the pole of a system, a simple controller is applied on a sDoF structure. A lead control law defined in the Laplace domain by Equation 1.10 is considered, where z_c and p_c are respectively the zero and the pole of the controller, g is its gain value and s is the complex Laplace variable. The numerical values used in this example can be found in Table 1.1.

$$C(s) = g\,\frac{s + z_c}{s + p_c} \tag{1.10}$$

The root locus analysis is a common tool to study how the closed-loop poles of the controlled system are moving within the complex plane when one parameter of the controller, usually the gain, is varied. Figure 1.5 shows the root locus obtained with the demonstration active damping system when varying the gain g from zero to infinity and using the different parameters provided in Table 1.1. As it can be seen, the lead control architecture allows to stir the closed-loop pole from its initial location ω_n (i.e. the open-loop pole when no control is applied) towards the left half-plane, increasing therefore the damping ratio ξ as wanted. The maximum achievable damping of about 0.45 is highlighted by the blue star which corresponds to a significant improvement compared to the initial structural value of 0.001.

1.2.3 Multiple-degree-of-freedom system

Real-life structures are continuous systems that present an infinite number of points. It is sometimes possible to study such systems using an analytic representation by simplifying

Table 1.1: Numerical values used for the demonstration active damping system.

Parameter	Value	Unit
System properties		
m	2	kg
k	200	N/m
ξ	0.001	–
Controller properties		
p_c	42	rad/s
z_c	5	rad/s

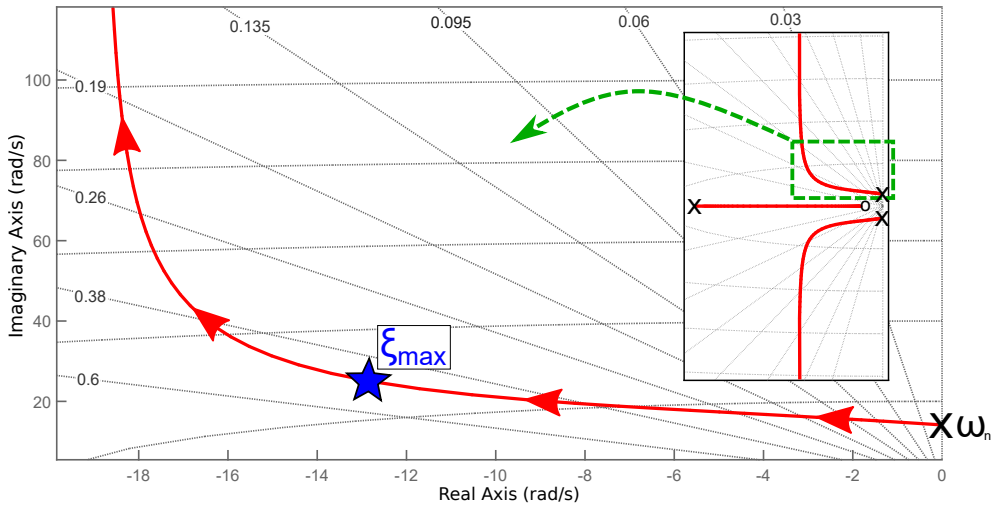

Figure 1.5: Root locus obtained with the demonstration active damping system.

their models. An emblematic example is the Euler–Bernoulli beam theory which neglects the shear stress, allowing simple strain and stress studies for small deflections [6]. Nevertheless, when simplifications are not possible or unwanted, engineers are enforced to use numerical tools such as a finite element (FE) software.

When a continuous structure is numerically modelled based on the FE method, the software produces a discrete system with n degrees of freedom (DoFs). The value of n strongly depends on (i) the geometry of the system (i.e. its size and complexity) and (ii) the required level of accuracy. The intended accuracy influences indeed the type of elements used in the model (e.g. triangular or quadrangular with respectively three and four nodes per element) as well as the number of DoFs for each node. The dynamical behaviour of the obtained discretized system is represented by a finite set of differential equations of motion as follows:

$$[\mathbf{M}]\{\ddot{\mathbf{x}}\} + [\mathbf{C_d}]\{\dot{\mathbf{x}}\} + [\mathbf{K}]\{\mathbf{x}\} = [\mathbf{B_a}]\{\mathbf{u}\} \tag{1.11}$$

where $\{\mathbf{x}\} \in \mathbb{R}^n$ is the vector of mechanical DoFs, $\{\mathbf{u}\} \in \mathbb{R}^r$ is the input vector with r being the total number of external forces and actuators, $[\mathbf{B_a}] \in \mathbb{R}^{n\times r}$ is the applied force distribution matrix whose columns are formed by zero vectors that present only one non-zero element corresponding to the mechanical DoF where the related external force or actuator is applied. Finally, $[\mathbf{M}]$, $[\mathbf{C_d}]$ and $[\mathbf{K}] \in \mathbb{R}^{n\times n}$ are, respectively, the mass, damping and stiffness matrices obtained from the FE software. The solution of Equation 1.11 can be obtained by considering the free and undamped system as done for the sDoF structure: the matrices $[\mathbf{C_d}]$ and $[\mathbf{B_a}]$ are set to zero and the response of the system

is assumed to be harmonic with the form $\{\mathbf{x}\} = \{\phi\}\, e^{j\omega t}$. This leads to the eigenvalue problem expressed by:

$$\Big([\mathbf{K}] - \omega^2\,[\mathbf{M}]\Big)\,\{\phi\} = 0 \tag{1.12}$$

The solutions of this eigenvalue problem are the poles of the system such that $\omega = \pm j\omega_i$ where ω_i $(i = 1,\, 2,\, \ldots,\, n)$ are the natural frequencies. Each frequency is related to a corresponding mode shape $\{\phi_\mathbf{i}\} \in \mathbb{R}^n$ which describes how the system resonates at the different DoFs for the particular ω_i. It can be mathematically demonstrated that different mode shapes of a system always satisfy those two important conditions [4]:

$$\{\phi_\mathbf{i}\}^T\,[\mathbf{M}]\,\{\phi_j\} = \mu_i\,\delta_{ij} \tag{1.13}$$

$$\{\phi_\mathbf{i}\}^T\,[\mathbf{K}]\,\{\phi_j\} = \mu_i\,\omega_i^2\,\delta_{ij} \tag{1.14}$$

where the superscript ^{T} denotes the transpose operator, μ_i is the modal mass and δ_{ij} is the Kronecker delta. Equations 1.13 and 1.14 are known as the orthogonality conditions which physically imply that all the modes shapes of a system are orthogonal between each other with respect to the mass and stiffness matrices. Interestingly, orthogonal vectors are often used to form a basis because they completely span the intended space [7]. Hence, a change of coordinates from the physical to the modal ones can be performed according to:

$$\{\mathbf{x}\} = [\mathbf{\Phi}]\,\{\mathbf{p}\} \tag{1.15}$$

where $[\mathbf{\Phi}] \in \mathbb{R}^{n\times n}$ is the mode shapes matrix defined by $[\mathbf{\Phi}] = \Big(\{\phi_\mathbf{1}\}, \{\phi_\mathbf{2}\}, \ldots, \{\phi_\mathbf{n}\}\Big)$ and $\{\mathbf{p}\} \in \mathbb{R}^n$ is the vector of modal coordinates. Using this modal basis physically means that the dynamics of the mechanical DoFs $\{\mathbf{x}\}$ can be depicted by the sum of each mode shape weighted by its related modal amplitude p_i. Because the damping matrix $[\mathbf{C_d}]$ is usually insufficiently known, a common approach consists of introducing the modal damping ξ_i for each mode i, which can be set independently. If the defined modal basis is injected in Equation 1.11 and both the modal damping model and the orthogonality conditions are considered, a new set of simplified equations are obtained:

$$\{\ddot{\mathbf{p}}\} + 2\,[\xi]\,[\mathbf{\Omega}]\,\{\dot{\mathbf{p}}\} + [\mathbf{\Omega}]^2\,\{\mathbf{p}\} = [\mu]^{-1}\,[\mathbf{\Phi}]^T\,[\mathbf{B_a}]\,\{\mathbf{u}\} \tag{1.16}$$

where $[\xi]$, $[\mathbf{\Omega}]$ and $[\mu]$ are diagonal matrices $\in \mathbb{R}^{n\times n}$ containing respectively each modal damping ξ_i, all the natural frequencies ω_i and all the modal masses μ_i with $i = 1,\, 2,\, \ldots,\, n$. The projection of the system in its modal basis allows therefore to transform the initial set of n coupled equations into n uncoupled ones that present the same form of n sDoF systems.

1.2.4 State-space representation

The solutions of Equation 1.16 can be numerically obtained using a ordinary differential equation (ODE) solver. Nevertheless and despite their simplification into uncoupled equations due to the applied change of coordinate, they are second-order differential equations. Yet, the ODE solver algorithms are mainly designed for first-order differential problems [8]. A common practice to address this concern is to reformulate each second-order ODE into two first-order ones by introducing the states variable vector:

$$\{\mathbf{q}\} = \begin{pmatrix} \{\mathbf{p}\} \\ \{\dot{\mathbf{p}}\} \end{pmatrix} \in \mathbb{R}^{2n} \tag{1.17}$$

Considering this state-vector and assuming that the mode shapes have been normalised with respect to the mass matrix $[\mathbf{M}]$ such that $[\mu]$ is an identity matrix $\mathbf{I_n}$, Equation 1.16 can be rewritten in its state-space representation as follows:

$$\begin{gathered}\{\dot{\mathbf{q}}\} = [\mathbf{A}]\{\mathbf{q}\} + [\mathbf{B}]\{\mathbf{u}\} \\ \text{with } [\mathbf{A}] = \begin{bmatrix} \mathbf{0_{n\times n}} & \mathbf{I_n} \\ -[\mathbf{\Omega}]^2 & -2[\xi][\mathbf{\Omega}] \end{bmatrix}, \quad B = \begin{bmatrix} \mathbf{0_{n\times r}} \\ [\mathbf{\Phi}]^T[\mathbf{B_a}] \end{bmatrix}\end{gathered} \tag{1.18}$$

where $[\mathbf{A}] \in \mathbb{R}^{2n\times 2n}$ is the state matrix, $[\mathbf{B}] \in \mathbb{R}^{2n\times r}$ is the input matrix and $\mathbf{0_{a\times b}}$ is a $a \times b$ zero matrix. Switching to the state-space representation expressed by Equation 1.18 ensures its resolution with the different available ODE solvers. Moreover, transient behaviours can be easily studied which is not the case with the frequency domain representation. Nevertheless, the consequence of simplifying second-order differential problems into first-order ones leads to an increase in the number of equations, shifting from n to $2n$.

The initial FE model on which the state-space expression is based integrates the external forces and the potential actuator(s) mounted on the system through the matrix $[B_a]$ and the input vector $\{u\}$. In active control, the command feeding the actuator(s) relies on the signal from the sensor(s) mounted on the structure. The location of the sensor(s) need consequently to be integrated in the state-space model as well, which is done with the sensor distribution matrix $[\mathbf{C_s}] \in \mathbb{R}^{m\times n}$ such that:

$$\{\mathbf{y}\} = [\mathbf{C_s}]\{\mathbf{x}\} \tag{1.19}$$

where $\{\mathbf{y}\} \in \mathbb{R}^m$ is the output vector and $[\mathbf{C_s}]$ contains only one non-zero element per row that corresponds to the mechanical DoF where the related sensor is mounted. By applying the modal change of coordinates given by Equation 1.15 and considering the state variable vector, Equation 1.19 is rewritten as follows:

$$\begin{gathered}\{\mathbf{y}\} = [\mathbf{C}]\{\mathbf{q}\} + [\mathbf{D}]\{\mathbf{u}\} \\ \text{with } [\mathbf{C}] = \begin{bmatrix} [\mathbf{C_s}][\mathbf{\Phi}] & \mathbf{0_{m\times n}} \end{bmatrix}\end{gathered} \tag{1.20}$$

where $[\mathbf{C}] \in \mathbb{R}^{m\times 2n}$ is the output matrix and $[\mathbf{D}] \in \mathbb{R}^{m\times r}$ is an additional matrix called the feedthrough that allows to mathematically express a direct effect of the actuator(s) and/or external force(s) on the sensor(s). The full system dynamics that includes the defined states as well as the external forces and the mounted transducers is obtained by combining Equations 1.18 and 1.20, which gives:

$$\begin{gathered}\{\dot{\mathbf{q}}\} = [\mathbf{A}]\{\mathbf{q}\} + [\mathbf{B}]\{\mathbf{u}\} \\ \{\mathbf{y}\} = [\mathbf{C}]\{\mathbf{q}\} + [\mathbf{D}]\{\mathbf{u}\}\end{gathered} \tag{1.21}$$

1.2.5 Modal decomposition and truncation

Although the system dynamics expressed by Equation 1.21 can be solved with numerical algorithms, the design of a feedback control architecture can also be performed in the frequency domain. It allows indeed to benefit from several assets, such as achievement of good performance with simple design rules, management of design uncertainty or easy use of experimental data for design [9]. Switching to the frequency domain consists of considering the solicitation of the system and its related response as harmonic signal, as done in Section 1.2.1. If so, the matrix transfer function representation that models the

outputs of the system from each possible input can be expressed in its modal decomposition by starting from Equation 1.16, which gives [10]:

$$[\mathbf{G}(\omega)] = \sum_{i=1}^{n} \frac{\{\phi_\mathbf{i}\}\,\{\phi_\mathbf{i}\}^T}{\mu_i(\omega_i^2 + 2j\xi_i\omega_i\omega - \omega^2)} \tag{1.22}$$

where $[\mathbf{G}(\omega)] \in \mathbb{R}^{n\times n}$. The element $\mathbf{G}_{\alpha\,\beta}(\omega)$ of $[\mathbf{G}(\omega)]$ expresses the complex structural response at the DoF α when a unit harmonic force is applied at the DoF β, which is mathematically expressed as follows:

$$\mathbf{G}_{\alpha\,\beta}(\omega) = \sum_{i=1}^{n} \frac{\phi_\mathbf{i}(\alpha)\,\phi_\mathbf{i}(\beta)}{\mu_i(\omega_i^2 + 2j\xi_i\omega_i\omega - \omega^2)} \tag{1.23}$$

This last equation indicates that each mode actively contributes to the response of the system with a weighing factor $\phi_\mathbf{i}(\alpha)\,\phi_\mathbf{i}(\beta)/\mu_i$ and that the full response is obtained by summing all the contributions. This is illustrated in Figure 1.6 where the transfer function of a 5 DoFs system is plotted along with its five modal contributions. Interestingly, whether the system is studied by using the mechanical DoFs (Equation 1.11), with its modal basis representation (Equation 1.16) or in the frequency domain with the modal decomposition (Equation 1.23), the impact of the sensor and actuator (SA) position on the system dynamics is always easily noticeable by the presence of the $[\mathbf{B_a}]$ matrix or the α and β parameters. This influence clearly shows that only the numerator of the transfer function is affected. Conversely, the position of the transducers does not modify the denominator of each modal contribution, which results in no influence on the value of the structural poles. This therefore verifies the specificity that the poles are global properties of the structure and its boundary conditions and that they do not depend on the position of the transducers on the system.

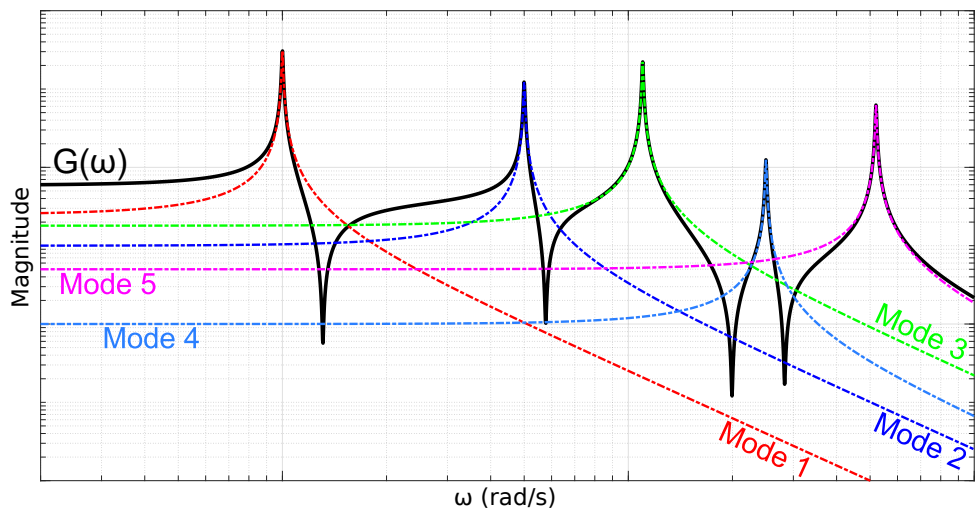

Figure 1.6: Illustration of the modal decomposition of a transfer function $G(\omega)$ with its five modal contributions.

As discussed in Section 1.2.3, the number of DoFs n in a system depends upon different parameters, including its size and complexity. Hence, a large and/or complex system can include more than hundreds of thousands of DoFs when building its FE model. The calculation of its transfer function as a sum of all the n modal contributions depicted by Equation 1.23 can consequently be extremely demanding in terms of computational effort. Nevertheless, and as shown in Figure 1.6, each modal contribution presents three different

behaviours depending on the frequency value: a static contribution for $\omega < \omega_i$, a dynamic amplification in the vicinity of ω_i and a constant decay after the resonance. Consequently, the contribution of a higher order mode on the lower ones is mainly static. Because the frequency band of interest is always limited, a modal truncation can be performed such that only the first N modes are retained, with $N < n$. A common practice is to select N such that its natural frequency is up to 1.5 times the highest frequency of interest, as done in [11]. The transfer function can therefore be expressed in its matrix form as follows [12]:

$$[\mathbf{G}(\omega)] \simeq \sum_{i=1}^{N} \frac{\{\phi_\mathbf{i}\}\{\phi_\mathbf{i}\}^T}{\mu_i(\omega_i^2 + 2j\xi_i\omega_i\omega - \omega^2)} + [R_s] \quad (N < n) \tag{1.24}$$

$$[R_s] = [K]^{-1} - \sum_{i=1}^{N} \frac{\{\phi_\mathbf{i}\}\{\phi_\mathbf{i}\}^T}{\mu_i\,\omega_i^2} \tag{1.25}$$

where $[R_s]$ is the static correction of high order modes that ensures the proper accuracy of the system dynamics. This frequency-independent correction adds indeed to the transfer function the static contributions of all the modes that have been truncated from $(N+1)$ to n. Figure 1.7 shows the truncation of a system for which the bandwidth of interest stops before its third mode. The truncated model is therefore built with only the first three modal contributions and the static correction, which provides an accurate dynamical behaviour within the targeted bandwidth.

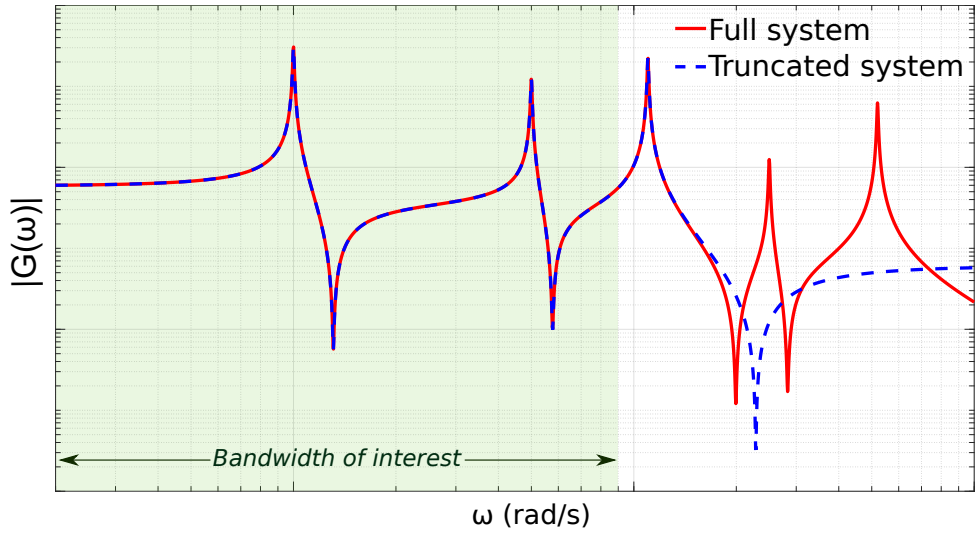

Figure 1.7: Illustration of the modal truncation where only the first three modes are retained.

The truncation of a model can also be expressed through its state-space representation. For this purpose, only the first N modes are retained from the change of coordinates according to Equation 1.15, which leads to:

$$\{\mathbf{x}\} = [\mathbf{\Phi}_N]\{\mathbf{p}_N\} \tag{1.26}$$

where $[\mathbf{\Phi}_N] = \left(\{\phi_\mathbf{1}\}, \{\phi_\mathbf{2}\}, \ldots, \{\phi_\mathbf{N}\}\right)$ and $\{\mathbf{p}_N\} \in \mathbb{R}^N$. By injecting this reduced modal basis into Equation 1.16 and by following the same approach as done in Section 1.2.4, the

reduced state-space representation is rewritten as follows:

$$\begin{gathered}\{\dot{\mathbf{q}}_N\} = [\mathbf{A}_N]\{\mathbf{q}_N\} + [\mathbf{B}_N]\{\mathbf{u}\} \\ \text{with } [\mathbf{A}_N] = \begin{bmatrix} \mathbf{0_{N\times N}} & \mathbf{I_N} \\ -[\mathbf{\Omega}_N]^2 & -2[\xi_N][\mathbf{\Omega}_N] \end{bmatrix}, \quad [\mathbf{B}_N] = \begin{bmatrix} \mathbf{0_{N\times r}} \\ [\mathbf{\Phi}_N]^T[\mathbf{B_a}] \end{bmatrix}\end{gathered} \tag{1.27}$$

where the subscript $_N$ indicates the reduction of the dimensions of the different vectors and matrices. As done with the static correction $[R_s]$, different approaches can be followed for the reduced state-space representation in order to ensure the proper accuracy of its dynamics, despite the truncation. One of the methods relies on the addition of a feedthrough term based on the residual static contributions as follows [13]:

$$[\mathbf{D}_R] = \left[[\mathbf{C_s}]\left([\mathbf{K}]^{-1} - [\mathbf{\Phi}_N][\mathbf{\Omega}_N]^{-2}[\mathbf{\Phi}_N]^T\right)[\mathbf{B_a}]\right] \tag{1.28}$$

where $[\mathbf{C_s}]$ is the sensor distribution matrix. The output matrix $[\mathbf{C}]$ expressed by Equation 1.20 can also be reduced according to the truncation, which leads to:

$$[\mathbf{C}_N] = \begin{bmatrix}[\mathbf{C_s}][\mathbf{\Phi}_N] & \mathbf{0_{m\times N}}\end{bmatrix} \tag{1.29}$$

By injecting the different reduced matrices defined by Equations 1.27, 1.28 and 1.29 into the non-reduced form expressed by Equation 1.21, the reduced state-space representation is obtained without any other difficulty, which gives:

$$\begin{gathered}\{\dot{\mathbf{q}}_N\} = [\mathbf{A}_N]\{\mathbf{q}_N\} + [\mathbf{B}_N]\{\mathbf{u}\} \\ \{\mathbf{y}\} = [\mathbf{C}_N]\{\mathbf{q}_N\} + [\mathbf{D}_R]\{\mathbf{u}\}\end{gathered} \tag{1.30}$$

1.3 Zeros in single input single output systems

A single input single output (SISO) system is a sDoF or multiple DoFs system that only presents one input and one output. The dynamic response of the considered SA pair is a frequency-dependent scalar function with the same form as Equation 1.23. By fully expressing the sum of each modal contributions and by switching in the Laplace domain, the transfer function can be expressed as the ratio of two polynomials:

$$\mathbf{G}(\mathbf{s}) = \frac{b_m s^m + b_{m-1}s^{m-1} + \ldots + b_1 s + b_0}{s^n + a_{n-1}s^{n-1} + \ldots + a_1 s + a_0} \tag{1.31}$$

where s is the Laplace complex variable. A factorization of both the numerator and the denominator of Equation 1.31 can be performed, which gives the following factor form of the SA transfer function:

$$\mathbf{G}(\mathbf{s}) = \frac{g\,(s-z_1)\,(s-z_2)\,\ldots\,(s-z_m)}{(s-p_1)\,(s-p_2)\,\ldots\,(s-p_n)} \tag{1.32}$$

which is known as the zero-pole-gain model definition. This name comes from the explicit appearance of the poles p, the zeros z and the gain g in the definition of $\mathbf{G}(\mathbf{s})$. As it can be seen, the zeros are the solutions that verify the equation obtained when the transfer function is set to zero. Accordingly, the zeros that are also called anti-resonances correspond to the frequencies at which a non-zero harmonic input leads to a zero output. It has been developed in the previous section that the position of the SA has a direct influence on the dynamic of the system through the numerator of its transfer function. Hence, the position of the transducers directly impacts the zero values: they are a local property of the system

and their values are associated to the DoF(s) on which the transducers are mounted on. This can be illustrated by considering a two DoFs system shown in Figure 1.8 where three configurations are considered: two collocated ones (i.e. the transducers of a pair are linked to the same DoF) and one non-collocated arrangement. Although the collocated responses G_{11} and G_{22} present a zero between the two resonance peaks that changes value with respect to the configuration, it can be seen that the non-collocated one G_{12} does not have any zero. It is consequently clear that the placement of the SA pair on the system and its configuration play a direct role in the appearance and the value of the anti-resonance.

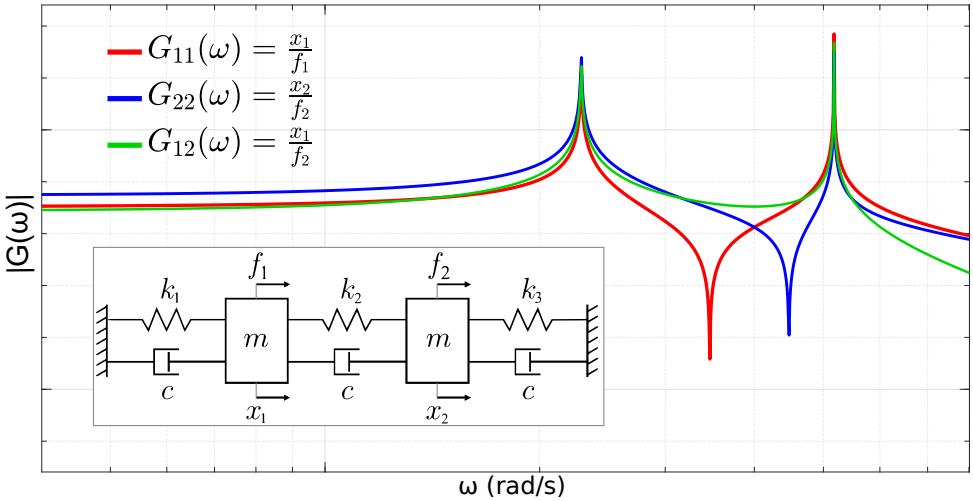

Figure 1.8: Effect of the SA position on the zero frequency.

The zeros play an important role in the dynamical behaviour of systems, which makes them essential for control theory. One major reason of this importance is because the closed-loop poles converge towards the zeros for high value of the feedback gain. This can be easily proven by considering the closed-loop transfer function given by Equation 1.9. The characteristic equation of this transfer function whose roots are the closed-loop poles is:

$$1 + C(s)G(s) = 0 \tag{1.33}$$

The control law $C(s)$ and the open-loop transfer function $G(s)$ can be expressed in their factorised forms such that:

$$C(s) = g_c \frac{\prod_i (s - z_{c,i})}{\prod_i (s - p_{c,i})}, \quad G(s) = g_G \frac{\prod_i (s - z_{G,i})}{\prod_i (s - p_{G,i})} \tag{1.34}$$

where the subscripts $_c$ and $_G$ serve to properly identify the poles and zeros from the control law and from the open-loop system, respectively. By injecting Equation 1.34 into the characteristic equation, the following simplification can be obtain:

$$\prod_i (s - p_{c,i}) \prod_i (s - p_{G,i}) + g_c \left(g_G \prod_i (s - z_{c,i}) \prod_i (s - z_{G,i}) \right) = 0 \tag{1.35}$$

When the gain of the control law g_c is zero, the solutions of Equation 1.35 are simply the poles of the open-loop system and the poles of the added controller. Such a result is fully expected because a zero control gain corresponds to an absence of control effort: the dynamic of the feedback system is identical to the non-controlled one (except for the addition of the control law poles). When g_c is asymptotically increased towards infinity, the equation can be simplified by neglecting its first term due to its small contribution

with respect to the second one. This leads to the zeros as solution of the closed-loop poles and confirms the mentioned convergence. Obviously, the intermediate positions of the closed-loop poles within the complex plane as a function of the gain depend directly on the initial and the final convergence values. This demonstrates therefore the importance of the zeros in control dynamics and, as a consequence, the importance of the SA placement and its configuration.

1.3.1 Zeros in SISO collocated system

In a collocated configuration, the SA are linked to the same DoF. Consequently, the transfer function expressed in its modal decomposition by Equation 1.23 is simplified as:

$$\mathbf{G}_\alpha(\omega) = \sum_{i=1}^{n} \frac{\phi_i^2(\alpha)}{\mu_i(\omega_i^2 + 2j\xi_i\omega_i\omega - \omega^2)} \tag{1.36}$$

where α is the considered DoF. This modification results in an always positive numerator which has a significant impact on the dynamics: it ensures the alternation of poles and zeros. This important property of collocated SISO systems has first been demonstrated by Foster in 1924 for electrical circuits [14] and generalised to flexible mechanical systems by Martin in 1978 [10]. In system dynamics, a pole induces a phase drop of 180 degrees while a zero provides a phase lead of 180 degrees. Consequently, the pole-zero alternating property ensures that the open-loop phase lag can never drop below 180 degrees, which makes it easier to control [15]. This is the main reason why the use of a collocated SA pair is often recommended whenever possible.

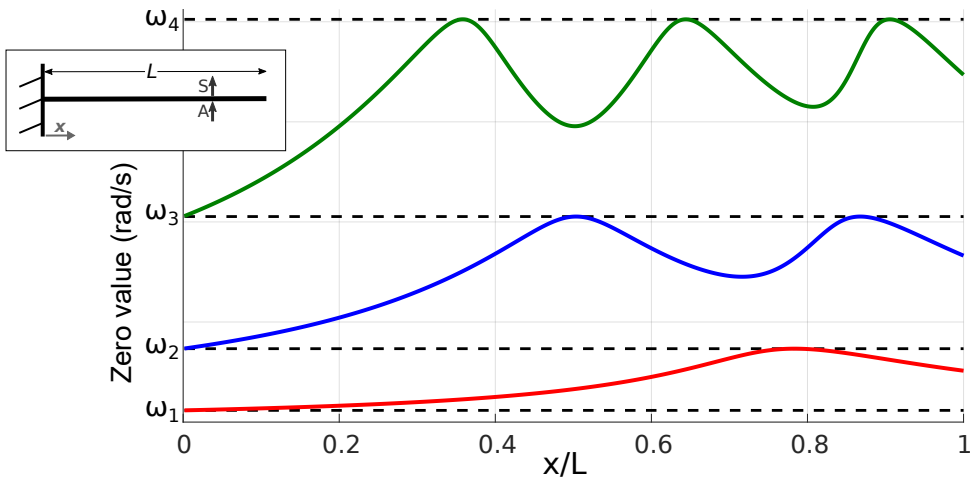

Figure 1.9: Evolution of the zeros (solid lines) and natural frequencies (dashed lines) as a function of a collocated SA pair position along a cantilever beam.

The interlacing property is illustrated in Figure 1.9 that analyses the evolution of the first three zeros when the position $\mathbf{x}$ of a collocated force actuator/displacement sensor pair is moved along the longitudinal axis of a cantilever beam. The cantilever beam of length L has been modelled using the Structural Dynamics Toolbox (SDT), an open and extendible FE modelling Matlab based toolbox for dynamics problems [16]. As it can be seen, each zero is always bounded between two natural frequencies ω. Moreover, the zeros are reaching the upper pole values for certain positions, which leads to pole-zero cancellations for those specific locations. Such cancellations induce a loss of controllability and observability which physically translates to the incapacity to sense or control the mode [5]. Figure 1.10 shows the normalised mode shapes of the first three bending modes of the

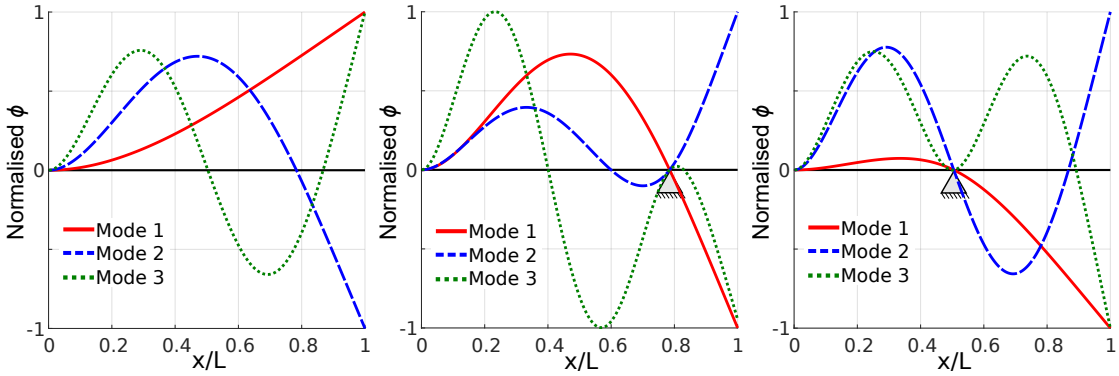

(a) Cantilever beam (b) Extra support at $0.78\,L$ (c) Extra support at $0.50\,L$

Figure 1.10: First three mode shapes of (a) a cantilever beam, (b) a cantilever beam with an extra support at $x/L = 0.78$, (c) a cantilever beam with an extra support at $x/L = 0.50$.

beam. Interestingly, the different pole-zero cancellations observed in Figure 1.9 appear when the SA pair is located at the stationary positions (called the nodal points) of the considered modes: around $x/L = 0.78$ for mode 2 and $x/L = 0.5$ or 0.87 for mode 3. This is consistent with physical considerations: the displacement sensor cannot sense the dynamics of a mode if it is located in the vicinity of an area without any motion.

The pole-zero cancellations that can occur for specific SA positions highlight the importance of a proper transducer placement to avoid any loss of controllability and observability. Furthermore, it clearly illustrates the existing link between the zero values and the mode shape dynamics. Several studies have been conducted to provide a clear physical interpretation of the zero frequencies. It has been proved that for collocated force actuators and displacement or velocity sensors, the zeros of a system correspond to the natural frequencies of the same structural system which is constrained at the SA location and in the same direction of the pair [17]. Such physical phenomenon is illustrated by Figures 1.10b and 1.10c that display the first three modes shapes of a cantilever beam constrained at the nodal points of modes two and three respectively. As expected, such additional constraint on the original cantilever beam induces a modification of the dynamics. More importantly, the original second mode shape becomes the first one when the system is constrained at its nodal point (Figure 1.10b). This translates, in terms of natural frequencies, that the first one of the modified system equals the second one of the unconstrained beam. Therefore and based on the mentioned physical interpretation, it is consistent that the first zero reaches ω_2 at $x/L = 0.78$. Similarly, the original third mode shape switched to the second one when the beam is constrained at its half, which is the nodal point of the original third mode (Figure 1.10c). Again, this implies that the second natural frequency of the constrained beam is equal to the third one of the original one. Consequently, observing the second zero reaching ω_3 at the half of the beam in Figure 1.9 is consistent with the physical interpretation.

1.3.2 Zeros in SISO non-collocated system

For non-collocated systems, a positive numerator for each modal contribution is no longer ensured. Consequently, the alternating pole-zero property demonstrated for collocated systems is not valid and the different zero frequencies are not necessary bounded between two poles. This has been illustrated in Figure 1.8 where the non-collocated transfer function $G_{12}(\omega)$ does not show any anti-resonance between the first and the second resonance

peak. The absence of zero between each resonance induces a possible large phase lag of the system, which can lead to stability issues.

Although the alternating property is no longer valid, non-collocated systems still present zeros. It was indeed proved by Davison in [18] that a n DoFs system with an equal number of inputs and outputs almost always presents at least $(n-1)$ zeros. Nevertheless, the zeros are not necessary bounded and their values migrate along the imaginary axis towards infinity when the distance between the sensor and the actuator increases [19]. As illustrated in Figure 1.11a, such a migration is coupled with the appearance of zeros on the real axis that are called non-minimum phase zeros [20]. Due to the convergence of the closed-loop poles towards the zeros when the gain is asymptotically increased, a system with zeros on the positive real axis can lead to stability issues. Moreover, non-minimum phase zero induces additional phase lag in the system, reducing consequently the tolerance of the control loop to unpredicted variations in the system before its destabilization.

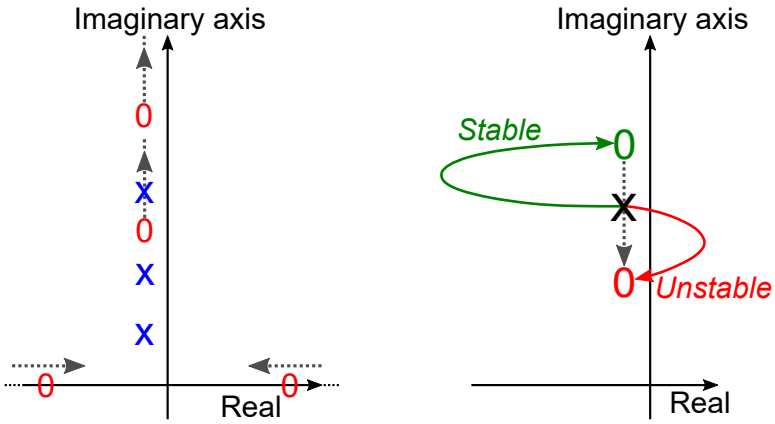

(a) (b)

Figure 1.11: Phenomena that can appear when a non-collocated pair is used: (a) migration of the zeros and appearance of non-minimum phase zeros, (b) pole-zero flipping inducing a switch from stable to unstable closed-loop.

Furthermore, the zeros of non-collocated system are extremely sensitive to parameter changes [21, 22]. Those changes can be due, for example, to the ageing of the system over time, to an inaccurate transducer placement with respect to the targeted one or to a poor quality of the FE model. Unfortunately, such a high sensitivity can lead to large variations of their expected values and, as a result, to the occurrence of a pole-zero flipping as illustrated in Figure 1.11b. This phenomenon consists in the inversion of the order of appearance of the poles and the zeros, which can drastically modify the shape of the root locus. Such a reshape can potentially cause the system to become unstable and must therefore be avoided.

The presence of non-minimum phase zeros, possible pole-zero flipping and small stability margin due to unbounded phase are factors that clearly limit the achievable closed-loop performance of non-collocated systems. This explains why collocated architectures are recommended whenever possible as they provide robustness and performance.

1.4 Computation of the zero value in SISO systems

The comparison between collocated and non-collocated systems highlighted the importance of the zeros in system dynamics and in control theory. Hence, their values should be accurately known when designing the control architecture or when studying the optimal position of a SA pair to be mounted on a system. The most straightforward method to obtain their values consists of solving the equation obtained by setting the transfer function to zero:

$$G(\omega) = 0 \tag{1.37}$$

Nevertheless, substituting the expression of the transfer function expressed by the sum of each modal contribution given by Equation 1.36 into Equation 1.37 shows that obtaining zero values for a specific SA configuration requires to solve, for ω, a $2 \times (n-1)^{th}$ order equation. Hence, for realistic structures that generally consist of a large number of DoFs, it can be extremely expensive to solve the related problem for one or several positions.

The physical interpretation of the zero can also be used to obtain its value. It is indeed possible to solve the eigenvalue problem of the system constrained at the SA pair, as done in [23]. However, in case of realistic structures with a high number of DoFs, solving the eigenvalue problem could be again expensive in terms of computational cost. Additionally, this method is not possible for piezoelectric transducers, restricting its use even further.

The anti-resonances can also be obtained using the state-space formulation where they are expressed by the frequencies at which the rank of a specific subspace (built with the state, input and output matrices) is reduced. Although this method could be more efficient with respect to the other two, it still presents three major drawbacks: (1) the state space formulation has to be built for each considered SA location, (2) the computational cost depends on the number of DoFs in the system and (3) it can be numerically difficult to obtain the solutions, requiring therefore extra computational operations [24, 25].

A common issue with these methods is that their computational complexity increases significantly with the number of DoFs of the system. For example, the simultaneous root-finding methods of a polynomial of degree $(N-1)$ present a time complexity of $\mathcal{O}(NlogN)$ [26] while the inversion of a $N \times N$ matrix is $\mathcal{O}(N^{2.78})$, at best [27]. Moreover, the zero corresponding to a defined SA position can be computed only after building a specific system (the transfer function, the constrained equivalent system or the state-space), consequently preventing the determination of the zero values for multiple SA positions at the same time. In view of the above, a computationally efficient approximation method has been proposed in [28] in order to estimate the zeros with reasonable accuracy. It can be used for a specific mode only and allows to simultaneously obtain the zero values for all the SA positioning candidates.

1.4.1 The analytical zero approximation for collocated systems

By assuming that the mode shapes have been normalised to obtain unitary modal masses and that the structure presents only small damping allowing to neglect the imaginary part of the pole, the transfer function of a collocated SA pair at position α expressed by Equation 1.36 can be rewritten in the Laplace domain as:

$$G(s)_\alpha = \frac{\phi_1^2(\alpha)}{s^2+\omega_1^2} + \frac{\phi_2^2(\alpha)}{s^2+\omega_2^2} + \ldots + \frac{\phi_{n-1}^2(\alpha)}{s^2+\omega_{n-1}^2} + \frac{\phi_n^2(\alpha)}{s^2+\omega_n^2} \tag{1.38}$$

Because of the interlacing property of collocated SISO systems, the presence of a zero bounded by the poles ω_i and ω_{i+1} is ensured. To estimate its value, it is important to not truncate the transfer function at mode $(i+1)$. Its dynamical behaviour in the vicinity of the resonance ω_{i+1} can indeed have an evident influence on the targeted zero value. Conversely, the dynamical contributions of all the modes before ω_i are rather limited and can be approximated by their roll-off components as follows:

$$\frac{1}{s^2+\omega_j^2} \simeq \frac{1}{s^2} \quad (j = 1, 2, ..., i-1) \tag{1.39}$$

Hence, by truncating the transfer function starting from mode $(i+2)$ with the static contribution and by approximating all the modes before the targeted one i with Equation 1.39, the transfer function of Equation 1.38 simplifies into:

$$G(s)_\alpha = \frac{\sum_{k=1}^{i-1} \phi_k^2(\alpha)}{s^2} + \frac{\phi_i^2(\alpha)}{s^2+\omega_i^2} + \frac{\phi_{i+1}^2(\alpha)}{s^2+\omega_{i+1}^2} + R_{s,\alpha} \tag{1.40}$$

By equating this transfer function to zero, the following 6th order equation which satisfies the zeros of the system is obtained:

$$as^6 + bs^4 + cs^2 + d = 0$$
$$\text{with} \begin{cases} a = R_{s,\alpha} \\ b = \sum_{k=1}^{i+1} \phi_k^2(\alpha) + R_{s,\alpha}(\omega_i^2 + \omega_{i+1}^2) \\ c = \sum_{k=1}^{i-1} \phi_k^2(\alpha)\,(\omega_i^2 + \omega_{i+1}^2) + \phi_i^2(\alpha)\,\omega_{i+1}^2 + \phi_{i+1}^2(\alpha)\,\omega_i^2 + R_{s,\alpha}\,\omega_i^2\,\omega_{i+1}^2 \\ d = \sum_{k=1}^{i-1} \phi_k^2(\alpha)\omega_i^2\omega_{i+1}^2 \end{cases} \tag{1.41}$$

As it can be observed, the four coefficients a, b, c and d of the 6th order equation only depend on the mode shapes of modes 1 to $(i+1)$, the natural frequencies ω_i and ω_{i+1} and the static correction R_s. Moreover, Equation 1.41 can be analytically solved as a cubic equation in s^2, which provides six solutions for s. However, due to the two approximations that have been performed (i.e. usage of the static correction for high-frequency modes and simplification into their roll-off components for low-frequency modes), the correct solution should be chosen carefully such that it satisfies the following inequality:

$$\omega_i^2 < z_i^2 < \omega_{i+1}^2 \tag{1.42}$$

Hence, the proposed approximation allows to easily compute the zero values bounded between the modes i and $(i+1)$ for multiple collocated SA positions at the same time. Such a simultaneous evaluation is feasible considering that it only requires simple arithmetic calculations.

Numerical validation

The computational efficiency and the accuracy of the proposed approximation is analysed with two numerical systems modelled in SDT: a cantilever beam with the dimension of 300 mm x 25 mm x 2 mm and a simply supported plate with the dimension of 310 mm x 200 mm x 2 mm. Both systems are defined with the same lightly damped steel with the following properties: Young's modulus $E = 210$ GPa, Poisson's ratio $\nu = 0.285$, mass density $\rho = 7800$ kg/m^3 and modal damping ratio $\xi = 0.004$. The FE model of the beam consists of 601 beam elements that only allow the 2 DoFs in-plane bending motion except for the one at the clamped end. Consequently, the model contains 1200 DoFs in total. As illustrated in Figure 1.12a, each non-constrained node along the longitudinal axis of the

beam is defined as a potential collocated force actuator/displacement sensor pair position, leading to 600 possible locations. The simply supported plate is discretized by 6 DoFs shell elements each 5 mm in the x and y directions (2583 nodes in total). The nodes located at the four edges of the plate allow only the three rotations, leading to 14886 DoFs in total. A SA pair is allowed each 20 mm in both the x and y directions, leading to 160 SA positioning candidates. The system representation as well as its Cartesian coordinates are shown in Figure 1.12b.

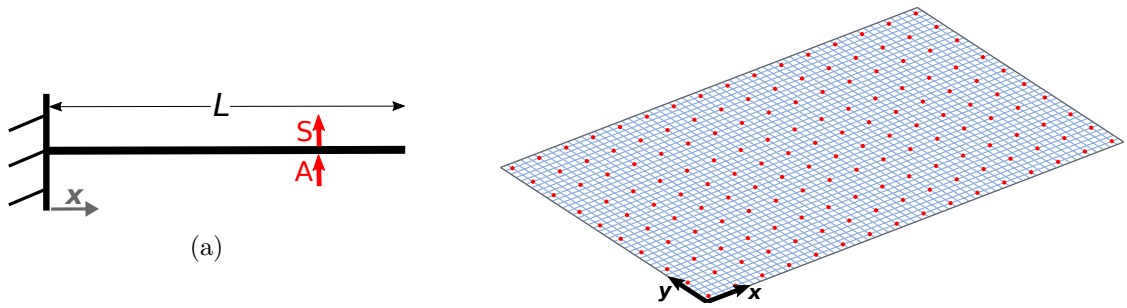

(a) (b)

Figure 1.12: Numerical systems used to assess the proposed analytical approximation of the zero: (a) a cantilever beam , (b) a simply supported plate where all the possible SA locations are highlighted with red dots.

To evaluate the computational efficiency of the proposed approximation, the value of the zero that stands between the 3rd and the 4th mode of the defined cantilever beam is computed for all the possible SA positions using three methods: (1) solving the eigenvalue problem of the corresponding constrained system, (2) solving the equation obtained by equating the transfer function to zero and (3) using the proposed approximation method. Because the zeros physically correspond to the natural frequencies of the corresponding constrained system, the values obtained with this method can be defined as references for all the SA positions. Hence, the relative error of a zero value can be defined as the ratio between the absolute error and its equivalent reference where the absolute error corresponds to the difference between the obtained zero value and its reference. Table 1.2 shows, for each approach, the maximum relative error value obtained among all the SA positions as well as the related computational time. Note that all computations have been performed on a 64-bit Windows 10 platform computer with an Intel(R) Core(TM) i5-8400 at 2.8GHz and 16Gb of RAM. It can be seen that although each method provides the same order of magnitude for the relative error, the proposed approximation computes the 600 zeros up to 500 times faster than the reference technique. This therefore demonstrates that the proposed approximation is highly efficient in terms of computational cost.

Table 1.2: Maximum relative error and processing time to compute the 3rd zero value at 600 SA positions with three different methods.

Method	Maximum relative error (%)	Processing time (s)
(1) Blocking DOF	0	184.75
(2) Equating $G(s)$ to zero	1	885.12
(3) Proposed approximation	1.1	0.36

In order to assess the accuracy of the proposed analytical approximation, the maximum relative error values obtained among all the SA positions for the first six modes and for the two systems are shown in Figure 1.13. As it can be seen, the maximum relative error

for the cantilever beam is limited to 2% only. Unfortunately, the maximum error goes up to 12% for the simply supported plate, which is at the limit of acceptability. The disparity in the accuracy of the approximation can be explained by the difference in modal density between the two systems. The cantilever beam presents indeed modes that are well separated, which complies with the roll-off approximation and the simplification of the higher order modes dynamics into their static contributions. There is however a strong modal interaction between nearby modes for the plate, which decreases the accuracy of the approximation and leads to the observed maximum error values.

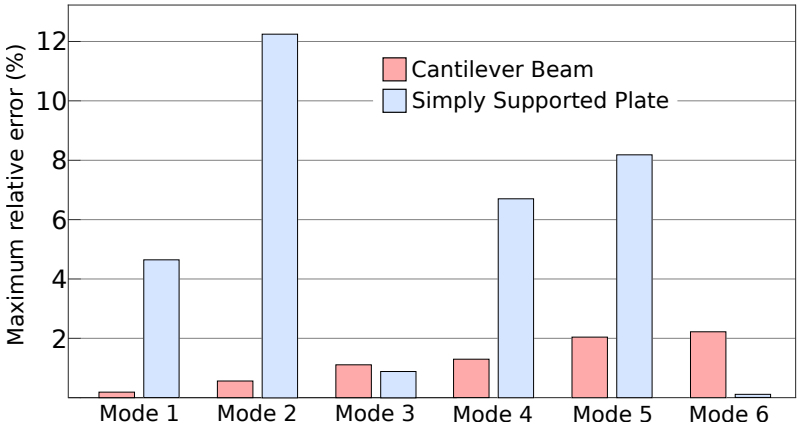

Figure 1.13: Maximum relative errors of the proposed zero approximation for the first six modes of the two considered systems.

Conclusion

From the previous observations, it is clear that the proposed zero approximation is highly efficient in terms of computational cost compared to other calculation methods. Nonetheless, a proper accuracy is not guaranteed for any type of system. Although the relative error is limited to a few percent for systems with well-separated modes, it can reach 10% in case of strong modal interactions. The presented analytical approximation can consequently be used as a first efficient estimation of the zero values for several SA pair positions. Afterwards, based on the obtained preliminary results and with respect to the intended purpose, an extensive calculation at specific positions can be performed to obtain the exact values.

Finally, it is worth mentioning that the proposed approximation is only valid for SISO systems and for SA pairs that (i) act on a single node and (ii) do not induce a local modification of the structural properties of the system. Those two restrictions are in line with the force actuator/displacement sensor pair that has been used for this numerical validation. Conversely, the selection of piezoelectric patches as transducers prevents the straightforward use of the proposed approximation. A local modification of the mass and the stiffness of the structure occurs indeed around the patches, which necessitates the recalculation of the eigenvalue problem accordingly and prevents consequently the evaluation of several positions in parallel. Additionally, it is extremely difficult to obtain a reliable value of the zeros for system equipped with piezoelectric patches, even with advanced FE modelling as investigated in [29].

1.5 Zeros in multiple inputs multiple outputs systems

A multiple inputs multiple outputs (MIMO) system is a system that presents multiple inputs and outputs. Consequently, the response of the entire system can no longer be expressed by a unique frequency-dependent scalar function but it requires the use of a transfer function matrix as follows:

$$[\mathbf{G}(\omega)] = \begin{bmatrix} G_{11}(\omega) & \dots & G_{1r}(\omega) \\ \vdots & \ddots & \\ G_{m1}(\omega) & & G_{mr}(\omega) \end{bmatrix} \tag{1.43}$$

where m and r are the numbers of inputs and outputs, respectively. For such MIMO systems, the zero frequencies are referred to as the transmission zeros (TZs) rather than anti-resonances because they are the frequencies for which there is no transmission from the inputs to all the outputs of the system. The TZs are therefore not simply equal to the anti-resonance frequencies of each individual entry of the transfer function matrix, they are associated to the global system.

1.5.1 Computation of the TZs in collocated MIMO systems

The impact of the collocation of the transducers on the system dynamics has been studied in Section 1.3. More specifically, it has been established that SISO collocated systems present larger stability margins and avoid the appearance of non-minimum phase zeros or the pole-zero flipping phenomenon. Collocated systems are consequently recommended, whether for SISO or MIMO configurations. Because the scope of this thesis concerns industrial applications for which the robustness of the system is essential, only collocated MIMO structures will be considered. Mathematically, a collocated MIMO system presents the same number of inputs and outputs such that $m = r$, leading to a square transfer function matrix. Multiple studies based on different approaches exist to compute the TZs of such MIMO systems. The most straightforward approach could consist in solving the following equation in the Laplace domain:

$$[\mathbf{G}(\mathbf{s})]\ \{u\} = \{0\} \tag{1.44}$$

where $\{u\} \in \mathbb{R}^r$ is the input vector and $\{0\} \in \mathbb{R}^r$ is the zero vector. Considering that the non-trivial solution must satisfy $\{u\} \neq \{0\}$, the TZs are the frequencies for which the transfer function matrix $[\mathbf{G}(\omega)]$ is non-invertible, i.e. they are the frequencies for which the system loses its full rank. Evaluating a loss of rank is usually performed by solving the related eigenvalue problem. Nevertheless, the estimation of the determinant of a complex transfer function matrix can be difficult to apprehend. The difficulty is reinforced by considering that the different transducers mounted on the system usually present cross-coupling effects. Hence, the non-diagonal terms of $[\mathbf{G}(\mathbf{s})]$ cannot be neglected, leading to a non-diagonal matrix. Thereby, a Smith-McMillan reduction is usually performed allowing to express the system in a diagonal canonical form [30, 31]. This diagonalization is achieved by first performing the Smith reduction which asserts that, from elementary row and column operations, a pseudo-diagonal monic polynomial matrix $[\mathbf{\Lambda}]$ of elements λ_i can be obtained from any matrix $[\mathbf{Q}]$ such that:

$$[\mathbf{P}]\,[\mathbf{Q}]\,[\mathbf{R}] = [\mathbf{\Lambda}] \tag{1.45}$$

where $[\mathbf{P}]$ and $[\mathbf{R}]$ contain the elementary row and column operations. Considering that for a mechanical system the different entries of the transfer function matrix have the same denominator d(s) due to the invariability of the resonance frequencies with respect to the

transducers placement, the Smith reduction can be applied to $[\mathbf{N}(\mathbf{s})]$, the numerators of $[\mathbf{G}(\mathbf{s})]$ such that $[\mathbf{G}(\mathbf{s})] = [\mathbf{N}(\mathbf{s})]/d(s)$. Hence, by considering $[\mathbf{N}(\mathbf{s})]$ as the generic matrix $[\mathbf{Q}]$ from Equation 1.45, the transfer function matrix can be rewritten as follows:

$$[\mathbf{G}(\mathbf{s})] = [\mathbf{P}(\mathbf{s})]^{-1} \frac{[\mathbf{\Lambda}(s)]}{d(s)} [\mathbf{R}(\mathbf{s})]^{-1} \tag{1.46}$$

The Smith-McMillan reduction is obtained from Equation 1.46 by reducing each diagonal element of $[\mathbf{\Lambda}(\mathbf{s})]$ to the lowest possible degree such that:

$$\frac{\lambda_i(s)}{d(s)} = \frac{\epsilon_i(s)}{\Phi_i(s)} \quad (i = 1, 2, ..., r) \tag{1.47}$$

where $\epsilon_i(s)/\Phi_i(s)$ is obtained by performing all the possible cancellations between $\lambda_i(s)$ and $d(s)$. Finally, the TZs values Z_0 are obtained by solving the following equation:

$$\prod_{i=1}^{r} \epsilon_i(Z_0) = 0 \tag{1.48}$$

Accordingly, the estimation of the TZs by solving Equation 1.44 is not that straightforward because it first requires to apply the two presented reduction mechanisms. Moreover, as the input vector $\{u\}$ cannot be cancelled out before solving the equation, each TZ is related to a specific zero input direction $\{u_0\}$. Further discussion related to those input directions can be found in Section 1.5.2.

Solving the Smith-McMillan form to obtain the Z_0 values can lead to three difficulties: (1) additional effort required to obtain the zero input directions $\{u_0\}$ if needed, (2) numerical imprecisions when Equation 1.48 is a polynomial of high order of s and (3) the omission of the TZ frequencies related to the uncontrollable and/or unobservable subsystems [32]. Consequently, the main technique used to compute the TZ frequencies is based on the state-space representation because it addresses the various disadvantages observed with the Smith-McMillan approach [5, 24]. By considering a MIMO system with n DoFs and r collocated inputs-outputs pairs, its state-space form can be expressed as follows (see Section 1.2):

$$\begin{aligned} \{\dot{\mathbf{q}}(\mathbf{t})\} &= [\mathbf{A}]\{\mathbf{q}(\mathbf{t})\} + [\mathbf{B}]\{\mathbf{u}(\mathbf{t})\} \\ \{\mathbf{y}(\mathbf{t})\} &= [\mathbf{C}]\{\mathbf{q}(\mathbf{t})\} + [\mathbf{D}]\{\mathbf{u}(\mathbf{t})\} \end{aligned} \tag{1.49}$$

where $\{\mathbf{q}(\mathbf{t})\} \in \mathbb{R}^{2n}$ is the state variable vector, $[\mathbf{A}] \in \mathbb{R}^{2n\times 2n}$ is the state matrix, $[\mathbf{B}] \in \mathbb{R}^{2n\times r}$ is the input matrix, $\{\mathbf{y}(\mathbf{t})\} \in \mathbb{R}^{r}$ is the output vector, $[\mathbf{C}] \in \mathbb{R}^{r\times 2n}$ is the output matrix and $[\mathbf{D}] \in \mathbb{R}^{r\times r}$ is the feedthrough matrix. Equation 1.49 can be easily rewritten in the Laplace domain and rearranged as follows:

$$\begin{bmatrix} s\,\mathbf{I_{2n}} - [\mathbf{A}] & -[\mathbf{B}] \\ [\mathbf{C}] & [\mathbf{D}] \end{bmatrix} \begin{bmatrix} \{\mathbf{q}\} \\ \{\mathbf{u}\} \end{bmatrix} = \begin{bmatrix} \mathbf{0_{2n\times 1}} \\ \{\mathbf{y}\} \end{bmatrix} \tag{1.50}$$

where s is the complex Laplace variable and the left hand side matrix is called the system matrix. Since the TZs Z_0 are the frequencies at which all the outputs of the system are zero when applying non-zero inputs, they are the solution of Equation 1.50 when $\{\mathbf{y}\}$ is set to zero:

$$\begin{bmatrix} Z_0\,\mathbf{I_{2n}} - [\mathbf{A}] & -[\mathbf{B}] \\ [\mathbf{C}] & [\mathbf{D}] \end{bmatrix} \begin{bmatrix} \{\mathbf{q_0}\} \\ \{\mathbf{u_0}\} \end{bmatrix} = \begin{bmatrix} \mathbf{0_{2n\times 1}} \\ \mathbf{0_{r\times 1}} \end{bmatrix} \tag{1.51}$$

Hence, the solutions of Equation 1.51 that are obtained by solving the generalised eigenvalue problem provide the different TZ frequencies Z_0 as well as each associated input vector direction $\{\mathbf{u_0}\}$. In addition to the direct computation of the input directions along with the Z_0 frequencies, using the state-space representation allows to obtain the entire set of TZ values while the Smith-McMillan approach might provide only a subset of them in case of not fully controllable and/or observable system [32].

1.5.2 Properties of the TZs in collocated MIMO systems

As explained, each TZ is associated to a input direction. This is physically reflected through the fact that in order to observe the cancellation of all the outputs at the ith TZ frequency $Z_{0,i}$, a linear combination based on the associated input direction $\{u_{0,i}\}$ needs to be applied to the inputs. To illustrate the necessity to combine both the frequency Z_o and the input directions to obtain the intended zero response, a cantilever beam with two collocated pairs (force actuator and displacement sensor) has been modelled in SDT. The two pairs are located at the third and at the half of the longitudinal axis of the beam. The open-loop responses of this simple MIMO system are illustrated in Figure 1.14 where the first two TZ frequencies $Z_{0,1}$ and $Z_{0,2}$ are highlighted with dashed red lines. As it can be seen, the different entries of the system do not present a zero at the TZ values, which confirms the dual need of frequencies and input direction. This also validates that the TZs are not frequencies for which all the entries drop to zero nor frequencies for which some entries are zero.

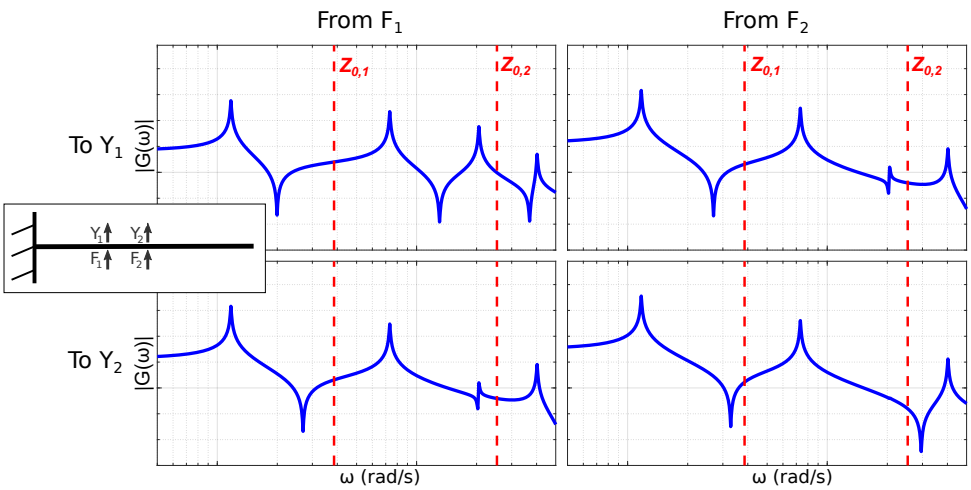

Figure 1.14: Response of a simple MIMO system where the first two TZ values are highlighted with dashed red lines.

As stated, a linear combination between the different inputs is required in order to observe the presence of a zero at a specific Z_0 value. The application of such a dependency based on the input vector $\{\mathbf{u_0}\}$ modifies the representation of the system from a MIMO to a single-input with multiple-outputs one. Figure 1.15 presents the response of the two displacement sensors mounted on the cantilever beam when the first and the second input directions are applied. As shown in Figure 1.15a, the use of the first zero input direction $\{u_{0,1}\}$ results in the appearance of a zero for both the outputs at the first TZ value $Z_{0,1}$. Moreover and as expected, there is no zero at the second TZ frequency $Z_{0,2}$, since it requires the usage of the related second input vector $\{u_{0,2}\}$. Similarly, Figure 1.15b shows the system responses when this second input vector is applied and it can be seen that a zero appears exactly at $Z_{0,2}$ and no longer at $Z_{0,1}$ at both outputs.

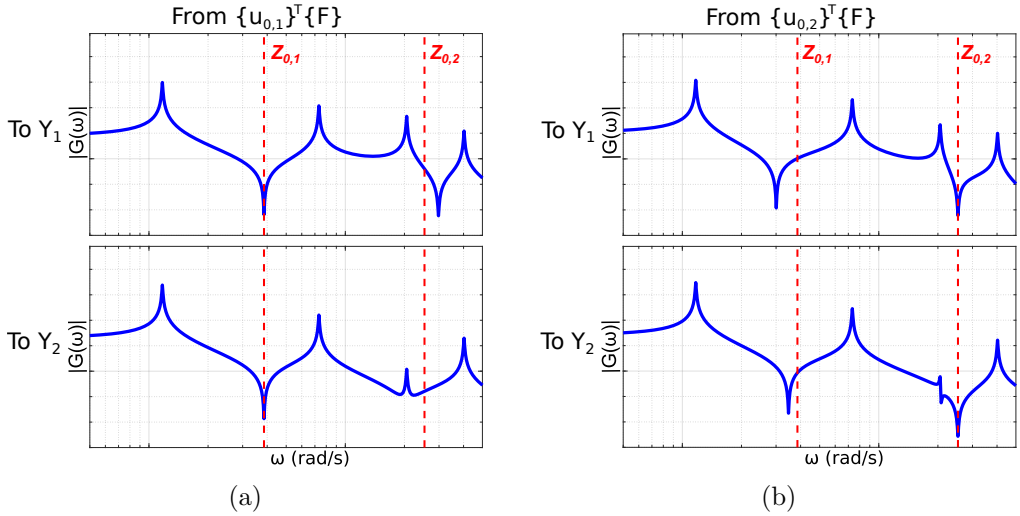

Figure 1.15: Response of a simple MIMO system when: (a) the input direction related to the first TZ frequency is applied, (b) the input direction related to the second TZ frequency is applied.

In addition to the dual necessity of applying a specific frequency and the related input vector direction to observe a zero response at all the outputs of the system, Figure 1.14 highlights that the alternating pole-zero property still holds on the diagonal terms of the transfer function response. This observation is as expected since each diagonal term corresponds to a collocated SA pair that behaves like a SISO system and, consequently, that presents the same properties. Conversely, the non-diagonal elements reflect the cross-coupling effect from one pair to another. Because such cross-coupling can be interpreted as a non-collocated configuration, the alternating pole-zero property is not guaranteed on these non-diagonal elements. They consequently need to be properly analysed when designing a control architecture to avoid any stability concern.

In SISO systems, it is well known that the closed-loop poles tend to the open-loop anti-resonances for high value of the feedback gain. Nevertheless, a MIMO system presents both (1) the anti-resonance frequencies that are related to each entry of the transfer function matrix and (2) the TZs that are associated to the global system. The question of the convergence of the closed-loop poles in such MIMO systems is therefore important: are the poles converging towards the anti-resonances, the TZs or neither of them? It has first been proved by Davison [18] and then analytically confirmed by Preumont [33] that when dealing with collocated MIMO systems, the closed-loop poles that do not tend to infinity when increasing asymptotically the gain are converging towards the TZs. Moreover, this asymptotic behaviour does not depend on the feedback control law and, consequently, not on the input directions $\{\mathbf{u_0}\}$ neither. Nevertheless, the shape of the root locus depends on both the TZ values and the control law. Those two properties can, for example, be observed in [34] where different control schemes are numerically tested on a MIMO rotating platform.

Finally, the TZs of MIMO systems with collocated displacement sensor-force actuator pairs correspond to the eigenvalues of an associated constrained problem [23]. Hence, the TZs of such configurations can be obtained by solving the corresponding eigenvalue problem, which is already well-known and used in SISO systems as stated in Section 1.3. Nonetheless, this physical interpretation does not hold for non-collocated configurations

where the TZs are obtained by solving a non-symmetric eigenvalue problem which leads to non-minimum phase zeros [35].

1.6 Conclusion

This chapter introduced important concepts of system dynamics. The notion of pole has first been mathematically and physically studied for single and multiple DoFs systems. It allowed to properly explain how a physical system can be modelled, what are the effects of active control on its dynamics and how the complexity of the numerical model can be reduced by truncation.

Additionally, the zeros of SISO and MIMO systems have been extensively studied. It was shown that those zeros play a major role in the system dynamics and should consequently be considered when designing any control architecture. Through its alternating pole-zero property and the resulting robustness, the benefits of designing a collocated architecture was highlighted.

Finally, the numerical complexity to obtain the zero values in SISO system led to the introduction of an analytic approximation. Based on a numerical validation, it has been shown that the proposed approximation can be used as a first efficient estimation of the zeros when needed.

References

[1] R. Brockett. "Poles, zeros, and feedback: State space interpretation". In: *IEEE Transactions on Automatic Control* 10.2 (1965), pp. 129–135. DOI: 10.1109/TAC.1965.1098118.

[2] H. H. Rosenbrock. *State-space and multivariable theory.* Vol. 3. Wiley Interscience Division, 1970.

[3] J. Den Hartog. *Mechanical Vibrations.* Dover Publicatios, 1985.

[4] A. Preumont. *Vibration Control of Active Structure, An Introduction.* Thrid Edition. Springer, 2011. DOI: 10.1007/978-94-007-2033-6.

[5] W. Levine. *The Control Handbook in two Volumes.* CRC Press, 1999.

[6] J. M. Gere and S. P. Timoshenko. *Mechanics of Materials.* Third Edition. Springer, 1991.

[7] G. Strang. *Linear algebra and its applications.* Belmont, CA: Thomson, Brooks/Cole, 2006.

[8] L. F. Shampine. *Numerical solution of ordinary differential equations.* Routledge, 2018.

[9] G. F. Franklin, J. D. Powell, and A. Emami-Naeini. *Feedback control of dynamic systems.* Sixth Edition. Pearson, 2009.

[10] G. D. Martin. "On the Control of Flexible Mechanical Systems". PhD thesis. Stanford University, 1978.

[11] S. Rubin. "Improved component-mode representation for structural dynamic analysis". In: *AIAA journal* 13.8 (1975), pp. 995–1006. DOI: 10.2514/3.60497.

[12] F. M. Fleming. "The Effect of Structure, Actuator, and Sensor on the Zeroes of Controlled Structures". PhD thesis. Massachusetts Institute of Technology, 1991.

[13] G. Raze, C. Dumoulin, and A. Deraemaeker. "Reduced-order state-space models of structures with imposed displacements and accelerations". In: *Mechanical Systems and Signal Processing* 191 (2023), p. 110156. DOI: 10.1016/j.ymssp.2023.110156.

[14] R. M. Foster. "A reactance theorem". In: *Bell System technical journal* 3.2 (1924), pp. 259–267. DOI: 10.1002/j.1538-7305.1924.tb01358.x.

[15] M. J. Balas. "Direct velocity feedback control of large space structures". In: *Journal of guidance and control* 2.3 (1979), pp. 252–253. DOI: 10.2514/3.55869.

[16] E. Balmes. *Structural Dynamics Toolbox 7.3 (for use with MATLAB)*. 1991. URL: https://www.sdtools.com.

[17] D. Miu. "Physical Interpretation of Transfer Function Zeros for Simple Control Systems with Mechanical Flexibilities". In: *Journal of Dynamic Systems, Measurement, and Control* 113.3 (1991), pp. 419–424. DOI: 10.1115/1.2896426.

[18] E. Davison and S. Wang. "Properties and calculation of transmission zeros of linear multivariable systems". In: *Automatica* 10.6 (1974), pp. 643–658. DOI: 10.1016/0005-1098(74)90085-5.

[19] B. Wie. "On the modeling and control of flexible space structures". PhD thesis. Stanford University, 1981.

[20] V. A. Spector and H. Flashner. "Modeling and Design Implications of Noncollocated Control in Flexible Systems". In: *Journal of Dynamic Systems, Measurement, and Control* 112.2 (1990), pp. 186–193. DOI: 10.1115/1.2896125.

[21] V. A. Spector and H. Flashner. "Sensitivity of Structural Models for Noncollocated Control Systems". In: *Journal of Dynamic Systems, Measurement, and Control* 111.4 (1989), pp. 646–655. DOI: 10.1115/1.3153108.

[22] C. Inniss and T. Williams. "Sensitivity of the zeros of flexible structures to sensor and actuator location". In: *Proceedings of 32nd IEEE Conference on Decision and Control*. 1993, 1402–1403 vol.2. DOI: 10.1109/CDC.1993.325418.

[23] T. Williams. "Constrained modes in control theory: Transmission zeros of uniform beams". In: *Journal of Sound and Vibration* 156.1 (1992), pp. 170–177. DOI: 10.1016/0022-460X(92)90819-J.

[24] W. Wolovich. "On determining the zeros of state-space systems". In: *IEEE Transactions on Automatic Control* 18.5 (1973), pp. 542–544. DOI: 10.1109/TAC.1973.1100379.

[25] A. Emami-Naeini and P. Van Dooren. "Computation of zeros of linear multivariable systems". In: *Automatica* 18.4 (1982), pp. 415–430. DOI: 10.1016/0005-1098(82)90070-X.

[26] J. McNamee. *Numerical Methods for Roots of Polynomials - Part I*. Studies in Computational Mathematics, Volume 14. Elsevier Science, 2007.

[27] V. Pan. "Complexity of computations with matrices and polynomials". In: *SIAM review* 34.2 (1992), pp. 225–262.

[28] D. Piron, S. Pathak, A. Deraemaeker, and C. Collette. "A pole-zero based criterion for optimal placement of collocated sensor-actuator pair". In: *Mechanical Systems and Signal Processing* 155 (2021), p. 107533. DOI: 10.1016/j.ymssp.2020.107533.

[29] S. Pathak, D. Piron, A. Paknejad, C. Collette, and A. Deraemaeker. "On transmission Zeros of piezoelectric structures". In: *Journal of Intelligent Material Systems and Structures* 33.12 (2022), pp. 1538–1561. DOI: 10.1177/1045389X211057209.

[30] T. Kailath. *Linear systems*. Prentice-Hall information and system sciences series. Prentice-Hall, 1980.

[31] J. M. Maciejowski. *Multivariable feedback design*. Electronic systems engineering series. Addison-Wesley, 1989.

[32] A. G. J. Macfarlane and N. Karcanias. "Poles and zeros of linear multivariable systems: a survey of the algebraic, geometric and complex-variable theory". In: *International Journal of Control* 24.1 (1976), pp. 33–74. DOI: 10.1080/00207177608932805.

[33] A. Preumont, B. De Marneffe, and S. Krenk. "Transmission zeros in structural control with collocated multi-input/multi-output pairs". In: *Journal of guidance, control, and dynamics* 31.2 (2008), pp. 428–432. DOI: 10.2514/1.31529.

[34] T. Dehaeze and C. Collette. "Active damping of rotating platforms using integral force feedback". In: *Engineering Research Express* 3.1 (2021), p. 015036. DOI: 10.1088/2631-8695/abe803.

[35] T. Williams. "Transmission zeros of non-collocated flexible structures: Finite-dimensional effects". In: *Dynamics Specialists Conference*. 1992, p. 2116.

Chapter 2

The pole-zero distance as a mean to evaluate damping

Abstract

This chapter first presents a brief comparison between low-authority and high-authority controllers, with a focus on their trade-off between performance and robustness. It is shown that low-authority controllers are more robust and can provide suitable damping for relatively small control efforts. Particular emphasis is placed on collocated SISO low-authority architectures that exhibit a direct link between pole-zero distance and maximum reachable damping. This well-known link in SISO is further extended to low-authority MIMO systems and numerically validated on two structures: a cantilever beam and a simply supported plate. Additionally, the extension is experimentally validated with a cantilever beam on which five pairs of collocated piezoelectric patches have been mounted. This proven extension introduces a valuable contribution to the field of control engineering, providing a fast open-loop assessment method to analyse the closed-loop performance of low-authority MIMO systems.

2.1 Introduction

The alleviation of structural vibrations by active damping involves two distinct elements: (1) the transducers that measure and act on the system dynamics and (2) the control law that adjusts, in real-time, the signal delivered to the actuator(s) based on the sensor one(s). Such active control architecture aims to add damping in the system so that it can better resist to oscillations and converge faster to steady-state conditions by reducing the settling time of transient behaviours. Mathematically, increasing the damping is achieved by pushing the poles of the system towards the left of the complex plane, which attenuates the resonance peak. As described in Chapter 1, the control law has a significant effect on the damping performance of the closed-loop architecture.

Controllers can be broadly classified into two types: low authority and high authority. The low authority controllers (LACs) provide a modification of the system dynamics in the vicinity of the resonances while the rest of the closed-loop response is barely affected [1]. This is because a LAC cannot significantly shift the eigenvalues of the system to any desired location. Nevertheless, such a limited authority enables the analytic approximation of the closed-loop system behaviour and ensures its robustness [2].

Conversely, a high authority controller (HAC) can perform a substantial modification of the poles position, leading to much better closed-loop performance. A such higher author-

ity is achieved because, unlike the LAC, the HAC is built based on the representation of the system using a model. Additionally, a HAC generally relies on a state feedback to build the controlled signal [3]. Yet, a state feedback controller usually requires an additional observer for practical implementations because the physical states of a system are difficult to determine by direct observation. A widely used observer is the Kalman filter, a recursive algorithm developed on the prediction of the states and the update of those states based on the resulting errors [4]. Besides the hypothetical need for a state observer, the HAC is highly sensitive to model uncertainties. Strong knowledge of the plant is consequently required, resulting in a trade-off between achievable performance and stability [5].

Numerous studies have combined both approaches to build a LAC-HAC architecture and benefit from the advantages of each. Such architectures are usually based on the division of the control effort with two loops: one based on the LAC to add damping and robustness and a second one with the HAC to reach the targeted performance, as done in [6, 7].

2.1.1 Link between pole-zero distance and damping in SISO systems

When a LAC is implemented on a linear and time-invariant collocated SISO system, a major property within the active damping domain emerges: the distance between the pole and the zero to which it converges when the gain is increased, for a specific mode, is directly proportional to the maximum attainable damping in closed-loop [5]. The pole-zero (PZ) distance, an open-loop information, can consequently be used to predict the performance of the controlled plant in closed-loop. This interesting property is illustrated in Figure 2.1 which clearly shows that the larger the PZ distance is, the more the maximum damping increases in consequence.

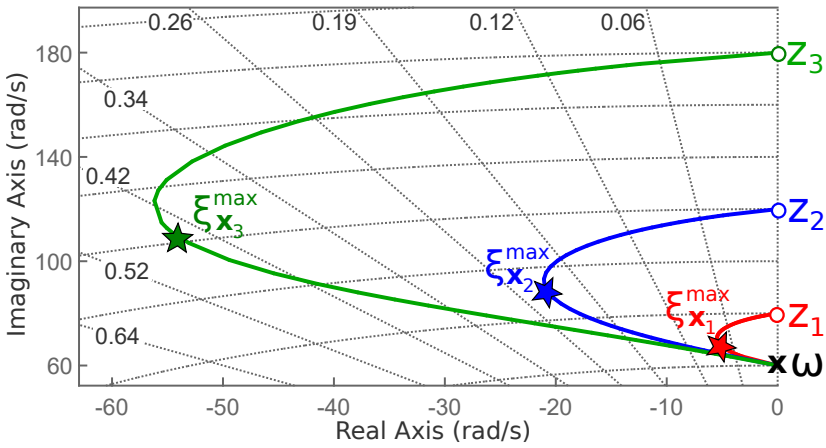

Figure 2.1: Graphical illustration of the link between the PZ distance and the maximum reachable damping ratio for three zero values (lead controller).

This well-established property is an important feature of low-authority collocated systems. For example, it allows to predict the performance of a control law based on a simple numerical model as done in [8] where an experimental validation confirms the estimation. The direct link between PZ distance and damping is also observed in [9] where a modified integral force feedback (IFF) [10] controller is used. Interestingly, the PZ distance observed in the impedance curve of a piezoelectric patch mounted on a structure is directly proportional to its coupling factor, which is itself related to the performance of the system [11]. The PZ distance is consequently an important feature of low-authority collocated SISO systems.

2.1.2 Motivation and chapter outline

The direct link between PZ distance and maximum reachable damping in SISO collocated systems reinforces the importance of the zeros in system dynamics, as demonstrated in Chapter 1. The aim of this chapter is to extend this link to MIMO systems as done in [12]. This extension is first performed from an analytical point of view and numerically validated in Section 2.2. An experimental validation is conducted in Section 2.3 in order to reinforce the validity of this new extension. Finally, some conclusions are drawn in Section 2.4.

2.2 Link between PZ distance and damping in MIMO systems

For SISO linear and time-invariant collocated systems, the maximum achievable damping of a mode directly depends on the distance between its related poles and zeros. A quick analysis of the zeros of a collocated SISO system allows therefore to obtain, for a reasonable computational cost, valuable information on the possible performance once in closed-loop. Unfortunately, and to the best of the author's knowledge, this link between PZ distance and damping has never been studied for MIMO systems. As discussed in Chapter 1, when dealing with such collocated MIMO systems, the closed-loop poles that do not tend to infinity when increasing asymptotically the gain are converging towards the TZs. Moreover, this asymptotic behaviour does not depend on the feedback control law, unlike the shape of the root locus. Nevertheless, it is stated in [13] that it is not possible to predict the precise trajectory of the closed-loop poles in the complex plane when dealing with a MIMO plant.

This inability to predict the shape of the root locus for MIMO systems precludes the hypothesis of regular closed-loops between the poles and the TZs as it can be observed in SISO systems, e.g. as shown in Figure 2.1. This prevents therefore the possibility of analytically expressing the maximum reachable damping for a specific configuration based on the poles and the TZs values. Yet, the impossibility of predicting the shape of the root locus for MIMO systems depicted in [13] is mainly due to its generalisation for any type of controller. Indeed, specific configurations can lead to expected behaviours similar to SISO systems and, consequently, the possibility to draw the root locus of the closed-loop system using only the open-loop poles and the TZs knowledge.

Let us consider a flexible system with low damping and a low modal density on which multiple collocated SA pairs are mounted. For some transducer configurations, it can be assumed that a TZ lies in the vicinity of each open-loop pole, mimicking therefore the alternating PZ property of SISO collocated systems. By recalling the physical interpretation of the TZs (i.e. they correspond to the frequencies of an associated constrained system), this condition is only possible when the transducers present a small authority on the system such that the corresponding constrained system is close to the unconstrained one. This can for example be observed when only a few force actuator-displacement sensor pairs are mounted on a very large system. When considering piezoelectric patch actuation, small authority occurs for example when the cumulated size of the patches is small with respect to the size of the system. When a control law is implemented, the closed-loop poles of the controlled system converge towards the TZs for large gain values. If the implemented controller presents a small authority, its effect is limited which restricts the migration of the closed-loop poles in the complex plane. Moreover, and because of the small modal density hypothesis, the different open-loop poles are located far away from each other,

limiting therefore the possible modal interaction. Consequently, each open-loop pole converges towards the TZ in its neighbourhood, forming thereby independent modal loops. This hypothesis is illustrated in Figure 2.2 where the real and the imaginary axes present different scales in order to ease the visualization.

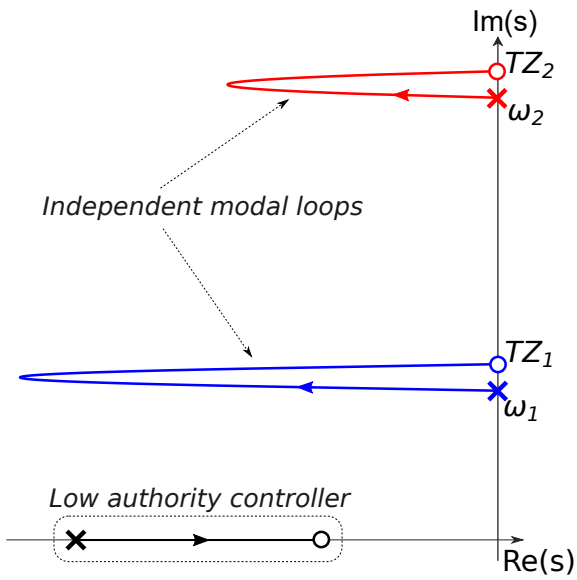

Figure 2.2: Hypothesis on the shape of the root locus in case of a MIMO decentralised low authority controller with small modal density and a TZ in the vicinity of each open-loop pole.

When considering the different hypotheses presented in Figure 2.2, independent root loci derived from each open-loop pole and the TZ in its neighbourhood can therefore be considered. It consequently allows to analyse the migration of every closed-loop pole independently by only considering the open-loop pole, the TZ in its neighbourhood and the LAC law. Let us for example consider a decentralised architecture with an identical low-authority control law, such as an IFF defined by:

$$C(s) = g\,\frac{1}{s} \tag{2.1}$$

where g is the gain of the controller and s is the Laplace variable. Because of the independent behaviour of each mode, the characteristic equation of the closed-loop system can be written in the modal coordinates as follows:

$$1 + g\,\frac{1}{s}\left(\frac{s^2 + Z_{0,i}^2}{s^2 + \omega_i^2}\right) = 0 \tag{2.2}$$

where ω_i is the open-loop pole of the mode of interest i and $Z_{0,i}$ is its related TZ, i.e. the TZ that lies in the vicinity of ω_i in accordance with the hypothesis. The full path of each closed-loop pole in the complex plane can thereby be computed by solving Equation 2.2 when the gain g is varied from 0 to infinity. Interestingly, Equation 2.2 presents the same form as the characteristic equation of a SISO integral force feedback controller architecture from [5], the only difference being that the anti-resonance z_i in the SISO configuration is replaced by the TZ values $Z_{0,i}$ in the considered MIMO architecture. Therefore, the existing link between the maximum reachable damping of mode i, ξ_i^{max}, and the PZ distance in collocated SISO systems that has been demonstrated in [8] can be extended

to collocated MIMO ones by replacing the anti-resonance frequency z_i with the TZ value $Z_{0,i}$, which leads to:

$$\xi_i^{max} = \frac{Z_{0,i} - \omega_i}{2\omega_i} \tag{2.3}$$

Consequently, Equation 2.3 shows that the link between damping and PZ distance holds in the case of MIMO systems. Nevertheless, this relationship is only valid when the three hypotheses that have been previously defined are satisfied, i.e. when (1) the considered system presents a low modal density, (2) a TZ lies in the vicinity of each open-loop pole and (3) the collocated control architecture has a small authority. Those properties can be encountered in different engineering applications such as communication antennas, solar panels or large mirrors for observatory purposes. Indeed, it is for example illustrated in [14] that a laminated membrane plate mirror modelled for space telescopes presents a small modal density for the first four modes. Hence, mounting collocated pairs of piezoelectric patches on such system induces TZs in the vicinity of the poles, satisfying therefore the required hypotheses.

Obviously, the expression of the maximum reachable modal damping given by Equation 2.3 is only valid when an integral force feedback controller is applied. However, even though using another control law can modify this expression, the maximum achievable damping will still be directly proportional to the distance between the open-loop pole ω_i and the nearby transmission zero $Z_{0,i}$. It is indeed shown in [5] that, for different SISO cases, the maximum damping ratio is always proportional to the PZ distance, no matter which LAC is used. Hence, when the defined hypotheses are satisfied, and therefore when the modal loops are independent which allows to replace the anti-resonances by the TZs, a more general expression can be defined as follows:

$$\xi_i^{max} \propto |P\ Z_0|_i \tag{2.4}$$

where $|P\ Z_0|_i$ expresses the pole-TZ distance of mode i. This distance can be obtained by the difference between the TZ and the nearby open-loop pole when the system exhibits a pole-TZ pattern (as applied in Equation 2.3) or by the difference between the open-loop pole and the nearby TZ when the latter appears first.

2.2.1 Numerical validation of the MIMO extension

The extension of the direct link between the maximum reachable damping and the pole-TZ distance for MIMO systems described by Equation 2.4 is subjected to some limiting hypotheses. The aim of this validation is to provide numerical examples of systems that satisfy those required hypotheses in order to prove that, in such a case, this direct link exists. Two numerical systems have been considered and numerically built in SDT: one with less modal density (a cantilever beam) and the other with a higher one (a simply supported plate). In both cases, the values of the TZs have been modified by changing the positions of the collocated transducer pairs. Moreover, the two systems are defined with the same lightly damped steel with the following properties: Young's modulus $E = 210\ GPa$, Poisson's ratio $\nu = 0.285$, mass density $\rho = 7800\ kg/m^3$ and modal damping ratio $\xi = 0.004$.

The cantilever beam is modelled with the dimension of 300 mm x 25 mm x 2 mm and its finite element model is built with 6 DoFs multilayer shell elements each 1 and 5 mm in the x and y direction respectively, leading to 1806 nodes in total. Two lead zirconate titanate (PZT) piezoelectric voltage actuators and two PZT sensors patches are considered, with

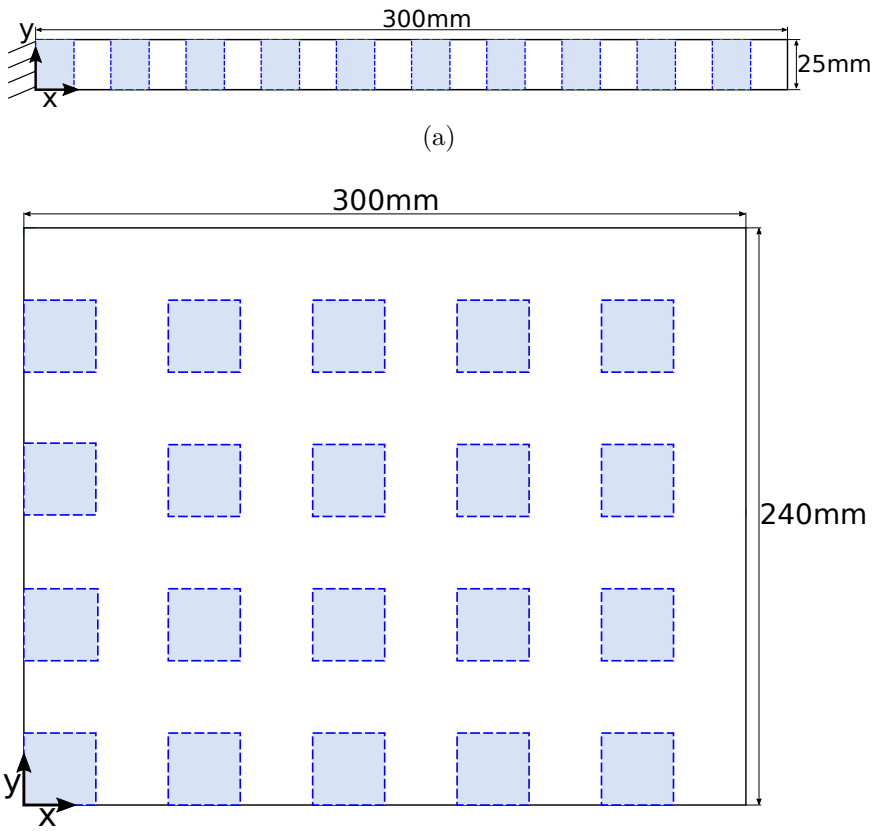

Figure 2.3: Representation of the two structural systems and the full set of possible patch positions in dotted blue lines: (a) top view of the cantilever beam that presents 10 possible patch positions along its longitudinal axis x, (b) top view of the simply supported plate with a total of 20 possible patch positions in the x and y directions.

the following dimension: 15 mm x 25 mm x 0.5 mm. A possible position is defined every 30 mm in the longitudinal direction of the beam starting from its clamped end, leading to 10 different placement locations. In order to perform this study on a MIMO system, two pairs of patches in voltage/voltage mode are used simultaneously, translating consequently the 10 possible patch locations into 45 different configurations in total. Moreover, to ensure the collocation of the transducers in the sense that there is the alternating PZ property on the open-loop transfer function of each pair in the frequency band of interest, each SA pair is placed at the same location but on the opposite faces of the structure for every tested configuration. Such configuration allows indeed to ensure this alternating property within the frequency band of interest when dealing with piezoelectric patches, as demonstrated in [15]. The entire set of the 10 possible patch positions is shown in Figure 2.3a, as well as the Cartesian coordinates of the beam. Finally, and because the different considered pair positions do not allow to control the torsional modes (the patches are symmetrically placed along the middle transversal axis), the study will be limited to the bending modes of the beam.

The simply supported plate defined by free rotation but fixed translation on its four edges is modelled with the dimension of 300 mm x 240 mm x 2 mm and is discretized by 6 DoFs multilayer shell elements each 3 mm in both x and y directions (8181 nodes in total). Again, two pairs of PZT piezoelectric voltage actuators and sensors patches are considered, with the following dimension: 30 mm x 30 mm x 0.5 mm. A pair of patches

can be placed each 60 mm in both the x and y directions starting from the origin of the Cartesian frame, leading to 20 possible patch positions. Because two pairs of patches are again considered simultaneously, those possible positions translate into a total of 190 different configurations. The alternating PZ property within the frequency band of interest is again ensured by placing the actuator and the sensor patches at the same location but on the opposite faces of the structure, for each considered configuration. The entire set of the 20 possible patch positions is shown in Figure 2.3b, as well as the Cartesian coordinates of the plate.

Regarding the control architecture, a decentralised identical direct velocity feedback (DVF) control law is selected. Such LAC introduces indeed the variation of only one parameter (the gain g), which avoids any additional variability in the control architecture when analysing the results obtained with the cantilever beam or the simply supported plate. Because the considered systems present, for each configuration, two collocated pairs of patches, the controller $C(s)$ is defined as a 2×2 matrix as follows:

$$C(s) = g \begin{bmatrix} s & 0 \\ 0 & s \end{bmatrix} \tag{2.5}$$

The root loci obtained for arbitrary configurations of the two systems when applying the decentralised controller defined by Equation 2.5 are shown in Figure 2.4. It can be seen that the three required conditions to ensure the MIMO extension are fulfilled. Indeed, (1) the open-loop poles of the considered modes are correctly well-separated (low modal density), (2) a TZ lies within the vicinity of each open-loop pole (mimicking the alternating PZ property of collocated SISO systems) and (3) each mode behaves independently from the others by making a loop from the open-loop poles towards the surrounding TZ (low authority control with no modal interaction). This therefore confirms the possibility to encounter systems that present the aforementioned conditions and, consequently, it reassures about the relevance of the presented extension of the link between damping and PZ distance for MIMO systems expressed by Equation 2.4.

It can be seen in Figures 2.4a and 2.4b that, for each configuration and each mode, an optimal gain value allows to obtain the maximum reachable damping ratio, i.e. the one obtained at the leftmost position of the closed-loop poles in the complex plane. Hence, the maximum reachable damping ratio can be easily extracted for each of the first three modes, for the entire set of the 45 (cantilever beam) and 190 (simply supported plate) possible pairs configurations. Moreover, the value of all the TZs can be obtained by using the state-space approach developed in Section 1.5. Hence, in addition to the maximum reachable damping ratio of each mode, the pole-TZ distance can be computed as well by calculating the difference between each TZ and each surrounding pole, for all the possible pair configurations. It therefore means that the link between the maximum reachable damping ratio and the pole-TZ distance can be plotted for all the considered configurations and for the first three modes of the two systems. In order to ease the visualization of this link for those three modes, the pole-TZ distance needs to be normalised to ensure the same order of magnitude for each mode. Consequently, the normalised pole-TZ distance $|P\ Z_0|_{i,norm.}$ of mode i is defined by [12]:

$$|P\ Z_0|_{i,norm.} = \frac{Z_{0,i} - \omega_i}{\omega_i} \tag{2.6}$$

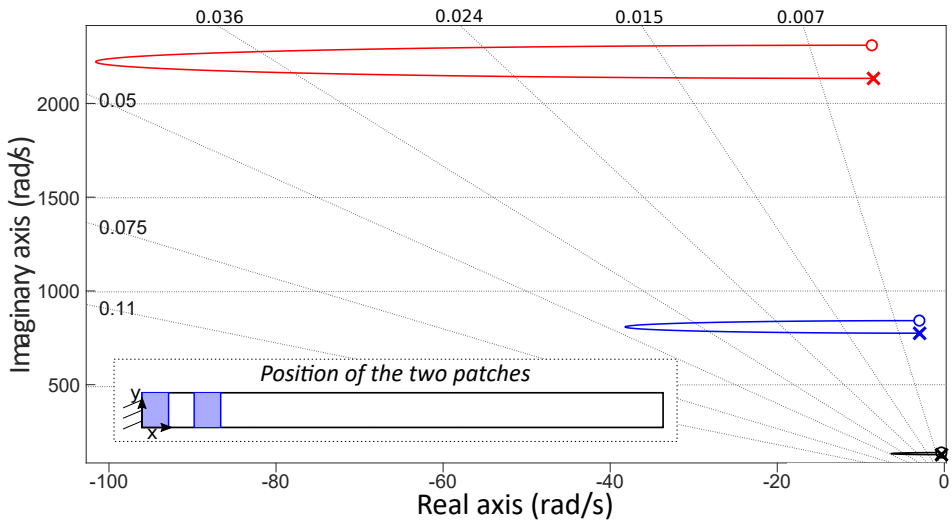

(a) Beam

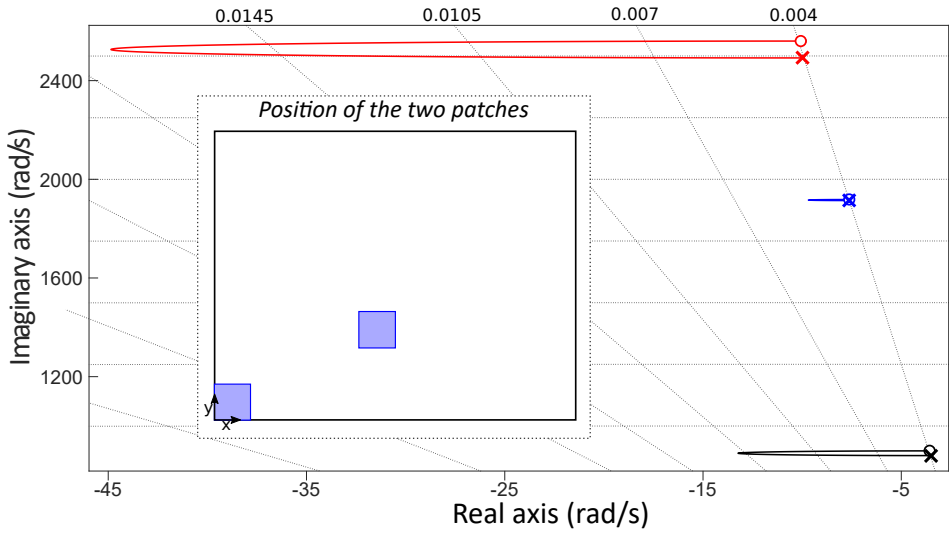

(b) Plate

Figure 2.4: Root locus obtained with an identical decentralised DVF controller for specific locations of two pairs of piezoelectric patches on: (a) the cantilever beam, (b) the simply supported plate.

Figures 2.5a and 2.5b show, for the cantilever beam and the simply supported plate respectively, the value of the maximum reachable damping ratio as a function of the corresponding normalised pole-TZ distance for the three first modes of interest. In addition, the dotted lines plotted on both figures correspond to a first-order fit based on a least-squares approach using the entire set of entries. The two figures clearly highlight the proportionality between the maximum reachable damping ratio and the pole-TZ distance, demonstrating therefore that the generalised linear link expressed by Equation 2.4 is verified for the two considered systems and all the modes of interest. Furthermore, and for each system, this linear link exhibits a common factor for all the modes, meaning that it would even be possible to find an analytical expression of the damping as a function of a normalised pole-TZ distance such as the one formulated by Equation 2.3. Those observations are therefore numerically proving the presented extension of the link between damping and PZ distance for collocated SISO systems to MIMO ones when the different defined conditions are satisfied.

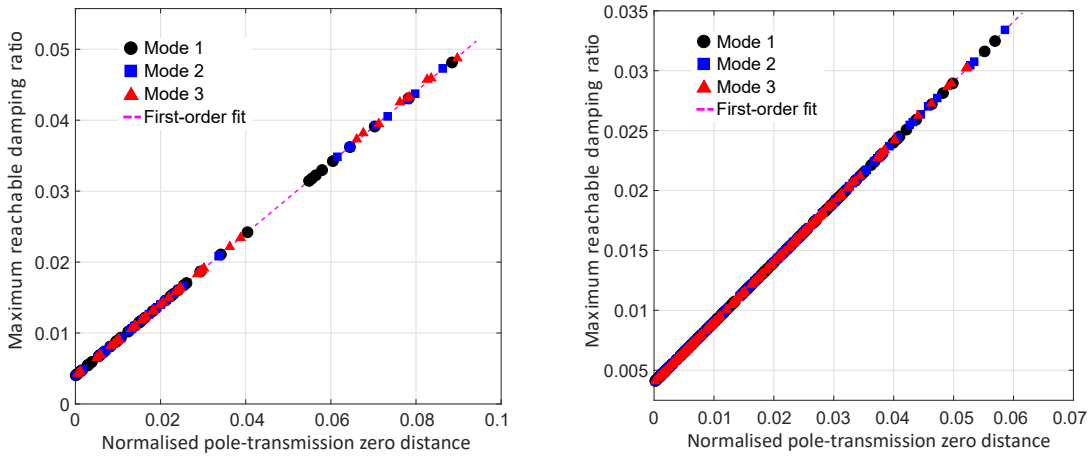

(a) Beam (b) Plate

Figure 2.5: Maximum reachable damping ratio as a function of the normalised pole-TZ distance for the first three modes of: (a) the cantilever beam, (b) the simply supported plate.

2.3 Experimental validation of the link in MIMO systems

The direct link between PZ distance and damping is well-established in SISO systems and its validity has been strengthened by experimental validations, such as performed in [8]. The extension of this link from SISO to MIMO systems is newly introduced in the previous section and validated by numerical simulations only. The aim of this section is consequently to reinforce the validity of the link given by Equation 2.4 by performing an experimental validation. Such experimental validation adds credibility to the numerical one because it corroborates the link under real conditions, i.e. without the different idealisations made when numerically modelling a structure. Indeed, those idealisations remove different difficulties that can be encountered with real-life systems, such as the presence of noise at different levels, the addition of mass and/or rigidity from the transducers (especially when considering a force/displacement pair) or the phase lag introduced by the numerical discretization.

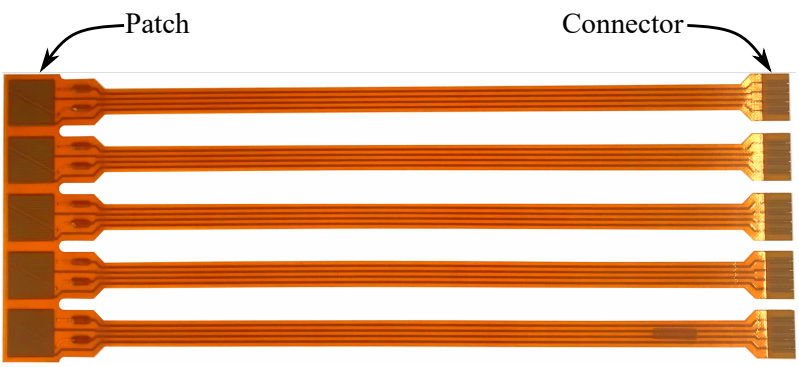

Figure 2.6: MFC patch array used for the experimental validation of the MIMO extension.

In order to experimentally validate the presented extension, a model is first implemented in SDT to determine the appropriate parameters of the experimental system, the size and the position of the active patches and the method that will be applied to estimate the performance index. This analysis provided the following plant: the structure consists of

a 250 mm x 36.4 mm x 0.75 mm cantilever steel beam. The same steel employed for the numerical validation is used again to build the model, i.e. Young's modulus $E = 210\ GPa$, Poisson's ratio $\nu = 0.285$, mass density $\rho = 7800\ kg/m^3$ and modal damping ratio $\xi = 0.004$. To reduce the inaccuracy caused by the mounting process, two piezoelectric patch arrays as shown in Figure 2.6 have been selected for actuation and sensing. Each array is composed of five identical piezoelectric patches of dimension 13 mm x 13 mm with a fixed spacing of 3 mm between them in the longitudinal direction. The patches are d_{31} P2 Macro Fiber Composite (MFC) [16] and have been ordered with a specific size and wiring scheme from Smart Material company, with an overall thickness of 0.3 mm (0.18 mm for the active layer) and a volume fraction of active fibres of 86% (identical volume fraction as for the regular MFCs). Both the arrays are mounted symmetrically to the centre of the beam, at 1.5 mm from its clamped end. Similarly to the numerical validation, each sensor-actuator pair is placed at the same location but on the opposite faces of the structure to ensure the pole-zero alternating property. It can be noted that modelling a MFC patch is challenging because it is composed of ceramic rods encapsulated between adhesive, electrodes and polymer. Nonetheless, SDT addresses this complex problem by relying on the equivalent piezoelectric properties obtained with homogenization presented in [17].

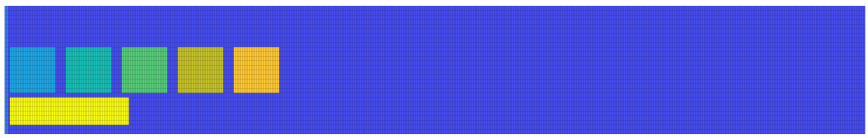

(a) Finite element model

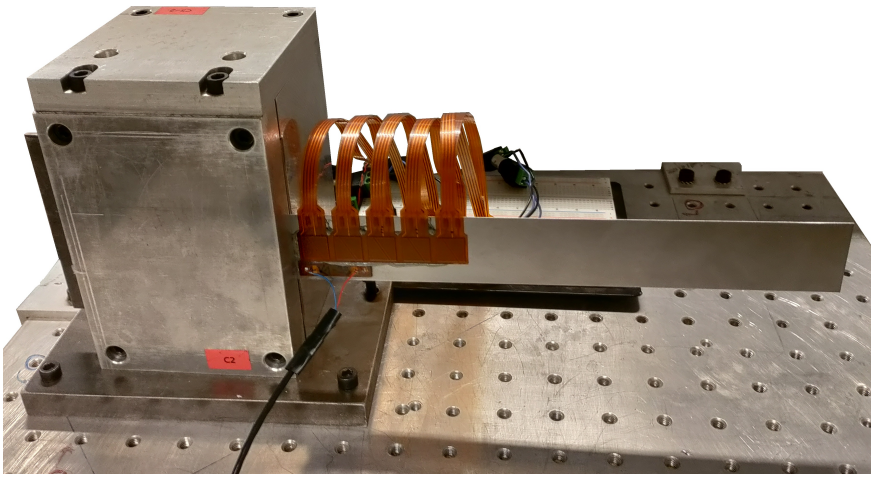

(b) Experimental setup

Figure 2.7: Experimental system with the five MFC sensor patches and the disturbance PZT patch: (a) illustration of the FE model built in SDT, (b) picture of the experimental setup.

Additionally to the two MFC arrays, a 0.1 mm thick PZT patch in d_{33} operational mode of dimension 34 mm x 7 mm in the longitudinal and transversal directions respectively is attached at 1.5 mm from the clamped end of the beam. This extra powerful patch aims to excite the structure to simulate an external disturbance. The entire system is modelled with a total of 16800 multilayer shell elements; an illustration of the FE model can be found in Figure 2.7a where the five MFC patches as well as the PZT actuator are displayed. Additionally, a picture of the experimental setup is shown in Figure 2.7b.

As considered for the numerical validation, configurations composed of two pairs of sensors-actuators patches are investigated. Because 5 locations are available, a total of 10 different MIMO configurations can be studied; each one being composed of two pairs of active patches. To avoid the addition of an extra transducer, one of the three unused MFC sensor patches will be chosen to measure the response of the system. Consequently, the five pairs of patches that are mounted on the beam can be sorted as follows, for each configuration: two pairs are dedicated to the control loop, two are not in use (i.e. open circuit connexion) while the sensor of the last pair is used to measure the response of the system.

Similarly to the numerical validation, a decentralised identical control law is selected for the control architecture. Nevertheless, and to avoid spillover issues or excessive sensor noise amplification, a first-order positive position feedback (PPF) is chosen instead of a DVF. Indeed, the PPF control law provides a $-20dB/$decade roll-off which is compulsory for systems that present non-negligible dynamics at high frequency, such as the considered voltage/voltage pairs of piezoelectric patches [18]. Because this study will be limited to the first two bending modes, the pole of the PPF is set to $\omega_c = 1.25 \times \omega_2$ where ω_2 is the second angular frequency of the beam, i.e. $\omega_c = 530\ rad/s$ based on the numerical simulation. Hence, the controller $C(s)$ is defined as a 2×2 matrix as follows:

$$C(s) = \frac{-g}{s + \omega_c} \begin{bmatrix} 1 & 0 \\ 0 & 1 \end{bmatrix} \tag{2.7}$$

where g is the gain and s is the Laplace variable. Although the use of the FE model is of high interest to design the experimental setup and to ensure its desired behaviour, it is well-known that deviations will appear between the model and the experimental system. Those deviations can be attributed to different factors, e.g. the inaccuracy of the material parameter values, imprecision on the placement of the patches during the mounting, the effect of the glue that is not considered in the model or the difficulty in accurately modelling piezoelectric structures because of the interaction between mechanical and electrical effects [19]. Consequently, an experimentally extracted model is built for all the ten configurations by first measuring the open-loop responses between the different patches and secondly by fitting those experimental transfer functions using the modal identification toolbox available within SDT. The identification method is based on the fitting of a pole-residue type model, with both high and low-frequency corrections, which can then be transformed into a state-space representation. Using the experimentally extracted model, the link between the maximum reachable damping and the normalised pole-TZ distance can be plotted for the 10 configurations and the first two considered modes, as previously done in the numerical validation.

As shown in Figure 2.8, the direct link between the maximum damping and the pole-TZ distance is again numerically established for this new system. Nevertheless, an interesting observation can be made: different slopes can be observed between the two modes of interest while this variation was not observed with the numerical simulations in Figure 2.5. Such fluctuation in the slope can in fact be explained by the filtration pole ω_c that presents a specific modal interaction with respect to each mode. This type of interaction was not present with the DVF that was used for the numerical validation (the control law being only one derivative zero), which therefore explained why similar slopes were being observed.

In order to experimentally validate the linear link obtained with the experimentally extracted model, a dSPACE MicroLabBox is used for both the data acquisition and the

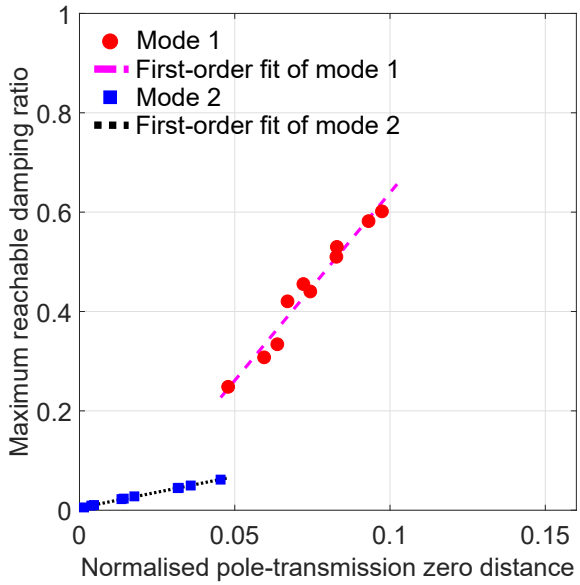

Figure 2.8: Maximum reachable damping ratio as a function of the normalised pole-TZ distance for the first two modes, from the experimentally extracted model.

control aspect, with the sampling frequency set to 20 kHz. Moreover, and because the capacitance of the MFC patches is low (approximatively 18 nF), a sensor signal conditioner from PCB Piezotronics (model 482C) with unitary gain is used to avoid any possible impedance issue in case of a direct connection from the patches to the MicroLabBox.

The experimental test campaign focuses on four of the ten available configurations such that all the patches are in use at least once, as illustrated by Figure 2.9 where the active patches for each selected configuration are filled in blue while the MFC sensor patches used for the performance index are highlighted in pink. Additionally, the configuration scheme of the experimental study is depicted in Figure 2.10 for the first considered configuration: a white noise generator is employed to excite the structure from 0 Hz to 300 Hz through the disturbance patch and the induced response of the system is measured by one of the MFC sensor. Simultaneously, the control architecture is applied to the two pairs of active patches while the unused remaining ones are kept open.

The experimental validation is done by comparing the theoretical and the experimental root loci obtained for each of the four considered configurations. Indeed, if the trajectories of the closed-loop poles in the complex plane obtained with the experimental setup match the numerical ones for the different tested configurations, it can be assumed that the correlation for the other six is also validated. Therefore, the maximum damping ratio and the TZ values obtained with the numerical simulation are confirmed, which validates the linear link between the maximum damping ratio and the pole-TZ distance shown in Figure 2.8. To obtain the experimental closed-loop poles, four different values of the gain g from Equation 2.7 are tested on the four configurations. For each gain value, the transfer function from the disturbance to the MFC sensor patches is measured. Then, the poles are obtained by fitting the experimental closed-loop transfer function using again the modal identification toolbox available within SDT. The comparison between the theoretical and the experimental closed-loop poles convergence, for each considered configuration, is shown in Figure 2.11 where the coloured solid lines correspond to the simulated root locus using the experimentally extracted model and the black crosses represent the closed-loop poles for the considered gain values. As it can be seen, none of the four selected gains ($g = 2500$, $g = 5000$, $g = 7500$ and $g = 10000$) is sufficient to reach the maximum damping value

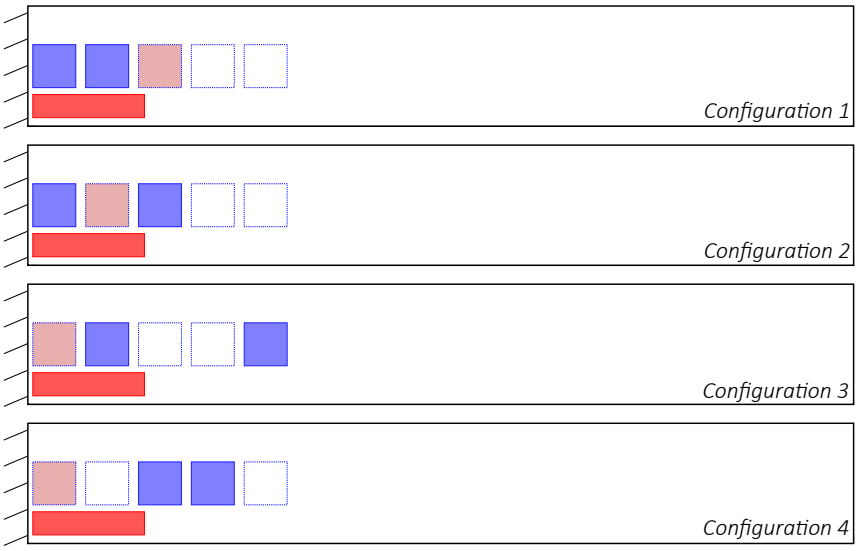

Figure 2.9: Illustration (top view) of the four configurations that have been experimentally tested. For each configuration, the filled blue patches are the MFC active ones used in the control loop, the red patch corresponds to the PZT disturbance actuator and the pink patch is the MFC used as a sensor to build the performance index.

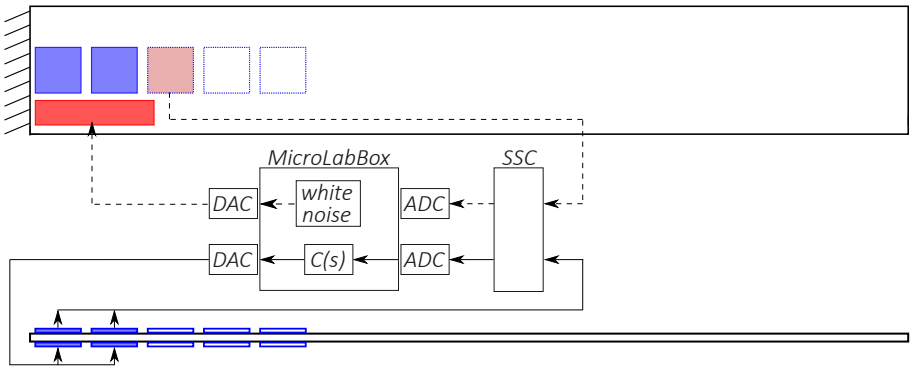

Figure 2.10: Top and side views of the control scheme (solid lines) and the performance index loop (dashed lines) for the experimental study of the first considered configuration. (ADC: Analog-to-Digital-Converter; DAC: Digital-to-Analog-Converter; SSC: Sensor Signal Conditioner).

for none of the two modes and any of the four configurations. This is because the first order PPF is not unconditionally stable: the additional pole brought by the control law on the real axis converges indeed towards the right half plane for large gains, limiting consequently its possible value [5]. Nevertheless, the trajectory of the closed-loop poles in the complex plane is correctly mimicking the simulated closed-loop behaviour, validating therefore the simulated root loci and, consequently, the maximum reachable damping values as well as the TZ positions. The slight mismatches observed in the four sub-figures can indeed be attributed to two minor reasons: (1) the unavoidable errors arising from the modal identification to obtain the damped closed-loop pole values and (2) the same unavoidable errors brought by the extraction of the experimental model. It can be noted that although the maximum reachable damping ratio is not attainable before the destabilisation of the system (in this specific case or for any other ones), the knowledge of the pole-TZ distance is still highly valuable. Indeed, having a high value of the maximum reachable damping translates to a system that exhibits its closed-loop poles further into the left half plane and a good authority for the corresponding mode.

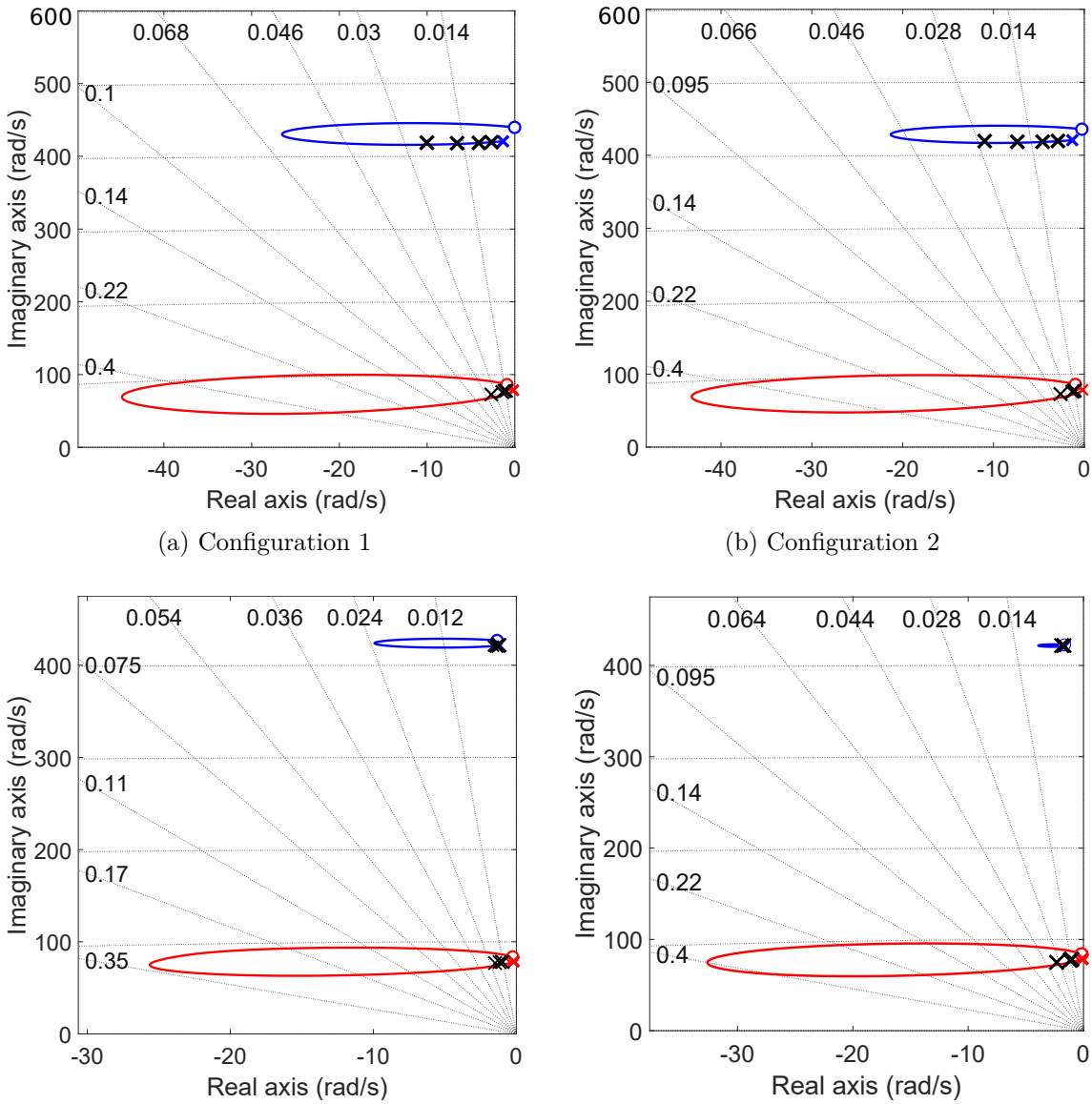

(a) Configuration 1

(b) Configuration 2

(c) Configuration 3

(d) Configuration 4

Figure 2.11: Comparison between the simulated (coloured solid lines) and the experimental (black crosses) closed-loop poles convergence when applying the MIMO control architecture for the four considered configurations.

In addition to the analysis of the closed-loop poles convergence, a correlation analysis between the loop gain functions can be performed to enhance the reliability of the presented experimental validation. Indeed, the loop gain function is defined as the multiplication of the open-loop system dynamics with the controller and can be easily measured on the experimental setup between each actuator/sensor pair. Such measurement is performed by (i) cutting the link between the controller and the digital-to-analogue-converter within the MicroLabBox (see Figure 2.10) and (ii) by injecting white noise directly to the actuator while measuring the output of the controller. The benefit of this approach is that it avoids the different stability concerns when applying high gain values and, consequently, it admits to study the dynamics of the experimental setup for such unreachable gains in closed-loop conditions. The comparison between the experimental loop gain functions and the numerically estimated ones for the five pairs of MFC patches and for $g = 12438$ are shown

in Figures 2.12 to 2.14. Note that this gain value has been selected because it provides the maximum reachable damping for the second mode when considering the first configuration.

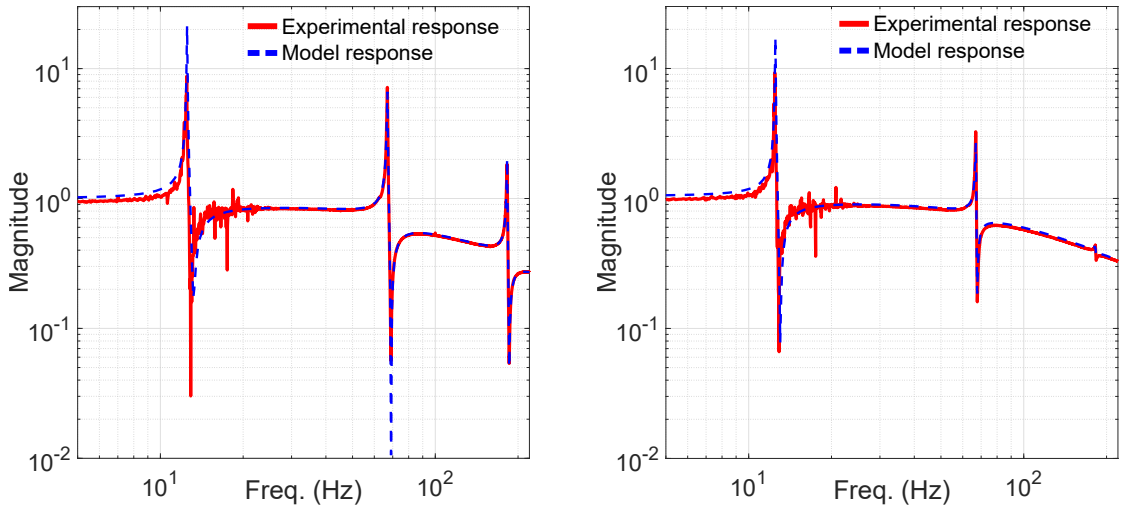

(a) Response of the pair 1 (b) Response of the pair 2

Figure 2.12: Comparison between the experimental loop gain and the simulated one with the gain value $g = 12438$ on: (a) the first pair of patches, (b) the second pair of patches.

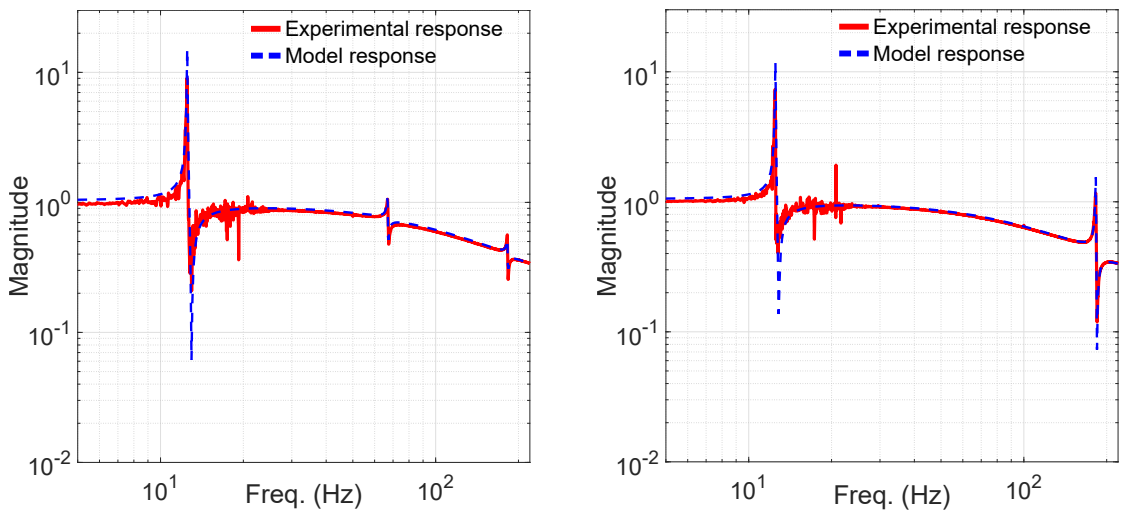

(a) Response of the pair 3 (b) Response of the pair 4

Figure 2.13: Comparison between the experimental loop gain and the simulated one with the gain value $g = 12438$ on: (a) the third pair of patches, (b) the fourth pair of patches.

As it can be seen, the gain loop functions obtained experimentally are perfectly following the numerically estimated ones. This demonstrates again the proper correlation between the simulations obtained with the experimentally extracted model and the experimental setup, which confirms the experimental validation of the linear link between the pole-TZ distance and the maximum reachable damping shown in Figure 2.8.

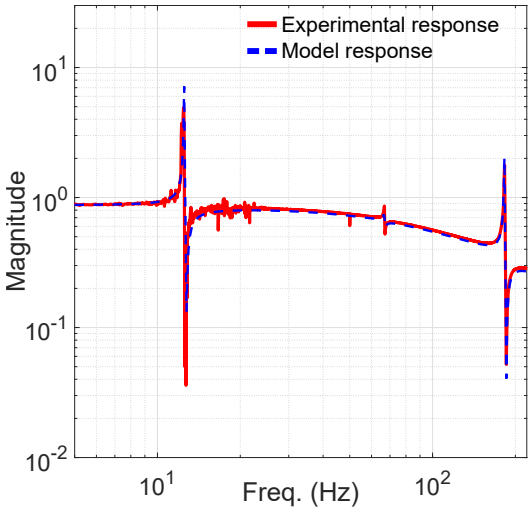

Figure 2.14: Comparison between the experimental loop gain and the simulated one with the gain value $g = 12438$ on the fifth pair of patches.

2.4 Conclusion

The LAC is the main architecture to consider when implementing active damping strategies. Additionally, a HAC can be implemented to enlarge the performance, for example to speed up system response. Nevertheless, the HAC requires a strong knowledge of the plant to control and it is highly sensitive to uncertainties. It presents consequently limited robustness, which can be a serious obstacle for their implementation in industrial structures where reliability is a key factor.

In contrast, the LAC ensures a very high level of robustness but at the expense of lower performance compared to the HAC. Nevertheless, fair levels of damping can be achieved with limited control effort. Additionally, the combination of a LAC with collocated transducers configurations can further increase the global robustness and even extend the robustness to unconditional stability for specific cases. LACs are consequently well-suited for active damping architectures, especially for industrial applications where robustness and cost are crucial.

Another major advantage of a collocated SISO configuration with a LAC is the direct link such a configuration exhibits between the PZ distance and the maximum reachable damping. Indeed, this well-known link allows to perform a fast estimation of the closed-loop performance by only analysing some open-loop parameters. This second chapter mainly studied the possibility to extend this link from SISO systems to MIMO ones. It is shown that such an extension is possible when the considered system presents the three following conditions: (1) the transducers are collocated and present a small authority on the system which leads to the presence of a TZ in the vicinity of each pole of interest, (2) the system possesses a low modal density in the frequency bandwidth of interest, and (3) a LAC is used in the feedback loop. When those three conditions are satisfied, the analytical expression of the closed-loop pole convergence is similar to the one observed in SISO systems, the only difference being that the anti-resonances are replaced by the TZs. Consequently, the direct link between the maximum damping ratio and the pole-TZ distance is confirmed. A numerical simulation with two different structures has been performed to validate this extension.

An experimental validation was performed as well, which provides additional validity for

the proposed extension. It is indeed shown that the experimental setup presents the three required properties and that the linear link between the maximum reachable damping ratio and the pole-TZ distance appears accordingly.

This linear link between the pole-TZ distance and the damping in MIMO systems introduced in this chapter could provide valuable information on the possible performance once in closed-loop while needing only open-loop knowledge. Requiring only open-loop knowledge translates by reasonable computational cost, which is highly valuable for large and/or complex structures.

References

[1] J. Aubrun. "Theory of the control of structures by low-authority controllers". In: *Journal of Guidance and Control* 3.5 (1980), pp. 444–451. DOI: 10.2514/3.56019.

[2] A. Hassibi, J. P. How, and S. P. Boyd. "Low-authority controller design by means of convex optimization". In: *Journal of guidance, control, and dynamics* 22.6 (1999), pp. 862–872. DOI: 10.2514/2.4464.

[3] T. Williams. "Transmission zeros and high-authority/low-authority control of flexible space structures". In: *Journal of guidance, control, and dynamics* 17.1 (1994), pp. 170–174. DOI: 10.2514/3.21174.

[4] P. Zarchan. *Progress in astronautics and aeronautics: fundamentals of Kalman filtering: a practical approach*. Vol. 208. Aiaa, 2005.

[5] A. Preumont. *Vibration Control of Active Structure, An Introduction*. Thrid Edition. Springer, 2011. DOI: 10.1007/978-94-007-2033-6.

[6] N. Schiller, C. Fuller, and R. Cabell. "A high-authority/low-authority control strategy for coupled aircraft-style bays". In: *ACTIVE 2006: 6th International Symposium on Active Noise and Vibration Control*. AIAA Paper a06_032. 2006.

[7] B. Mokrani, F. Palazzo, J. E. Mottershead, and S. Fichera. "Multiple-input multiple-output experimental aeroelastic control using a receptance-based method". In: *Aiaa Journal* 57.7 (2019), pp. 3066–3077. DOI: 10.2514/1.J057855.

[8] A. Preumont, M. Voltan, A. Sangiovanni, B. Mokrani, and D. Alaluf. "Active tendon control of suspension bridges". In: *Smart Struct. Syst* 18.1 (2016), pp. 31–52. DOI: 10.12989/sss.2016.18.1.031.

[9] S. Chesné, A. Milhomem, and C. Collette. "Enhanced damping of flexible structures using force feedback". In: *Journal of Guidance, Control, and Dynamics* 39.7 (2016), pp. 1654–1658. DOI: 10.2514/1.G001620.

[10] A. Preumont, B. De Marneffe, A. Deraemaeker, and F. Bossens. "The damping of a truss structure with a piezoelectric transducer". In: *Computers & structures* 86.3-5 (2008), pp. 227–239. DOI: 10.1016/j.compstruc.2007.01.038.

[11] K. Nakamura. "Electrical evaluation of piezoelectric transducers". In: *Ultrasonic Transducers*. Woodhead Publishing, 2012, pp. 264–276. DOI: 10.1533/9780857096302.2.264.

[12] D. Piron, S. Pathak, A. Deraemaeker, and C. Collette. "On the link between pole-zero distance and maximum reachable damping in MIMO systems". In: *Mechanical Systems and Signal Processing* 181 (2022), p. 109519. DOI: 10.1016/j.ymssp.2022.109519.

[13] A. Preumont, B. De Marneffe, and S. Krenk. "Transmission zeros in structural control with collocated multi-input/multi-output pairs". In: *Journal of guidance, control, and dynamics* 31.2 (2008), pp. 428–432. DOI: 10.2514/1.31529.

[14] Y. Lu, M. Amabili, J. Wang, F. Yang, H. Yue, Y. Xu, and H. Tzou. "Active vibration control of a polyvinylidene fluoride laminated membrane plate mirror". In: *Journal of Vibration and Control* 25.19-20 (2019), pp. 2611–2626. DOI: 10.1177/1077546319862445.

[15] S. Pathak, D. Piron, A. Paknejad, C. Collette, and A. Deraemaeker. "On transmission Zeros of piezoelectric structures". In: *Journal of Intelligent Material Systems and Structures* 33.12 (2022), pp. 1538–1561. DOI: 10.1177/1045389X211057209.

[16] Smart Material. *Macro Fiber Composite^{TM}*. https://www.smart-material.com/MFC-product-mainV2.html. 2002.

[17] A. Deraemaeker, H. Nasser, A. Benjeddou, and A. Preumont. "Mixing rules for the piezoelectricproperties of Macro Fiber Composites". In: *Journal of Intelligent Material Systems and Structures* 20.12 (2009), pp. 1391–1518. DOI: 10.1177/1045389X0933561.

[18] J. Fanson and T. Caughey. "Positive position feedback control for large space structures". In: *AIAA journal* 28.4 (1990), pp. 717–724. DOI: 10.2514/3.10451.

[19] S. R. Moheimani and A. J. Fleming. *Piezoelectric transducers for vibration control and damping*. Vol. 1. Springer, 2006.

Chapter 3

Introduction of the pole-zero distance criterion

Abstract

This chapter first reviews the different criteria for the optimal positioning of transducers in control architecture. It is shown through this literature review that a trade-off exists: either the criterion is based on the open-loop configuration and it is easy to implement and evaluate, but it provides limited performance or it is evaluated in closed-loop and ensures higher performance but requires a very large computational effort to be computed. To address this trade-off, the PZ distance criterion is proposed for collocated LAC systems. The criterion relies on the direct link between the PZ distance of a mode (open-loop knowledge) and the maximum reachable damping ratio the mode can achieve once in closed-loop. The criterion is first mathematically introduced and multiple discussions are then devoted to illustrate its physical meaning. Additionally, its effectiveness is numerically validated on SISO and MIMO systems, using a force actuator/displacement sensor pair as well as piezoelectric patches. It is shown that the PZ distance criterion provides better performance compared to other widely used open-loop criteria such as the Gramian controllability, the spatial H_2 norm or the strain map-based approach. The proposed criterion provides consequently a novel approach for efficient SA placement optimization.

3.1 Introduction

The impact of the control law implemented in active damping systems has been discussed in Chapter 2. More precisely, how the authority of the control law influences the performance and the robustness of the architecture. Besides the control law, the position of the transducers involved in the control strategy plays an important role as well with respect to the authority of the architecture. It has indeed been demonstrated in Chapter 1 that a modification of the transducer(s) position modifies directly the values of the zeros, which are strongly involved in the closed-loop dynamics. A discussion of the crucial effect of the zeros can be found in Chapter 2, where the direct link between the PZ distance and the maximum reachable damping is analysed in SISO systems and extended for MIMO ones.

The appropriate number of transducers to use as well as their suitable positioning on the system to be controlled is consequently a well-established concern. A poor choice of their locations can indeed deteriorate the performance of the control architecture by inducing a lack of observability and/or controllability or, in the worst case, it can lead to stability concerns as described in [1] where non-collocated SA pairs are considered. Additionally,

the use of too many transducers could increase the cost and the weight of the system without a real improvement in the mitigation of the vibrations. The question of the optimal transducer placement is consequently substantial and its interest is highlighted by the numerous researches that have been performed during the past decades. The availability of several technical reviews that analyse those different optimal placement techniques such as [2–4] clearly confirms this interest. Nonetheless, the major difficulty related to the optimal SA placement is that the obtained positioning solution highly depends on the criterion used to perform the optimization, impacting therefore the performance of the controlled structure. Hence, the optimization criterion needs to be chosen with utmost care.

The aim of the present chapter is to introduce a new placement criterion based on the maximization of the PZ distance for collocated SISO and MIMO systems. This criterion is proposed to address the existing trade-off between the achievable performance obtained with the current optimization criteria and the computational time required for their evaluations. This concern is highlighted by a brief literature review in Section 3.2 while the PZ distance criterion is introduced in Section 3.3. Numerical validations are conducted in Section 3.4 for SISO and MIMO systems. The performance obtained with the proposed criterion is compared to other criteria, with different types of transducers. Finally, some conclusions are given in Section 3.5.

3.2 Literature review on optimal placement criteria

The selection of the placement criterion to use among all the ones that are available in the literature is of major importance. Indeed, different optimal positions can be obtained depending on the chosen objective function, influencing the performance of the closed-loop system. When considering active control, although the transducers are part of the closed-loop architecture, their optimal placement can be performed in open-loop or closed-loop configuration. The open-loop optimization is focusing on the plant open-loop model only, i.e. the dynamics of the control law is not included in the calculations. The optimal placement of the transducers in closed-loop configuration adds, to the optimization process, the control law and optimizes therefore the control parameters simultaneously with the positioning of the transducers.

3.2.1 Criterion in open-loop configuration

When the optimization of the SA placement is performed in open-loop configuration, the additional dynamics introduced by the controller is not considered in the optimization process. Such open-loop optimization is consequently well-suited for passive architectures because the controlled system dynamics is only slightly modified. This is for example illustrated in [5] for passive damping where the optimal position of piezoelectric patches that maximize the coupling factor is found without having to model the patches.

Nevertheless, the open-loop optimization is also suitable for active architectures without having to consider the control law that will be applied. It is indeed well-known that the open-loop zeros of a system characterize the asymptomatic behaviour of the closed-loop poles submitted to high control gain, no matter which controller is used. Hence, Maghami and Joshi suggested to optimize the SA placement for flexible space structures by maximizing the real part of the open-loop transmission zeros [6]. Indeed, maximizing the real part of those zeros ensures, once in closed-loop and with a high gain value applied, a small settling time and, therefore, a fast system response. Although such an approach is inter-

esting for tracking purposes, it is not suited for vibration alleviation. Indeed, reducing the vibration level requires an increase in the structural damping. Yet, the transmission zeros of a system are bounded within the complex plane by the poles of the system [7], i.e. the damping of the zeros cannot exceed the highest one from the poles. Consequently, converging towards the transmission zero can indeed decrease the settling time of the system but will not increase its damping.

To add damping to a system, the different transducers must be mounted in a place that ensures their authority over the structure. This is reflected in the ability of the actuator(s) to modify the current state(s) of the system towards the intended one(s) in a finite amount of time, and the ability of the sensor(s) to determine the current state(s) of the system, again in a finite amount of time and from all the possible initial one(s). By considering a time-invariant linear system in its state-space representation as expressed by Equation 1.21, the controllability matrix $\mathcal{C}$ and the observability matrix $\mathcal{O}$ can be built as follows:

$$[\mathcal{C}] = \begin{bmatrix} [\mathbf{B}] & [\mathbf{A}]\,[\mathbf{B}] & [\mathbf{A}]^2\,[\mathbf{B}] & \cdots & [\mathbf{A}]^{n-1}\,[\mathbf{B}] \end{bmatrix}, \quad [\mathcal{O}] = \begin{bmatrix} [\mathbf{C}] \\ [\mathbf{C}]\,[\mathbf{A}] \\ [\mathbf{C}]\,[\mathbf{A}]^2 \\ \vdots \\ [\mathbf{C}]\,[\mathbf{A}]^{n-1} \end{bmatrix} \tag{3.1}$$

where n is the number of state variables and $[\mathbf{A}]$, $[\mathbf{B}]$ and $[\mathbf{C}]$ are the state matrix, the input matrix and the output matrix, respectively. The $\mathcal{C}$ and $\mathcal{O}$ matrices allow to mathematically analyse the controllability and the observability of the related system: if they are full rank, the system is fully controllable and observable. Nevertheless, if one of those two matrices has a rank lower than n, one or several states are not controllable/observable [8]. Because of this binary aspect, the controllability and observability matrices cannot be used for the SA placement optimization. Indeed, it does not provide any information on which state is not controllable/observable nor a qualitative level in case of a fully observable/controllable system.

If the system is subjected to an external disturbance which forces it towards the initial state(s) $\{\mathbf{q_0}\}$, the aim of the control architecture is to bring it back to the desired one(s) $\{\mathbf{q_t}\}$. Therefore, by defining the signal energy as the integral of the square of the signal magnitude [9], it is possible to find the minimum control signal energy u that is required to restore the system from $\{\mathbf{q_0}\}$ to $\{\mathbf{q_t}\}$, in a certain amount of time t. The solution of this linear quadratic problem provides the optimal control input signal which leads to the total control energy expressed as follows [10]:

$$\int_0^t \|\{\mathbf{u}(\tau)\}\|^2 d\tau = (e^{[\mathbf{A}]t}\,\{\mathbf{q_0}\} - \{\mathbf{q_t}\})^T\ [\mathbf{W_c}(\mathbf{t})]^{-1}\ (e^{[\mathbf{A}]t}\,\{\mathbf{q_0}\} - \{\mathbf{q_t}\}) \tag{3.2}$$

where $[\mathbf{W_c}(\mathbf{t})] \in \mathbb{R}^{n\times n}$ is the controllability Gramian matrix defined by:

$$[\mathbf{W_c}(\mathbf{t})] = \int_0^t e^{[\mathbf{A}]\tau}\,[\mathbf{B}]\,[\mathbf{B}]^T\,e^{[\mathbf{A}]^T\tau} d\tau \tag{3.3}$$

If λ_k is defined as the eigenvalue of $[\mathbf{W_c}(\mathbf{t})]$ linked to the specified mode of interest k, the higher λ_k is, the easier mode k can be controlled and, subsequently, the less control energy it requires to attenuate the structural vibrations of this mode. The Gramian controllability can therefore be used for the selection of the proper actuator(s) positioning that minimizes the total control energy, i.e. the position that maximizes the eigenvalues of $[\mathbf{W_c}(\mathbf{t})]$. Of course, the same reasoning can be performed for the sensor(s) where the goal is to maximize the total measurement signal energy captured by the sensor(s), which

leads to the observability Gramian matrix. Hac and Liu [10] first introduced the use of the controllability and observability Gramians as performance indexes for the SA placement which has been later widely used in various problems, e.g. for the optimization of the location of piezoelectric sensors and actuators on a simply supported beam [11], for the positioning of piezoelectric patches on plates [12, 13], or for the piezoelectric positioning on a large flexible structure [14].

Although the use of the controllability and observability Gramians does not require complex calculations, it presents a notable drawback. Indeed, it has been mathematically demonstrated that for a lightly damped structure with well-spaced natural frequencies, the kth eigenvalue of $[\mathbf{W_c(t)}]$ can be simplified as follows [10]:

$$\lambda_k(\alpha) = \frac{\phi_{\mathbf{k}}(\alpha)^2}{4\xi_k\omega_k} \tag{3.4}$$

where α corresponds to the position of the actuator, $\{\phi_{\mathbf{k}}\}$ is the mode shape of mode k, ω_k is the related natural frequency and ξ_k the corresponding modal damping. It can therefore be concluded from Equation 3.4 that the Gramian criterion relies on the modal amplitude of the targeted mode(s) only.

Another method for the optimal placement of SAs in open-loop configuration consists of using the H_2 norm. The H_2 norm can indeed be interpreted as the average gain of the system subjected to an impulse response, which therefore provides the response characteristics of the system at the sensor location. Mathematically, the H_2 norm of a SISO linear and time-invariant system described by its transfer function $G(\omega)$ is defined by:

$$\|G\|_2 = \sqrt{\frac{1}{2\pi}\int_{-\infty}^{\infty} tr(G^H(\omega)\, G(\omega))\, d\omega} \tag{3.5}$$

where the superscript ^{H} refers to the complex-conjugate transpose and the notation $tr(\,)$ corresponds to the trace of the matrix, i.e. the sum of all the elements on its main diagonal. Based on its physical interpretation, an optimal SA placement criterion can be derived from the H_2 norm in order to find the position that maximises the importance of the transducer pair over the structure in the sense of the amplitude of vibration the input can induce at the output, as done in [15].

Nonetheless, it can be important, in some cases, to analyse the response of the system on a specific area rather than just at the position of the sensor(s). The H_2 norm criterion has consequently been extended by Moheimani and Ryall to the spatial H_2 norm $\ll G \gg_2$, allowing to compute the average input-output characteristics over a domain of interest $\mathcal{R}$ as follows [16]:

$$\ll G \gg_2 = \sqrt{\frac{1}{2\pi}\int_{-\infty}^{\infty}\int_{\mathcal{R}} tr(G^*(\omega, r)\, G(\omega, r))\, dr\, d\omega} \tag{3.6}$$

where $\mathcal{R}$ contains all the spatial coordinates of interest $r \in \mathbb{R}^n$ with n being the structural dimension and $G(\omega, r)$ corresponds to the transfer function $G(\omega)$ at position r. Several SA placement optimizations have been conducted using this spatial H_2 norm, such as the piezoelectric patch placement on a thin plate discussed in [17] or the reduction of the spillover phenomena studied in [18]. Nevertheless, injecting the expression of the transfer function in its modal form (as expressed by Equation 1.23) into Equation 3.6 exhibits a direct link between the spatial H_2 norm and the modal amplitudes, as already

observed with the Gramian eigenvalues. This consequently highlights that the open-loop SA placement criteria are rather simple to implement and evaluate but rely again on limited information, which can lead to poor performance.

3.2.2 Criterion in closed-loop configuration

Open-loop SA placement criteria are rather simple to implement and, consequently, do not require large computational efforts to be evaluated. Yet, in addition to being mainly based on the modal amplitude as explained in the previous section, they do not account for the additional dynamics brought by the controller in the system as they only focus on the structure to be controlled. Considering that a strong interaction between this extra dynamics and the one from the plant is highly probable, performing the SA optimization in open-loop can lead to sub-optimal solutions, as demonstrated for instance by Devasia et al. [19]. To overcome this notable inconvenience, SA optimization can be performed in closed-loop configuration by adding the control law to the optimization process.

Schulz and Heimbold [20] studied the SA positioning optimization based on the maximization of the damping energy dissipated through the controller action when considering a DVF control law. Because the obtained solution was depending on the initial conditions and because those conditions are not always known a priori, Dhingra and Lee [21] adapted the criterion by associating them to a randomly distributed variable, which allowed to remove this dependency. The maximization of the modal damping has been studied as well, e.g. by Kang et al. for a laminated beam with piezoelectric patches, where the dynamical interaction between the SA and the structure was considered [22].

The closed-loop SA placement optimization can also be performed by designing a H_2 optimal controller that relies on the H_2 norm defined by Equation 3.5. Such controller aims to find the feedback parameters that lower the H_2 norm of the system, which physically translates to a reduction of its overall response when submitted to white noise disturbances [23]. The optimal placement based on such an objective is performed by combining the simultaneous determination of the controller parameters and the transducer(s) position. Such optimization is for example studied in [24] where an economic selection of the SA position and number is performed by combining the H_2 controller with a H_∞ one, i.e. a feedback control law that intends to reduce the maximum peak value of the system response. The H_∞ controller is also used in [25] to find the best sensors location based on the already defined actuators one where the major objective is to maximize the slope value of the roll-off to decrease the possible destabilization effects at high frequency. Additionally, numerous studies that use complex feedback controllers can be found in literature, for example to study the best piezoelectric patches location on plates as done in [26–28]. Interestingly, closed-loop SA placement optimization can also be applied for large civil structures such as in [29] where the optimal number and position of hydraulic actuators is studied by applying the H_2 controller.

Although including the control law in the optimization process certainly delivers improved performance compared to the one obtained with open-loop optimizations [19], the computational costs drastically increase because the optimization has to be performed together for the SA positions and the controller parameters. Moreover, using modern controllers such as the state feedback ones requires a strong knowledge of the system dynamics, which is often not fully available and/or presents imprecisions.

Despite the long processing time required to compute the solution as just mentioned, it is possible to extend the closed-loop SA optimal placement one step further by including a

topological optimization in it. Indeed, and as a result of the recent improvement of additive techniques, it is now possible to print parts that are crack-free and with a strength comparable to that of the raw material [30]. Additionally, a new class of titanium alloys has been printed using oxygen and iron instead of the regular aluminium and vanadium additives [31]. This new titanium alloy presents a high manufacturability and a wide and tunable range of mechanical properties, which may lead to multiple applications in aerospace technologies. Moreover, advances in the integration of the transducers within the structure have been recently achieved as well, in particular with the use of piezoelectric fibre composites such as the MFC. Their main advantage is the possibility to integrate them inside composites as well as to tailor the directions of actuation or to design specific shapes [32]. It is also possible to optimize their shape, which can lead to very interesting transducers, e.g. the piezo-composite triangular point load actuator [33]. Furthermore, new manufacturing techniques for ceramic material are currently being developed, such as the research published by Zhao et al. [34]. Their work presents a new 3-dimensional (3D) printing process that allows to manufacturer ceramic parts without any support, enabling to achieve complex shapes that were previously impossible to produce.

Because of those different breakthroughs, the simultaneous optimization of the structural design with its control architecture becomes feasible and multiple studies start consequently to emerge. Indeed, several investigations have been conducted such as the optimization of the combined control and structural designs of a piezoelectric truss structure [35], the simultaneous design of the structure topology with the optimization of the actuator location on a beam [36], or the optimization of the integrated topology and the optimal control law when the positions of the transducers are chosen a priori, again illustrated on a beam [37]. Additionally, the simultaneous optimization of the control architecture with the system topology is also starting to be carried out for real industrial structures. Those optimizations are currently mainly performed in the context of high-speed motion systems, such as in [38, 39].

Extending the SA optimal placement to a complete topological optimization during the early design phase shows promising results and interesting perspectives. It indeed presents three major advantages: (1) the number of transducers required to achieve the intended performance is reduced because the optimal shape of the structure already contributes to the vibration alleviation, (2) the positioning candidates for the transducers are not restricted to a small part of the structure (because not implemented afterwards but in the early design), which can lead to improved performance and (3) additional mounting elements can be avoided because already integrated into the design, which ensures the absence of interfering parts such as loose electrical wires. However, a major limitation of the current research studies is that they are mainly considering modern control techniques such as full-state feedback controllers [40], which are complex to implement and require a strong knowledge of the system dynamics. Another common issue with such multi-disciplinary optimizations concerns the computational costs required to ensure the convergence towards the optimal solution. Indeed, because the different parameters have strong mutual interactions and because such challenging optimization is usually performed with a complex and costly search algorithm, performing the optimization for large structures would require prohibitive computational time for their evaluations.

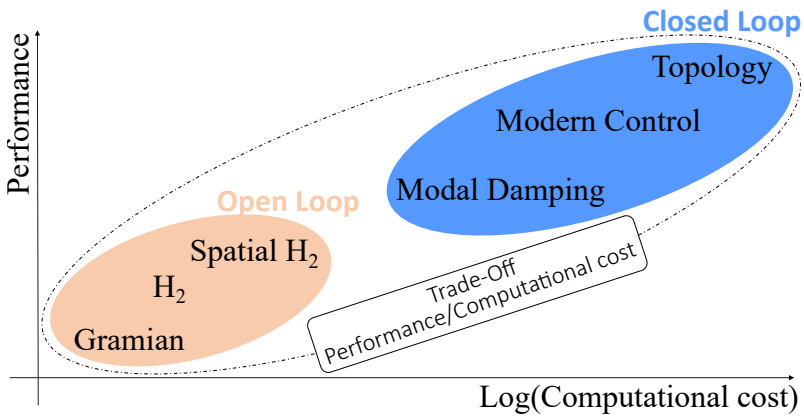

Figure 3.1: Illustration of the current trade-off between performance and computational cost for the optimal placement criteria.

3.3 The proposed PZ distance criterion

As discussed, the selection of the optimal SA positioning criterion is a critical concern. Indeed, the resulting performance as well as the required computational effort strongly depend on the chosen one. Moreover, an important trade-off exists in the field of optimal transducer positioning for smart structures: improving the achievable performance entails a major increase in the computational costs related to the evaluation of the criterion. This trade-off is illustrated in Figure 3.1, where the open-loop and closed-loop configurations are distinctly divided.

In industrial contexts where large and complex structures are prevalent, the computational cost associated with conventional optimal criteria is unfortunately prohibitive. Extremely long computation time (up to several days or weeks) is indeed not efficient enough, especially when multiple optimization iterations are required. In order to address this computational challenge and enable the deployment of high-performance control strategies for large and complex structures, a novel criterion is proposed.

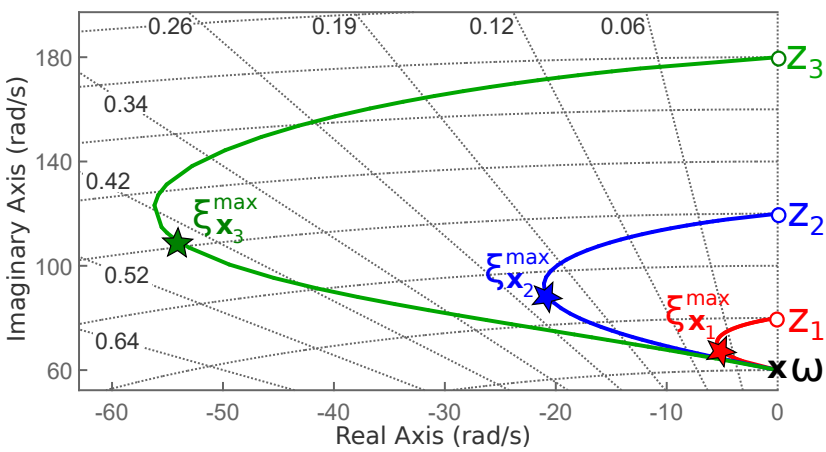

Figure 3.2: Graphical illustration of the link between the PZ distance and the maximum reachable damping ratio for three zero values (lead controller).

This efficient new criterion, introduced in [41], relies on the concept of PZ distance that has been widely discussed in Chapter 2 for LAC systems. As illustrated in Figure 2.1 and recalled in Figure 3.2, the distance between the pole and the zero to which it converges

when the gain is increased, for a specific mode, is directly proportional to the maximum reachable damping in closed-loop. Additionally, the position of the transducers mounted on the structure has a substantial impact on the zero values. The PZ distance criterion aims consequently to find the optimal position of collocated SA pair(s) that maximize the PZ distance in order to ensure high maximum reachable damping values once a LAC is applied. Establishing the SA positioning optimization based on such proposed PZ distance criterion allows therefore to perform the optimization in open-loop configuration (limiting consequently the related computational cost) while ensuring high modal damping ratio once the low-authority control law is applied.

When considering a LAC with collocated SA pair(s), the root locus usually exhibits disconnected loops similar to the ones shown in Figure 3.2. The PZ distance of the ith mode $|PZ|_i$ can therefore always be computed using the same procedure but requires however to know in advance which type of control law will be used once in closed-loop. For example, mechanical systems with a SISO lead controller present, in closed-loop, a pole before each zero [42]. The PZ distance is consequently obtained by the difference between the zero and the pole of the targeted mode i, as follows:

$$|PZ(\mathbf{x})|_i = z_i(\mathbf{x}) - \omega_i \tag{3.7}$$

where $\mathbf{x}$ corresponds to the SA pair position on the structure and $z_i(\mathbf{x})$ is the zero of the targeted mode which depends upon $\mathbf{x}$. To guarantee high performance in terms of modal damping, the proposed criterion consists of three factors. The first one focuses on the overall maximization of the PZ distances and is therefore represented as an arithmetic mean of the normalized PZ distances related to all the modes of interest. Because each individual mode of interest should present a PZ distance that is as large as possible in addition to the overall maximization, the second factor consists of the geometric mean of the normalized distances. Using the geometric mean allows indeed to drop the value of the criterion if one mode presents a narrow distance. Finally, the third factor prevents that a zero adjacent to the modes of interest lies too close to the targeted poles. This has to be avoided because it can induce (i) a PZ cancellation with a mode of interest and, consequently, a loss of controllability and observability and (ii) a root locus reshaping, leading to wrong damping predictions. Such a situation is illustrated in Figure 3.3 where the same lead controller is applied on a SISO system at two different positions. When the SA pair is mounted at position $\mathbf{x}_1$ (Figure 3.3a), the system presents two controllable modes and two related well-disconnected loops. Nevertheless, position $\mathbf{x}_2$ leads to a loss of controllability of the second mode due to the first zero that lies too close to ω_2, as illustrated in Figure 3.3b. Hence, the third term of the criterion is assigned to the geometric mean of the normalized PZ distances computed with the poles of the modes of interest and their adjacent zeros.

Consequently, the proposed SA placement criterion for collocated SISO and MIMO systems with a LAC that ensures high modal damping ratios for the targeted modes is defined as follows:

$$J(\mathbf{x}) = \left(\frac{1}{n}\sum_{k=1}^{n}\frac{|PZ(\mathbf{x})|_k}{max(|PZ\{\mathbf{x}\}|_k)}\right)\times\left(\sqrt[n]{\prod_{k=1}^{n}\frac{|PZ(\mathbf{x})|_k}{max(|PZ\{\mathbf{x}\}|_k)}}\right)\times\left(\sqrt[n]{\prod_{k=1}^{n}\frac{|P_kZ_{adj}(\mathbf{x})|}{max(|P_kZ_{adj}\{\mathbf{x}\}|)}}\right) \tag{3.8}$$

where k contains the n modes of interest, $|PZ(\mathbf{x})|_k$ is the PZ distance of the targeted mode at position $\mathbf{x}$, $|PZ\{\mathbf{x}\}|$ contains the PZ distances of the targeted modes at all the considered positions $\{\mathbf{x}\}$, $|P_kZ_{adj}(\mathbf{x})|$ corresponds to the adjacent PZ distance at position

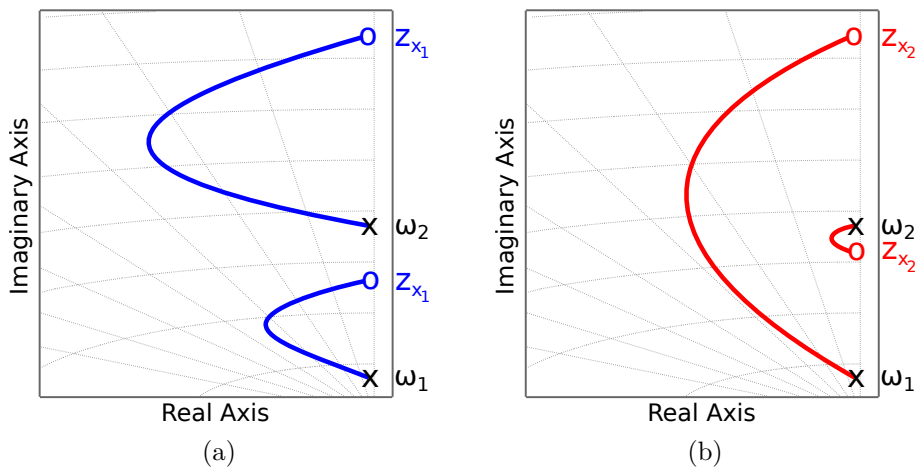

Figure 3.3: Illustration of the loss of controllability and root locus reshaping due to adjacent zero when a lead control law is applied: (a) modes 1 and 2 are controllable, (b) only mode 1 is controllable.

$\mathbf{x}$ while $|P_k Z_{adj}\{\mathbf{x}\}|$ contains all the adjacent PZ distances at $\{\mathbf{x}\}$. Accordingly, all the PZ distances are normalized with respect to the maximum obtained distance among all the considered positions $\{\mathbf{x}\}$. This normalization ensures therefore that each modal distance has the same weight in the criterion. A graphical representation of the three factors is shown in Figure 3.4 where only the second mode of the system is targeted and when it is assumed that each pole converges towards the upper zero due to the applied control law.

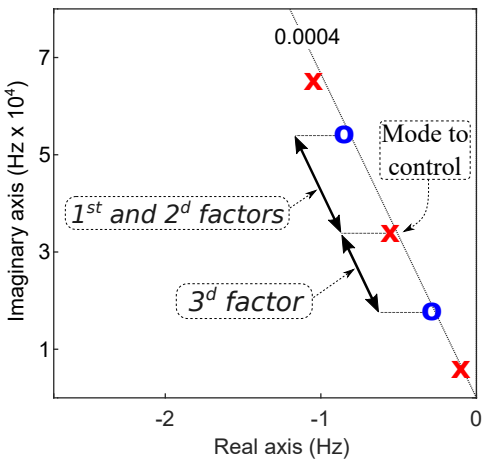

Figure 3.4: Graphical representation of the PZ distance criterion factors when the second mode is targeted.

Based on the different considerations discussed about the PZ distance and how the criterion has been established with its three terms, the SA position that maximises the proposed positioning criterion given by Equation 3.8 will ensure the best compromise between the different maximum achievable modal damping ratios for the n targeted modes once the feedback control law is added to the system. Additionally, while ensuring effective closed-loop predictions, the evaluation of the criterion is conducted in open-loop configuration because it only requires the different poles and zeros values, which guarantees a very high efficiency. The proposed PZ distance criterion solves consequently the trade-off between performance and computational time that is encountered with the different placement criteria available in the literature.

3.4 Discussion and numerical validation of the PZ distance criterion

This section aims to numerically demonstrate the effectiveness of the proposed PZ distance criterion and to discuss its performance in comparison with other open-loop criteria. The analysis is first performed on a SISO structure equipped with a collocated force actuator/displacement sensor pair. The discussion then focuses on a MIMO system with two pairs of collocated piezoelectric patches

3.4.1 Application to a SISO system

The discussion and the numerical validation in SISO configuration is performed on a cantilever beam. The structure is modelled in SDT [43] with lightly damped steel with the following material properties: Young's modulus $E = 210\ GPa$, Poisson's ratio $\nu = 0.285$, mass density $\rho = 7800\ kg/m^3$ and modal damping ratio $\xi = 0.004$. The dimensions of the beam are 300 mm x 25 mm x 2 mm and it is modelled with 301 beam elements that allow the 2 DoFs in-plane bending motions except for the first node at its fixed end. Each non-constrained node along the longitudinal axis of the beam is defined as a potential collocated force actuator/displacement sensor pair position, leading to 300 possible locations. The model presents consequently 600 DoFs in total. A simple representation of the beam along its longitudinal axis is shown in Figure 3.5.

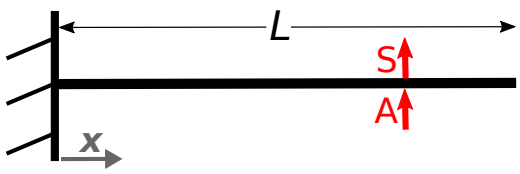

Figure 3.5: Numerical cantilever beam used to validate the PZ distance criterion in SISO systems

The PZ distance criterion expressed by Equation 3.8 is intended to be evaluated in open-loop, but still requires to know which type of control law will be used once in closed-loop. A lead controller is consequently chosen, which implies that each pole of the system converges towards the nearest upper zero. This reflects in the evaluation of the PZ distance by computing the difference between the upper zero and the pole of interest, while the third term is obtained by the difference between the pole linked to the mode of interest and the previous zero, i.e. the first zero that appears under the pole. Mathematically, this is expressed as follows:

$$\begin{aligned} |PZ(\mathbf{x})|_i &= z_i(\mathbf{x}) - \omega_i \\ |P_i Z_{adj}(\mathbf{x})| &= \omega_i - z_{i-1}(\mathbf{x}) \end{aligned} \tag{3.9}$$

To validate the criterion, different cases are considered: single-mode damping (mode 1, mode 2 and mode 3) and multi-modal damping (modes 1 & 2 and modes 2 & 3). For each case, the PZ distance criterion $J(\mathbf{x})$ is evaluated at all the possible SA positions on the system. In order to ease the visualization of the results, the criterion is graphically represented by $\tilde{J}(\mathbf{x})$, which corresponds to the normalization of $J(\mathbf{x})$ by its maximum obtained value. The results obtained for the single mode damping on the cantilever beam are shown in Figure 3.6, where L refers to its length. As it can be seen, the optimal value obtained for the damping of mode 1 is located at a distance of $0.7833 \times L$ away from the clamped end of the beam. For the second and third modes, the positions that maximize the PZ

criterion are respectively at a distance of $0.49 \times L$ and $0.3367 \times L$ from the clamped end. Moreover and as expected, the criterion value drops to zero in the vicinity of the different modal nodes as a result of the third term. For multi-modal damping, the positions that maximize the criterion are at a distance of $0.9166 \times L$ for modes 1 & 2 and $0.3566 \times L$ for modes 2 & 3, as shown in Figure 3.7.

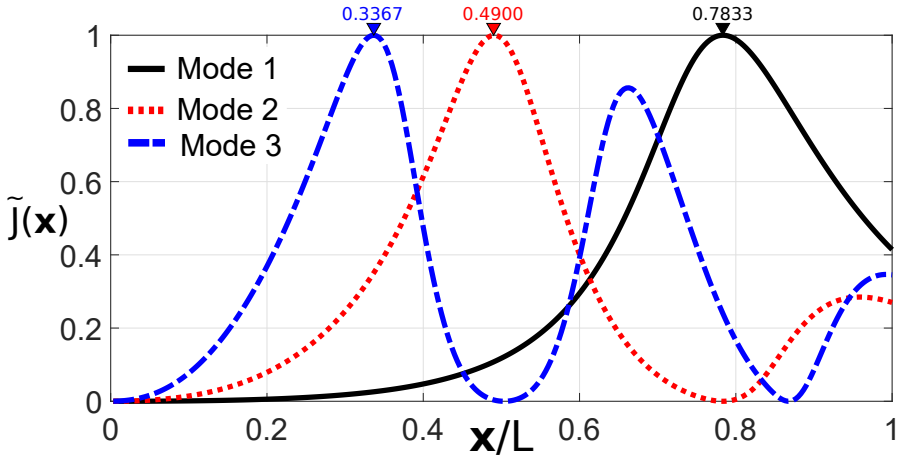

Figure 3.6: Normalized PZ distance criterion obtained on the cantilever beam for modes 1, 2 and 3.

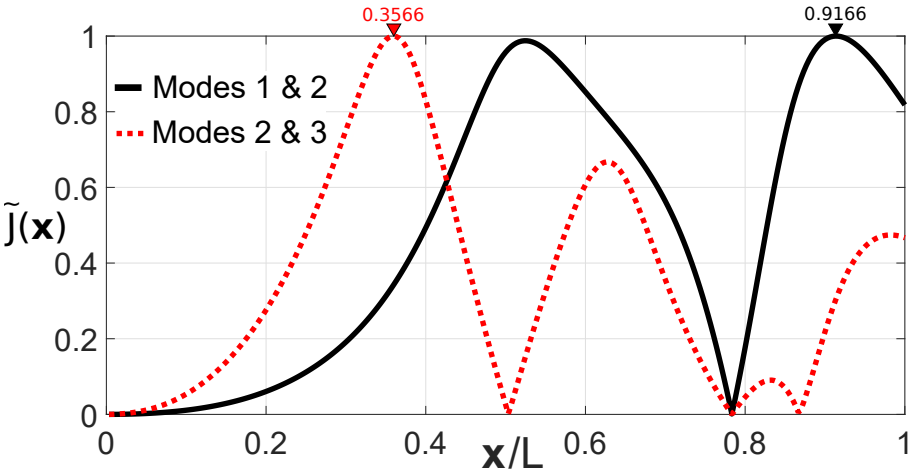

Figure 3.7: Normalized PZ distance criterion obtained on the cantilever beam for modes 1 & 2 and modes 2 & 3.

The performance obtained with those different optimal positions has to be compared with the solutions computed with other placement criteria. To guarantee a fair comparison, two open-loop criteria are selected: the Gramian controllability and the spatial H_2 norm. By recalling λ_k, the eigenvalue of the controllability Gramian matrix as described in Section 3.2.1, the optimal position based on the Gramian controllability is the one that maximises the following cost function [13]:

$$J_{Gram}(\mathbf{x}) = \left(\sum_k \lambda_k(\mathbf{x})\right) \times \left(\sqrt{\prod_k \lambda_k(\mathbf{x})}\right) \tag{3.10}$$

where k contains the n modes of interest. When the SA positioning optimization is performed with the spatial H_2 criterion, the optimal location is the one that maximises

the spatial H_2 controllability index $J_{H_2}(\mathbf{x})$, which is expressed as follows [16]:

$$J_{H_2}(\mathbf{x}) = \frac{1}{\beta}\sqrt{\sum_k f_k(\mathbf{x})} * 100 \quad \text{with } f_k(\mathbf{x})/\alpha_k \geqslant b_k \tag{3.11}$$

where $f_k(\mathbf{x})$ is the spatial H_2 norm of mode k, β is the maximum value of the criterion obtained among all the candidates, α_k is the maximum value of $f_k(\mathbf{x})$ among all the candidates and b_k is a threshold value for the controllability of mode k. Hence, the spatial H_2 norm $f_k(\mathbf{x})$ is a measure of the actuator authority on mode k over the defined subset $\mathcal{R}$. Consequently, maximizing $J_{H_2}(\mathbf{x})$ while ensuring high enough value for each $f_k(\mathbf{x})$ through b_k allows to maximize the average authority on all the targeted modes without a loss of modal authority. By fixing the threshold value b_k to 0.5 for all the targeted modes as done in [16] and by setting $\mathcal{R}$ as all the SA position candidates, the optimal positions on the two considered systems for the different modal cases are computed using Equations 3.10 and 3.11.

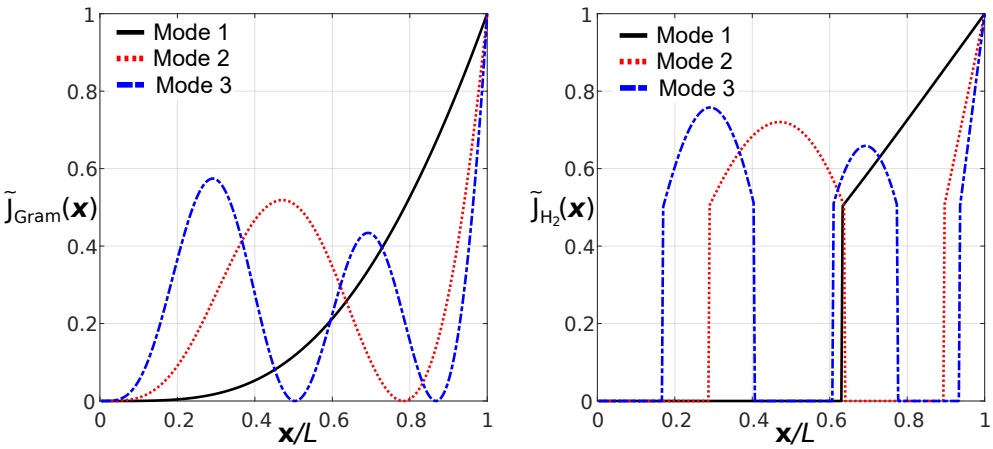

(a) Normalised Gramian criterion (b) Normalised spatial H_2 criterion

Figure 3.8: Normalised Gramian and normalised spatial H_2 criteria obtained on the cantilever beam for modes 1, 2 and 3.

To ease the visualization, the criteria $J_{Gram}(\mathbf{x})$ and $J_{H_2}(\mathbf{x})$ are again normalised with their maximum values observed among all their positioning candidates, leading to $\tilde{J}_{Gram}(\mathbf{x})$ and $\tilde{J}_{H_2}(\mathbf{x})$ that are shown in Figure 3.8. As it can be seen, the free end of the beam corresponds to the position that maximizes both criteria, for the three considered modes. The free end of the beam is consequently the optimal position for the multi-modal cases as well, i.e. for the damping of modes 1 & 2 and modes 2 & 3. Interestingly, it is clear that both criteria are directly correlated with the modal amplitude of each targeted mode, the spatial H_2 criterion showing just drops of its value to zero when below 0.5 due to the threshold value b_k expressed in Equation 3.5. To further corroborate this consideration, the normalised criterion $\tilde{J}_{Gram}(\mathbf{x})$ and the modal amplitude have been extracted for each evaluated position along the beam, for the three single mode damping cases. The relationship between $\tilde{J}_{Gram}$ and the normalised modal amplitude $\tilde{\Phi}$ is shown in Figure 3.9 for those three modes, where each entry corresponds to one position. As illustrated, a perfect parabolic shape emerges from the three modes, which confirms therefore the correctness of Equation 3.4 and indicates that the Gramian criterion depends on the modal amplitude only.

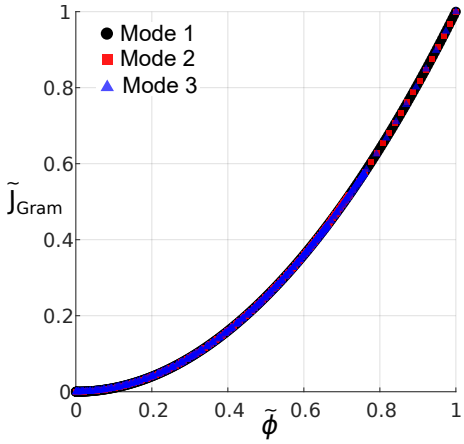

Figure 3.9: Normalised Gramian criterion as function of the normalised modal amplitude obtained on the cantilever beam for modes 1, 2 and 3.

As observed in Figure 3.8 and confirmed by Figure 3.9, the two widely used open-loop criteria are mainly based on the modal amplitude of the targeted mode(s). It is therefore worthy to analyse the link between the PZ distance criterion and the modal amplitude in order to establish the standpoint of the proposed criterion with respect to the most important parameter in open-loop placement criteria, the modal amplitude. Such analysis is shown in Figure 3.10 that displays, for each single-modal damping case, the relationship between $\tilde{J}(\mathbf{x})$ and the normalised modal amplitude $\tilde{\Phi}$ where each entry corresponds to one tested position. As expected due to the different optimal solutions obtained with the PZ distance criterion and the Gramian and spatial H_2 criteria, the positions that maximize the PZ criterion do not correspond to the ones that maximize the modal amplitudes. Additionally, the same modal amplitude can lead to multiple PZ criterion values and, conversely, a PZ criterion value can show different modal amplitudes. This phenomenon is explained because the PZ criterion relies on the modification of the zero value, which depends on various parameters. The zero values are indeed derived from the contribution of all the surrounding modes and not only based on the targeted one through its modal amplitude.

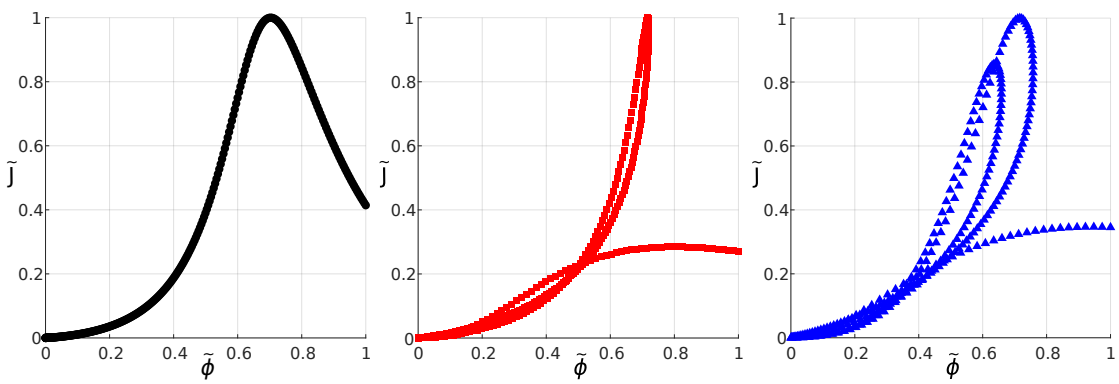

(a) Mode 1 (b) Mode 2 (c) Mode 3

Figure 3.10: Normalised PZ criterion as function of the normalised modal amplitude obtained on the cantilever beam for modes 1, 2 and 3.

The analysis of the link between the PZ criterion and the modal amplitude of a targeted mode shown in Figure 3.10 provided interesting information to better understand the dif-

ference between the optimal solutions. But this analysis can be extended even further by extracting the PZ distance from the criterion in order to plot the link between this distance and the modal amplitude. Using the distance rather than the full criterion allows indeed a more in-depth analysis of the distance of the targeted mode without the intervention of the third term, i.e. the adjacent distance which is not directly related to the dynamics of the mode of interest. The relationship between the normalised PZ distance of the second mode, $\widetilde{|PZ|}_2$, and its related normalised modal amplitude $\tilde{\Phi}_2$ is shown in Figure 3.11, where each entry corresponds again to a specific SA pair position on the beam. As it can be seen, no correlation can be drawn between the PZ distance and the modal amplitude. Moreover, the position that maximises the distance does not correspond to the one that maximises the modal amplitude, as already observed for the PZ criterion. Those observations are directly related to the definition of the zero and the related involvement of several parameters as already discussed.

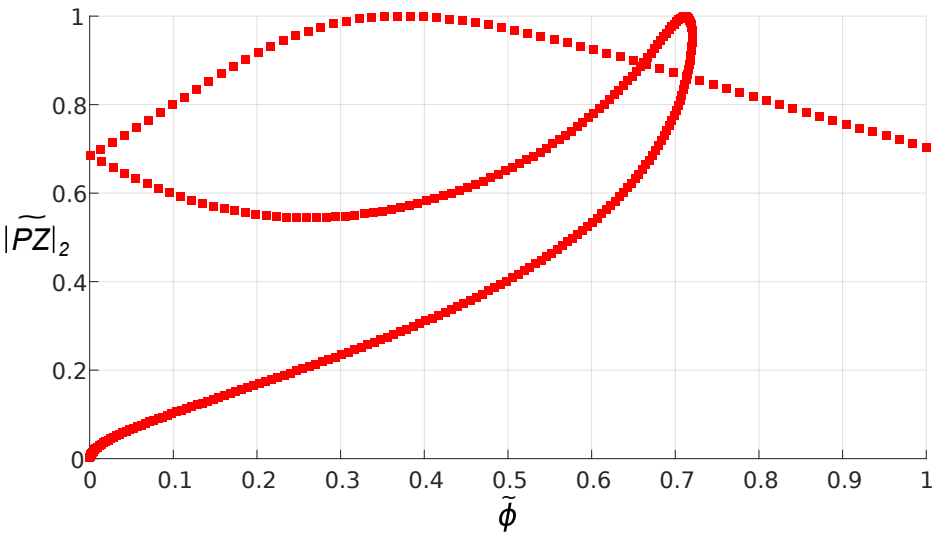

Figure 3.11: Normalised PZ distance as function of the normalised modal amplitude obtained on the cantilever beam for the second mode.

Interestingly, several positions present low modal amplitudes while relatively large PZ distance values. Such a situation is questionable, as the modal amplitude still reflects the ability of the related mode to be controlled while large PZ distance indicates a high maximum reachable damping ratio. In order to explain this paradox, the root locus obtained at one of the concerned positions is shown in Figure 3.12. The SA pair is located at 0.77 $\times$ L from the clamped end of the beam and the root locus has been obtained by applying a lead controller. As it can be seen, the PZ distance of the second mode $|PZ|_2$ is indeed large. However, the second pole of the system does not converge to the second zero as it is supposed to do when the criterion is applied. On the contrary, it is converging towards the first zero which is extremely close. As a consequence, the second mode undergoes a PZ cancellation and stays completely undamped in closed-loop. This therefore coincides with the low modal amplitude observed at this SA location and explains the paradox of obtaining a large distance but low controllability. This situation is caused by the first zero approaching the target mode too closely, which reinforces therefore the usefulness of the third term $|P_2A_{adj}|$, i.e. the inclusion of the adjacent distance of the targeted mode(s) to control into the criterion. This additional distance avoids indeed any PZ cancellation or any possible root locus reshaping that could lead to bad damping prediction and, consequently, poor performance. The third term is consequently the reason why the different positions that have a reduced modal amplitude in Figure 3.10 systematically present a low

PZ criterion as well.

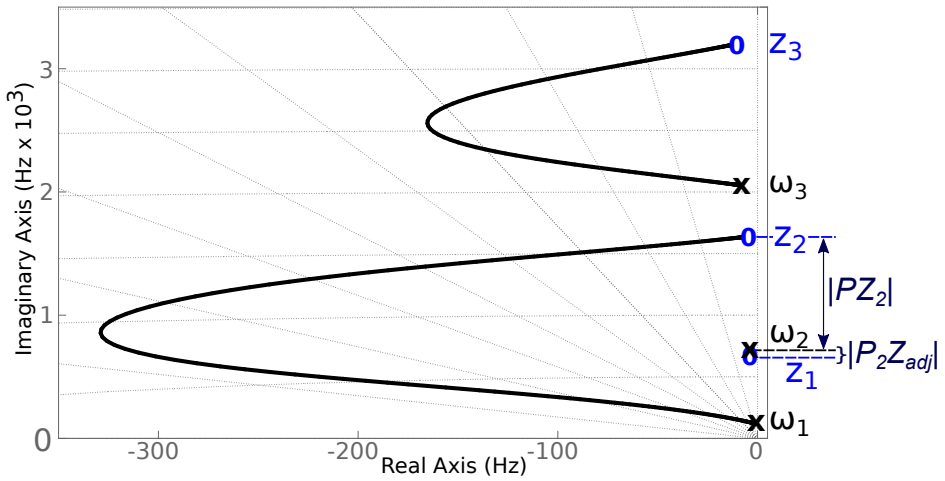

Figure 3.12: Root locus obtained at a position that presents a large PZ distance but a small modal amplitude for the second mode, highlighting the importance of the third term of the PZ distance criterion.

Following this in-depth analysis, it is valuable to assess the closed-loop performance obtained with the different optimal placement solutions. As stated, the PZ distance has been evaluated by considering that a lead control law will be used once in closed-loop. Consequently, such a lead needs to be considered in order to analyse the closed-loop performance provided by the different positions. The control law of a lead is recalled by Equation 3.12 where z_c and p_c are respectively the zero and the pole of the controller, g is its gain value and s is the complex Laplace variable.

$$C(s) = g\,\frac{s + z_c}{s + p_c} \tag{3.12}$$

The zero z_c and the pole p_c only depend on the targeted modes as follows: $z_c = \omega_p/2$ and $p_c = 2 * \omega_q$, where ω_p and ω_q are respectively the smallest and the highest natural frequencies of the targeted modes. Although of limited authority due to the narrow frequency band used, the choice of these parameters allows to restrain the variability of the controller to its gain value, and ensures a comprehensive comparison between different positions when considering a specific modal case. The value of the gain g is tuned for each tested position in order to maximize the damping ratios. This tuning is performed numerically by maximizing the cost function $J_{Gain}(g)$ defined by:

$$J_{Gain}(g) = \left(\sum_k \xi_k(g)\right) \times \left(\sqrt{\prod_k \xi_k(g)}\right) \tag{3.13}$$

where k contains all the considered modes. The modal damping ratios obtained for the single mode cases and the different criteria are compared in Figure 3.13. It is straightforward from the different results that the proposed criterion provides higher damping ratios compared to the Gramian or the spatial H_2 norm criteria. Such a better performance can be explained by the fact that those two criteria only depend on the modal amplitude of the targeted modes. Conversely, the proposed PZ distance criterion is based on the information contained within the zero frequencies which includes the contribution of the surrounding modes and the possible modal interactions even if they are computed in open-loop configuration. Hence, the information is richer, which leads to better performance in

terms of damping.

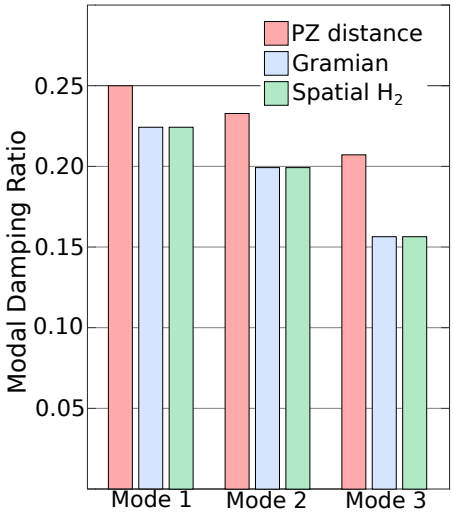

Figure 3.13: Damping ratios in closed-loop obtained with three open-loop criteria on the cantilever beam for single mode damping.

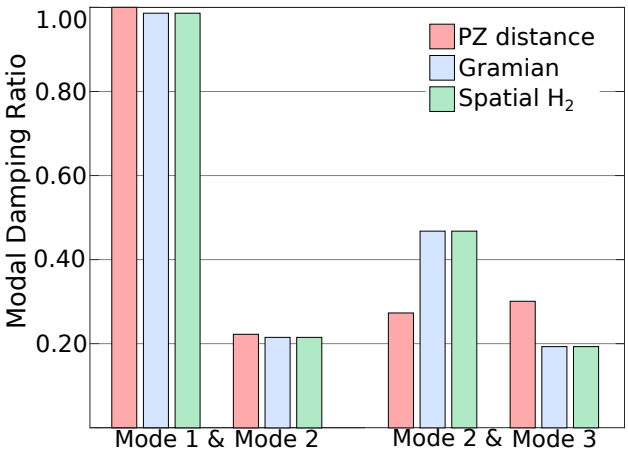

Figure 3.14: Damping ratios in closed-loop obtained with three open-loop criteria on the cantilever beam for multi-modal damping.

The comparison of the damping obtained with the different criteria for multi-modal cases is available in Figure 3.14. It can be observed for the two cases that the proposed PZ distance criterion allows to have a better compromise between the different modes to be damped. Indeed, the other criteria provide a bigger difference between the two damping ratios, which can result in sub-performance due to modal interaction: if one of the two modes to control shows a high modal damping value while the other one is significantly less damped, the dynamical amplification of this less damped mode can reduce the overall damping performance in the frequency band of interest.

The effectiveness of the proposed criterion can be verified with the frequency response functions obtained in the case of multi-modal damping optimization of, for example, modes 1 & 2. To ensure the excitation of the two modes, the force disturbance is located at the free end of the beam while the measurement of the performance is achieved by a displacement sensor which is collocated with the disturbance. For each tested criterion, the position of

the SA pair and the parameters of the control law are implemented with the previously obtained results. The different frequency response functions can be found in Figure 3.15 where it can be observed that the proposed criterion shows better performance, which confirms therefore its effectiveness.

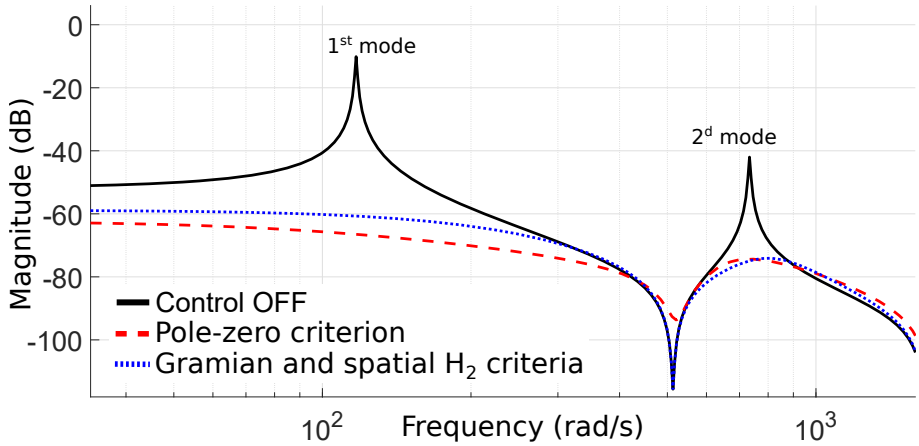

Figure 3.15: Frequency response functions obtained with three open-loop criteria on a cantilever beam for multi-modal damping of modes 1 & 2.

3.4.2 Application to a MIMO system

In order to broaden the scope of applications as much as possible, the analysis of the proposed PZ distance criterion and its numerical validation in MIMO configuration is performed with piezoelectric patches. The same cantilever beam used for the SISO validation is modelled again, i.e. with the dimensions of 300 mm x 25 mm x 2 mm and a lightly damped steel with the following material properties: Young's modulus $E = 210$ GPa, Poisson's ratio $\nu = 0.285$, mass density $\rho = 7800$ kg/m^3 and modal damping ratio $\xi = 0.004$. Nevertheless, six DoFs multilayer shell elements as described in [44] are adopted rather than the simple beam ones as done for the SISO validation. The beam elements show indeed only two DoFs and have consequently insufficient capability to properly model piezoelectric patches (further details can be found in Appendix A). The system is discretized each 1 and 5 mm, respectively in the x and y directions, leading to a total of 1806 nodes and 10800 DoFs. Additionally, an extra boundary condition is applied to the beam in order to increase the complexity of its dynamic behaviour. It is indeed well-known that mounting piezoelectric patches on a regular cantilever beam should mainly be performed at its clamped end for maximum controllability [3], which reduces the relevance of such a study. Adding an extra boundary condition modifies the mode shapes of the beam, ensuring therefore the interest of the validation. This additional condition is modelled with a linear spring which presents a high stiffness value (10^{14} N/m) to ensure relevant dynamical changes. It is located on an edge, 75 mm from its clamped end in the longitudinal axis and works perpendicular to the plane formed by the beam. The system representation as well as the linear spring and the Cartesian coordinates are shown in Figure 3.16.

The piezoelectric patches are defined as PZT d_{31} PIC 255 from Physik Instrumente (PI) [45]. A rectangular shape has been selected such that they fully cover the width of the beam, leading to the following dimensions: 10 mm x 25 mm in the longitudinal and transversal directions respectively, and a thickness of 0.5 mm. A possible position is considered every 10 mm in the longitudinal axis, starting from the clamped end of the beam.

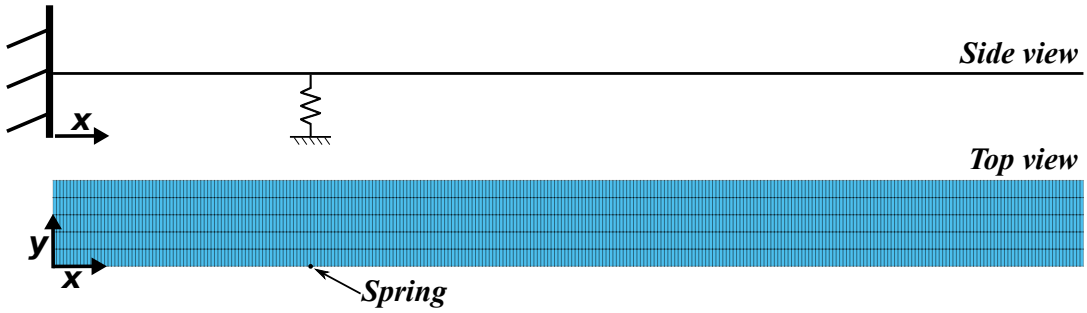

Figure 3.16: Numerical cantilever beam used to validate the PZ distance criterion with MIMO systems, including the additional linear spring.

To ensure the MIMO configuration, two pairs of collocated patches are used simultaneously in voltage/voltage mode, where each pair consists of an actuator located at the same position as its corresponding sensor but on the opposite face of the beam. Based on the dimension of the patches and the possible defined locations, a total of 435 different MIMO configurations can be studied.

Because the first three modes of the beam were considered in the SISO validation and as it is interesting to apply the PZ distance criterion at a higher frequency range as well, the MIMO validation is focussed on the simultaneous damping of modes 4, 5 & 6 of the system. The dynamics of the beam being altered due to the linear spring mounted on one of the edges, the mode shapes of the three considered modes are shown in Figure 3.17 to provide a clear overview of the considered modes to be damped. As expected, the system presents mode shapes with coupled bending and torsional motions, increasing the complexity of the dynamics with respect to a regular cantilever beam.

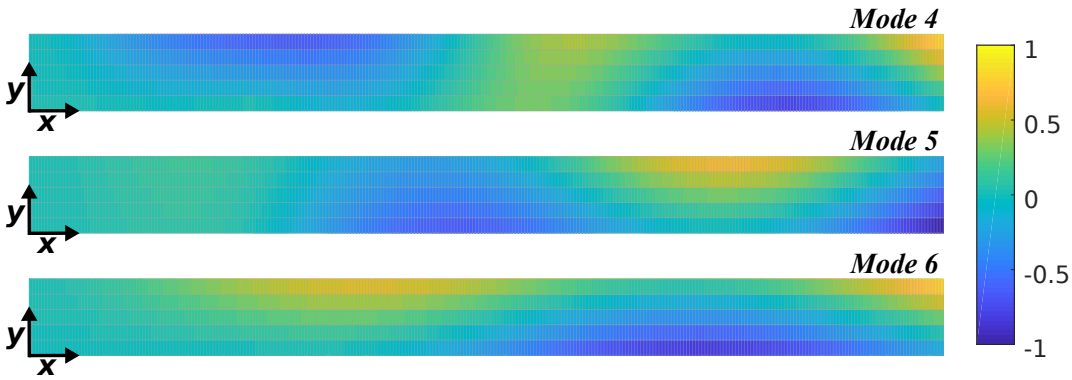

Figure 3.17: Modal amplitudes of the modes of interest 4, 5 & 6 obtained with the MIMO cantilever beam.

The first stage of the MIMO validation consists to compute the PZ distance for the different configurations and the three considered modes. As performed in the SISO analysis, computing the PZ distance requires to anticipate the control law that will be used once in closed-loop. In order to ensure unconditional stability and no influence of additional parameters, a DVF is chosen again. The controller $C(s)$ is consequently defined as a 2×2 matrix as follows:

$$C(s) = g \begin{bmatrix} s & 0 \\ 0 & s \end{bmatrix} \tag{3.14}$$

where g is the gain of the controller and s is the Laplace variable. As discussed in Section 2.3 where the experimental validation of the link in MIMO systems was performed, the use of a DVF is not suitable for a real-life structure because it induces high-frequency amplification. Nonetheless, it ensures unconditional stability and avoids the influence of additional parameters such as encountered when applying a PPF because of the filtration pole. When applying a DVF control law, the PZ distance is obtained by the difference between the upper TZ and the pole of interest while the adjacent distance is obtained by the difference between the pole of interest and the TZ that appears under the pole. Mathematically, it is expressed as follows:

$$\begin{aligned} |PZ(\{\mathbf{x}\})|_i &= TZ_i(\{\mathbf{x}\}) - \omega_i(\{\mathbf{x}\}) \\ |P_i Z_{adj}(\{\mathbf{x}\})| &= \omega_i(\{\mathbf{x}\}) - TZ_{i-1}(\{\mathbf{x}\}) \end{aligned} \tag{3.15}$$

where $\{\mathbf{x}\} = \{x_1, x_2\}^T$ contains the position of the two pairs of patches along the longitudinal axis of the beam. Interestingly, the poles of the systems $\omega_i(\{\mathbf{x}\})$ directly depend on the patches positions while such dependency was not present in the SISO analysis, e.g. in Equation 3.9. This is caused by the use of piezoelectric patches rather than force actuator/displacement sensor pairs. A piezoelectric patch is indeed mounted on a specific area of the system, which induces a local change of its stiffness and mass and, consequently, a modification in the solutions of the eigenvalue problem. Conversely, force actuator/displacement sensor pairs are considered to be attached to a single node (hence no stiffness modification) and their masses are neglected. It is however worth mentioning that such idealisation can lead to unsatisfactory results when, for example, a low-frequency sensor is mounted on the system. Low-frequency sensors are indeed bulky and the related addition of mass can be non-negligible, inducing a change of the natural frequencies of the system.

Injecting the two PZ distance definitions given in Equation 3.15 into the proposed criterion expressed by Equation 3.8 allows to compute $J(\{\mathbf{x}\})$ considering the simultaneous damping of modes 4, 5 & 6. The results obtained for the 435 configurations are shown in Figure 3.18. Because each configuration is identified by the position of the two pairs of patches x_1 and x_2, the results are displayed in 3D where the $x - y$ plane represents the normalised centre positions of the two patches in the longitudinal axis of the beam and the z-axis depicts $\tilde{J}(\{\mathbf{x}\})$ through a given colour-code, where $\tilde{J}(\{\mathbf{x}\})$ refers to the criterion that has been normalised by its maximum obtained value. As it can be seen, the criterion takes higher values when a patch is located at the clamped-end of the beam (vertical line starting around $x_1/L = 0$) or when a patch is positioned at $0.8 \times L$ from the clamped-end (horizontal trace starting from around $x_2/L = 0.8$). The optimal configuration that maximizes the PZ criterion $J(\{\mathbf{x}\})$ is obtained for $x_1 = 0$ and $x_2 = 0.766 \times L$. A graphical representation of the optimal configuration is drawn in Figure 3.18 as well to ease its physical representation.

Table 3.1: Damping ratios in closed-loop obtained with the PZ distance criterion on the MIMO beam for multi-modal damping.

	Mode 4	Mode 5	Mode 6
PZ Criterion	0.9 %	1.3 %	1.2 %
Strain Criterion	0.7 %	1.7 %	1.2%

The closed-loop performance of the optimal configuration can be numerically assessed by applying the DVF control law defined by Equation 3.14. The value of the gain g is tuned

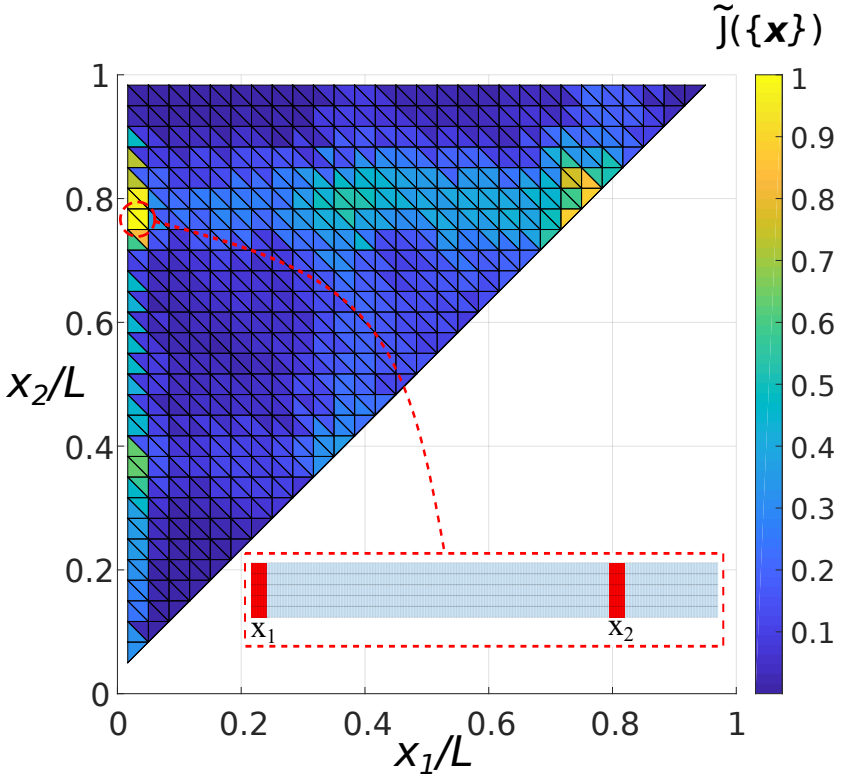

Figure 3.18: Normalised PZ distance criterion obtained on the MIMO cantilever beam for the simultaneous damping of modes 4, 5 & 6 where the optimal configuration is highlighted and physically represented.

to maximize the damping ratios using the same cost function $J_{Gain}(g)$ that has been developed in the SISO configuration analysis (Equation 3.13). The closed-loop damping ratios obtained with the optimal configuration (and the tuned gain value) are available in Table 3.1. As it can be seen, the three targeted modes present a damping ratio value of around 1 %. Interestingly, the SISO configuration analysis already resulted in damping values within a similar range when considering multi-modal cases. It consequently shows again that maximizing the PZ distance criterion ensures an adequate level of damping for all the considered modes, even for systems with complex dynamics or when higher modes are considered such as in the current case. Nonetheless, and similarly to the SISO analysis, a comparison of the optimal configuration obtained with the proposed PZ distance criterion should be performed with respect to other placement criteria. In the case of open-loop optimization and the use of piezoelectric patches, the strain map is often used to locate the potential positioning of the transducers. The piezoelectricity relies indeed on the conversion of mechanical stress into electrical charges, an area of high strain is usually preferred to mount the patches.

The strain maps of the three considered modes are shown in Figure 3.19, where the optimal positions $x_{1,PZ}$ and $x_{2,PZ}$ that have been obtained with the PZ distance criterion are displayed as well. When dealing with multi-modal control, the location of the patches based on the strain energy is often determined through a visual inspection of the complete strain map, which results in a conscious choice that favours the value of all the targeted modes. Nonetheless, when the maps of the targeted modes present large differences between them as it is the case with the considered structure, it is possible to quantify the total strain each configuration provides for a mode i by summing the different values contained within

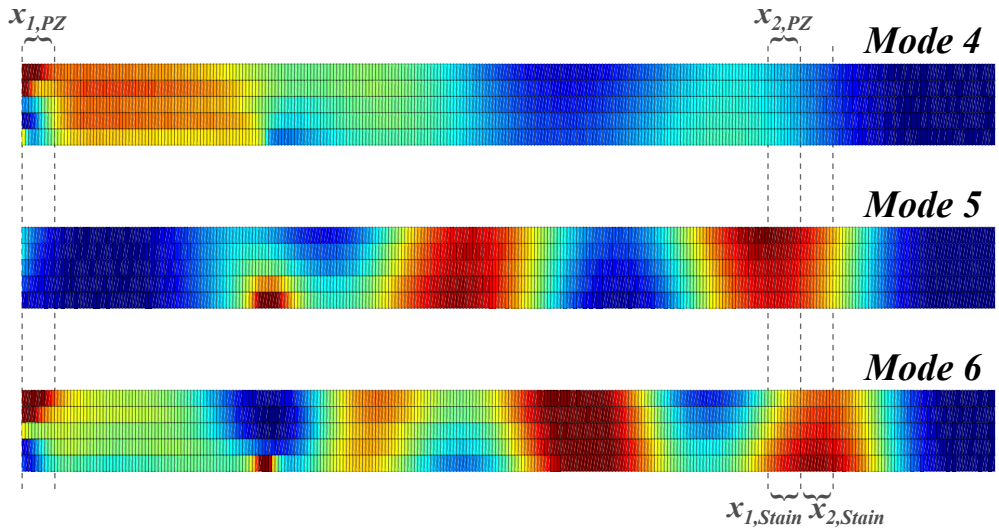

Figure 3.19: Strain map of the modes of interest 4, 5 & 6 obtained with the MIMO cantilever beam and visualization of the optimal configuration based on the PZ distance criterion.

the patch areas as follows:

$$s_i(\{\mathbf{x}\}) = \sum_{\mathcal{R}_1,\mathcal{R}_2} \Big(\gamma_{yz,i}(\{\mathbf{x}\}) + \gamma_{zx,i}(\{\mathbf{x}\})\Big) \tag{3.16}$$

where $s_i(\{\mathbf{x}\})$ is the total strain of mode i for the configuration defined by the patch positions $\{\mathbf{x}\}$, $\mathcal{R}_1$ and $\mathcal{R}_2$ are the two patch areas that depend upon $\{\mathbf{x}\}$ and $\gamma_{yz,i}$ and $\gamma_{zx,i}$ are the bending strains of mode i. For multi-modal control, a simple strain criterion based on the same structure as the Gramian one can be built, which gives:

$$J_{Strain}(\{\mathbf{x}\}) = \Big(\sum_k s_k(\{\mathbf{x}\})\Big) \times \Big(\sqrt{\prod_k s_k(\{\mathbf{x}\})}\Big) \tag{3.17}$$

where k contains the n modes of interest. Applying the strain criterion to the 435 considered configurations allows the extraction of the optimal placement that maximizes the strain. Those two optimal positions $x_{1,Strain}$ and $x_{2,Strain}$ are located at $0.766 \times L$ and $0.8000 \times L$ from the clamped end of the beam, as shown in Figure 3.19. It can be seen that they correctly correspond to the configuration that ensures the largest area of high strain value by a visual inspection of the maps. The closed-loop performance of the optimal configuration is numerically computed as done with the optimal PZ distance criterion, and the damping ratios obtained are available in Table 3.1. It can be difficult to qualitatively compare the performance when considering multi-modal damping, especially if the values are within the same interval. Nevertheless, it can be seen that the strain criterion leads to more disparate values whereas the PZ criterion ensures the same range between the modes. This consequently confirms the advantage of its use and the important link between PZ distance and damping that was already demonstrated in the SISO system validation.

Similarly to the SISO study, the relationship between the PZ distance and the strain can be plotted for each mode. There is indeed an inherent necessity of strain to guarantee the authority of the configuration over a system. Without authority, the transducers cannot act on the dynamics nor add damping. Moreover, and because the PZ distance directly reflects the amount of damping that the closed-loop system can reach, a certain degree

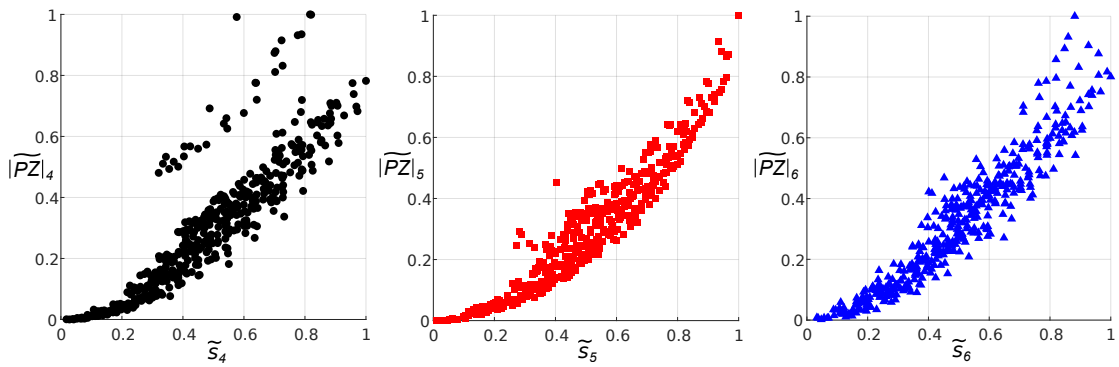

(a) Mode 4 (b) Mode 5 (c) Mode 6

Figure 3.20: Normalised PZ distance as function of the normalised strain amplitude obtained on the cantilever beam for modes 4, 5 and 6.

of correlation between the distance and the strain is consequently to be expected. Those different links can be found in Figure 3.20, where $|\tilde{PZ}|_i$ is the normalised PZ distance of mode i and $\tilde{s}_i$ is the normalised strain value of mode i, both defined by:

$$\begin{aligned} |\tilde{PZ}|_i &= \frac{|PZ|_i}{max(|PZ|_i)} \\ \tilde{s}_i &= \frac{s_i}{max(s_i)} \end{aligned} \tag{3.18}$$

As expected, a clear trend exists between the PZ distance and the strain of each mode. Nevertheless, it is interesting to note that the configurations that maximise the strain are not those that maximise the PZ distance for modes 4 and 6. Because the PZ distance is directly proportional to the maximum reachable damping once in closed-loop, it indicates that placing the piezoelectric patches within the area that maximises the strain does not translate to the maximization of the damping performance. This comment is validated by Figure 3.21, which shows the root-locus obtained with two specific configurations of mode 4: the one that maximises the PZ distance and the one that maximises the strain. It can be seen that the positions $\{\mathbf{x}\}_{PZ}$ that maximise the PZ distance provide higher reachable damping compared to the positions $\{\mathbf{x}\}_{Strain}$ that maximise the strain, validating consequently again the concept behind the proposed PZ distance criterion for MIMO systems.

3.5 Conclusion

The optimal placement of the transducers involved in a control strategy plays a critical role with respect to the authority, the performance and the robustness of the architecture. Two major types of placement criteria have been identified: the criteria computed in open-loop and the ones calculated in closed-loop configurations. The outcome of the literature review highlighted the current trade-off that exists: while open-loop criteria allow simple mathematical implementations and evaluations, they offer limited performance because they rely on limited information. On the other hand, the closed-loop criteria provide better performance but require significant computational effort and complex search algorithms to be implemented.

To address this important trade-off, the PZ distance criterion has been proposed for collocated LAC systems. This criterion relies on the direct link that exists between the PZ

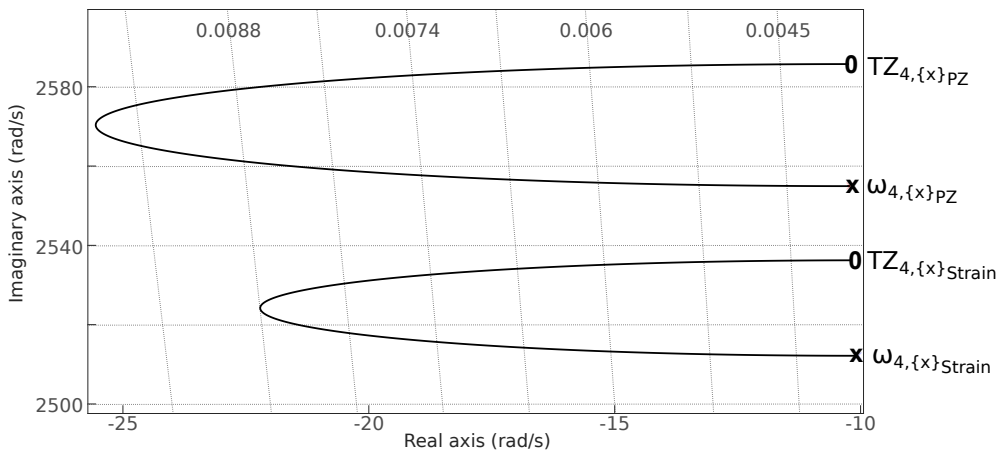

Figure 3.21: Root locus obtained at the configuration that maximises the PZ distance $\{\mathbf{x}\}_{PZ}$ and the configuration that maximises the strain $\{\mathbf{x}\}_{Strain}$ of mode 4, clearly showing that the PZ distance ensures higher damping ratio compared to the strain.

distance of a specific mode and the maximum reachable damping ratio the mode can achieve once in closed-loop. The PZ distance criterion is consequently computed in an open-loop configuration but provides effective closed-loop prediction in terms of damping. As a result, it offers an efficient solution compared with the current placement criteria by allowing fast evaluation and high performance.

Being evaluated in open-loop, the PZ distance criterion still requires to know in advance which type of control law will be used once in closed-loop. This enables to properly define how the PZ distance is computed, i.e. if the pole of interest converges towards a zero located above or below its position. The criterion is built using this defined distance but also with the adjacent distance that is obtained with the additional zero surrounding the targeted pole. Such additional distance avoids indeed any PZ cancellation, loss of controllability or incorrect closed-loop predictions due to unwanted root locus reshaping.

The effectiveness of the criterion has been numerically validated for SISO systems through the example of a force actuator/displacement sensor pair mounted on a cantilever beam. A comparison with other open-loop criteria (the Gramian controllability and the spatial H_2 norm) demonstrated the effectiveness of the PZ distance criterion. Furthermore, the numerical validation of the criterion has been extended to MIMO systems by analysing its efficiency when two pairs of piezoelectric patches are mounted on a cantilever beam that presents an additional boundary condition. For this architecture, the performance of the criterion was evaluated considering higher modes, confirming its ability to maximize damping in diverse scenarios. Again, the results indicate that the PZ distance criterion provides better performance compared to the widely used strain map-based approach in selecting positions that optimize damping.

Overall, the PZ distance criterion offers a valuable solution to the challenge of transducer placement in both SISO and MIMO systems. Its open-loop computation, combined with closed-loop prediction capabilities, ensures its efficiency. The numerical validations that have been conducted on both SISO and MIMO systems demonstrated its effectiveness in maximizing the damping, providing thereby a novel alternative for efficient SA placement optimization.

References

[1] Z.-c. Qiu, X.-m. Zhang, Y.-c. Wang, Z.-w. Wu, et al. "Active vibration control of a flexible beam using a non-collocated acceleration sensor and piezoelectric patch actuator". In: *Journal of Sound and Vibration* 326.3 (2009), pp. 438–455. DOI: 10.1016/j.jsv.2009.05.034.

[2] M. I. Frecker. "Recent advances in optimization of smart structures and actuators". In: *Journal of Intelligent Material Systems and Structures* 14.4-5 (2003), pp. 207–216. DOI: 10.1177/1045389X03031062.

[3] V. Gupta, M. Sharma, and N. Thakur. "Optimization Criteria for Optimal Placement of Piezoelectric Sensors and Actuators on a Smart Structure: A Technical Review". In: *Journal of Intelligent Material Systems and Structures* 21.12 (2010), pp. 1147–1156. DOI: 10.1177/1045389X10381659.

[4] K. Morris and S. Yang. "Comparison of actuator placement criteria for control of structures". In: *Journal of Sound and Vibration* 353 (2015), pp. 1–18. DOI: 10.1016/j.jsv.2015.05.002.

[5] B. Lossouarn. "Positionnement optimal de couches minces piézoélectriques dans un objectif de maximisation de couplages modaux". In: *15ème colloque national en calcul des structures*. 2022.

[6] P. Maghami and S. Joshi. "Sensor/Actuator Placement for Flexible Space Structures". In: *American Control Conference*. Vol. 2. 1990, pp. 1941–1948.

[7] T. Williams. "Transmission-zero bounds for large space structures, with applications". In: *Journal of Guidance, Control, and Dynamics* 12.1 (1989), pp. 33–38. DOI: 10.2514/3.20365.

[8] W. Levine. *The Control Handbook in two Volumes*. CRC Press, 1999.

[9] B. Boashash. *Time-Frequency Signal Analysis and Processing, A Comprehensive Reference*. Second Edition. Academic Press, 2016.

[10] A. Hac and L. Liu. "Sensor And Actuator Location In Motion Control Of Flexible Structures". In: *Journal of Sound and Vibration* 167.2 (1992), pp. 239–261. DOI: 10.1006/jsvi.1993.1333.

[11] I. Bruant and L. Proslier. "Optimal Location of Actuators and Sensors in Active Vibration Control". In: *Journal of Intelligent Material Systems and Structures* 16.3 (2005), pp. 197–206. DOI: 10.1177/1045389X05047989.

[12] A. Sadri, J. Wright, and R. Wynne. "Modelling and optimal placement of piezoelectric actuators in isotropic plates using genetic algorithms". In: *Smart Materials and Structures* 8 (1999), pp. 490–498. DOI: 10.1088/0964-1726/8/4/306.

[13] F. Peng, A. Ng, and Y.-R. Hu. "Actuator Placement Optimization and Adaptive Vibration Control of Plate Smart Structures". In: *Journal of Intelligent Material Systems and Structures* 16.3 (2005), pp. 263–271. DOI: 10.1177/1045389X05050105.

[14] K. Lim. "Method for optimal actuator and sensor placement for large flexible structures". In: *Journal of Guidance, Control, and Dynamics* 15.1 (1992), pp. 49–57. DOI: 10.2514/3.20800.

[15] W. Gawronski. *Advanced Structural Dynamics and Active Control of Structures*. Mechanical Engineering Series. Springer-Verlag New York, 2004. DOI: 10.1007/978-0-387-72133-0.

[16] S. Moheimani and T. Ryall. "Considerations on placement of piezoceramic actuators that are used in structural vibration control". In: *38th IEEE Conference on Decision and Control*. Vol. 2. 1999, pp. 1118–1123. DOI: 10.1109/CDC.1999.830077.

[17] D. Halim and S. Moheimani. "An optimization approach to optimal placement of collocated piezoelectric actuators and sensors on a thin plate". In: *Mechatronics* 13.1 (2003), pp. 27–47. DOI: 10.1016/S0957-4158(01)00079-4.

[18] W. Liu, Z. Hou, and M. Demetriou. "A computational scheme for the optimal sensor/actuator placement of flexible structures using spatial H_2 measures". In: *Mechanical Systems and Signal Processing* 20.4 (2006), pp. 881–895. DOI: 10.1016/j.ymssp.2005.08.030.

[19] S. Devasia, T. Meressi, B. Paden, and E. Bayo. "Piezoelectric actuator design for vibration suppression - Placement and sizing". In: *Journal of Guidance, Control, and Dynamics* 16.5 (1993), pp. 859–864. DOI: 10.2514/3.21093.

[20] G. Schulz and G. Heimbold. "Dislocated actuator/sensor positioning and feedback design for flexible structures". In: *Journal of Guidance, Control, and Dynamics* 6.5 (1983), pp. 361–367. DOI: 10.2514/3.19843.

[21] A. Dhingra and B. Lee. "Optimal Placement Of Actuators In Actively Controlled Structures". In: *Engineering Optimization* 23.2 (1994), pp. 99–118. DOI: 10.1080/03052159408941347.

[22] Y. Kang, H. Park, W. Hwang, and K. Han. "Optimum Placement of Piezoelectric Sensor/Actuator for Vibration Control of Laminated Beams". In: *AIAA Journal* 34.9 (1996), pp. 1921–1926. DOI: 10.2514/3.13326.

[23] S. Skogestad and I. Postlethwaite. *Multivariable feedback control: analysis and design*. Second Edition. john Wiley & sons, 2005.

[24] T. Singh, M. De Mauri, W. Decré, J. Swevers, and G. Pipeleers. "Combined Hinf/H2 controller design and optimal selection of sensors and actuators". In: *IFAC-PapersOnLine* 51.25 (2018), pp. 73–77. DOI: 10.1016/j.ifacol.2018.11.084.

[25] M. A. Khushnood, W. Xiaogang, and C. Naigang. "A criterion for optimal sensor placement for minimizing spillover effects on optimal controllers". In: *Journal of Vibration and Control* 24.8 (2018), pp. 1469–1487. DOI: 10.1177/1077546316661471.

[26] K. Bendine, F. Boukhoulda, and M. Haddag B. andNouari. "Active vibration control of composite plate with optimal placement of piezoelectric patches". In: *Mechanics of Advanced Materials and Structures* 26.4 (2017), pp. 341–349. DOI: 10.1080/15376494.2017.1387324.

[27] A. Daraji and J. Hale. "Reduction of structural weight, costs and complexity of a control system in the active vibration reduction of flexible structures". In: *Smart Materials and Structures* 23.9 (2014), p. 095013. DOI: 10.1088/0964-1726/23/9/095013.

[28] K. R. Kumar and S. Narayanan. "The optimal location of piezoelectric actuators and sensors for vibration control of plates". In: *Smart Materials and Structures* 16.6 (2007), pp. 2680–2691. DOI: 10.1088/0964-1726/16/6/073.

[29] Y.-J. Cha, A. K. Agrawal, Y. Kim, and A. M. Raich. "Multi-objective genetic algorithms for cost-effective distributions of actuators and sensors in large structures". In: *Expert Systems with Applications* 39.9 (2012), pp. 7822–7833. DOI: 10.1016/j.eswa.2012.01.070.

[30] J. H. Martin, B. D. Yahata, E. C. Clough, J. A. Mayer, J. M. Hundley, and T. A. Schaedler. "Additive manufacturing of metal matrix composites via nanofunctionalization". In: *MRS Communications* 8.2 (2018), pp. 297–302. DOI: 10.1557/mrc.2018.95.

[31] T. Song, Z. Chen, X. Cui, S. Lu, H. Chen, H. Wang, T. Dong, B. Qin, K. C. Chan, M. Brandt, et al. "Strong and ductile titanium–oxygen–iron alloys by additive manufacturing". In: *Nature* 618.7963 (2023), pp. 63–68. DOI: 10.1038/s41586-023-05952-6.

[32] A. Deraemaeker, G. Tondreau, and F. Bourgeois. "Equivalent loads for two-dimensional distributed anisotropic piezoelectric transducers with arbitrary shapes attached to thin plate structures". In: *The Journal of the Acoustical Society of America* 129.2 (2011), pp. 681–690. DOI: 10.1121/1.3523338.

[33] G. Tondreau, S. Raman, and A. Deraemaeker. "Point load actuation on plate structures based on triangular piezoelectric patches". In: *Smart Structures and Systems* 13.4 (2014), pp. 547–565. DOI: 10.12989/sss.2014.13.4.547.

[34] Y. Zhao, J. Zhu, W. He, Y. Liu, X. Sang, and R. Liu. "3D printing of unsupported multi-scale and large-span ceramic via near-infrared assisted direct ink writing". In: *Nature Communications* 14.1 (2023), p. 2381. DOI: 10.1038/s41467-023-38082-8.

[35] G. Zhao, B. Chen, and Y. Gu. "Control–structural design optimization for vibration of piezoelectric intelligent truss structures". In: *Struct Multidisc Optim* 37 (2009). DOI: 10.1007/s00158-008-0245-4.

[36] O. A. da Silveira and J. S. Fonseca. "Simultaneous design of structural topology and control for vibration reduction using piezoelectric material". In: *Mecanica Computacional* 29.85 (2010), pp. 8375–8389.

[37] A. Molter, O. A. Silveira, V. Bottega, and J. Fonseca. "Integrated topology optimization and optimal control for vibration suppression in structural design". In: *Structural and Multidisciplinary Optimization* 47 (2013). DOI: 10.1007/s00158-012-0829-x.

[38] A. Delissen, F. van Keulen, and M. Langelaar. "Integrated topology and controller optimization using the Nyquist curve". In: *Structural and Multidisciplinary Optimization* 66.4 (2023), p. 80. DOI: 10.1007/s00158-023-03515-x.

[39] E. C. Hooijkamp and F. v. Keulen. "Topology optimization for linear thermo-mechanical transient problems: modal reduction and adjoint sensitivities". In: *International Journal for Numerical Methods in Engineering* 113.8 (2018), pp. 1230–1257. DOI: 10.1002/nme.5635.

[40] G. van der Veen, M. Langelaar, S. van der Meulen, D. Laro, W. Aangenent, and F. van Keulen. "Integrating topology optimization in precision motion system design for optimal closed-loop control performance". In: *Mechatronics* 47 (2017), pp. 1–13. DOI: 10.1016/j.mechatronics.2017.06.003.

[41] D. Piron, S. Pathak, A. Deraemaeker, and C. Collette. "A pole-zero based criterion for optimal placement of collocated sensor-actuator pair". In: *Mechanical Systems and Signal Processing* 155 (2021), p. 107533. DOI: 10.1016/j.ymssp.2020.107533.

[42] A. Preumont. *Vibration Control of Active Structure, An Introduction*. Thrid Edition. Springer, 2011. DOI: 10.1007/978-94-007-2033-6.

[43] E. Balmes. *Structural Dynamics Toolbox 7.3 (for use with MATLAB)*. 1991. URL: https://www.sdtools.com.

[44] V. Piefort. "Finite element modelling of piezoelectric active structures". PhD thesis. Université Libre de Bruxelles, Faculté des sciences appliquées, 2001.

[45] *Physik Instrumente (PI)*. URL: https://www.piceramic.com/en/.

Chapter 4

The pole-zero distance criterion for fast transducer placement optimization

Abstract

The use of a search algorithm is essential when seeking optimal transducer position by means of a placement criterion. This chapter first reviews the convergence mechanism of the genetic evolutionary algorithms (GAs), the most popular algorithms for such studies. Through this analysis, it is demonstrated that although the GA are well-suited to find the optimal position, they need extremely long computational time to obtain the solution. Unfortunately, simpler search algorithms usually require prior knowledge to initiate the convergence, which is not compatible with the current placement criteria. To address this issue, a new approach based on the PZ distance criterion is proposed. This method that targets collocated SA pairs consists in evaluating the PZ criterion on a limited number of positions and the location that maximises its value is considered as the starting point for a non-evolutionary algorithm. It is numerically demonstrated that this novel approach allows to drastically reduce the number of evaluations required to reach convergence compared to other optimization methods. Additionally, the obtained solutions ensure high performance in terms of damping as well as high robustness to transducer misplacement. Consequently, the proposed approach presents a viable substitute for existing methods, thereby facilitating the expansion of transducer placement optimization to complex systems which was previously avoided due to the related high computational costs.

4.1 Introduction

The crucial aspect of properly selecting the placement criterion in control architecture has been highlighted in Chapter 3. More specifically, the related trade-off between the performance of the obtained solution and the time required to evaluate the criterion was discussed through a literature review. To address this trade-off, the PZ distance criterion has been proposed for collocated LAC systems and extensively analysed with numerical systems. It has been shown that the proposed criterion outperforms the other existing open-loop criteria.

Nevertheless, the different analyses and comparisons were conducted by evaluating all the possible SA positions. While such a comprehensive analysis was necessary to thoroughly

examine the proposed criterion and compare it with alternative approaches, it is impractical to consider all the possible positions when dealing with optimal transducer placements for real-life structures. A full analysis can indeed be prohibitive when the evaluation of the criterion is expensive in terms of computational time and/or when too many combinations are possible. In such cases, the application of a search algorithm becomes essential, whose aim is to converge towards the best solution without exhaustively computing all the available combinations.

GAs are fairly suited for the optimal SA placement studies because: (i) they are appropriate to apply in situations where no-prior knowledge is required, (ii) they can solve linear and non-linear problems and (iii) they can find the global optimum despite the presence of multiple local ones [1]. A GA is for example applied in [2, 3] to find the optimal placement of piezoelectric actuators based on the maximization of the controllability, or in [4] to locate the optimal sensor placement using a modified modal assurance criterion. Moreover, several placement criteria in closed-loop also use GAs to converge towards the optimal solution such as in [5] which seeks to reduce the average closed-loop gain or in [6, 7] that are based on the implementation of linear quadratic controllers.

Despite the advantages of using a GA to obtain the optimal solution, a major drawback inherent to such a search algorithm is that it compels numerous iterations to properly converge. Therefore, even if a convergence algorithm is used, an extremely long computational time may be required for large and/or complex structures. Indeed, each evaluation of the cost function can be very demanding in terms of processing time for such structures. For example, the optimal placement of two piezoelectric patches on a thin plate using a GA in [1] requires already 600 evaluations. Knowing that the time complexity for the inversion of a $n \times n$ matrix is $\mathcal{O}(n^{2.78})$ at best [8], such a simple optimization demands already a large computational effort. Consequently, and due to this possible prohibitive convergence duration, SA placement optimizations are not commonly implemented for real industrial applications.

To overcome this major drawback, simpler algorithms that need fewer evaluations could be considered, e.g. the first or second-order optimization methods that only rely on the derivative of the cost function to obtain the convergence direction [9]. Nevertheless, although such type of algorithm needs substantially fewer evaluations to generate an optimum, the effectiveness of the solution highly depends on the provided starting parameter(s) value. This major drawback is also encountered for other non-evolutionary methods, such as the derivative-free optimization where the convergence does not rely on the calculation of the gradient [10]. This prerequisite to initiate convergence explains why non-evolutionary algorithms are not commonly employed for optimal placement studies. Nonetheless, if the provided starting values are wisely selected (i.e. in the vicinity of the global optimal solution), the usage of a simpler algorithm can be highly efficient since it requires significantly fewer evaluations to converge than the frequently used GAs.

This chapter aims to investigate the use of the proposed PZ distance placement criterion as a preliminary analysis to obtain a suitable starting point for a simple convergence algorithm. This criterion being based on the direct link between open-loop information (the PZ distance) and closed-loop prediction (the maximum reachable damping), it should allow to use, unlike the other available placement criteria, a limited number of candidates while ensuring a solution in the vicinity of a high damping area. Section 4.2 briefly recalls the basics of a non-evolutionary optimization method (the gradient descent) and the basics of the genetic search algorithms, and discusses which type of search algorithm is commonly

used for optimal transducer placement studies. After that, Section 4.3 introduces the use of the PZ distance criterion as a means to select a starting position for running a non-evolutionary algorithm. The establishment of the proposed approach is followed by a numerical validation of the method on a cantilever beam. The validation includes the comparison of the performance with respect to the use of another open-loop criterion (the Gramian controllability) as well as the performance obtained with a GA. Finally, some conclusions are given in the last section.

4.2 Genetic algorithms and gradient descent convergence

The GAs are stochastic algorithms inspired by the process of natural selection [11]. First, an initial population that contains a defined number of members is randomly generated where each member encloses the parameters to be optimised. Next, each member of this first generation is scored based on the performance obtained by evaluating the objective function with respect to its parameter(s) value. From this, a fraction of the members with the highest scores, called elite children, are kept for the next generation without modification while new children are created by crossover and mutation. The process of crossover ensures the convergence of the algorithm by combining two members with high scores whereas the mutation adds diversity to the new generation by randomly changing single members. Once the new generation is completed, its members are evaluated again and the same process is applied: elite children, crossover and mutation to produce another new generation. This procedure is stopped when one of the termination conditions is met, e.g. a defined threshold value for the average relative change in the cost function has been reached or a specified number of generations has been obtained. The optimal solution is then selected as the member that maximises the objective function among the final generation. An illustration of the convergence process of a GA is shown in Figure 4.1 where the optimization is achieved on four parameters that can take an integer value from 0 to 9. The parameters that are kept from one generation to the newly generated one are highlighted in a bold and underlined font to ease comprehension.

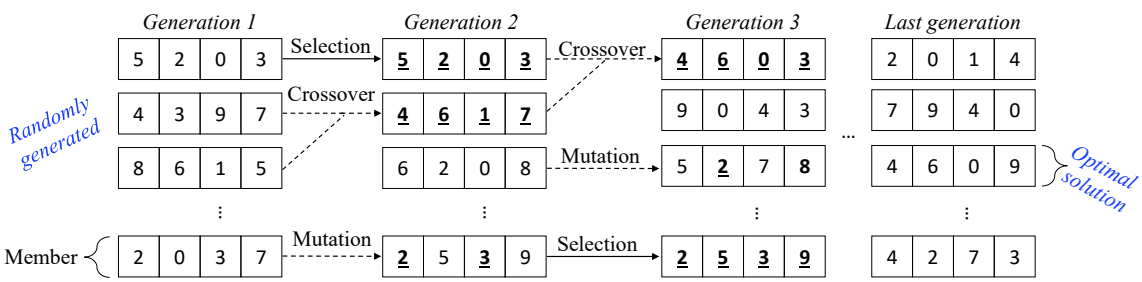

Figure 4.1: Illustration of the convergence process of a GA where 4 parameters that can take an integer value from 0 to 9 are optimized. The values that are kept from the previous generation are highlighted by a bold and underlined font.

The application of the crossover and the mutation mechanisms performed by the GAs, illustrated in Figure 4.1, is one of the main advantages of these algorithms [11]. They indeed reduce the risk that the retained parameters correspond to a local optimal solution. Nevertheless, reaching an optimal solution is not mathematically ensured and finding the global optimum is only possible if the different parameters of the GA are properly defined to avoid too fast convergence or not enough global research. Those parameters are, for example, the size of the population, the number of retained elite children or the number of crossover and mutated children. Furthermore, and because the objective function has to be evaluated for the entire population of each generation, identifying the global optimum

comes at the expense of an extremely long computational time [12].

Conversely, non-evolutionary algorithms such as the first or second-order optimization methods are known to be much less time-consuming than the GAs to reach convergence. Based on the differentiability of the cost function with respect to the parameter(s) to optimize, those algorithms use the value of the gradient at the current point to obtain the direction of convergence. For example, the gradient descent method consists of a first-order optimization that uses the gradient to proportionally modify the value of the parameter(s) to obtain the next iteration. Once the cost function reaches a local optimal solution, the gradient value tends to zero and the optimization process stops when the defined threshold is reached. Although very simple and cost-effective in terms of computational time, this method is highly sensitive to the provided starting value(s) of the parameter(s) to be optimized. The algorithm converges indeed towards the local optimal solution [13], as illustrated in Figure 4.2 where the convergence points towards a local optimum instead of the global one. The proper convergence towards the global optimum can be achieved only if the starting point is located within a region that does not contain a local optimum, i.e. the convergence process does not face a local optimum before reaching the global one. Such a region is for example highlighted in Figure 4.2 by the green suitable starting area square.

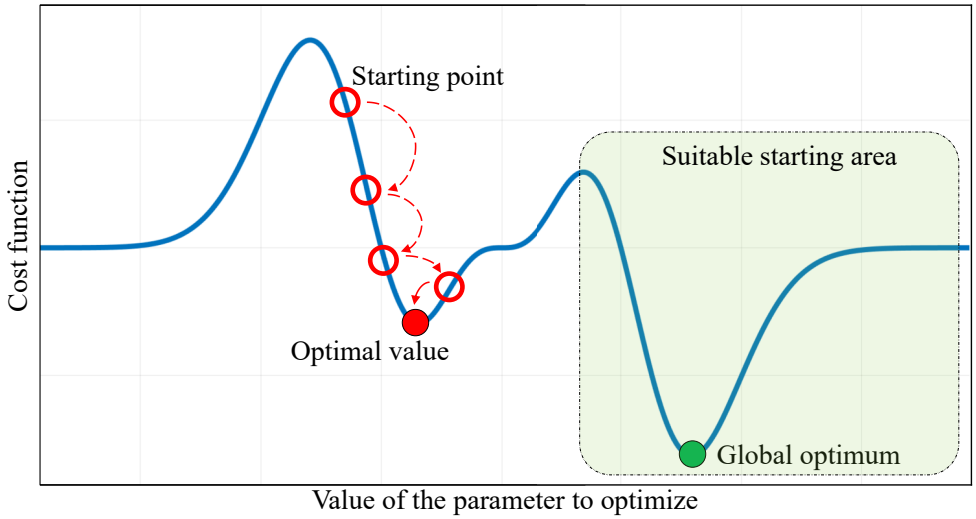

Figure 4.2: Illustration of the convergence process of the gradient descent algorithm where 1 parameter is optimized. The algorithm converges towards a local optimum instead of the global one due to a poor selection of the starting point.

The requirement of an adequate starting position for non-evolutionary optimization methods is the major reason why GAs are mainly used for the SA placement studies. The different criteria are indeed not intended to provide prior knowledge that could ensure the appropriate selection of the starting values. Initiating the convergence with a random distribution, as carried out with the GAs, avoids consequently this challenging selection.

Nevertheless, if the starting values are wisely chosen (e.g. in the vicinity of the global optimal solution), the non-evolutionary methods can be highly efficient since they require significantly fewer evaluations to converge than other complex algorithms. Such a suitable starting position could be obtained by using an approximated analytic expression of the optimal solution. This approach is, for example, studied in [14] where the analytic solution of the parameters for a tuned mass damper is derived. It is shown that this analytic solution reduces the convergence effort while leading to valuable performance. Yet, it is

often not feasible to develop an analytical solution for complex systems and, especially, if it needs to be done in a closed-loop configuration.

Another method could consist of performing a preliminary and limited analysis with an efficient criterion. But this analysis should ensure, despite its limited nature, that the obtained solution is reliable enough to serve as a starting point. Nonetheless, the optimal placement criteria are not intended to be computed at only a few possible positions. This is explaining again why GAs are rather used than more simple algorithms for the SA placement optimization.

4.3 On the use of the PZ distance criterion to apply a non-evolutionary algorithm

As detailed in Chapter 3 and unlike the other placement criteria, the PZ distance criterion is based on a direct and physical link between open-loop knowledge and closed-loop behaviour (respectively the PZ distance and the maximum reachable damping). Regarding the zeros, it is well known that their values are always bounded between two surrounding eigen frequencies when considering collocated systems because of the interlacing property. Additionally, it is reasonable to assume that the values of the zeros, in a structural system, do not show any sudden change when the collocated transducers are slightly relocated. Establishing a mathematically rigorous proof poses considerable complexity, as it necessitates deriving it from the general solution of the zero frequencies, which are obtained by solving a high-order equation (see Section 1.4 for the calculation of the zero values). Nonetheless, the validity of this assumption is supported by various studies that provide numerical evidence of the continuous behaviour of the zero values, such as in [15, 16]. The evolution of the zeros as a function the SA pair position along a cantilever beam illustrated in Figure 1.9 reinforces as well the validity of the assumption.

Due to the properties of the PZ distance criterion and the continuous behaviour of the zeros, it is clear that only a limited number of positions would need to be evaluated by the PZ criterion to produce a preliminary trend of the PZ distance. Consequently, the position among all the limited tested ones that maximizes the criterion should translate to a SA placement that exhibits high closed-loop performance. This placement could therefore be reliable enough to serve as the starting value for a non-evolutionary algorithm.

Considering the aforementioned properties of the zeros, it is clear that to obtain a reliable trend of the PZ distance, the number of limited positions to be evaluated by the criterion should be directly related to the dynamical behaviour of the mode(s) of interest. A good indicator of the dynamics can be the wavelength of the targeted mode shape(s). Indeed, the higher the mode, the smaller its mode shape wavelength and, consequently, the higher the number of points needed to accurately describe the dynamics. Hence, the number of positions to be computed by the PZ criterion on the system in direction d and for mode i can be defined as follows:

$$r_{i,d} = \left\lceil \gamma \times \frac{\|d\|}{\lambda_{i,d}} \right\rceil \tag{4.1}$$

where the notation $\lceil\ \rceil$ corresponds to the ceiling function that expresses the least integer greater than or equal to its input, γ is the number of positions per effective wavelength, $\|d\|$ is the dimension of the system in direction d and $\lambda_{i,d}$ is the wavelength of mode i in direction d. Accordingly, and if the system contains $D = \{d_1, d_2, ...\}$ dimensions, the

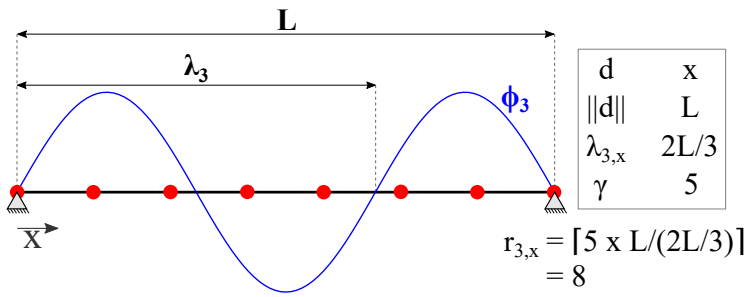

Figure 4.3: Illustration of the identification method for establishing the r limited positions to be evaluated by the PZ distance criterion on a simply supported beam.

PZ distance criterion introduced by Equation 3.8 (and recalled in Equation 4.2) requires only $\prod_D r_{i,d}$ times its evaluations to obtain a first trend of the PZ distance of mode i as a function of the SA pair positions. An illustration of the application of the limited position formula is shown in Figure 4.3, which focuses on the third bending mode of a simply supported beam. For such a simple structure, the mode shape can be analytically expressed as done in [17], which allows to easily extract its corresponding wavelength. Once the wavelength is identified, applying Equation 4.1 is straightforward, which leads to 8 limited positions for the considered example.

$$J(\mathbf{x}) = \left(\frac{1}{n}\sum_{k=1}^{n}\frac{|PZ(\mathbf{x})|_k}{max(|PZ\{\mathbf{x}\}|_k)}\right)\times\left(\sqrt[n]{\prod_{k=1}^{n}\frac{|PZ(\mathbf{x})|_k}{max(|PZ\{\mathbf{x}\}|_k)}}\right)\times\left(\sqrt[n]{\prod_{k=1}^{n}\frac{|P_kZ_{adj}(\mathbf{x})|}{max(|P_kZ_{adj}\{\mathbf{x}\}|)}}\right) \tag{4.2}$$

It is not always easy or possible to obtain the wavelength value of a mode, especially for complex structures. For such a situation, a regular grid pattern could be considered in which the density of the limited positions should depend on the system complexity as well as on the mode(s) of interest.

Due to the physical link between the PZ distance and the maximum reachable damping, the position that provides the maximum criterion value among the evaluated ones can be defined as the starting point for a non-evolutionary search algorithm, which will converge towards the optimum that locates in its vicinity. Therefore, and unlike the GA convergence, only a small amount of evaluations is needed, reducing considerably the overall processing time for the optimization study. The flowchart of the proposed optimization method is shown in Figure 4.4 where four major steps can be identified. The first step relies on the development of a FE model of the system. When available, the second step consists of selecting the limited positions to be evaluated. As discussed above, this selection depends upon the complexity of the system, as well as on the targeted modes to be damped. Once the positions are identified, the third step is to compute the PZ distance criterion to evaluate them. Nonetheless, it first requires to select the intended control law to properly define the distance. The last step consists in extracting the position that maximizes the PZ criterion and to start the closed-loop convergence of the selected non-evolutionary algorithm to obtain the optimal solution. In order to demonstrate the effectiveness of this approach, a numerical validation is performed in the next sub-section.

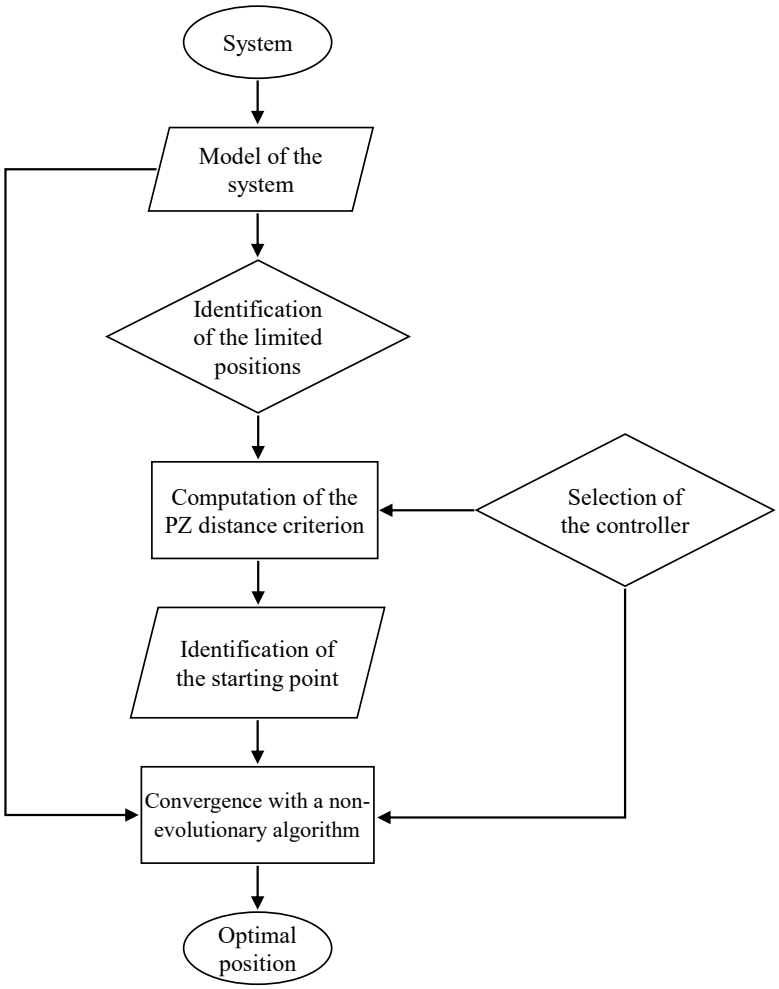

Figure 4.4: Flowchart of the proposed optimization method.

4.3.1 Numerical validation of the proposed approach

The proposed strategy is numerically illustrated on a cantilever beam for the optimal placement of a collocated force actuator/displacement sensor pair whose purpose is to separately maximize the modal damping of the first three bending modes. The system is modelled using SDT [18] according to the dimensions of 300 mm x 25 mm x 2 mm and with a lightly damped steel with the following properties: Young's modulus $E = 210$ GPa, Poisson's ratio $\nu = 0.285$, mass density $\rho = 7800$ kg/m^3 and modal damping ratio $\xi = 0.004$. Because only the bending modes of the beam are considered, its FE model is built using beam elements that allow only the 2 DoFs in-plane bending motion (a comprehensive description of those elements can be found in Appendix A). The mesh accuracy in the longitudinal direction x is set to 0.1 mm which leads to a total of 3001 elements, each node being a potential SA pair position except for the constrained node at the clamped end of the cantilever beam. The convenience to apply such high accuracy for the mesh size is that it provides an extensive number of positioning candidates while using a simple demonstration structure. A simplified illustration of the cantilever beam as well as its Cartesian coordinate are shown in Figure 4.5.

As illustrated in Figure 4.4, the proposed approach consists of (1) choosing the limited positions and evaluating them with the PZ distance criterion and (2) using the position that maximizes the computed distances as starting value for a non-evolutionary algorithm. Because the analytic expression of the wavelength of the bending modes of a cantilever beam

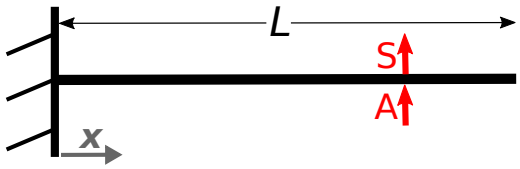

Figure 4.5: Numerical cantilever beam used to validate the proposed approach

can be easily obtained, the number of limited positions is computed using Equation 4.1. Based on the analytic expression of the mode shapes of a cantilever beam from [17], the related wavelength of mode i can be approximated by $\lambda_{i,x} \approx 4L/(2\,i-1)$ where L is the length of the beam in the x direction. Because 5 to 10 elements per wavelength are usually considered in FE modelling, the number of positions per effective wavelength γ from Equation 4.1 can be set to the lower bound 5. This leads to only 2 positions for the first mode while 4 and 7 positions are required for the second and third ones, respectively. Those numbers prove consequently that the proposed approach limits considerably the preliminary check needed before using the non-evolutionary convergence. The actual placement of those limited positions on the system is obtained by generating $r_{i,x}$ equally spaced points between the first and the last non-constrained nodes in the longitudinal direction of the beam, which translates to the positions marked in red in Figure 4.6.

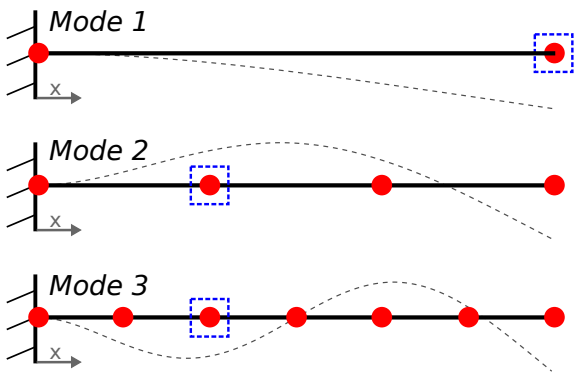

Figure 4.6: Graphical representation of the limited positions to be evaluated by the PZ distance criterion for the three bending modes of the beam (red dots), as well as the positions that maximise the criterion (blue squares). The mode shapes are drawn as well in grey dashed-line.

The aim of the optimization being to separately maximize the modal damping of the first three bending modes, the non-evolutionary algorithm can directly focus on the closed-loop performance by applying the cost function $\tilde{J}$ defined by Equation 4.3, where $\mathbf{x}$ contains the position of the SA pair, g is the gain value of the applied controller and ξ_i is the closed-loop modal damping of mode i. The search algorithm will therefore perform the optimization on two parameters: the position x and the gain value g.

$$\tilde{J}(\mathbf{x}, g) = \xi_i(\mathbf{x}, g) \tag{4.3}$$

Regarding the controller, a lead control law as described by Equation 4.4 is considered where the zero z_c and the pole p_c only depend on the targeted mode as follows: $z_c = \omega_i/2$ and $p_c = \omega_i \times 2$ where ω_i is the natural angular frequency of the targeted mode i. Although of limited authority due to the narrow frequency band used, the choice of these parameters allows to restrain the variability of the controller to its gain value, and ensures

a comprehensive comparison between different positions when considering a specific modal case. Because the PZ distance criterion does not deal with the optimal gain, the starting value of g needs to be computed as well. Even if analytic values of the optimal gain have been developed in [19], the presented expressions are only applicable when the zero value is close enough to the pole of interest. Such a situation does not comply with the intended PZ criterion since it aims to maximize the distance. Consequently, the starting gain value g_{start} will be obtained by using the *rlocus* function of Matlab: the damping of each complex root location will be computed and the related feedback gain that maximises the damping within the vector of all the extracted closed-loop poles will be selected. This approach allows indeed to obtain a reliable starting gain value with only one evaluation of the closed-loop system (when using the *rlocus* function, which provides around 50 gain values) and limited analytic calculations.

$$C(s) = g\,\frac{s + z_c}{s + p_c} \tag{4.4}$$

As the controller has been characterized, it is possible to properly define the PZ distance: because the pole appears at a lower frequency than the zero when applying a lead controller, the PZ distance is computed by subtracting the pole from its corresponding zero [19]. The evaluation of those distances starts with the computation of the zeros at the studied positions $\{\mathbf{x}\}$. To ensure high accuracy of the zero values, such evaluation is based on their physical interpretation which defines the zeros as the natural frequencies of the system that is constrained at the considered SA location [20]. Based on this definition, an eigenvalue problem is solved for each numerically constrained system at the different positions $\mathbf{x}$. The evaluation of the PZ distance criterion expressed by Equation 4.2 for the first three bending modes at the limited positions provides the following locations that maximise its value: $1.000 \times L$ for the first bending mode and $0.334 \times L$ for the second and third ones. Those different locations are highlighted by the blue dashed boxes in Figure 4.6. Each of those results needs to be used as starting position for a non-evolutionary algorithm. For this purpose, the *'fminsearch'* function available within the Global Optimization Toolbox of Matlab is selected. Indeed, such function searches for the local minimum while relying on a non-evolutionary method. More specifically, it is based on a direct search algorithm that minimizes the cost function by searching in the vicinity of the current position, without computing the derivative. A comprehensive description of the method used in the *'fminsearch'* function is provided in Appendix B, where the optimization parameters are provided as well. The cost function used by the search algorithm is defined by Equation 4.3 where the damping value ξ_i is evaluated by computing the closed-loop complex eigenvalues.

For the sake of completeness, the performance obtained with the proposed approach can be compared to the one achieved by combining the *'fminsearch'* algorithm with another open-loop criterion: the Gramian controllability. The Gramian controllability is based on the reduction of the control energy required to attenuate the structural vibrations of the system and directly relates to the modal amplitude of the targeted mode(s) [21]. For additional details on this criterion, Section 3.2 provides an in-depth analysis. To guarantee a fair comparison, the Gramian criterion is computed at the same limited positions highlighted by the red dots in Figure 4.6. As expected, the free end of the beam corresponds to the location that maximises the Gramian for the three bending modes of the beam. Similarly to what has been done with the PZ distance criterion, those locations are used as starting positions for the convergence of the *'fminsearch'* algorithm and the starting gains are obtained with the same *rlocus* method.

Furthermore, the performance of the proposed approach can be compared to the one obtained with the commonly used genetic search algorithm as well. To this end, the GA available within the Global Optimization Toolbox of Matlab and called by the *'ga'* function is implemented with the main parameters that are listed in Table 4.1. Similarly to the direct search method (i.e. the non-evolutionary algorithm), a more comprehensive description of the Matlab GA can be found in Appendix B, where the optimization parameters are provided as well.

It is worth mentioning that although the GA can handle both continuous and discrete variables, the *'fminsearch'* function can only handle continuous values of the design variables g and $\mathbf{x}$. To avoid any re-meshing of the system during convergence, a discretization of $\mathbf{x}$ is consequently performed at each evaluation of the cost function. This discretization ensures that the provided continuous position obtained from the search algorithm matches the closest node of the FE model.

Table 4.1: Parameter settings used for the implementation of the GA.

Parameters	Settings
Design variables	$\mathbf{x}$, g
Optimization objective	Maximize $\tilde{J}(\mathbf{x}, g)$
Population size	50
Mutation probability	Gaussian distribution
Crossover probability	0.8
Elite children per generation	Minimum 2

The optimal placement solutions that derive from the three approaches can be found in Table 4.2 and the comparison of the performance obtained with those solutions is shown in Figure 4.7. The total number of cost-function evaluations encompassing both the open-loop computations (for assessing the PZ distances and the Gramian criterion) as well as the closed-loop ones (for computing the closed-loop cost function defined by 4.3) that are required to reach convergence are represented by the blue thick bars. Each corresponding closed-loop modal damping is highlighted by the thin red ones. As expected and because the starting positions are identical, the convergence process as well as the optimal solutions obtained for the first mode of the beam are similar for the PZ and the Gramian approaches. A comparable damping is obtained with the GA, yet it demands significantly more evaluations to reach convergence. This observation is validated for the three modal cases, as the ratio between the number of evaluations for the GA and the *'fminsearch'* algorithm convergence goes indeed up to 23, confirming therefore the fast convergence of the proposed method, as previously mentioned.

Table 4.2: Normalised optimal positions obtained with the PZ, the Gramian and the GA approaches on the cantilever beam for the first three bending modes.

	Normalised optimal position (/L)		
	PZ	Gramian	GA
Mode 1	0.7923	0.7923	0.7867
Mode 2	0.5077	0.8567	0.8570
Mode 3	0.3593	0.9287	0.9287

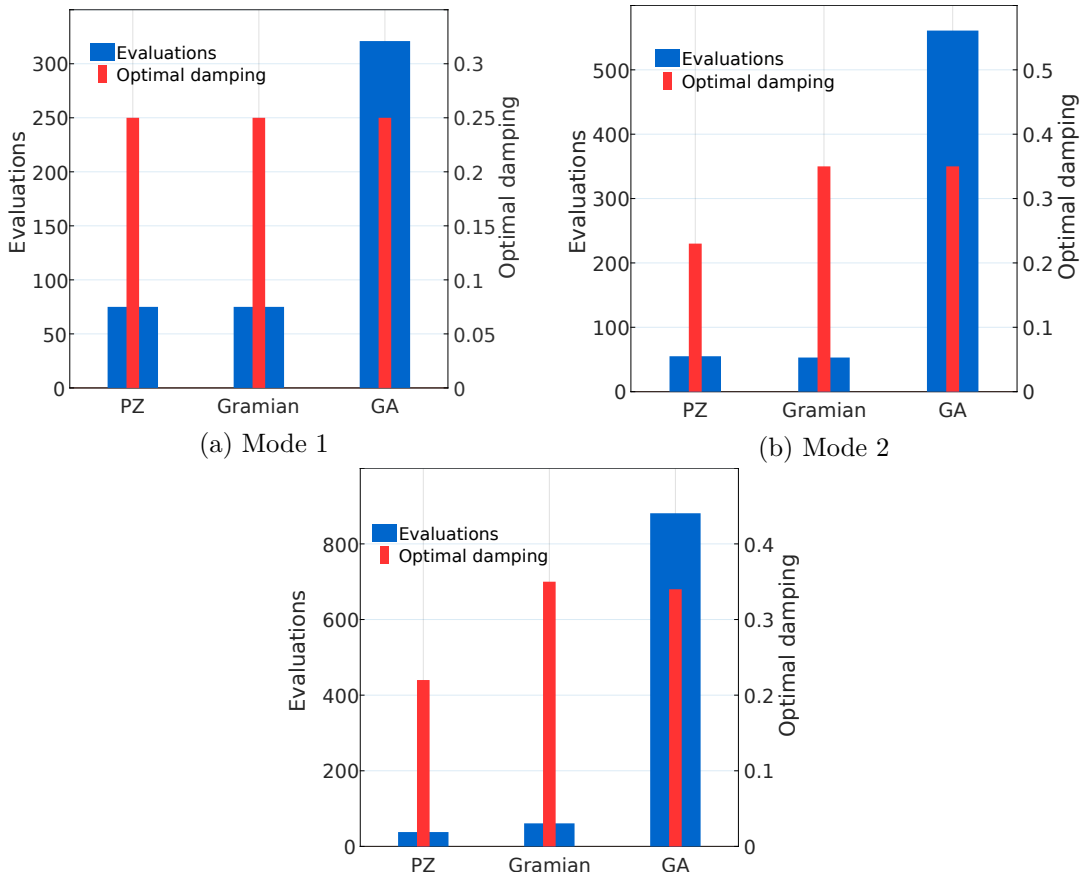

(a) Mode 1

(b) Mode 2

(c) Mode 3

Figure 4.7: Total number of evaluations of the cost function to reach convergence and the optimal damping values obtained with the PZ, the Gramian and the GA approaches on the cantilever beam, for: (a) mode 1, (b) mode 2 and (c) mode 3.

The optimization process for the first mode is investigated in Figure 4.8, where the evolution of the modal damping values during the direct search algorithm and the GA optimizations is compared (as discussed, the PZ and the Gramian criteria provide the same convergence for this specific case due to the similar starting values). It reveals the superior convergence speed of the direct search method over the GA one, as already observed in Figure 4.7. As it can be seen, the proper direction of convergence is indeed rapidly determined for the direct search algorithm which then only requires 75 evaluations in total to find the optimum. The stabilization of the progression without further improvement of the cost function value around the 40th evaluation is induced by the stopping condition tolerance that is not met yet, as well as by the fact that the algorithm used in the *'fminsearch'* function requires more than one evaluation to switch to a new iteration of the algorithm [22] (further details on the algorithm are provided in Appendix B). Conversely, the GA is based on a stochastic approach and starts with a randomly initiated population of 50 members. This initial population is first entirely evaluated in order to generate, based on the selection, mutation and crossover mechanisms, the newly evolved generation. The effect of the convergence consequently emerge only after the evaluation of each entire population, when a new generation is created. This phenomenon is clearly apparent in Figure 4.8b where each generation is delimited by an alternating background colour. As a result, the algorithm requires numerous evaluations of the cost function, which leads to a total of 321 to converge.

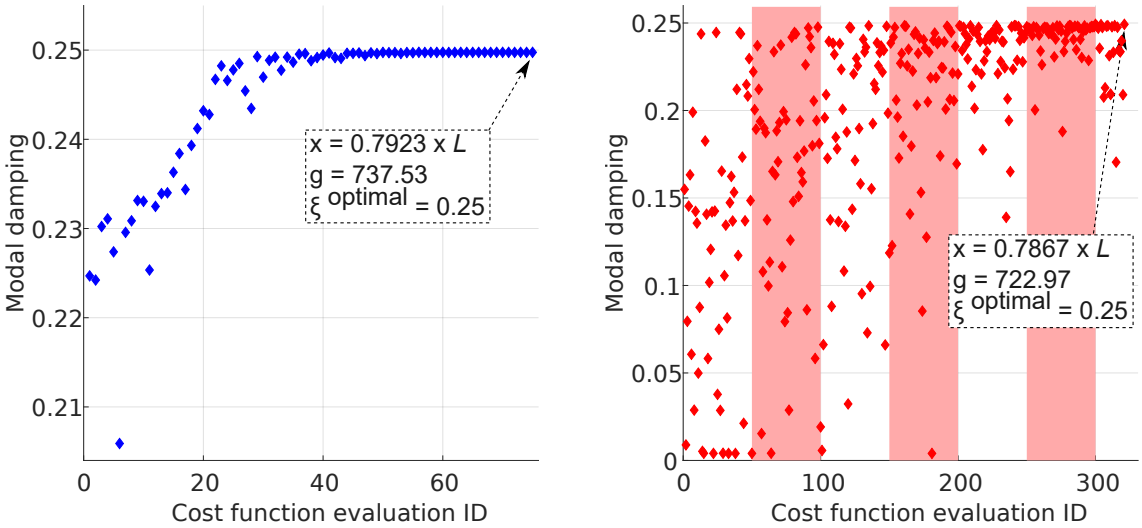

(a) Direct search algorithm (b) GA

Figure 4.8: Damping convergence of the first bending mode of the cantilever beam for: (a) the direct search algorithm, (b) the GA.

The fast convergence obtained with the direct search algorithm depicted in Figure 4.8a is further analysed in Figure 4.9 which shows the evolution of the design variables $\mathbf{x}$ and g during the optimization process. As it can be seen, the starting point for the SA position and the one for the gain value are already quite close to the optimal values. It confirms that the small number of limited positions evaluated by the PZ criterion is sufficient to properly identify a location with high damping performance. Additionally and as already discussed, the proper convergence direction is quickly found, which limits consequently the total number of evaluations required to reach the optimal values.

Conversely, the GA presents a slow convergence because it requires the evaluation of the full population before enforcing the convergence with a new generation. This is highlighted in Figure 4.10 which shows the evolution of the position and the gain values during its optimization. As shown, the full possible range defined for the SA position and the gain value is tested, which increases the probability to find the global optimal solution. Yet, it leads to a more erratic convergence and, therefore, a substantial number of evaluations.

Although the direct search algorithm allows faster convergence, it can be seen in Figure 4.7 that the solutions obtained with the proposed PZ criterion provide lower damping than the two other methods for the second and third modes. This therefore means that, for those specific cases, the PZ distance criterion induces the convergence towards local optima while the GA and the Gramian/direct search approach correctly converge towards the global solutions. Nevertheless, even if the maximization of the damping is the main objective of the optimizations, the robustness of the obtained solutions with respect to transducer misplacement should be considered as well. Such misplacement presents indeed a plausible occurrence when SA pairs are mounted on real-life structures. A sensitivity analysis of the damping with respect to the transducer misplacement is therefore performed to assess the robustness of the various optimal positions.

The sensitivity analysis is conducted as follows: starting from the different solutions obtained for each mode and with the three convergence methods, the SA pair is moved along the longitudinal axis of the beam around the optimal position. A misplacement up to 1% of its length is chosen, leading to a positioning error interval of ± 3 mm. Naturally, and

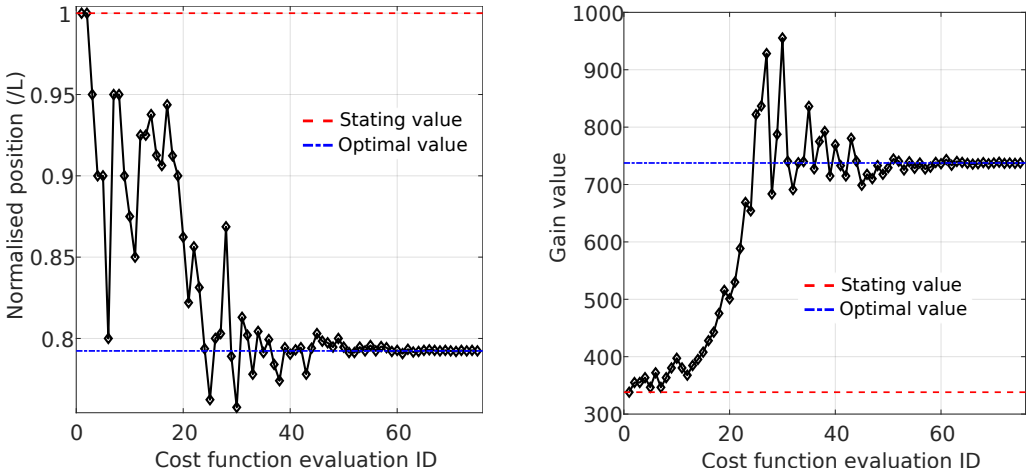

(a) SA pair position (b) Gain value

Figure 4.9: Convergence of the direct search algorithm for the first bending mode of the cantilever beam for: (a) the SA pair position, (b) the gain value.

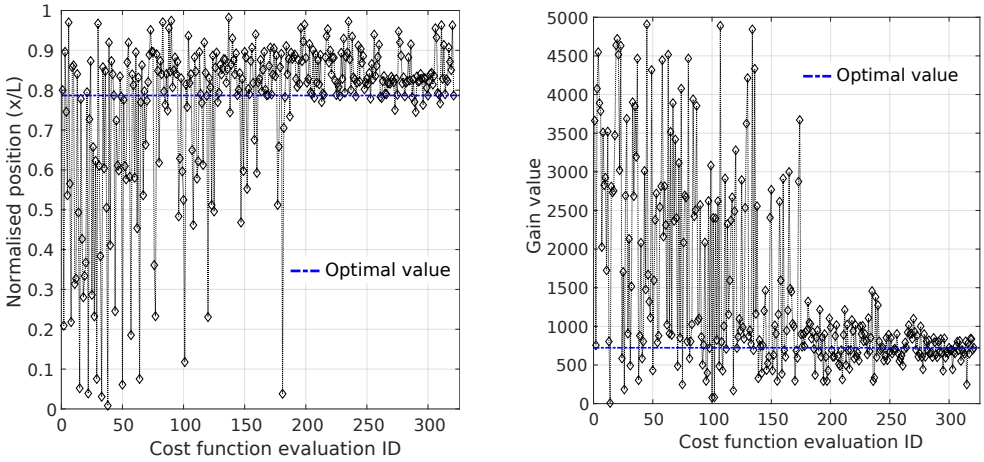

(a) SA pair position (b) Gain value

Figure 4.10: Convergence of the GA for the first bending mode for: (a) the SA pair position, (b) the gain value.

to mimic a real-life transducer placement error, the optimal gains as well as the control laws are kept without any changes. To ease the visualization and the comparison of the different sensitivities between the three modes, the relative positioning error $\Delta\mathbf{x}$ is defined as follows:

$$\Delta\mathbf{x} = \frac{\mathbf{x_m} - \mathbf{x}_{optimal}}{L} \tag{4.5}$$

where $\mathbf{x}_m$ corresponds to the misplacement position while $\mathbf{x}_{optimal}$ is the optimal one. The results obtained with the sensitivity analysis can be found in Figure 4.11 where the modifications of the damping ratio introduced by the SA misplacement are displayed. As it can be seen, the optimal positions obtained with the direct search algorithm based on the PZ distance criterion show a strong resilience to misplacement. Indeed, the damping ratio remains within the same range over the full misplacement area, for the three considered modes. This consequently translates into the assurance of undiminished performance in case of such a limited misplacement error. On the contrary, the optimal positions obtained with the two other convergence methods present important damping reductions. Addi-

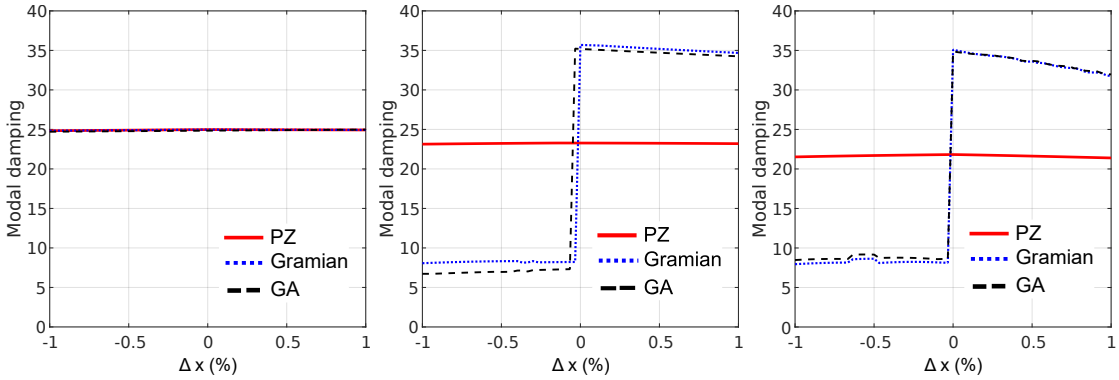

(a) Mode 1 (b) Mode 2 (c) Mode 3

Figure 4.11: Sensitivity analysis of the SA pair misplacement with respect to the optimal positions obtained with the three methods for: (a) mode 1, (b) mode 2, (c) mode 3.

tionally, those large reductions arise for a relative error of less than 0.1% (i.e. less than 0.3 mm), for the second and third modes. Such fluctuations can be explained by the fact that those optimal positions locate in the vicinity of a complete root-locus reshaping. A root-locus reshaping can, for example, be due to the position of a zero that lies too close to the pole of the targeted mode, which induces a pole-zero cancellation as depicted in Figure 3.3b. As soon as the misplacement of the SA pair reaches such an area, the entire dynamics of the system changes and the damping can drop abruptly.

The important damping reduction of the second mode observed in Figure 4.11b is further analysed in Figure 4.12 where the maximum reachable modal damping along the longitudinal axis of the beam is plotted. The curve has been obtained by extensively computing, for each possible SA position, the maximum reachable damping that can be obtained, i.e. by tuning the gain to its optimal value. Additionally, the starting positions obtained with the PZ and the Gramian criteria are highlighted, as well as the optimal locations that result from the three different optimization approaches. As it can be observed, the Gramian and the GA methods precisely reach the global optimum while the PZ distance criterion converges towards a local optimum. Nevertheless, the global optimum locates right next to an area where a pole-zero cancellation occurs, reducing consequently the overall controllability and the achievable damping in case of misplacement. This clearly explains the poor misplacement robustness of the optimal solutions obtained with the Gramian and the GA methods that were observed in Figure 4.11.

Interestingly, the positions that stand in the vicinity of such sudden controllability loss are directly rejected by the PZ distance criterion. The third term that analyses the dynamics of the adjacent mode avoids indeed a possible pole-zero cancellation, as illustrated by Figure 3.4. Consequently, although the damping values obtained with the proposed approach are slightly below the two other methods, they present high robustness to misplacement while ensuring good performance because of the valuable information contained within the criterion. In addition and as discussed, the number of evaluations to reach convergence for the PZ/direct search approach is significantly reduced compared to the commonly used GA, which validates therefore the proposed method by confirming again its effectiveness.

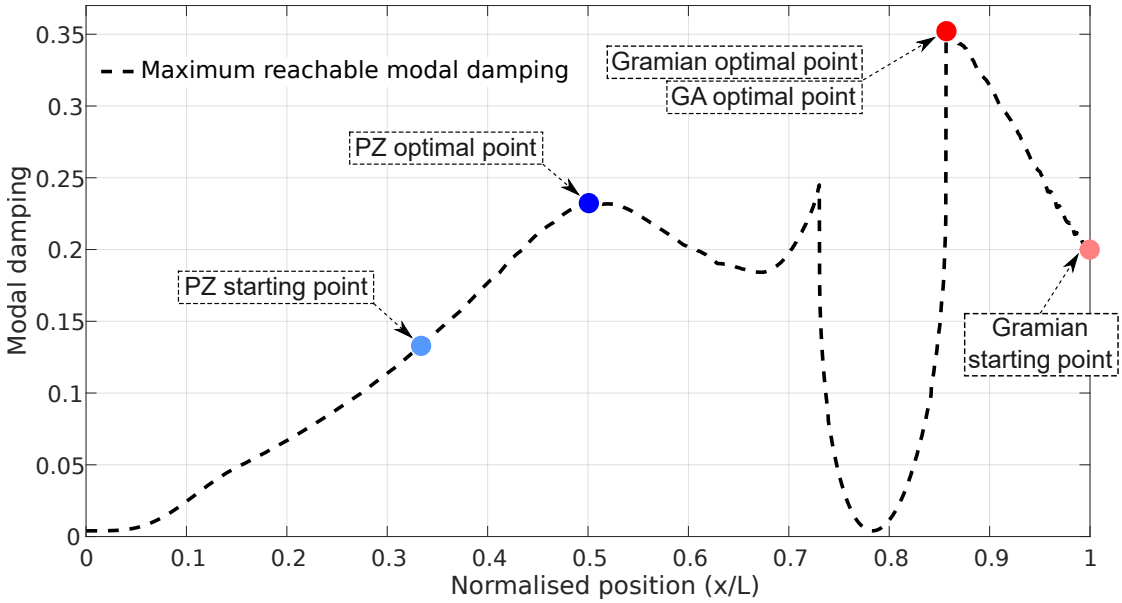

Figure 4.12: Maximum reachable modal damping along the longitudinal axis of the cantilever beam for the second bending mode.

4.4 Conclusion

Search algorithms are widely used when dealing with optimal transducer placements. No matter which optimal placement criterion is selected, it is not feasible to evaluate all the possible positions on the structure. Such a full analysis can be prohibitive when the evaluation of the criterion is expensive in terms of computational time and/or when too many combinations are possible.

The GAs have been intensively employed for the optimal placement studies for three main reasons: (1) they are appropriate to apply in situations where non-prior knowledge is required, (2) they can solve linear and non-linear problems and (3) they can find the global optimum despite the presence of multiple local ones. Nevertheless, their usage comes at the expense of a major drawback: extremely long computational time to reach convergence.

A non-evolutionary search algorithm, such as the gradient descent method or the direct search approach, could substantially reduce the overall computational cost of the optimization. Yet, the use of such algorithms is not a convenient alternative because they necessitate a starting point to initiate the converge process, and the optimal solution highly depends on the choice of this starting value.

To address this challenge, the current chapter introduced a novel approach based on the PZ distance criterion. The method consists of evaluating the PZ distance criterion on a limited number of positions such that the one that maximises the criterion is used as the starting point for a non-evolutionary algorithm. This method offers numerous advantages: (1) the PZ criterion is evaluated in open-loop (reduced the processing time), (2) only a limited number of positions is required to provide an accurate trend, (3) the position that maximises the PZ criterion is associated with an area of high damping (ensuring the effectiveness of the starting point), and (4) non-evolutionary algorithms require substantially fewer evaluations before reaching convergence compared to the GAs.

A numerical validation has been conducted by considering a collocated SA pair on a cantilever beam. In order to demonstrate the validity of the proposed approach, another open-loop criterion (the Gramian controllability) and the direct closed-loop convergence of a GA have been included in the study. It has been shown that for the considered cases, the proposed method decreases the required number of evaluations up to a factor of 23 with respect to the commonly used genetic search algorithm. Moreover, despite the slightly lower damping values obtained with the proposed approach, it is shown that the optimal solutions present a strong robustness with respect to transducer misplacement, unlike the solutions obtained with all the other tested methods.

The high effectiveness of the proposed approach and the weak sensitivity to transducer misplacement of the related solutions make it a suitable choice for optimal placement studies, especially for large and/or complex systems. Hence, the next chapter is dedicated to the implementation of the proposed method to two industrial structures.

References

[1] A. Sadri, J. Wright, and R. Wynne. "Modelling and optimal placement of piezoelectric actuators in isotropic plates using genetic algorithms". In: *Smart Materials and Structures* 8 (1999), pp. 490–498. DOI: 10.1088/0964-1726/8/4/306.

[2] K. Dhuri and P. Seshu. "Multi-objective optimization of piezo actuator placement and sizing using genetic algorithm". In: *Journal of sound and vibration* 323.3-5 (2009), pp. 495–514. DOI: 10.1016/j.jsv.2009.01.007.

[3] F. Peng, A. Ng, and Y.-R. Hu. "Actuator Placement Optimization and Adaptive Vibration Control of Plate Smart Structures". In: *Journal of Intelligent Material Systems and Structures* 16.3 (2005), pp. 263–271. DOI: 10.1177/1045389X05050105.

[4] C. He, J. Xing, J. Li, Q. Yang, R. Wang, and X. Zhang. "A new optimal sensor placement strategy based on modified modal assurance criterion and improved adaptive genetic algorithm for structural health monitoring". In: *Mathematical Problems in Engineering* 2015 (2015). DOI: 10.1155/2015/626342.

[5] A. Daraji and J. Hale. "Reduction of structural weight, costs and complexity of a control system in the active vibration reduction of flexible structures". In: *Smart Materials and Structures* 23.9 (2014), p. 095013. DOI: 10.1088/0964-1726/23/9/095013.

[6] W. Li and H. Huang. "Integrated optimization of actuator placement and vibration control for piezoelectric adaptive trusses". In: *Journal of Sound and Vibration* 332.1 (2013), pp. 17–32. DOI: 10.1016/j.jsv.2012.08.005.

[7] K. Bendine, F. Boukhoulda, and M. Haddag B. andNouari. "Active vibration control of composite plate with optimal placement of piezoelectric patches". In: *Mechanics of Advanced Materials and Structures* 26.4 (2017), pp. 341–349. DOI: 10.1080/15376494.2017.1387324.

[8] V. Pan. "Complexity of computations with matrices and polynomials". In: *SIAM review* 34.2 (1992), pp. 225–262.

[9] E. K. Chong and S. H. Zak. *An introduction to optimization*. Fourth Edition. John Wiley & Sons, 2013.

[10] C. Audet and W. Hare. *Derivative-Free and Blackbox Optimization*. First Edition. Springer Series in Operations Research and Financial Engineering. Springer Nature, 2017.

[11] M. Mitchell. *An Introduction to Genetic Algorithms*. MIT Press, 1998.

[12] J. A. Snyman and D. N. Wilke. *Practical Mathematical Optimization - Basic Optimization Theory and Gradient Based Algorithms*. Second Edition. Springer, 2018.

[13] S. Boyd and L. Vandenberghe. *Convex Optimization*. Cambridge University Press, 2004.

[14] M. Soubeyroux, C. Dumoulin, and A. Deraemaeker. "Optimization of tuned mass damper parameters based on numerical optimization and model reduction". In: Katholieke Universiteit Leuven Leuven, Belgium, 2018, pp. 201–251.

[15] W. Feng-Quan, H. Xiao-Ling, and G. Ying-Zheng. "Analysis of the Characteristics of Pseudo-Resonance and Anti-Resonance". In: *Journal of Vibration and Acoustics* 118.4 (1996), pp. 663–667. DOI: 10.1115/1.2888349.

[16] T. Williams. "Constrained modes in control theory: Transmission zeros of uniform beams". In: *Journal of Sound and Vibration* 156.1 (1992), pp. 170–177. DOI: 10.1016/0022-460X(92)90819-J.

[17] S. S. Rao. *Vibration of continuous systems*. John Wiley & Sons, 2019.

[18] E. Balmes. *Structural Dynamics Toolbox 7.3 (for use with MATLAB)*. 1991. URL: https://www.sdtools.com.

[19] A. Preumont. *Vibration Control of Active Structure, An Introduction*. Thrid Edition. Springer, 2011. DOI: 10.1007/978-94-007-2033-6.

[20] D. Miu. "Physical Interpretation of Transfer Function Zeros for Simple Control Systems with Mechanical Flexibilities". In: *Journal of Dynamic Systems, Measurement, and Control* 113.3 (1991), pp. 419–424. DOI: 10.1115/1.2896426.

[21] A. Hac and L. Liu. "Sensor And Actuator Location In Motion Control Of Flexible Structures". In: *Journal of Sound and Vibration* 167.2 (1992), pp. 239–261. DOI: 10.1006/jsvi.1993.1333.

[22] J. C. Lagarias, J. A. Reeds, M. H. Wright, and P. E. Wright. "Convergence properties of the Nelder–Mead simplex method in low dimensions". In: *SIAM Journal on optimization* 9.1 (1998), pp. 112–147. DOI: 10.1137/S1052623496303470.

Chapter 5

Application of the optimization method to industrial structures

Abstract

The purpose of this chapter is to apply the optimal PZ distance criterion approach that has been proposed in the previous chapters to industrial structures. Two numerical systems are considered: the wing of a Boeing 777-200ER and a stiff wafer gripper. The optimal transducer placement for the wing consists of a single collocated force actuator/displacement sensor while the gripper focuses on two collocated pairs of piezoelectric patches. The different numerical analyses demonstrated that the proposed methodology delivers superior performance outcomes, especially when compared to conventional modal amplitude approach. Furthermore, a limited number of evaluations is guaranteed to obtain the optimal solution. Combined with its straightforward implementation, the PZ distance approach is consequently well suited to industrial framework where the imperatives of performance enhancement are anchored in a context of limited complexity and limited processing time. Finally, it is shown that matching a model and its experimental response can be challenging, which reinforces the need for robustness for the optimal transducer positions. Specific methods for model matching are subsequently discussed to reduce possible deviations and enhance the reliability of FE models.

5.1 Introduction

In addition to the proper selection of the placement criterion, the appropriate selection and implementation of a search algorithm is a critical factor for obtaining the adequate optimal solution in a reasonable amount of time. The importance of the search algorithm has been studied and discussed in Chapter 4. While GAs have been extensively employed for this purpose, they commonly require a tremendous number of evaluations before reaching convergence, which poses efficiency challenges when dealing with large and/or complex industrial systems.

In light of this, an alternative approach has been proposed, which combines the PZ distance criterion introduced in Chapter 3 with a non-evolutionary algorithm. This method offers numerous advantages in terms of performance and computational cost, as demonstrated by the numerical validation performed in Section 4.3.

Although this new method enables to perform optimizations on complex and/or large systems, its numerical validation has only been performed on a cantilever beam so far. The

use of such a simple system has permitted to conduct a detailed analysis, including the implementation of a GA and various performance analysis studies. Implementing a GA on a larger system would have required a tremendous number of evaluations, as more than 800 have already been required for the cantilever beam (see Figure 4.7 for detailed results).

The goal of this chapter is consequently to numerically assess the proposed placement optimization strategy on two industrial structures. Section 5.2 studies its approach on the wing of a Boeing 777-200ER while Section 5.3 focusses on a wafer gripper from ASML, a Dutch company specialised in the development and manufacturing of photolithography machines used to produce computer chips [1]. The optimal placement of the first structure consists of a single collocated force actuator/displacement sensor pair while the second one targets two collocated pairs of piezoelectric patches. Because of the complexity of the two systems, no comparison with a GA is carried out. Yet, another widely used open-loop criterion, the Gramian controllability, is implemented for the wing in order to enable a comparative analysis. As the proposed method is based on the use of a numerical model to achieve the optimization, Section 5.4 analyses the reliability of the models and discusses the robustness of the different solutions. Finally, conclusions are drawn in Section 5.5.

5.2 Wing of a Boeing 777-200ER

The Boeing 777-200ER was first delivered to the British Airways airline company in 1997. With a maximum cruising speed of 920 km/h, a length of 63.7 m and a wingspan of 60.9 m [2], the 200ER revision was conceived to increase the volume of available fuel from the original Boeing 777 and grant transoceanic connections [3]. In 2018, 338 units were in service all around the world [4]. Figure 5.1 shows a 777-200ER from the Swiss International Air Lines company which is taking off.

Figure 5.1: Picture of a Boeing 777-200ER that proceeds to its take-off [5].

The wings are critical components of commercial airliners. They serve multiple purposes, such as mounting the engines and other important components. They are also lift generators based on their shapes, or stability and control devices through their different control surfaces (flaps, spoilers and ailerons). Additionally, the wings undergo multiple effects of disturbances and turbulences during a flight. Because of their high importance, they are continuously monitored to ensure the efficiency of the flight, as well as the safety of the passengers.

The large wingspan of the Boeing 777-200ER and the flexible nature of an aircraft wing favour its sensitivity to vibrations. Dampers are consequently mounted to mitigate the vibration effects, aiming to enhance the comfort of the passengers and to ensure the structural integrity of the system. The objective of this section is to conduct a numerical analysis to determine the ideal placement of a collocated force actuator/displacement sensor pair for an active control architecture. The aim of such an active system would be to increase the overall damping of the wing.

Besides the inherent difficulties of deploying this extra control architecture on an aircraft wing (e.g. increase of the drag, increase of the air resistance, additional components and wiring required), the primary mechanisms to mitigate the disturbances during flights are performed by the active control systems already implemented within the control surfaces, or by the pilot. Nevertheless, this case study permits the application of the optimization approach introduced in Chapter 4 to an industrial structure which (i) is large and (ii) presents a more complex 3D shape compared to the ones that were previously studied.

5.2.1 Description of the model

The proposed method, as illustrated in Figure 4.4, is based on the computation of the PZ distance criterion (Equation 4.2) at a limited number of positions. The SA location that maximizes the criterion is then used as the starting value for a non-evolutionary algorithm to converge towards the local optimum. A model of the system is consequently needed to (i) evaluate the PZ distance at the selected positions and (ii) evaluate the closed-loop performance at each iteration of the search algorithm (i.e. for a specific position and specific control parameters).

The construction of the model can be performed by experimental identifications or by designing a FE representation based on the available knowledge. The use of an experimentally extracted model is not conceivable because, in addition to the questionable public availability of such data, it would require considerable effort to extract a model on this type of structure. Indeed, the SA position has a direct impact on the dynamics of the system and, more specifically, on the zero values. As a result, the model would require a significant number of tested positions, making it impractical to empirically extract the dynamics at each of those positions.

Because the procurement of a FE model is recommended for the considered system, the NASA Common Research Model (CRM) has been considered. The CRM is a platform created in 2008 that enables worldwide researchers to study the different aspects of aircraft design, including aerodynamics, acoustics, propulsion and structural analysis [6]. It contains various FE systems, including a full-scale wingbox structure (i.e. the primary load-carrying structures of the wing) of the considered Boeing 777-200ER. The *CRM_V12wingbox* model [1], in its coarse version, has been selected for the study. The model contains spars (i.e. the main structural members of the wing) and skin elements, as well as ribs, stringers and stiffeners. Natively provided in the *.bdf* Nastran format (a FE analysis software developed by the NASA and released for the public in 1971), the FEMLink toolbox of SDT [7] has been employed to switch into a Matlab-based model. Additionally, a transformation from the imperial units to the metric ones has been performed.

[1] Downloaded from the CRM platform at the address: `https://commonresearchmodel.larc.nasa.gov/fem-file/wingbox-fem-files/` (last accessed: December 2022)

The numerical model is built with 6687 nodes that are located in 3D. Quadrangular 4-node and triangular 3-node elements are both used, depending on the local topology of the wing. Additionally, a total of 17 thickness values are employed to ensure consistent modelling between the different parts and elements of the structure. The material consists of an isotropic lightly damped aluminium, with the following properties: Young's modulus $E = 69\ GPa$, shear modulus $G = 26.2\ GPa$, Poisson's ratio $\nu = 0.32$, mass density $\rho = 2768\ kg/m^3$ and modal damping ratio $\xi = 0.004$. Finally, all the nodes that present a zero y coordinate are fully constrained to simulate a cantilevered boundary condition of the wing. A 3D illustration of the numerical FE model as well as the Cartesian coordinates are shown in Figure 5.2.

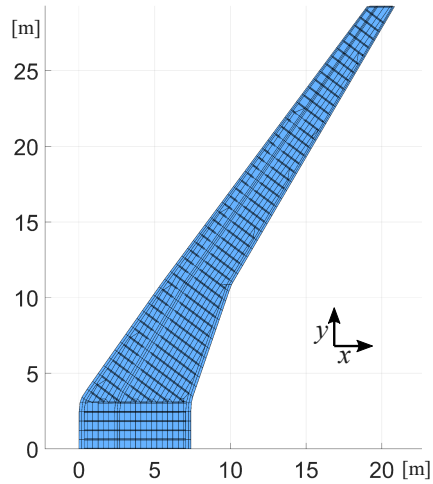

(a) Top view (xy plane)

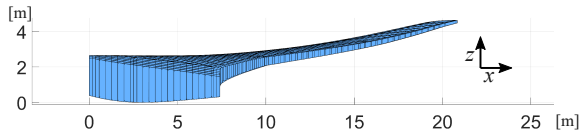

(b) Side view (xz plane)

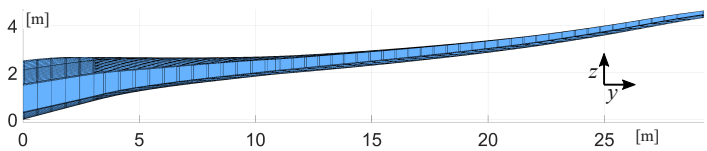

(c) Side view (yz plane)

Figure 5.2: Illustration of the numerical wing of the Boeing 777-200ER used to validate the proposed approach from the: (a) top view (xy plane), (b) side view (xz plane), (c) side view (yz plane).

Before conducting the optimization study, a preliminary modal analysis can be executed on the FE model to analyse the behaviour of the structure. The validity of the model is indeed an interesting aspect to question because the proposed optimization method completely relies on it. The results obtained with the mode shape calculation tool of SDT are provided in Table 5.1, where the first four resonance frequencies and the type of each related mode shape are given. Additionally, the visualization of the mode shapes is provided in Figure 5.3.

Table 5.1: First four natural frequencies of the Boeing 777-200ER wing and the type of each related mode shape.

	Mode 1	Mode 2	Mode 3	Mode 4
Natural frequency (rad/s)	13.0	36.4	55.5	74.2
Type of the mode shape	Bending	Bending	Torsion	Bending

A direct validation of the numerical results shown in Table 5.1 with respect to real-life measurements poses challenges, primarily due to the unavailability of relevant data. Additionally, even if some data are accessible, the presence of engines in real systems significantly alters the dynamical behaviour of the wing due to the addition of local masses, complicating even further a possible accurate comparison. Yet, the validity of the selected model is supported by two considerations. Firstly, the topology, discretization and material properties of the FE model are derived from the CRM, a reliable platform established by NASA and widely employed by researchers worldwide. Secondly, a comparison of the obtained results with other numerical studies reveals a clear match between the type of the mode shapes and their resonance frequencies. For example, the *Transport airliner T4* presented in [8], which exhibits similar parameters for its wings, shows the same dynamical behaviour. The resonance frequencies are indeed in the same range and the same type of related mode shapes can be observed. This is particularly valuable considering that the simulation relies on a different approach (the dynamic stiffness method) and the model of the wing is built with an assembly of uniform dynamic stiffness elements. Based on those observations, the model can be considered valid for conducting the intended optimisation. Nevertheless, Section 5.4 can be referred to for a more comprehensive analysis on the reliability of FE models.

(a) Mode 1 (Bending)

(b) Mode 2 (Bending)

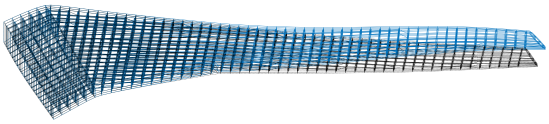

(c) Mode 3 (Torsion)

(d) Mode 4 (Bending)

Figure 5.3: First four mode shapes of the Boeing 777-200ER wing: (a) mode 1 (bending), (b) mode 2 (bending), (3) mode 3 (torsion), (d) mode 4 (bending).

5.2.2 Application of the optimization method

Different cases are investigated for the optimization: the maximization of single-mode damping (mode 1, mode 2 and mode 3) and multi-modal damping (modes 1 & 2). As mentioned, a single force actuator/displacement sensor is considered as the collocated SISO pair. To ensure consistency, only the nodes that are located at the skin of the wing (i.e. its outer surface) are retained as possible SA positions, leading to a total of 1353 potential locations in the 3D space. For the sake of simplicity, actuation and sensing are defined in the z direction only, which provides the highest authority of the targeted modes based on a performed preliminary mode shape analysis.

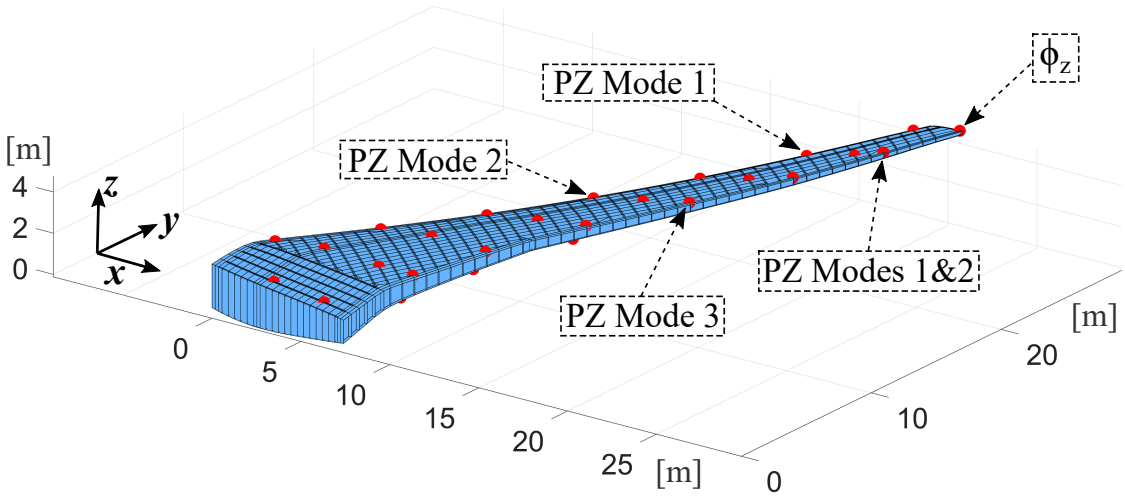

Figure 5.4: Limited positions to be evaluated by the PZ distance criterion (red dots) and positions that maximize it for the considered cases. The position that maximizes the modal amplitude is highlighted as well by the ϕ_z indicator.

As the model of the structure is available and validated, the subsequent step involves determining the limited number of positions to be evaluated by the PZ criterion (see Figure 4.4 for the complete flowchart of the proposed approach). Because the structure presents a complex 3D shape, it becomes challenging to analytically express the wavelength of the modes in the three different directions, similarly to what has been done for the cantilever beam in Section 4.3. A regular grid pattern is consequently considered where, based on the initial mode shape analysis, a density of 8 positions in both x and y directions is chosen. Regarding the z direction, the upper and lower surfaces of the wing can be retained, leading to a total of 128 candidates. Given the diagonal orientation of the wing in the xy plane (see Figure 5.2a), the 128 candidates need to be filtered out such that all the positions outside of the wing topology are discarded. Furthermore, each intended position that lies within the geometrical boundaries needs to be calibrated to the nearest mesh node, since no re-meshing is considered for this study. A final number of 35 limited positions is consequently obtained, which corresponds to only 2.6% of the possible placement candidates. Their locations on the wing are highlighted in Figure 5.4 by red dots. To evaluate the PZ distance criterion at those 35 limited positions, the control law requires to be selected such that the appropriate PZ distance can be defined. A lead control law described as follows is consequently considered:

$$C(s) = g\,\frac{s + z_c}{s + p_c} \tag{5.1}$$

where the zero z_c and the pole p_c only depend on the targeted mode as follows: $z_c = \omega_i/2$

and $p_c = \omega_j \times 2$ where ω_i is the angular frequency of the smallest targeted mode and ω_j is the highest one. Although of limited authority due to the narrow frequency band used, the choice of these parameters allows to restrain the variability of the controller to its gain value, and ensures a comprehensive comparison between different positions when considering a specific modal case. The selection of the control law allows to properly define the PZ distance: because the pole of the closed-loop system appears at a lower frequency than the zero when applying a lead controller, the PZ distance is computed by subtracting the pole from its corresponding zero [9]. The general PZ distance criterion expressed by Equation 4.2 can consequently be defined as follows:

$$J(\{\mathbf{x}\}) = \left(\frac{1}{n}\sum_{k=1}^{n}\frac{z_k(\{\mathbf{x}\})-\omega_k}{max(z_k(\{\mathbf{x}\})-\omega_k)}\right) \times \left(\sqrt[n]{\prod_{k=1}^{n}\frac{z_k(\{\mathbf{x}\})-\omega_k}{max(z_k(\{\mathbf{x}\})-\omega_k)}}\right) \times \left(\sqrt[n]{\prod_{k=1}^{n}\frac{\omega_k-z_{k-1}(\{\mathbf{x}\})}{max(\omega_k-z_{k-1}(\{\mathbf{x}\}))}}\right) \tag{5.2}$$

where $\{\mathbf{x}\} = \{x, y, z\}$ contains the complete coordinates of the considered position and k contains the targeted mode(s) to damp. The evaluation of the criterion starts with the computation of the zeros at the studied positions $\{\mathbf{x}\}$. The selected methodology is based on the identification of the frequencies for which the rank of the system drops using the algorithm that was firstly introduced in [10]. Based on the computed zero values, the PZ distances can be obtained and the criterion evaluated. The positions that maximize the PZ distance criterion for the different cases are highlighted in Figure 5.4. Interestingly, each modal case presents a distinct position. Following the proposed optimization method, those different positions are defined as starting values for a non-evolutionary algorithm. Similarly to what has been done in Section 4.3.1, the *'fminsearch'* function from Matlab that relies on a direct search algorithm is used for the convergence. A comprehensive description of its method is provided in Appendix B, where the optimization parameters are given as well.

For the sake of completeness, the positions that maximize the modal amplitudes are analysed as well. The modal amplitude corresponds indeed to the principal factor taken into account for optimal transducer placement in open-loop configuration. Hence, its analysis enables a second optimization to be carried out by the direct search algorithm and a consistent comparison of the two approaches. It should be noted that a comparison based on a GA is not conceivable because the wing presents a shape that is both too large and too complex, which would require an excessive number of evaluations. Nevertheless, a comprehensive study with such a GA is available in Section 4.3.

The position that maximizes the modal amplitude value is always located at the same node, for all the considered cases. This position corresponds to the tip of the wing, as shown in Figure 5.4 with the Φ_z indicator where the subscript $_z$ informs that the modal amplitude is considered in the z direction. The tip is therefore defined as the starting position for the different modal cases when performing the optimization method based on the direct search algorithm. The selection of the initial gain value for each modal case and the two optimization methods is performed by following the same approach described in Chapter 4. It consists of using the *rlocus* Matlab function that allows to easily find the gain value that maximizes the damping with only one closed-loop evaluation of the system. Starting from the initial values, the *'fminsearch'* algorithm performs the optimization in closed-loop configuration with a total of 4 parameters (the positions x, y and z, and the

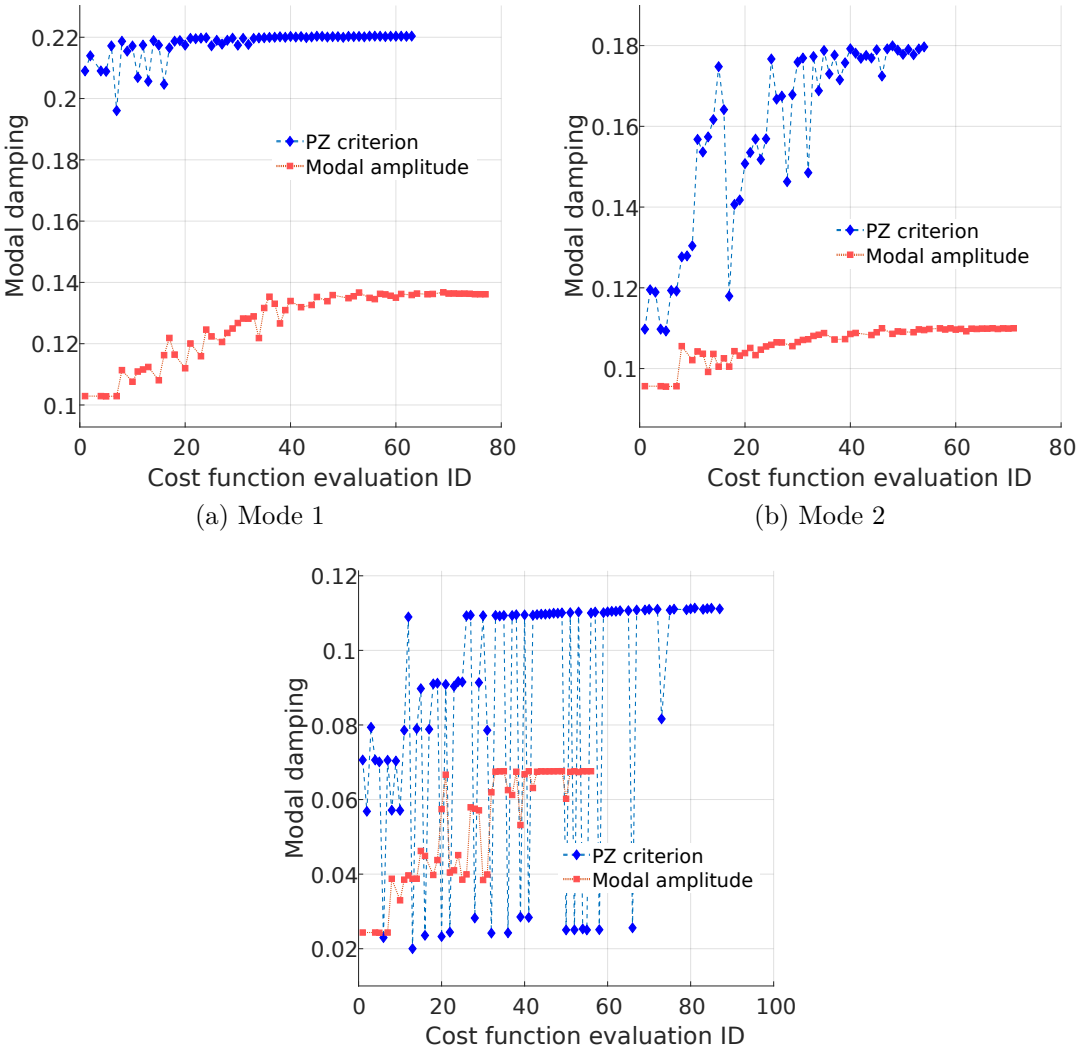

(a) Mode 1

(b) Mode 2

(c) Mode 3

Figure 5.5: Comparison of the damping convergences obtained with the PZ distance criterion and the modal amplitude on the Boeing 777-200ER wing for: (a) mode 1, (b) mode 2, (c) mode 3.

gain value g), where the objective is to maximize the cost function $\tilde{J}$ defined as follows:

$$\tilde{J}(\{\mathbf{x}\}, g) = \left(\sum_k \xi_k(\{\mathbf{x}\}, g)\right) \times \left(\sqrt{\prod_k \xi_k(\{\mathbf{x}\}, g)}\right) \tag{5.3}$$

where ξ is the closed-loop modal damping evaluated by computing the closed-loop complex eigenvalues and k contains all the considered modes. Because the *'fminsearch'* function can only handle continuous values of the design variables g and $\{\mathbf{x}\}$, a discretization of the positions is performed at each evaluation of the cost function. This discretization avoids any re-meshing of the system during convergence and ensures that the provided continuous positions obtained from the search algorithm matches the closest node of the FE model.

The convergence processes, for the single-modal damping cases, are shown in Figure 5.5. For each considered case, the evolution of the damping values obtained with the two methods is plotted on the same sub-figure, which offers a clear graphical comparison. Interestingly, the number of evaluations required to reach convergence remains consistently low for both approaches. This is particularly noteworthy considering that the optimization

process involves four parameters, which adds complexity to the optimization. This first observation confirms the efficiency of utilizing the *'fminsearch'* method as direct search algorithm for optimal transducer placement.

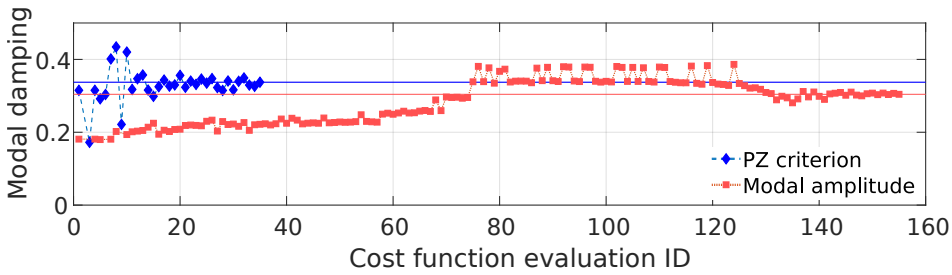

(a) Mode 1

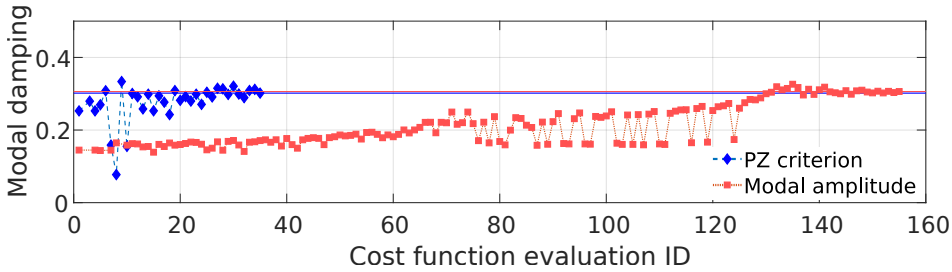

(b) Mode 2

Figure 5.6: Comparison of the convergence for multi-modal damping obtained with the PZ distance criterion and the modal amplitude on the Boeing 777-200ER wing for: (a) mode 1, (b) mode 2.

In addition to the fast convergence of the direct search algorithm, the appropriate selection of its starting value(s) is essential to obtain efficient final results, i.e. a solution that is approaching the performance of the global optimum. The PZ distance criterion emerges as a suitable approach because, as depicted in Figure 5.5, it consistently yields higher damping values compared to the modal amplitude approach. The modal amplitude is indeed not intended to be evaluated at a few possible locations only, nor expected to deliver high performance while, conversely, the PZ distance does. The results obtained for the multi-modal damping case of modes 1 & 2 reinforce this analysis, as shown in Figure 5.6 where each sub-figure corresponds to one mode. The PZ criterion approach results in starting damping values close to the maximum ones obtained after convergence. Hence, this validates that the PZ distance criterion allows to target an area with large modal damping for the two considered modes. Conversely, the modal amplitude approach generates starting positions characterized by lower damping values. It results in substantially extended convergence effort to reach the optimal solution, necessitating more than four times the number of evaluations compared to the PZ method.

The convergence obtained for the first mode based on the PZ distance criterion approach is further analysed in Figure 5.7, where the evolution of the gain value g as well as the x, y and z positions of the SA pair are shown for each evaluation of the cost function. The figure clearly stresses the challenge associated with simultaneously optimizing multiple parameters. This is particularly clear when the calibrated position (i.e. the position that is calibrated to the nearest mesh node) remains unchanged over several evaluations while the algorithm considers a change in its value. Such a situation introduces additional complexities for the algorithm to accurately measure the different sensitivities of the pa-

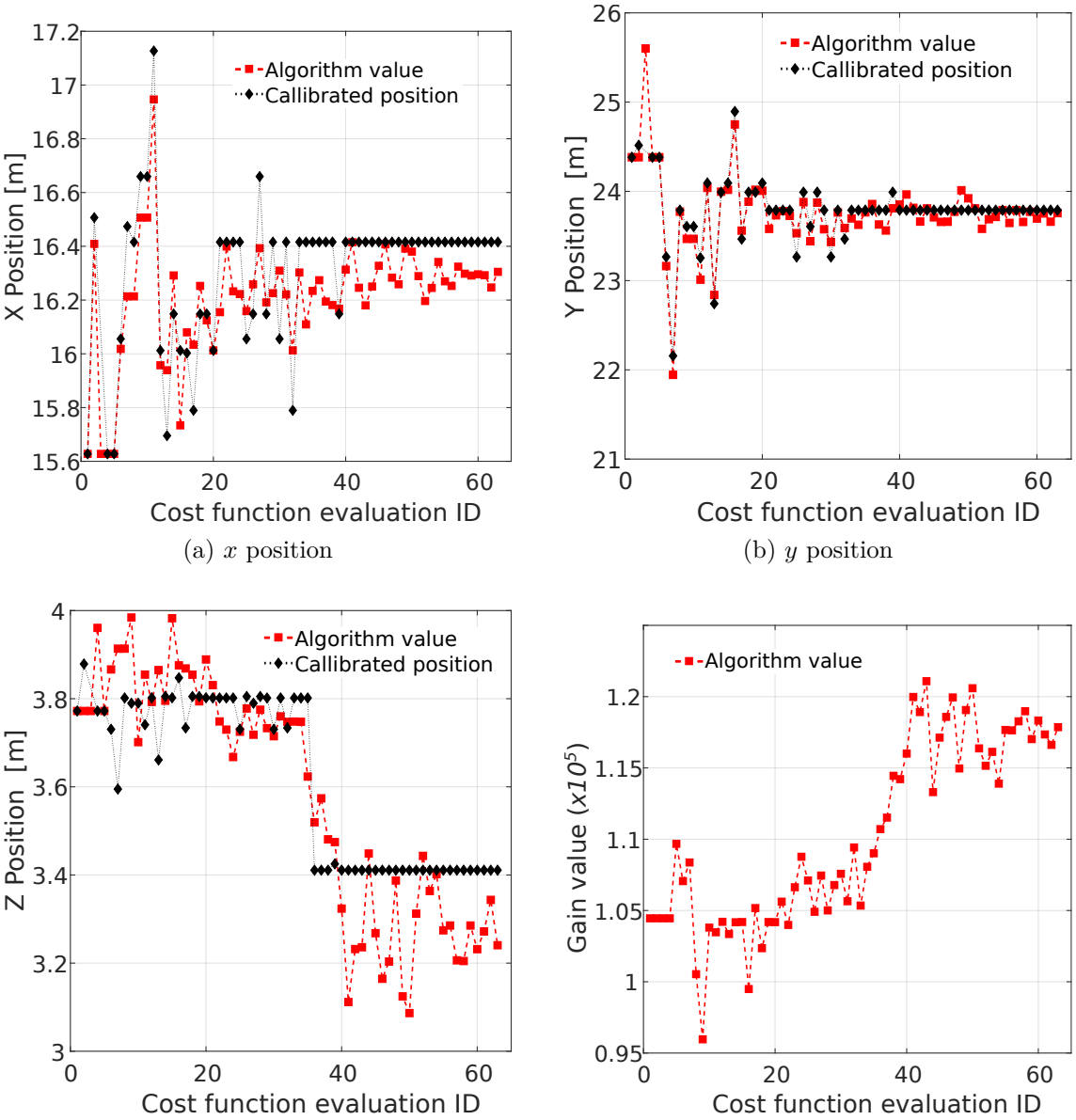

(a) x position (b) y position

(c) z position (d) Gain value

Figure 5.7: Convergence of the *'fminsearch'* algorithm for the first mode of the wing for: (a) the x position, (b) the y position, (c) the z position, (d) the gain value.

rameters. Despite this hard challenge, Figure 5.7 highlights the efficiency of using the *'fminsearch'* algorithm when the appropriate starting values are chosen. Given that the PZ distance criterion precisely provides such an effective starting position, the proposed approach can be considered accordingly as a highly efficient method to study the optimal transducer position of large systems that encompass numerous parameters.

When considering industrial structures and real-life applications, a strong robustness to misplacement with respect to the optimal position is of critical importance. The objective of an optimization placement study consists indeed in identifying the most optimal positions for mounting the transducers on the system, based on a numerical simulation. However, due to the inherent complexities and practical challenges, uncertainties during the mounting process are inevitable. To address this crucial concern and assess the optimal solutions, a sensitivity analysis is conducted. This sensitivity analysis to misplacement

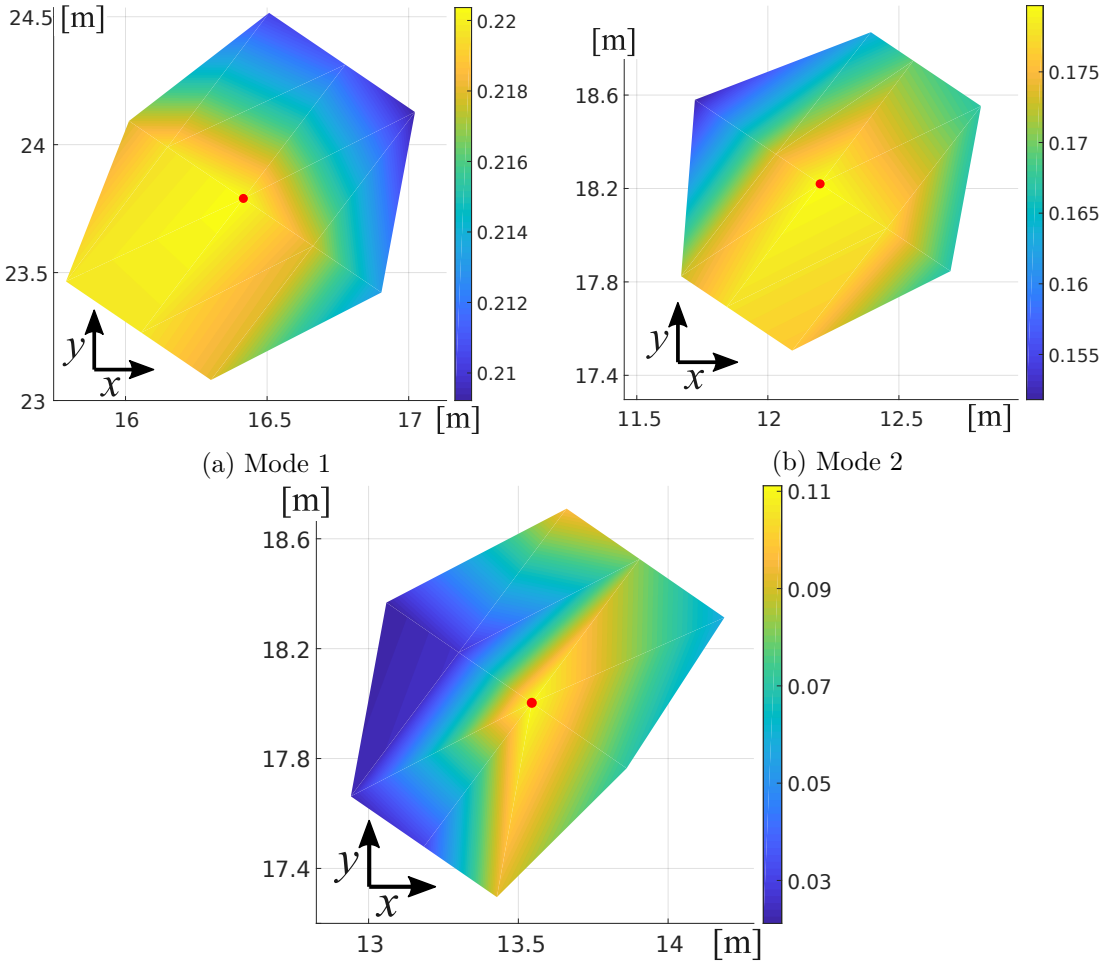

(a) Mode 1

(b) Mode 2

(c) Mode 3

Figure 5.8: Sensitivity analysis of the SA pair misplacement on the Boeing 777-200ER wing where the optimal positions are identified with the red dots and the modification of the damping with respect to the SA misplacement is represented by colour maps for: (a) mode 1, (b) mode 2, (c) mode 3.

is performed as follows: a virtual circle is drawn around each optimal solution obtained with the proposed PZ distance approach. The circle is defined by a radius of 0.5 m and introduces a virtual misplacement surface on the wing that presents 25 points. Those virtual 25 positions are then calibrated to the nearest mesh node such that no re-meshing of the structure is needed. To mimic the conditions of a real-life transducer placement error, the optimal gains as well as the control laws are kept without any changes. The results obtained with the sensitivity analysis can be found in Figure 5.8, where the optimal positions are identified by the red dots and the modifications of the damping ratio induced by the SA misplacement are displayed through colour maps. As it can be seen, the optimal solutions obtained for the first and second modes exhibit remarkable robustness to misplacement. Indeed, even with a 0.5 m misplacement in each direction, only a marginal few percent drop of the damping value is observed. The third mode shows however a substantial reduction of the damping when misplacement occurs. Such decrease in robustness can be attributed to its torsional characteristic, which significantly increases the sensitivity of the SA pair position given its fixed z direction. Nonetheless, this higher sensitivity is effectively mitigated when considering a smaller range of misplacements (i.e. an error of only 0.25 m in each direction), which aligns more realistically with real-life sce-

narios. Consequently, the proposed approach not only demonstrates remarkable efficiency and high performance but also proves strong robustness to misplacement on the studied Boeing wing.

The effect of the control law on the performance of the optimal architecture is an interesting analysis to perform as well. The proposed method relies indeed on a preliminary selection of the controller and focuses on finding the optimal transducer positions and gain value that maximise the damping. Nonetheless, the parameters of the control law also have significant effects on the closed-loop dynamics. All the convergences that have been presented were based on a lead controller expressed by Equation 5.1 and the following parameters: $z_c = \omega_i/2$ and $p_c = \omega_j \times 2$, where ω_i is the angular frequency of the smallest targeted mode and ω_j is the highest one. In order to study the impact of the control law on the performance, different control laws can be implemented at the optimal positions. Only the first mode and the optimal solutions obtained with the proposed PZ distance criterion are analysed, but similar results can be obtained with higher order modes. Moreover, a lead control law is still considered such that a rational comparison is ensured (i.e. no excessive modification of the dynamics). Two new lead controllers are derived, by modifying the original parameter values as follows: $z_c = \omega_1/4$ and $\omega_c = 4 \times \omega_1$ for the first one, $z_c = \omega_1/6$ and $\omega_c = 6 \times \omega_1$ for the second.

Table 5.2: Modal damping results obtained for the first mode of the wing when the lead control law parameters are tuned at the optimal position derived with the proposed approach.

Parameters of the lead	$z_c = \omega_1/2$ $\omega_c = 2 \times \omega_1$	$z_c = \omega_1/4$ $\omega_c = 4 \times \omega_1$	$z_c = \omega_1/6$ $\omega_c = 6 \times \omega_1$
Modal damping (%)	22.04	53.69	78.76

The maximum modal damping obtained by tuning the gain of each new controller can be found in Table 5.2, where the results from the original control law are displayed as well. As it can be seen, enhancing the authority of the controller by enlarging its bandwidth allows to increase performance. This expected result consequently means that the parameters of the control law could still be tuned to maximise the damping. For example, based on the optimal architecture obtained with the proposed approach, a secondary optimization could be performed on the parameters of the control law only. Nonetheless, running two optimizations consecutively is not efficient. Hence, the aggressiveness of the controller should be directly based on the damping requirement considered when applying the optimization process. This is illustrated by Table 5.3 which compares the outcomes obtained when a more aggressive lead is implemented for the first mode of the wing. As it can be seen, both controllers require roughly the same amount of evaluations to reach convergence. Moreover, the two optimal positions locate within the same area. This observation arises from their identical starting positions but reaffirms as well that the optimal solutions obtained with the proposed approach consistently locate in inherently high performance regions, with low influence from the control law. This outcome can be attributed to the proper starting position obtained by the PZ distance criterion. Interestingly, modifying the control law once the optimization has been done (shown in Table 5.2) or directly using such modified controller for the optimization process (shown in Table 5.3) leads to the same damping results, as it can be seen by comparing the results obtained in both Tables. A similar damping value of 53% can indeed be observed when considering the $z_c = \omega_1/4$ and $\omega_c = 4 \times \omega_1$ controller. It confirms again that the optimal solutions are clearly suitable for a specific type of control law, no matter its level of authority. Only

one optimization based on the proposed method is consequently required and, depending on the obtained performance, a more aggressive control law can be implemented if needed.

Table 5.3: Comparison of the convergence outcomes when two different lead control laws are implemented for the convergence of the first mode of the wing.

Parameters of the lead	$z_c = \omega_1/2$ $\omega_c = 2 \times \omega_1$	$z_c = \omega_1/4$ $\omega_c = 4 \times \omega_1$
Number of evaluations	63	47
Optimal position (m)	(16.42, 23.79, 3.41)	(16.78, 24.31, 3.88)
Modal damping (%)	22.04	53.00

5.2.3 Conclusion

The study that has been performed on the wing of the Boeing 777-200ER provided a practical application of the proposed methodology to a large and complex industrial structure while involving the simultaneous optimization of four parameters. Although an implementation in real life of the optimal active damping systems that have been obtained may not be feasible, the study demonstrated the high efficiency of the proposed method when dealing with such complex structures. Despite its complexity and having four parameters to optimize, the optimal solutions were indeed derived with only a few number of evaluations, highlighting the efficiency of the approach. Furthermore, the obtained solutions exhibited high damping performance and strong resistance to misplacement. Finally, it has been shown that the accurate initial position provided by the PZ distance criterion enables a simple adaptation of the controller authority if the performance needs to be increased.

5.3 Wafer gripper from ASML

Microchips are fundamental components for a large range of technological and digital products. With the current digital transformation that the industry is facing, an efficient and sufficient production of those elements is consequently crucial. The design and production aspects of those microchips are actually turning into geopolitical assets, as demonstrated by the European Chips Act. This act, adopted by the European Union, committed to release public and private investments of more than € 43 billion in this field [11].

The wafer is an important element of a microchip because it serves as the substrate for the different electronic devices built on it, as shown in Figure 5.9a [12]. Composed of a thin slice of semiconductor material (usually silicon), the wafer goes under more than hundreds of steps and involves multiple layers to become a functional microchip. Wafer grippers are consequently required to handle and manipulate the wafers during their manufacturing processes. Although various designs exist, their primary role is to securely and precisely grip and release the wafers. A picture of a model designed by Semiconductor Production Systems is shown in Figure 5.9b [13].

To increase productivity and reduce production costs, significant speeds are reached by the grippers allowing very fast point-to-point displacements. Yet, high levels of accelerations inevitably lead to residual vibrations that need to be addressed to guarantee the high degree of precision required for the considered process (down to an accuracy of 10^{-9} m [1]). Different studies can be found in this particular field, such as [14] where a simple

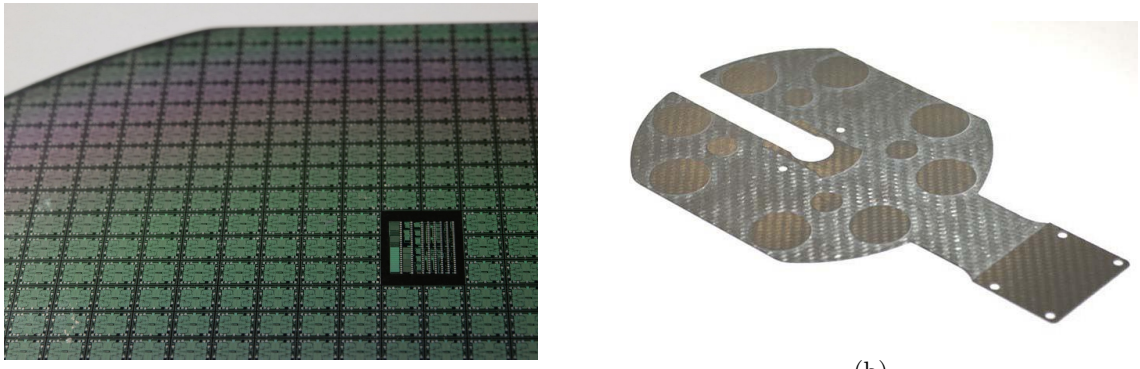

(a) (b)

Figure 5.9: Illustration of: (a) a silicon wafer with engraved transistors and circuits [12], (b) a thin wafer gripper from Semiconductor Production Systems [13].

proportional–integral–derivative controller is applied, or in [15] which is based on the input shaping approach. Additionally, an interesting research is being carried out at the *Department of Precision and Microsystems Engineering*, from TU Delft (The Netherlands), where piezoelectric patches are physically mounted on a gripper from ASML [16]. A picture of the system with the active architecture is shown in Figure 5.10 where the grippers can be identified by the three round metallic shapes and the two piezoelectric actuators are the orange rectangles. Although a modal damping of 3.3% is already achieved on one of the two targeted modes through the use of a PPF on this setup, the objective of getting 5% is not met. Nonetheless, it provides a proof-of-concept on the feasibility of damping highly rigid and thin grippers.

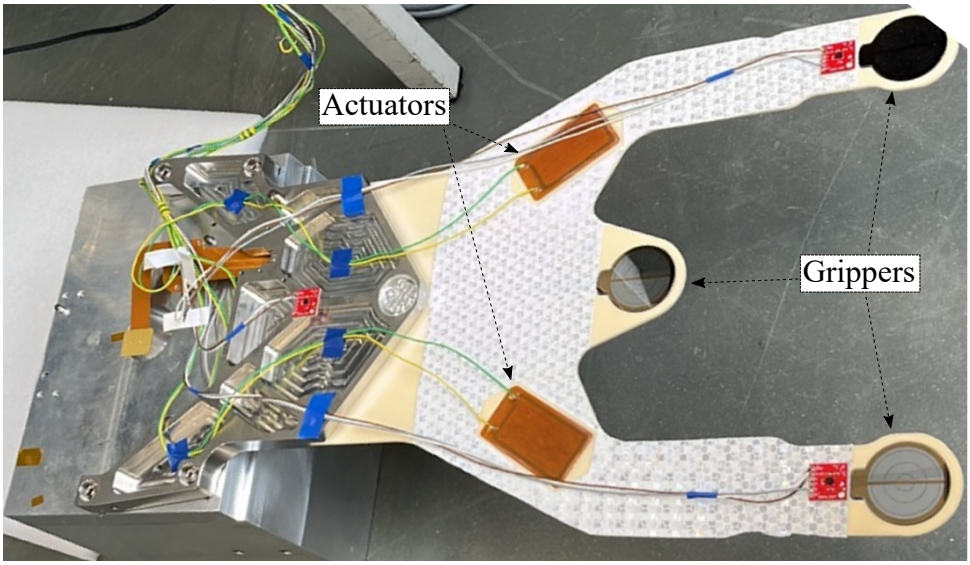

Figure 5.10: Experimental setup of the ASML wafer gripper available at the Department of Precision and Microsystems Engineering [17].

This section aims to enhance the performance obtained in [16] by optimizing the position of the piezoelectric patches. The placement methodology employed in [16] relies indeed on the maximization of the modal amplitude, which provides limited performance as demonstrated throughout this thesis. Consequently, the proposed optimal placement method based on the PZ distance criterion is numerically applied in order to improve the global

damping performance of the system. This study results from the collaboration between the authors of [16], ASML, and the present author. To ensure intellectual property aspects, specific numerical values may be removed or switched to relative figures.

5.3.1 Description of the model

The modal amplitude that has been analysed to find the piezoelectric patch position in [16] has been obtained by experimental measurements with a vibrometer. Although those measurements give valuable information about the structure and its dynamical behaviour, a numerical model is needed to apply the proposed PZ optimization. For this purpose, ASML provided a simplified representation of the gripper's geometry as well as the different properties of the material, a hard aluminium alloy. Based on this geometry, a mesh is generated by *Gmsh* (revision 3.0.6), an open-source 3D FE mesh generator [18]. The obtained mesh is then imported in SDT to build the FE model. As a consequence of this approach, the numerical model relies on a fixed number of nodes and elements. Surely, implementing a re-meshing with respect to the required piezoelectric patch position during the optimization convergence would provide a better accuracy. But performing such dynamic re-meshing would also be a major undertaking. Nonetheless, a high-density mesh (190 elements per cm^2) has been generated with *Gmsh*, allowing the patch to be easily positioned through the mesh without any interconnection issues to ensure accuracy. An illustration of the numerical model of the wafer gripper as well as its high node density and the Cartesian coordinates can be found in Figure 5.11.

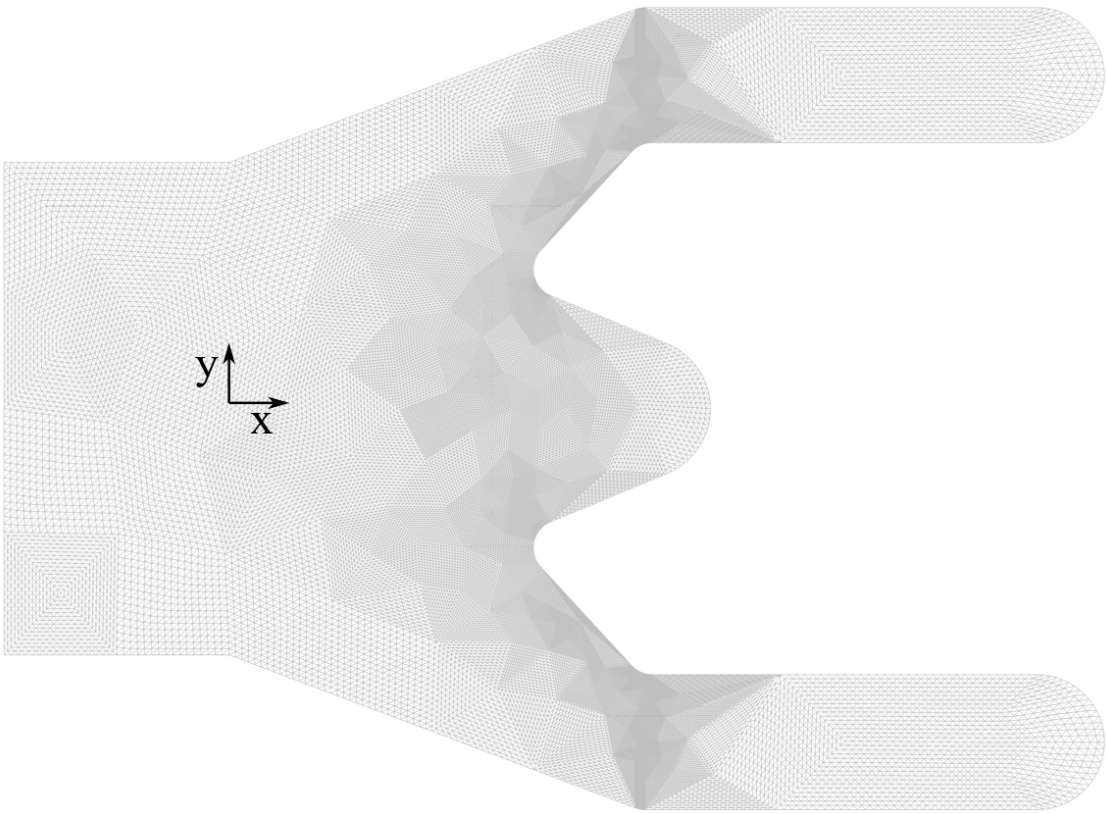

Figure 5.11: Illustration of the numerical ASML wafer gripper model and its high mesh density used to perform the optimal placement optimization based on the PZ methodology.

(a) Mode 1

(b) Mode 2

Figure 5.12: Natural frequencies of the wafer gripper and illustration of their related mode shapes for: (a) mode 1 (bending), (b) mode 2 (torsion).

As it can be seen in Figure 5.10, the experimental structure is attached to a fixed metal block on its left side. This clamp is physically performed by three M4 screws that form a triangular shape. To simulate such boundary conditions, the three nodes that locate at the same positions are restricted with respect to the six DoFs. Similarly to what has been done for the wing of the Boeing 777-200ER in Section 5.2, a preliminary mode shape analysis has been executed with the FE model to examine the dynamical behaviour of the structure. The natural frequencies as well as their related mode shapes can be found in Figure 5.12. Interestingly, each mode shape exactly corresponds to the observations made on the experimental setup in clamping conditions for both their types and frequencies (the relative error for the first and second natural frequencies is 1% and 3%, respectively). This preliminary check confirms the validity of the model and allows to conduct the optimization process.

5.3.2 Application of the optimization method

This optimization aims to improve the damping performance obtained in [16] by finding a potentially better transducer positioning. The same type of active architecture is therefore considered, i.e. two pairs of piezoelectric patches that are symmetrically positioned with respect to the x axis and a PPF control law for the controller. Nevertheless, a minor modification is considered: instead of using two different types of patches for the actuators and the sensors as done in [16], a unique type is selected. This choice aims to reduce the complexity of the optimization as the two previously chosen ones (the *P-876.A15 DuraAct* for the actuators and the *P-876.SP1 DuraAct* for the sensors, both from Physik Instrumente (PI) [19]) present different sizes. An additional numerical implementation would therefore be needed to properly place the sensor with respect to the actuator. Furthermore, the use of different sizes for two collocated patches could induce a loss of the alternating pole-zero property and lead to stability concerns. Hence, the P-876.A15 is selected and the FE model of the patch is built in accordance with its data sheet (piezoelectric material:

PIC255, piezoceramic heigh: 0.5 mm, epoxy layer: 0.15 mm on the top and 0.15 mm on the bottom of the PIC255). To ensure an accurate modelling of the patches, multilayer shell elements are considered for the model (further details can be found in Appendix A).

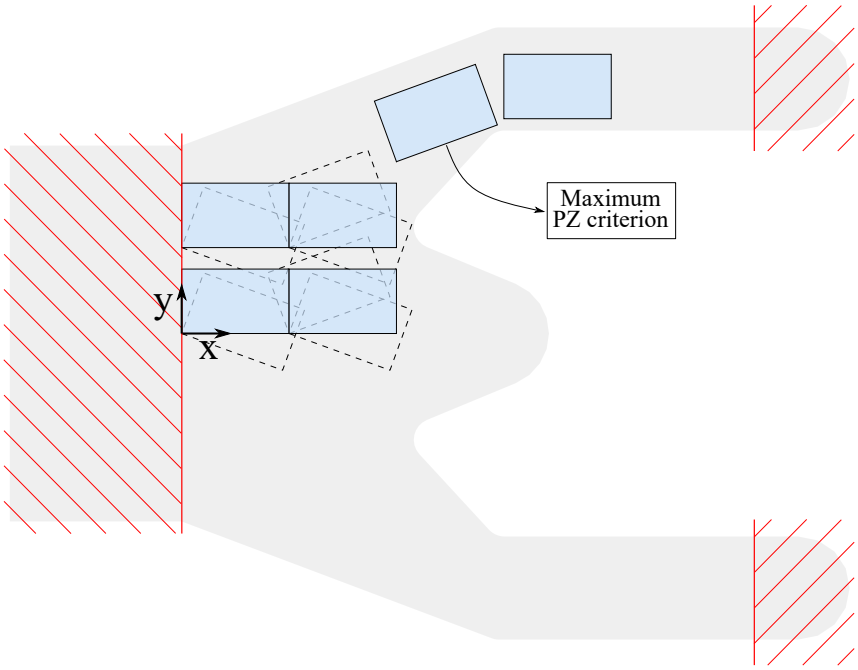

Figure 5.13: Limited configurations to be evaluated by the PZ distance criterion (solid blue and black dashed rectangles) and the restricted areas (red crossed sections). The configuration that maximizes the PZ distance criterion is also highlighted.

The first step of the optimization is to determine the limited number of positions to be evaluated by the PZ criterion. As the transducers are piezoelectric patches, their orientation has a direct impact on the authority and, consequently, on the PZ distance. Hence, different orientations should be tested for each considered position. Moreover, the specific areas that are highlighted by the red crossed sections in Figure 5.13 should not be evaluated by the criterion. Those areas concern all the positions that (1) present a negative x coordinate used for the clamping of the structure and (2) locate where the grippers are placed (i.e. the right-most part of each leg). Finally, because the two pairs of patches are symmetrically positioned, only one symmetrical side of the gripper can be considered to ease the optimization.

Based on those different elements and considering, for each position, a possible angle of +20°, 0°and -20°with respect to the longitudinal axis of the patch and the x-axis, a total of 12 configurations are retained to be evaluated by the criterion. Those 12 configurations are shown in Figure 5.13.

Since the control law is already defined as a first order PPF, the PZ distance criterion can be expressed by the same definition used for the wing in the previous Section, i.e. by Equation 5.2. The PZ distance is indeed obtained by subtracting the pole from its corresponding zero as the pole appears before the zero when using a PPF [9]. The configuration that maximizes the criterion is highlighted in Figure 5.13 and selected as the starting position for the search algorithm. Interestingly, it can be noticed that it is located close to the experimental configuration from [16], as shown in Figure 5.10. The starting gain value is obtained by the *rlocus* method discussed in the previous section, i.e. by

evaluating the closed-loop damping at different gains based on the *rlocus* function from Matlab and extracting the value that maximises it.

In order to reduce the complexity of the optimization process, the closed-loop convergence is performed in a SISO configuration, i.e. by considering only one pair of piezoelectric patches at one side of the gripper. Nonetheless, the closed-loop performance in MIMO configuration will be assessed by adding a second pair of patches that will be symmetrically placed based on the optimal solution. This simplification restricts the optimization in closed-loop to four parameters only: the positions x and y of the patch (considered at its bottom left edge), the angle θ it forms with the x-axis and the gain value g of the first order PPF defined as follows:

$$C(s) = \frac{-g}{s + \omega_c} \tag{5.4}$$

where s is the Laplace variable and ω_c is the pole of the control law. Its value is set to $\omega_c = 1.25 \times \omega_2$ where ω_2 is the second angular frequency of the wafer gripper. This definition has been selected in accordance with the PPF used for the experimental validation conducted in Section 2.3. It follows that the direct search algorithm will maximize the cost function $\tilde{J}$ defined by:

$$\tilde{J}(\{\mathbf{x}\}, \theta, g) = \left(\sum_{k=1,2} \xi_k(\{\mathbf{x}\}, \theta, g) \right) \times \left(\sqrt{\prod_{k=1,2} \xi_k(\{\mathbf{x}\}, \theta, g)} \right) \times F_{\text{stable}}(\{\mathbf{x}\}, \theta, g) \tag{5.5}$$

where $\{\mathbf{x}\} = \{x, y\}$, ξ is the closed-loop modal damping and F_{stable} is the stability flag. As the first order PPF does not ensure unconditional stability, an extra analysis is indeed required during the convergence of the search algorithm to assess the stability of the closed-loop system with respect to the four parameters. If the system is stable, F_{stable} is set to 1 whereas if unstable, it drops to zero, penalising the cost function. Regarding the damping value ξ_k, it is evaluated by computing the closed-loop pole of the system from the state-space system obtained at the specific configuration. Similarly to what has been done for the wing, the *'fminsearch'* function is used. A complete description of the related method and the optimization parameters are provided in Appendix B.

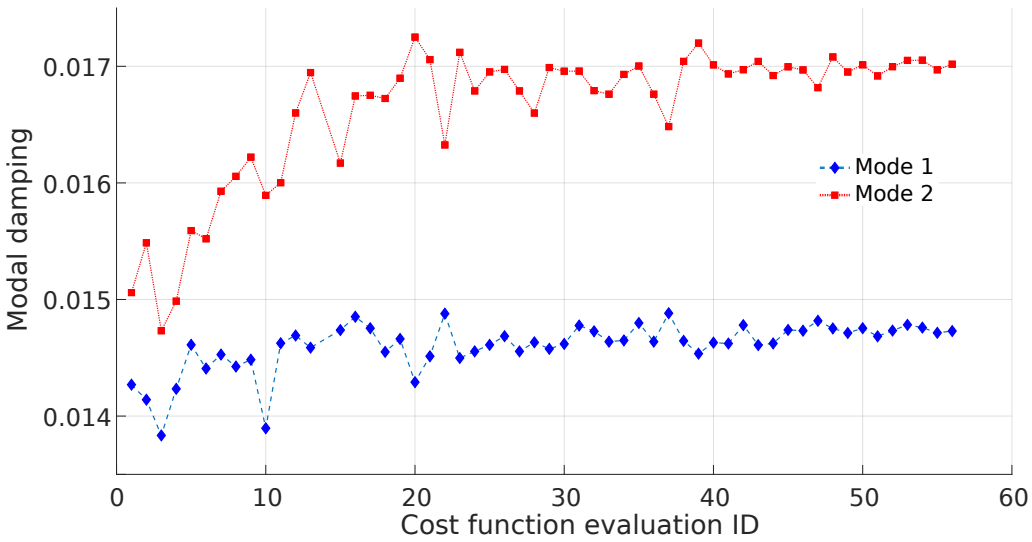

Figure 5.14: Convergence of the *'fminsearch'* algorithm for the multi-modal damping of modes 1 & 2 performed on the ASML wafer gripper model.

The convergence of the *'fminsearch'* algorithm is shown in Figure 5.14. Interestingly, the number of evaluations required to reach convergence remains consistently low despite the optimization of four parameters. Additionally, the PZ distance criterion clearly pointed out a proper starting configuration that already presents a substantial modal damping for the two considered modes. The modal damping of the FE model has indeed been defined to 0.4% , leading to an increase of 256% and 276% for modes 1 and 2 respectively. As a result of the closed-loop optimization, the damping value of the second mode remains stable throughout the convergence while the first one benefits from a 13% improvement. A more detailed analysis of the convergence is available in Figure 5.15 where the evolution of the different parameter values is shown. The physical values (i.e. the x and y positions as well as the angle θ) are expressed by relative figures that are defined by Equation 5.6. The analysis of both Figures 5.14 and 5.15 reinforces the validity of the PZ criterion and its usage as a preliminary check for a non-evolutionary algorithm. This simple optimization method allows indeed to increase the damping up to 325% in this specific case (final damping of 0.01702 for mode 2) without requiring an extreme amount of evaluations despite the inherent complexity of piezoelectric actuation.

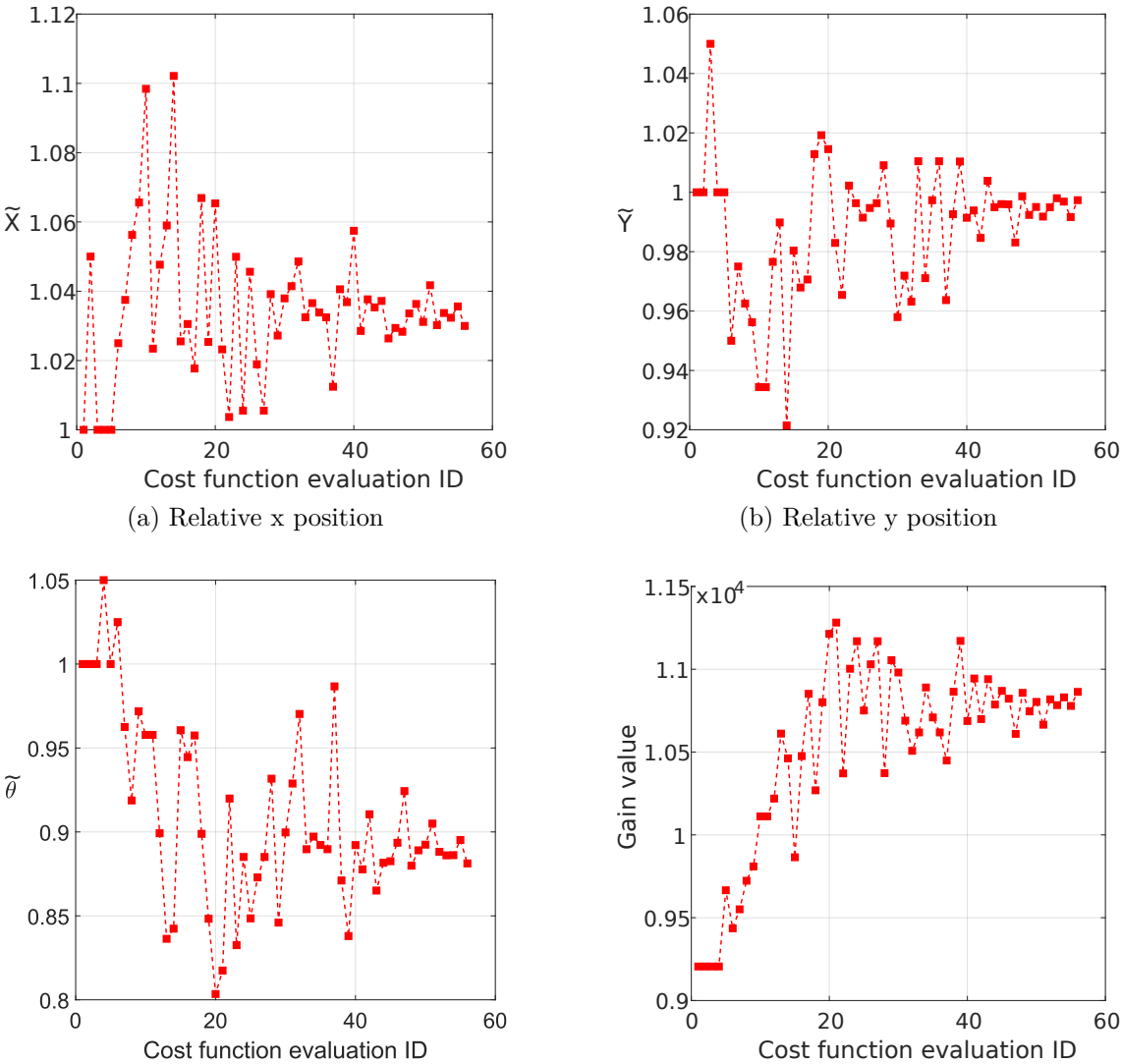

(a) Relative x position

(b) Relative y position

(c) Relative θ position

(d) Gain value

Figure 5.15: Convergence of the *'fminsearch'* algorithm for the multi-modal damping of modes 1 & 2 of the ASML wafer gripper for the relative positions and the gain value.

$$\begin{aligned} \tilde{x} &= x/x_{starting} \\ \tilde{y} &= y/y_{starting} \\ \tilde{\theta} &= \theta/\theta_{starting} \end{aligned} \tag{5.6}$$

Although the optimization has been performed in a SISO configuration, the final active architecture is intended to be a MIMO one. Yet, the two pairs of piezoelectric patches need to be symmetrically positioned with respect to the x-axis of the gripper. Switching from the optimal SISO configuration obtained with the direct search algorithm to the targeted MIMO architecture requires consequently a limited effort. Such process involves two steps: (1) adding a second pair of patches to the gripper by respecting the symmetry of the optimal placement and (2) applying a decentralised PPF as follows:

$$C(s) = \frac{-g_{opti}}{s + \omega_c} \begin{bmatrix} 1 & 0 \\ 0 & 1 \end{bmatrix} \tag{5.7}$$

where g_{opti} is the gain that maximises the closed-loop damping of the system while ensuring its stability. Its value is therefore obtained by Equation 5.5 where $\{\mathbf{x}\}$ and θ are fixed. In addition to the optimal MIMO architecture based on the proposed PZ distance method, the original positioning of the piezoelectric pairs derived from the experimental setup in [16] can be simulated to compare the closed-loop performance. A graphical comparison of the two considered configurations is provided in Figure 5.16 and the obtained damping values are available in Table 5.4. The comparative analysis of the damping performance obtained with the two configurations highlights the effectiveness of the proposed method. While maintaining an equivalent level of damping for the first mode, a substantial augmentation of nearly 70% has been achieved for the second one. This increase corroborates the added value of the proposed PZ criterion and its potential to refine the preliminary findings documented in [16]. An experimental validation of these findings could be pursued at TU Delft depending on the availability of the setup. Nonetheless, the efficiency of the criterion and the related methodology that has been proposed is again numerically validated by this industrial case.

Table 5.4: Comparison of the MIMO closed-loop performance on the ASML wafer gripper obtained with the original configuration from the experimental setup and the optimised one based on the PZ distance approach.

	Mode 1	Mode 2
Original configuration (from experimental setup)	0.023	0.016
Optimized configuration (based on the PZ criterion method)	0.025	0.027

5.3.3 Conclusion

Applying the PZ distance criterion approach on the wafer gripper allowed the application of the proposed methodology to an actual industrial case study. It has been shown that starting from a basic geometry of a complex structure such as the considered gripper, the proposed method can be readily applied. An enhancement of nearly 70% with respect to the original performance has indeed been achieved based on a limited number of evaluations. The application of the PZ distance criterion facilitates the precise targeting of a high-potential area, enabling thereby a fast implementation of a non-evolutionary search algorithm. Hence, it has been numerically demonstrated that the adoption of the optimization methodology proposed in this thesis induces a genuine increase in performance

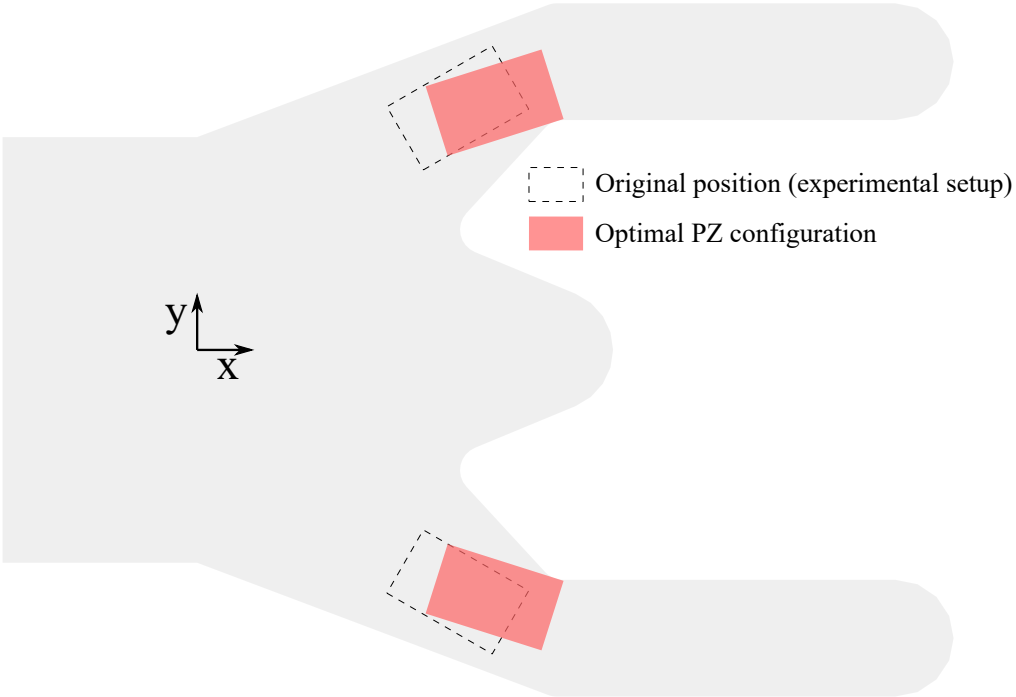

Figure 5.16: Illustration of the original MIMO configuration (experimental setup) and the optimised one based on the PZ distance approach on the ASML wafer gripper model.

for industrial frameworks that demand performance enhancement while ensuring restricted complexity and optimization time.

5.4 Reliability of the FE models and methodology for model matching

The optimal transducer placement studies are always conducted based on a model of the structure. Such a model is required to evaluate the cost function of the selected placement criterion at various positions in order to find the best solution. The model that is used can be based on experimental extractions, but it is most often generated by numerical means. A numerical model (e.g. obtained from a FE software) allows indeed a wide range of positions to be evaluated without having to experimentally extract the dynamics at each one of them. With the proposed method, the model built in SDT (or any other FE software) is used to provide the limited PZ distances to compute the PZ criterion and extract a suitable starting position for a non-evolutionary search algorithm. Additionally, the model is used to evaluate the closed-loop performance during the convergence of the search algorithm. The FE model consequently constitutes a major element of the optimization approach and should be considered as an important aspect of the method.

5.4.1 Discussion on the reliability of the FE model

Because the optimal solutions directly depend on the FE model, it is essential to establish that it is accurate enough to ensure a correct fit between the numerical predictions and real-world performance. However, it is well-known that unavoidable deviations occur between the model and the experimental system [20, 21]. Those deviations can be attributed

to a variety of factors, such as inaccuracies in the material parameter values, local heterogeneity, unconsidered temperature-dependent effects, oversimplified boundary conditions and inaccuracies when mounting the transducers on the structure. When dealing with piezoelectric patches, additional difficulties arise such as the effect of the glue that is not considered in the model or the difficulty in accurately modelling piezoelectric structures because of the interaction between mechanical and electrical effects [22].

Although the robustness to misplacement of the optimal solution has been addressed and identified as an important factor in the previous sections and chapters, the reliability of the model and its validity with respect to experimental results has not been investigated yet. This section consequently aims to analyse such validity by comparing numerical predictions and experimental results. Considering that (i) an experimental validation on the Boeing 777-200ER wing is not feasible and (ii) the experimental application of the findings obtained for the wafer gripper will demand additional efforts, the comparison will be conducted on a simple system: the cantilever beam studied in Section 2.3 for the experimental validation of the PZ link in MIMO systems. A numerical model was indeed developed to design the experimental setup while the validation has been performed on an experimentally extracted one. This choice has precisely been made to avoid having to deal with possible deviations between the model and the experimental setup.

The complete characteristics of the cantilever beam are detailed in Section 2.3 and an illustration of its FE model as well as a picture of the experimental setup are shown in Figure 2.7. Nonetheless, there are pertinent details to be recalled: made of steel, it is equipped with five pairs of MFC piezoelectric patches and one additional single PZT actuator. Each MFC SA pair is placed at the same location but on the opposite faces of the structure. The analysis will focus on two specific responses: the collocated response involving the first MFC pair (i.e. the one located at the left-most clamped side of the beam) and the response involving the second one that locates right next to the first pair. The FE model is built in SDT with a total of 14001 shell elements while the experimental frequency response functions are obtained by injecting a chirp (i.e. a sine sweep) from 3 to 300 Hz to the MFC actuator. The response is measured by its collocated sensor through a signal conditioner from PCB Piezotronics (model 482C) using a dSPACE MicroLabBox (sampling frequency set to 20 kHz). The comparison between the model and the experimental responses is shown in Figure 5.17 for both collocated pairs. As it can be seen, even though the same overall dynamic is observed, the FE model built with SDT shows important deviations for the poles, zeros and gain values. Obviously, such deviations observed in open-loop directly impact the closed-loop dynamics, which can lead to a deterioration of the performance predicted by simulation once the control architecture is implemented on the experimental structure.

The large deviations obtained between the experimental responses and the FE predictions shown in Figure 5.17 inevitably trigger concerns, as they derive from a simple structure. Additionally, SDT incorporates powerful tools to properly manage the modelling of the piezoelectric patches. One of them relies on the use of multi-layer shell elements developed in [23] while another one includes the equivalent piezoelectric properties for MFC patches obtained by homogenization technique from [24]. Yet, such a simple structure that is expected to be straightforward to model already exhibits large divergences. A more complex structure would consequently present deviations as well, which could be extremely significant and lead to major mismatches between the numerical predictions and real-life behaviour.

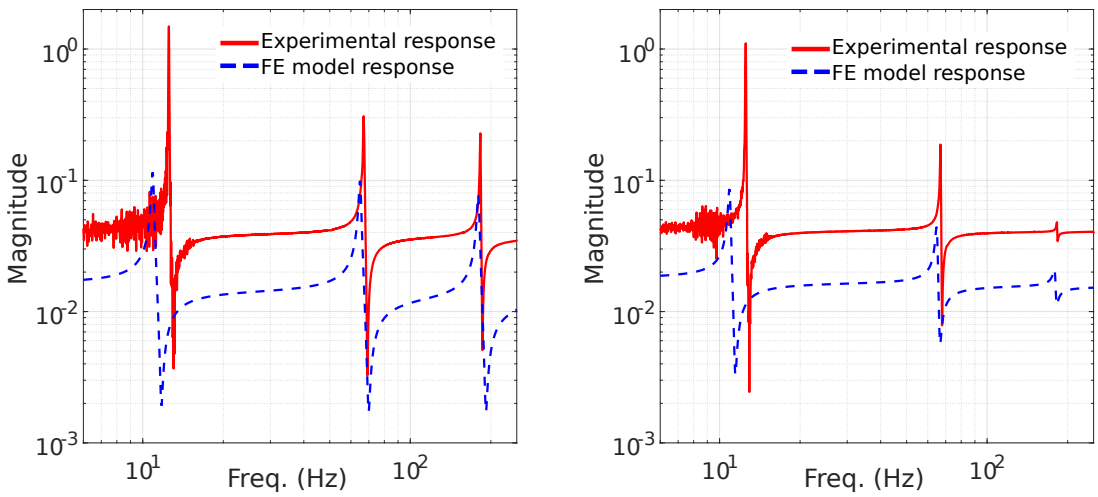

(a) Actuator 1 to sensor 1 (b) Actuator 2 to sensor 2

Figure 5.17: Comparison between the experimental response and the FE prediction obtained on a cantilever beam with five pairs of MFC piezoelectric patches for: (a) the first collocated pair, (b) the second collocated pair.

This consequently confirms again the importance of getting optimal solutions that are not located in an area that presents a high risk of dynamical change, e.g. where a zero lies too close to a pole. This mismatch between the model and the experimental setup can be similar to the deviations obtained when a misplacement of the transducers is encountered on the experimental setup. Both lead indeed to the same end-effect: change in the gain and zero values and, for piezoelectric patches, modification of the resonance frequencies.

Based on the different discussions held in this thesis and the numerical simulations that have been performed, it can be assumed that the optimal solutions obtained with the proposed approach should be resilient to deviations introduced by model mismatching. Those solutions are indeed located in an area with high damping and low misplacement sensitivity. Nonetheless, it is still essential to reduce as much as possible any misplacement while mounting the transducers on the structure in order to reduce the risk of performance decrease and/or the apparition of destabilization effect. Reducing the level of deviations between the model and the experimental system should also be considered to avoid cumulative effects with placement errors.

Model matching techniques can be applied in order to reduce the mismatch between the FE model and the experimental setup caused by the different modelling inaccuracies. A consistent step-by-step matching approach, from the piezoelectric patch sub-system to the global structure, is proposed hereafter. The initial step, described in Section 5.4.2, consists of matching the piezoelectric properties. The structural properties are assessed in the second step, as presented in Section 5.4.3. Finally, the boundary conditions are studied in Section 5.4.4. To illustrate the method, each step is applied on the cantilever beam equipped with the five pairs of MFC patches whose deviations between the model and the experimental setup were shown in Figure 5.17 for two collocated pairs.

5.4.2 Matching of the piezoelectric patch

Although the use of multi-layer shell elements from [23] or the implementation of the equivalent piezoelectric properties from [24] in SDT clearly helps to improve the accuracy of the FE model, getting a perfectly correlated response between the physical patch and

the model remains extremely challenging. Two main reasons can explain such difficulty. The first one is because the electrical and the mechanical interactions of the piezoelectric patch present different orders of magnitude, which convolutes its numerical handling. The second reason is directly linked to the manufacturing process of a patch, which is not perfectly repeatable leading to high levels of tolerance for its parameters. Such tolerance can for example go up to 20% for the permittivity, resulting in different responses from various patches of the same type, even if belonging to the same production batch. It therefore implies that building an accurate model of a system with one or multiple piezoelectric patches is highly complex.

The first step of the proposed method consists of matching the model of the piezoelectric patch(es). Starting by only considering the piezoelectric patch is valuable because it allows to study its behaviour without parasitic effects such as the influence of the glue or a possible inaccuracy in its placement. The calibration of the model of the patch is performed by means of impedance curve measurements. The piezoelectric patch impedance $Z_p(\omega)$, expressed in Ohms, is the magnitude of the ratio between the voltage and the current, at different excitation frequencies. To fully appreciate why the impedance curve is singularly useful, the physical functioning of a piezoelectric patch is first briefly recalled.

A piezoelectric patch is capable to convert mechanical stress into electrical charges (direct piezoelectric effect) and, inversely, to induce mechanical strain when a voltage is applied on its electrodes (inverse piezoelectric effect). The general constitutive equations for linear piezoelectricity can be expressed as follows [25]:

$$\begin{aligned} \{\mathbf{S}\} &= \left[\mathbf{s}^{\mathbf{E}}\right]\{\mathbf{T}\} + [\mathbf{d}]^T\{\mathbf{E}\} \\ \{\mathbf{D}\} &= [\mathbf{d}]\{\mathbf{T}\} + \left[\epsilon^{\mathbf{T}}\right]\{\mathbf{E}\} \end{aligned} \tag{5.8}$$

where $\{\mathbf{S}\} \in \mathbb{R}^6$ is the strain vector, $\{\mathbf{T}\} \in \mathbb{R}^6$ is the stress vector, $\{\mathbf{E}\} \in \mathbb{R}^3$ is the electric field vector and $\{\mathbf{D}\} \in \mathbb{R}^3$ is the electric displacement vectors. $\left[\mathbf{s}^{\mathbf{E}}\right] \in \mathbb{R}^{6\times 6}$ and $\left[\epsilon^{\mathbf{T}}\right] \in \mathbb{R}^{3\times 3}$ are respectively the compliance and permittivity matrices where the superscript inside the matrix bracket indicates a zero value for its corresponding parameter. Finally, $[\mathbf{d}] \in \mathbb{R}^{3\times 6}$ is the direct piezoelectric matrix that expresses the electromechanical coupling. To ensure a correct correspondence between the physical patch and its FE model, accurate values of all the parameters matrices need to be properly integrated in the FE software. Nevertheless, those values are difficult to obtain from the suppliers and, if available, they are usually based on large volumes and over long term average causing inaccuracies for individual system. Nonetheless, by integrating Equation 5.8 over the volume of the patch when considering it as connected to a sDoF of mass M, the admittance of the transducer (i.e. the ratio between the current and the voltage I/V) can be obtained. For example, this has been computed in [26] for an uniaxial d_{33} piezoelectric transducer, i.e. a stack of thin ceramic disks separated by electrodes as illustrated in Figure 5.18a. For such stack, the coefficient d_{33} dominates the other piezoelectric constants in the constitutive equations and it follows:

$$\frac{I}{V}(s) = s\,C^T(1-k^2)\left[\frac{Ms^2 + K_a/(1-k^2)}{Ms^2 + Ka}\right] \tag{5.9}$$

where s is the Laplace variable, C^T is the capacitance of the piezoelectric stack when it is free of stress, K_a is its stiffness in short-circuit condition and k is the electromechanical

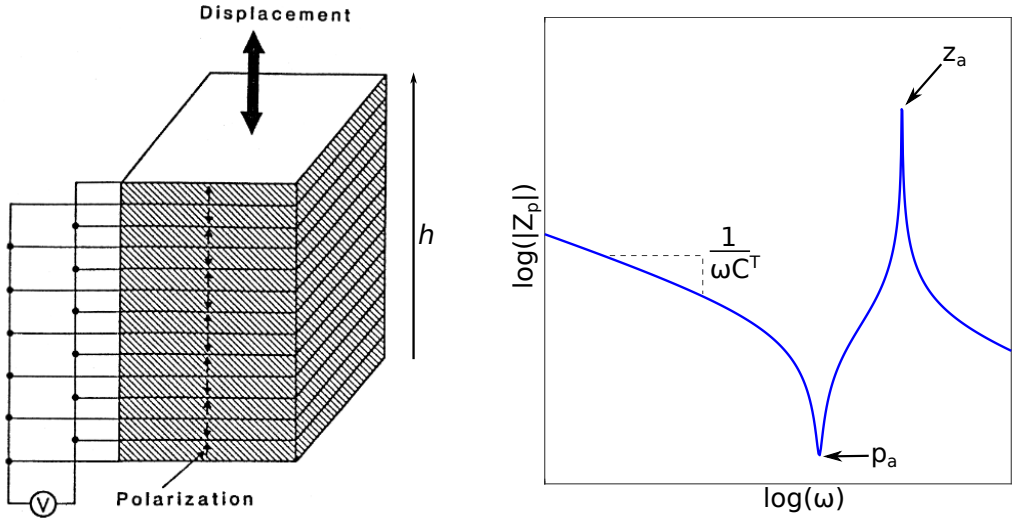

(a) A piezoelectric stack [27]

(b) Impedance curve

Figure 5.18: Illustration of (a) a piezoelectric stack, (b) the general shape of the impedance curve of a piezoelectric transducer.

coupling factor that can be both expressed as follows:

$$K_a = \frac{A}{s^E h} \tag{5.10}$$

$$k^2 = \frac{d_{33}^2 K_a}{C^T} \tag{5.11}$$

where A is the cross section of the stack, s^E is the compliance in short circuit (i.e. the inverse of c^E, the Young's modulus in short circuit), h is the total height of the stack and d_{33} is the piezoelectric coupling factor.

Consequently, a pole p_A and a zero z_A consistently appear on the admittance curve at the frequencies where Equation 5.9 cancels out at its denominator and at its numerator, respectively. Physically, p_A corresponds to the natural frequency of the patch with short-circuit electrodes (no voltage) while z_A is the natural frequency with open-electrodes (no current). They are both expressed as follows:

$$p_A^2 = \frac{K_a}{M} \tag{5.12}$$

$$z_A^2 = \frac{K_a/(1-k^2)}{M} \tag{5.13}$$

Interestingly, the impedance of the patch $Z_p(s)$ is the inverse of the admittance. Indeed, by switching from the Laplace domain to the frequency one, it follows:

$$Z_p(\omega) = \left[\frac{I}{V}(\omega)\right]^{-1} \tag{5.14}$$

Hence, the notable value of p_A and z_A can be extracted from the experimental impedance curve by inverting it and measuring the corresponding frequencies (respectively the zero and the pole frequencies due to the inversion).

In addition to p_A and z_A, the capacitance value of a piezoelectric patch can also be obtained from its impedance curve, by simply analysing its behaviour in the quasi-static frequency bandwidth. When considering piezoelectric patch, the capacitive effect at low frequency is indeed predominant compared to the resistive and the inductance ones, such that [28]:

$$|Z_p(0)| \simeq \frac{1}{\omega\, C^T} \tag{5.15}$$

where $|\,.\,|$ denotes the modulus operator of a complex number. From Equations 5.14 and 5.15, it follows that the admittance in the quasi-static frequency bandwidth is directly proportional to C:

$$\left|\frac{I}{V}(0)\right| \simeq \omega\, C^T \tag{5.16}$$

Such experimental measurement of the capacitance value of C based on the impedance or admittance curve is of high interest. Indeed, when the piezoelectric patch is in free condition (i.e. without any mechanical restriction), the capacitance is directly proportional to the permittivity factor ϵ^T as follows:

$$C^T = \frac{\epsilon^T A}{h} \tag{5.17}$$

Hence, if the complete dimensions are known, the permittivity of the patch ϵ^T can be accurately computed based on a simple impedance measurement. Figure 5.18b illustrates the general shape of an impedance curve and highlights the positions at which C^T, p_A and z_A can be extracted.

Although Equation 5.9 and the subsequent reasoning are derived from an uniaxial d_{33} piezoelectric stack, a similar logic can be applied for in-plane (laminar) piezoelectric patches. If applicable, the d_{31} and d_{32} coupling factors will dominate the equations rather than d_{33} because the useful direction of expansion is normal to the electric field.

Description of the proposed approach

Based on the previous physical and mathematical discussions, a specific step-by-step matching approach is proposed to properly match the FE model of a piezoelectric patch with its experimental response. This method, which should be implemented in the given order to avoid any cross-modifications of interconnected parameters, is defined as follows:

Step 1:
Experimentally extract the impedance curve of the piezoelectric patch in free condition.

Step 2:
Implement the FE model of the patch with its known geometry and the parameters provided in the data sheet from the supplier.

Step 3:
Graphically represent, on a *log/log* scale, the experimental admittance (obtained by inverting the experimental impedance from the first step) and the numerical one (obtained from the FE software).

Step 4:
Adjust the structural modal damping of the model to approach the resonance peak amplitude.

Step 5:
Adjust the permittivity factor of the patch in the model to match the capacitance of the experimental one (low frequency amplitude).

Step 6:
Adjust the Young's modulus value of the patch in the model to match the pole frequency of the experimental one.

Step 7:
Adjust the piezoelectric coupling factor of the patch in the model to match the zero frequency of the experimental curve.

This procedure provides a straightforward approach for matching the model of a piezoelectric patch with its experimental response, aiming to improve its accuracy once used in a more complex system. Nonetheless, achieving a perfect match is extremely challenging due to the inherent complexities and limitations of FE modelling, and potential inaccuracies related to experimental results. Some discrepancies may consequently remain after applying the matching procedure, as illustrated by implementing it in the next sub-section.

Illustration of the piezoelectric matching procedure

In order to illustrate the proposed piezoelectric matching procedure, it is applied to one of the five MFC patches used in Section 2.3 for the experimental validation of the PZ link in MIMO systems. To this end, a model of the patch (13 mm × 13 mm) is built in SDT. Its structure is modelled in free boundary conditions by 677 shell elements that present 3 layers (the active layer is sandwiched between two epoxy ones). A voltage actuator and a charge sensor are simulated, allowing to obtain the charge over voltage response, $Q/V(\omega)$.

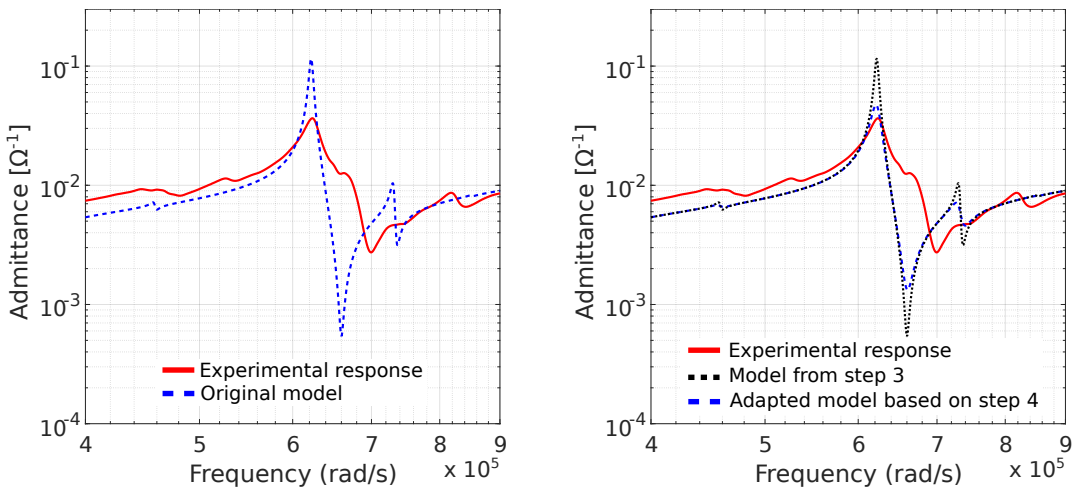

(a) Step 3 (b) Step 4

Figure 5.19: Illustration of the matching procedure for the piezoelectric patch on a MFC example with: (a) step 3 (preliminary comparison), (b) step 4 (damping adjustment).

The experimental impedance is measured with an *Agilent* 4294A impedance analyser, using a low voltage actuation of 50 mV and 801 points of measurement between 55 kHz and 160 kHz. The experimental admittance is then obtained by simple inverting the impedance. The comparison between the experimental curve and the initial FE model (step 3 of the procedure) is shown in Figure 5.19a. It can be seen that despite the specific tools implemented in SDT that aim to maximize the accuracy of the piezoelectric

response, major deviations still appear between the two curves confirming the need of the proposed model matching method.

The adjustment of the internal damping value as defined by the fourth step of the procedure allows to match the resonance amplification peak, as illustrated in Figure 5.19b. Furthermore, the fifth step and the related modification of the permittivity ensures a proper magnitude correlation at low frequency, as highlighted in Figure 5.20a. Yet, the pole and the zero frequencies obtained with the experimental setup still do not match the ones from the numerical model. A clear improvement is achieved by implementing the sixth and the seventh steps, where the stiffness and the coupling factor of the patch are adjusted, as shown respectively in Figures 5.20b and 5.21a.

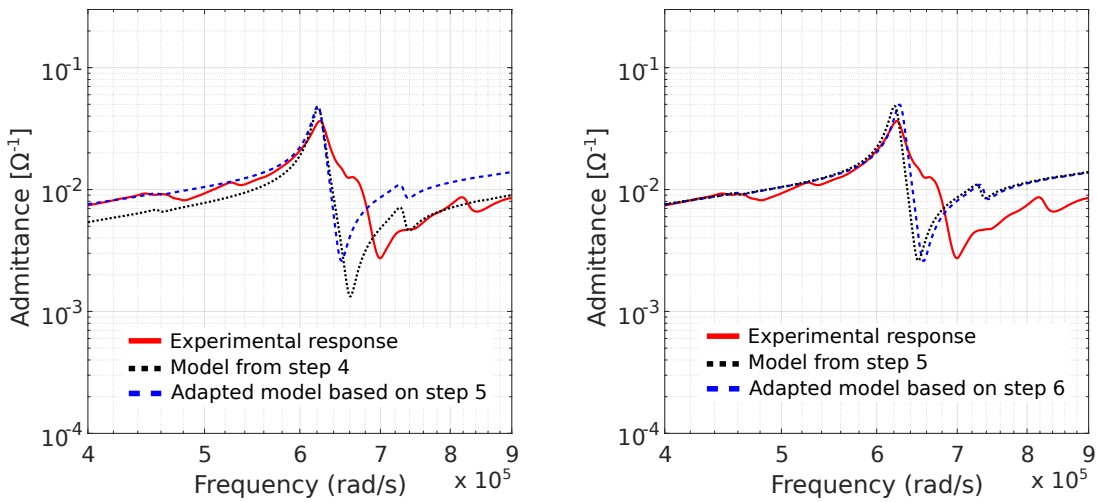

(a) Step 5 (b) Step 6

Figure 5.20: Illustration of the matching procedure for the piezoelectric patch on a MFC example with the: (a) step 5 (low frequency amplitude adjustment), (b) step 6 (pole frequency adjustment).

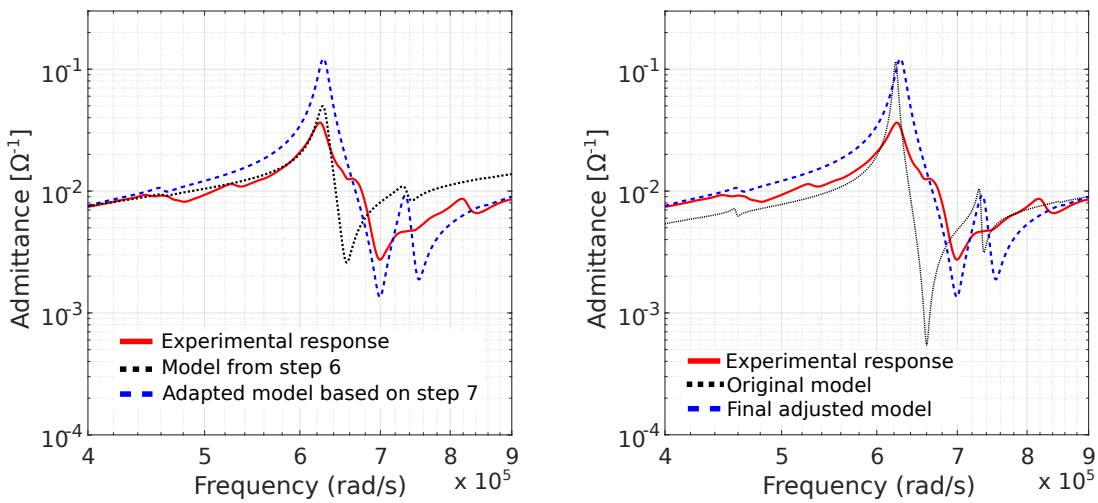

(a) Step 7 (b) Final comparison

Figure 5.21: (a) Illustration of the matching procedure for the piezoelectric patch on a MFC example with step 7 (zero frequency adjustment), (b) Final comparison between the experimental response of the MFC patch and its tuned model

The final comparison between the adjusted numerical model and the experimental response is illustrated in Figure 5.21b, where the initial non-tuned model is plotted as well. In addition, the comparison between the original values and the tuned ones of the different numerical parameters is given in Table 5.5, where E_L denotes the longitudinal Young's modulus (in the fibre direction) while E_T relates to the transverse one. It can be seen from the graphical comparison in Figure 5.21b that the final dynamical behaviour of the model mirrors more closely the experimental curve, demonstrating therefore the efficiency of the proposed matching procedure. Nonetheless, the model is still not completely aligned with the experimental curve despite the different tuning. The primary deviations observed are associated with the peaks at the pole and zero frequencies, which arise during the process of matching the main zero frequency (step 7). Indeed, the frequency from the model was successfully shifted closer to the experimental value, but at the expense of a very substantial increase of d_{31} as displayed in Table 5.5. This need to significantly increase the d_{31} value in order to match the zero frequency is because the FE model does not account the inherent imperfections of MFC patches. These imperfections induce an orthotropic behaviour, which notably influences the zero values. More specifically, these imperfections, stemming from the non-ideal manufacturing process, lead to a higher modal density compared to the model one, which significantly affects the zero frequencies.

Table 5.5: Comparison between the original and the tuned values of the MFC parameters based on the piezoelectric matching procedure.

Parameter	Original value	Tuned value
ξ (-)	0.004	0.01
ϵ_{33}^{T} (F/m)	0.1410 $\times 10^{-7}$	0.1997 $\times 10^{-7}$
E_L (GPa)	47.17	47.11
E_T (GPa)	16.98	17.32
d_{31} (pC/N)	-183	-292

This is reassuring again the difficulty to accurately model a piezoelectric patch. Hence, if multiple patches are considered in a system, it is recommended to assess the validity of the tuned FE model for each one of them. A certain disparity between one patch to another may indeed exist, even if they originate from the same supplier and the same batch. As the experimental system from Section 2.3 is mounted with a total of ten MFCs patches (five collocated pairs), such additional consistency check can be performed on all of them. Every impedance curve is experimentally extracted with the same Agilent analyser and their corresponding admittance curves are plotted in Figure 5.22, where the final adjusted model is available as well. As it can be observed, a similar overall dynamical behaviour is obtained for the different patches. Yet, some disparities emerge between the pole and zero frequencies, as well as between the low frequency gains. Those deviations are due to the unavoidable fluctuations from one patch to another as mentioned at the beginning of the section. Nonetheless, as the dynamical behaviours are similar and match the adjusted model response, the consistency check is passed and the matching of the patch is completed. The next step of the proposed approach, the matching of the structural properties, is therefore analysed hereafter.

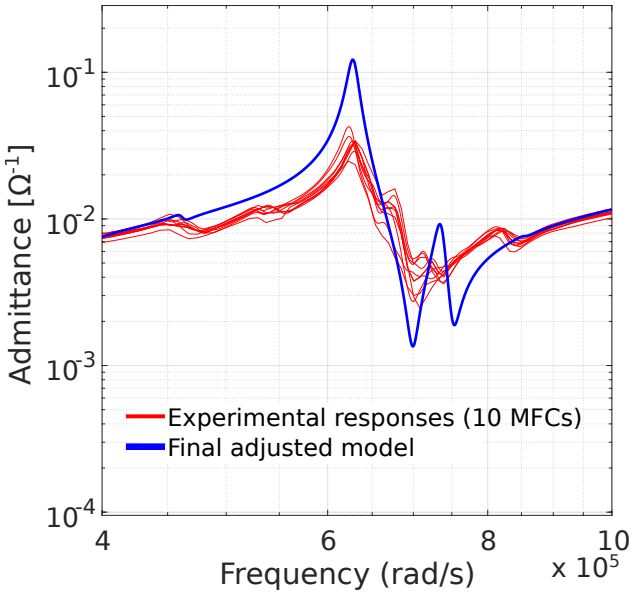

Figure 5.22: Consistency analysis on the 10 MFC piezoelectric patches

5.4.3 Matching of the structural properties

When a mechanical part, system or (sub-)assembly is manufactured, deviations always occur with respect to the original intended design. Depending on the manufacturing process and the required degree of accuracy, tolerances are defined to maintain the level of deviations under specified values (e.g. by using the GD&T system, or with the different ISO standards). Hence, the size and the geometry of a physical system will always be altered compared to its FE model, at different degrees. The quality of the materials used in mechanical systems are subjected to tolerances as well. For example, the German standard DIN 17100 (which has gradually been replaced by the European standard EN 10025) specifies the chemical composition of Carbon in different steels, by defining the lower and upper bounds (in percentage). As the Carbon is a primary element that directly affects the strength of metal, such a permissible range leads to uncertainties on the value of the Young's modulus. Additionally, local deformities and/or defects can appear due to the non-perfect manufacturing process. Because those local irregularities are usually not known, they are not included in the FE model neither.

Those different possible deviations lead to a mismatch between the physical system and its FE model. This therefore affects the different outcomes obtained with the FE software, such as the exact value of the natural frequencies, the dynamical behaviour in closed-loop, or the optimal positions for the transducers.

To assess the accuracy of the FE model with respect to its physical system, a mode shape analysis can be conducted. The natural frequencies of a system are indeed intrinsic to the structure and depend upon multiple physical parameters. A close match of the numerical values compared to the experimental ones can reinforce the assurance in the different parameters used to build the model, as well as in the dynamic simulations run afterwards. This analysis should consider the structure only, i.e. without any transducers mounted on and preferably in free boundary conditions. Having as few external parameters as possible allows indeed to focus on the ones related to the structure without considering external uncertainties. Surely, the FE model must reflect the physical state of the structure before running the mode shape analysis.

Following the adjustment of the FE model to reflect the experimental test conditions (i.e. without boundary conditions and without any transducers if possible), the numerical mode shape analysis can be performed and the obtained natural frequencies within the bandwidth of interest can be compared to the experimental ones. Based on the outcomes from this comparison, the parameters used to build the model can be adapted to reduce the deviations, if any. Three main parameters can be modified to establish a closer match: the Young's modulus of the material, its mass density and the geometry of the structure. The next sub-section provides an example and illustrates how such matching of the structural properties can be done.

Illustration of the structural properties matching procedure

The procedure to match the structural properties is illustrated on the cantilever beam used to demonstrate the experimental validation of the PZ link in MIMO systems, from Section 2.3. This cantilever beam is made out of a lightly damped steel (250 mm x 36.4 mm x 0.75 mm) and presents 5 pairs of d_{31} MFC patches as well as an extra d_{33} PZT patch for actuation.

As presented, matching the structural properties is conducted by running a mode shape analysis that should be performed with as few elements as possible, and in free boundary conditions. Hence, only the steel structure should be analysed for this example, i.e. without the different piezoelectric patches and without the clamp. But as the d_{33} PZT patch is used for actuation, it can be preserved to avoid having to implement an external feature. The FE model of the beam is consequently modified as a free 330 mm long steel structure (i.e. 80 mm longer than the original cantilever beam from the portion that was contained in the clamp), with one d_{33} PZT patch whose location matches the physical system. For the experimental setup, the steel beam with the PZT patch is hanged at its two sides with strings to mimic the free boundary conditions when considering the first three bending modes. Its modal response is obtained by actuating the structure through the piezoelectric patch using a chirp signal from 3 to 300 Hz, while its response is measured with a laser vibrometer (Polytech OFV-505).

Table 5.6 provides the comparison between the first three resonance frequencies. As it can be seen, the dynamical behaviour of the experimental setup perfectly matches the simulated one. The first three resonance frequencies of interest are indeed extremely close with a maximum deviation of 2%. This consequently indicates that the different structural properties of the beam and the PZT patch used in the FE model can be validated and no further actions are required.

Table 5.6: Comparison of the first three resonance frequencies of a beam between the experimental setup and its FE model for the structural properties matching procedure.

	Mode 1	Mode 2	Mode 3
Resonance frequency from the FE model (Hz)	36.82	101.64	199.53
Resonance frequency from the experimental setup (Hz)	36.80	101.40	204.30

5.4.4 Matching of the boundary conditions

Designing an accurate model of the boundary conditions can be a real challenge when building a FE model. Real-world structures present indeed non-perfect conditions, which is extremely complex to represent. For example, the fully clamped condition of a cantilever beam is modelled by restricting all the DoFs of every node that lies at the considered boundary. Yet, physical systems can present a small gap at the edge of the clamping that leads to parasitical movements. The physical system can also present a distorted boundary geometry, even though the model uses an idealised, perfectly continuous curve for it. An additional discrepancy could consequently arise because the FE model approximates a smooth physical system while the actual boundary might experience irregularities or distortions that are not accurately captured.

Analysing and matching the parameters linked to the boundary conditions should consequently be considered as well in order to maximise the accuracy of the model. This analysis should be conducted as the final step in the model matching procedure, ensuring that all other variables have been thoroughly validated beforehand. Similarly to the previous step, the improvement of the boundary condition representation can be performed by comparing the natural frequencies of the physical structure with the ones from the model. In case of mismatch, the deviation can be reduce by two techniques. The first one consists of modifying the size of the structure in the dimensions impacted by the boundary condition, as the addition of the boundary conditions can modify the nominal size of the structure when being implemented. The second method involves the adjustment of the Young's modulus value for the elements in the vicinity of the condition. Non perfect conditions can indeed locally modify the stiffness of the structure. In the interest of clarity, the following sub-section presents the matching procedure on an example.

Illustration of the boundary conditions matching procedure

The matching procedure for the boundary conditions is again illustrated on the cantilever beam from Section 2.3, i.e. the lightly damped steel beam (250 mm x 36.4 mm x 0.75 mm) that presents 5 pairs of d_{31} MFC patches as well as an extra d_{33} PZT patch for actuation. As it corresponds to the last step of the procedure, the full system is considered. Hence, the mode shape analysis is performed on the clamped beam where the PZT patch and the five pairs of MFCs are mounted.

The testing method consists of injecting a chirp signal from 3 to 200 Hz through the PZT patch while the Polytech OFV-505 vibrometer measures the structural response. The first three resonance frequencies that have been experientially obtained as well as the predicted values based on the FE model are given in Table 5.7. Importantly, the model was built by incorporating all the parameter changes from the previous matching procedures, i.e. from sections 5.4.2 to 5.4.3. As it can be seen in the table, the natural frequencies of the experimental system deviate with respect to the simulated ones, especially for the third mode (relative deviation of 11%). A modification of the boundary conditions for the model is therefore necessary.

Given that the experimental system operates at higher frequencies, the overall stiffness of the model should be increased. Consequently, a reduction of its length is considered, together with an increase of the Young's modulus in the vicinity of the clamping nodes. The optimal adjustment of these parameters must be achieved by iterative modifications until an appropriate balance between the three frequencies is obtained. An important

Table 5.7: Comparison of the first three resonance frequencies of a beam between the experimental setup, its original FE model and the adjusted one (boundary conditions matching).

	Mode 1	Mode 2	Mode 3
Frequency from the experimental setup (Hz)	12.34	66.52	158
Frequency from the original model (Hz)	10.96	65.10	140.64
Frequency from the adjusted model (Hz)	11.36	67.37	143.17

aspect to consider is that the clamping obtained on an experimental setup is generally less effective compared to its ideal FE model. Hence, the stiffness often needs to be reduced instead of increased as suggested for this particular case. A poor mounting of the beam in its clamping structure leading to a overall length reduction would explain the observed over-stiffness. Based on the modification of the local stiffness and length of the beam, a reduction of the deviations is obtained, as displayed in Table 5.7. More precisely, the relative errors of modes 1 and 2 are reduced to 8 and 1% respectively. Yet, the error for the third mode remains at 9% due to the challenge of targeting one specific mode without affecting the others. For a sake of completeness, the comparison between the original and tuned values of the cantilever beam parameters are provided in Table 5.8, where E_{Steel} at clamping refers to the Young's modulus of the elements that locate on the first row next to the clamp, on its entire width.

Table 5.8: Comparison between the original and the tuned values of the cantilever beam parameters based on the boundary conditions matching procedure.

Parameter	Original value	Tuned value
Total length (mm)	250	246
E_{Steel} at clamping (GPa)	210	262

5.4.5 Final comparison and conclusion

As the proposed step by step matching procedure has been completed (i.e. matching the piezoelectric patch properties as described in sub-section 5.4.2, matching the structural properties in sub-section 5.4.3 and finally matching the boundary conditions based on sub-section 5.4.4), a final comparison between the original model, the experimental response and the tuned model can be performed. Figure 5.23 provides such visual comparison, where clear improvements with respect to the accuracy of the model can be observed. Indeed, the major off-set shown in the original model response is correctly compensated by the tuned one. Additionally, the modelled resonance frequencies are closer to the experimental ones, as well as the zero values except for the third mode where the deviation slightly increased.

Although the tuned model based on the proposed matching procedure demonstrates a better fit with respect to the experimental response, the final match is not flawless. This discrepancy can be attributed to several factors. An important one relates to the fact that the accurate positioning of the MFC patches has not been calibrated. Indeed, only the resonance frequencies have been analysed once the patches were mounted on the beam. But the SA positions have a real impact on the zero values (see Sections 1.3 and 1.5), and the different relative positions between each pair also affect the responses.

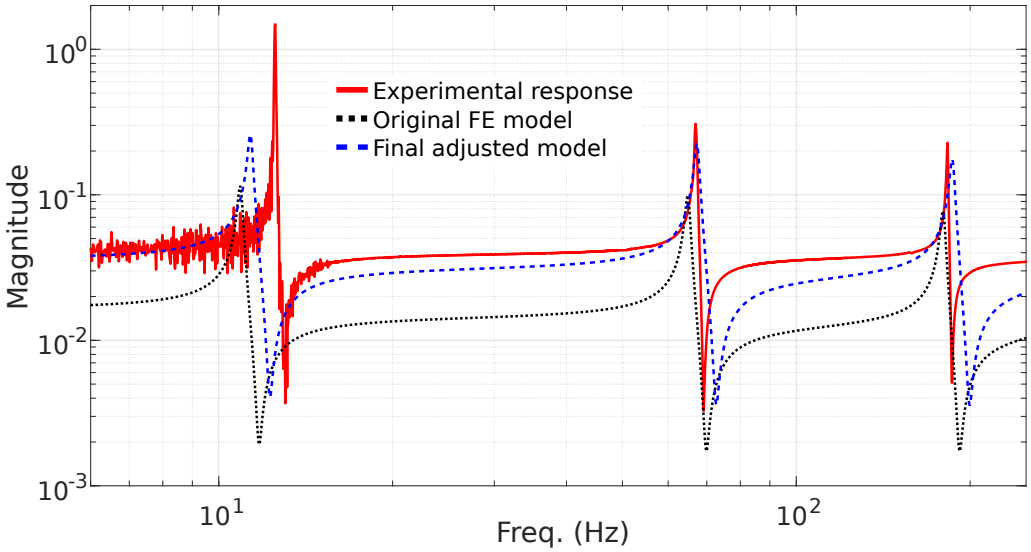

Figure 5.23: Visual comparison between the original FE model, its experimental response and the tuned model response based on the proposed model matching procedure.

Achieving a perfect fit is also challenging because of the inherent co-dependency of the structural parameters: modifying a single value can influence multiple other ones simultaneously as described in sub-section 5.4.4. Because of this interdependency, it becomes almost impossible to obtain no deviation for the different relevant values of a parameter.

Consequently, the proposed matching procedure clearly allows to reduce any deviations that may occur but obtaining a perfect model is extremely unlikely. The example used to illustrates the procedure highlighted the difficulty to obtain an accurate FE model with respect to its experimental response. Indeed, even if the SA architecture of the example is complex (a total of ten MFC patches forming five collocated pairs and one d_{33} PZT), the structure itself is relatively simple (a cantilever beam). As a mismatch of the pole, zero and gain values have major impact on the dynamics and response of a system, especially in closed-loop, understanding the limitation of each FE model is important. Additionally, the controllers that are implemented should include enough robustness to account such mismatch. Preferably, a model matching should always be performed if possible, to reduce as much as possible the mismatch between the numerical model and its corresponding physical response.

5.5 Conclusion

The proposed SA placement method that relies on the use of the PZ distance criterion and a non-evolutionary search algorithm has been introduced in Chapter 4 and validated on a cantilever beam. Although rather simple, such structure allowed to extensively analyse the performance of the proposed method while comparing it to other ones. This chapter aimed to apply the proposed methodology on more complex structures, in order to validate it on industrial systems.

The first case study focused on the model of a Boeing 777-200ER wing, characterised by its 3D structural complexity. A single collocated force actuator/displacement sensor has been considered, leading to a vast amount of possible transducer placements. The second example addressed a stiff wafer gripper system in a MIMO configuration, in which two

pairs of collocated piezoelectric patches have been selected as transducers.

Across both validations, the proposed placement method consistently provided an initial solution located in a high performance area resulting in a limited number of evaluations to converge. Interestingly, it clearly outperformed the conventional modal amplitude-based strategy in terms of control effectiveness when applied on the Boeing 777-200ER wing. An additional analysis has been performed as well on the wing, which showed that the obtained solutions have strong robustness to misplacement. These different findings and the fact that there is no need to implement a complex search algorithm underscored the practicality of the proposed method for industrial applications, particularly where performance improvements must be achieved under constraints of limited complexity and computational effort. Its ease of implementation clearly supports its integration into design workflow for advanced applications, including large and/or complex structures.

Although very promising, the proposed method relies on numerical optimizations that need a FE model of the system. It has been demonstrated that deviations between the predictions obtained from a FE model and its physical system response can occur, even when considering simple systems. Those deviations can highly impact the overall system behaviour once in closed-loop and consequently degrade the predicted performance. To address this concern, a step-by-step strategy to match the FE model with its related structure has been proposed and illustrated on a cantilever beam with ten piezoelectric patches. It was shown that applying the matching procedure allowed to reduce the observed deviations between the different model predictions and the related system responses. Nonetheless, it also demonstrated that achieving a perfect match is unrealistic which highlighted the critical importance of designing robust control systems. Such observations added significant value to the proposed placement methodology presented in this thesis, particularly for large and complex structures that are typically not optimized due to the inherent challenges associated with the implementation of an optimization.

References

[1] *ASML Holding N.V.* URL: https://www.asml.com/en.

[2] L. R. Jenkinson, P. Simpkin, D. Rhodes, L. R. Jenkison, and R. Royce. *Civil jet aircraft design*. Arnold London, 1999.

[3] P. Eden. *Civil Aircraft Today - The World's Most Successful Commercial Aircraft*. Amber Books, 2008.

[4] D. Thisdell and R. Morris. *World Airliner Census 2018 - Eastern promise*. Tech. rep. Flight International, 2018.

[5] b1-foto. *Plane, Swiss, Boeing 777 image*. 2016. URL: https://pixabay.com/photos/plane-swiss-boeing-777-airport-1679203/.

[6] M. B. Rivers. "NASA common research model: a history and future plans". In: *AIAA Aviation 2019 Forum*. 2019, p. 3725. DOI: 10.2514/6.2019-2188.

[7] E. Balmes. *Structural Dynamics Toolbox 7.3 (for use with MATLAB)*. 1991. URL: https://www.sdtools.com.

[8] J. Banerjee. "Modal analysis of sailplane and transport aircraft wings using the dynamic stiffness method". In: *Journal of Physics: Conference Series*. Vol. 721. 1. IOP Publishing. 2016, p. 012005. DOI: 10.1088/1742-6596/721/1/012005.

[9] A. Preumont. *Vibration Control of Active Structure, An Introduction*. Thrid Edition. Springer, 2011. DOI: 10.1007/978-94-007-2033-6.

[10] A. Emami-Naeini and P. Van Dooren. "Computation of zeros of linear multivariable systems". In: *Automatica* 18.4 (1982), pp. 415–430. DOI: 10.1016/0005-1098(82)90070-X.

[11] European Commission. *Proposal for a Regulation of the European Parlement and of the Concil establishing a framework of measures for strengthening Europe's semiconductor ecosystem (Chips Act)*. 2022. URL: https://eur-lex.europa.eu/resource.html?uri=cellar:ca05000a-89d4-11ec-8c40-01aa75ed71a1.0001.02/DOC_1&format=PDF.

[12] L. Ockel. *Green and black checkered textile*. 2020. URL: https://unsplash.com/photos/vWSqLGd_d6s.

[13] *Thin Wafer Gripper 200mm from Semiconductor Production Systems*. URL: https://www.sps-international.com/product/thin-wafer-gripper-200mm/542/.

[14] W. Tao, M. Zhang, M. Liu, and X. Yun. "Residual vibration analysis and suppression for SCARA robot arm in semiconductor manufacturing". In: *2006 IEEE/RSJ International Conference on Intelligent Robots and Systems*. IEEE. 2006, pp. 5153–5158. DOI: 10.1109/IROS.2006.282610.

[15] W. Aribowo, T. Yamashita, K. Terashima, Y. Masui, T. Saeki, T. Kamigaki, and H. Kawamura. "Vibration control of semiconductor wafer transfer robot by building an integrated tool of parameter identification and input shaping". In: *IFAC Proceedings Volumes* 44.1 (2011), pp. 14367–14373. DOI: 10.3182/20110828-6-IT-1002.02675.

[16] M. El Ajjaj, M. Kaczmarek, M. van den Hurk, and S. HosseinNia. "Vibration suppression of a state-of-the-art wafer gripper". In: Euspen, 22nd International Conference & Exhibition. 2022. DOI: 10.48550/arXiv.2212.01854.

[17] M. Kaczmarek. *Internal repport from the Department of Precession and Microsystem Engineering, TU Delft*. 2023.

[18] C. Geuzaine and J.-F. Remacle. *Gmsh*. 2003. URL: https://gmsh.info/.

[19] *Physik Instrumente (PI)*. URL: https://www.piceramic.com/en/.

[20] B. Szabó and I. Babuška. *Introduction to finite element analysis: formulation, verification and validation*. Vol. 35. John Wiley & Sons, 2011.

[21] M. K. Vakilzadeh, V. Yaghoubi, A. T. Johansson, and T. J. Abrahamsson. "Stochastic finite element model calibration based on frequency responses and bootstrap sampling". In: *Mechanical systems and signal processing* 88 (2017), pp. 180–198. DOI: 10.1016/j.ymssp.2016.11.014.

[22] S. R. Moheimani and A. J. Fleming. *Piezoelectric transducers for vibration control and damping*. Vol. 1. Springer, 2006.

[23] V. Piefort. "Finite element modelling of piezoelectric active structures". PhD thesis. Université Libre de Bruxelles, Faculté des sciences appliquées, 2001.

[24] A. Deraemaeker, H. Nasser, A. Benjeddou, and A. Preumont. "Mixing rules for the piezoelectricproperties of Macro Fiber Composites". In: *Journal of Intelligent Material Systems and Structures* 20.12 (2009), pp. 1391–1518. DOI: 10.1177/1045389X0933561.

[25] E. Balmes and A. Deraemaeker. "Modeling structures with piezoelectric materials". In: *SDT tutorial* (2014).

[26] A. Preumont. *Dynamics of electromechanical and piezoelectric systems*. Mechatronics: Solid Mechanics and Its Applications. Springer, 2006.

[27] S. Sōmiya. "Ceramics". In: *Encyclopedia of Physical Science and Technology (Third Edition)*. Ed. by R. A. Meyers. Third Edition. New York: Academic Press, 2003, pp. 569–619. DOI: 10.1016/B0-12-227410-5/00092-2.

[28] Agilent Technologies. *Impedance Measurement Handbook: A Guide to Measurement Technology and Techniques*. Fourth Edition. Hewlett-Packard Company, 2013.

Chapter 6

Conclusions

This thesis aimed to develop an efficient and robust methodology for the design and implementation of active damping strategies in flexible structures through a novel optimized transducer placement methodology. This method focusses on SISO and MIMO configurations with collocated SA pair(s) and LAC architecture. Intended to be used on large and/or complex structures for which an optimization is often not considered because of too complex implementations, it proved to be efficient on various numerical examples.

Chapter 1 recalled the fundamental concepts of system dynamics, placing emphasis on the role of poles and zeros in the behaviour of single and multiple DoFs systems. More specifically, the mathematical and physical interpretation of poles and zeros in both SISO and MIMO configurations was analysed in relation to control design, system robustness and stability. An analytic approximation method to efficiently estimate zeros in SISO systems has been proposed, which was validated numerically and proved effective for preliminary analyses.

Chapter 2 focussed on the direct link between the PZ distance and the maximum reachable damping for low authority architectures. The known link in SISO systems has been extended to MIMO configurations, where the PZ distance is the distance between the pole and the TZ. Important conditions have been identified to maintain this direct link: the use of collocated SA pairs that have low authority and a low modal density on the bandwidth of interest. Various numerical examples have been analysed to demonstrate the extension, and an experimental setup has been used to successfully validate it.

Chapter 3 addressed the challenge of optimal transducer placement and highlighted the existing trade-off between computational efficiency and performance of the criteria. The new PZ distance criterion was proposed as a solution that combines the simplicity of open-loop evaluation with the predictive accuracy of closed-loop behaviour. Through numerical validation on both SISO and MIMO systems, the criterion was shown to outperform traditional open-loop criteria, particularly in maximizing damping performance across various modes.

The need of a search algorithm when performing optimal placement study is analysed in Chapter 4. It is demonstrated that although widely used, the GAs need extremely long computational time to obtain the solution, preventing optimization for large and/or complex structures. To overcome this limitation, a hybrid approach combining the PZ distance criterion with a non-evolutionary algorithm was proposed. By using the maximum PZ distance position to identify a suited starting point, the method significantly reduced the number of evaluations required for convergence while ensuring high perfor-

mance. Additionally, it has been shown through a numerical example that the obtained solution presents high robustness to misplacement.

Chapter 5 demonstrated the practical implementation of the proposed placement methodology on two industrial structures: a Boeing 777-200ER wing and a stiff wafer gripper system. In both cases, the method efficiently identified high-performance regions, requiring few evaluations to achieve effective solutions. The approach notably outperformed conventional strategies and ensured again strong robustness to placement errors.
Additionally, the necessity of an accurate FE model for reliable implementation was discussed. To address such concern, a dedicated model matching procedure to reduce deviations between simulated and physical system responses was proposed. The numerical validation of this proposed method highlighted the importance of designing robust control systems capable of accommodating model uncertainties, thereby enhancing the practical value of the new placement methodology proposed in this thesis.

This thesis contributes therefore to the development of new advances transducer placement strategies, with a focus on the efficiency of the method and the robustness of the obtained solutions. It is well suited for large and/or complex systems, which are usually not optimised because of the too high computational cost. More specifically, the main achievements of this thesis are:

- The extension of the direct link between the pole-zero distance and the damping in collocated SISO systems to MIMO ones. This extension is numerically demonstrated and experimentally validated.
- The proposed PZ distance criterion that directly links open-loop knowledge to closed-loop performance. It allows a limited number of evaluations to obtain a position with high damping area and strong robustness to transducer misplacement.
- The effective optimization method that combines the PZ distance criterion and a non-evolutionary algorithm, substantially reducing the computational effort to reach convergence.
- The matching procedure for FE model, which allows to reduce deviations between the physical response and its model.

Perspectives for future research

The research presented in this thesis can be extended in multiple directions. Three main topics are described here below:

Optimization of the transducer properties together with its placement

The optimization method proposed in this thesis focusses on the optimal placement of the SA pair(s) on a system in order to increase its damping. As demonstrated in Chapter 2, the positioning of the transducers on a structure has a significant impact on the performance of the control architecture. Nonetheless, several other parameters can be optimised to increase the performance.

For example, the orientation of a force actuator/displacement sensor pair can be strategically optimised to maximize its effectiveness in relation to the authority of the specific mode being targeted. When considering piezoelectric patches, their size and shape can be adapted could also be adapted to obtain a better patch/structure interaction.

In both cases, modifying those parameters would lead to a modification of the PZ distance. Hence, it is possible to include such additional parameters in the initial PZ distance criterion check of the propose methodology as the number of configurations to be tested remains limited. This would translate to the possibility to include more parameters for the optimization without significantly increasing the computational cost. Once the best initial configuration is identified based on the PZ distance criterion, the selected non-evolutionary algorithm can be used. Because more parameters will need to be optimised, the algorithm will need a higher number of iterations to converge. But due to its inherent efficiency, it should be limited and still presents manageable computational effort.

Use of the proposed method to perform a complete topology optimization

When external transducers are added to a structure for vibration control purpose (retrofit approach), the available positions where the SA pair(s) can be mounted are often restricted to a physical domain (as for example shown in Figure 5.13 with the wafer gripper). Additionally, a growth of the mass due to the required mounting parts can be encountered, as well as a restriction on the usable types of sensors and actuators. This consequently enforces further constraints on the control architecture design which can lead to sub-optimal configurations.

A possible extension of the work performed in this thesis would be to use the proposed PZ method to optimize the topology of a structure and include its required control architecture during the design phase. It would indeed allow to design high-performance active structures with a strong transducer integration, including the number of sensors and actuators, their types and positions and the control design. The new additive manufacturing techniques could be used for the complex shapes that would be difficult to manufacture with subtractive methods. Additionally, MFC patches could be considered because of the possibility to integrate them inside composites as well as to tailor the directions of actuation.

Nonetheless, such a complete topology optimization would require an extremely accurate model of the structure and the related transducers. As demonstrated in Section 5.4, the reliability of the numerical models built with FE software can present large deviations with respect to the experimental response, even for relatively simple systems. It consequently means that using the proposed method to perform a complete topology optimization would only be possible together with a major improvement in the field of FE modelling.

Experimental validation of the proposed methodology

Performing an experimental validation is usually valued when presenting new concepts and methods in the field of engineering. The experimental validation of the extension of the well-known direct link between the PZ distance and the damping in SISO systems to MIMO ones provided in Chapter 2 is notable.

Nonetheless, the research presented in this thesis does not provide experimental validation of the proposed optimization methodology. Developing such experimental validation would consequently be beneficial, and could be considered as an insightful final validation.

Publications associated with this thesis

The complete list of the author's publications is available in the institutional repositories DI-fusion (ULB) and ORBi (ULiège).

Journal articles

Pathak, Shashank, **Dimitri Piron**, Ahmad Paknejad, Christophe Collette, and Arnaud Deraemaeker. "On transmission Zeros of piezoelectric structures." Journal of Intelligent Material Systems and Structures 33, no. 12 (2022): 1538-1561.

Piron, Dimitri, Shashank Pathak, Arnaud Deraemaeker, and Christophe Collette. "On the link between pole-zero distance and maximum reachable damping in MIMO systems." Mechanical Systems and Signal Processing 181 (2022): 109519.

Piron, Dimitri, Shashank Pathak, Arnaud Deraemaeker, and Christophe Collette. "A pole-zero based criterion for optimal placement of collocated sensor-actuator pair." Mechanical Systems and Signal Processing 155 (2021): 107533.

Conference articles

Piron, Dimitri, Arnaud Deraemaeker, and Christophe Collette. "Determination of optimal sensor-actuator position for active vibration damping in collocated SISO systems using a pole-zero distance criterion for fast convergence of the search algorithm." Proceedings of ISMA2022-USD2022 (2022).

Journal article to be submitted

Piron, Dimitri, Christophe Collette, and Arnaud Deraemaeker. "A fast method of transducer placement for structural vibration damping based on the pole-zero distance criterion".

Appendices

Appendix A

Analysis of the beam and shell elements

This Appendix focusses on the finite elements that are used throughout this thesis. Section A.1 briefly introduces the beam elements, while Section A.2 illustrates how the multi-layer shell elements are modelled in SDT [1]. Finally, Section A.3 demonstrates why shell elements should be employed to properly model a piezoelectric patch when using FE structures rather than the beam ones.

A.1 Description of the beam elements

The beam elements are based on the Euler-Bernoulli beam theory which assumes that [2]:

1. The cross-sectional planes of the beam remain flat and perpendicular to the longitudinal axis of the beam even after deformation
2. The shear deformation is insignificant and can therefore be neglected
3. The deflections of the beam are assumed to be small
4. Slender beams are considered (i.e. high ratio between the length and the height of the beam)

Those elements only allow the 2 DoF in-plane bending motion, i.e. the transversal displacement (translation perpendicular to the longitudinal axis of the beam) and the out-of-plane rotation (rotation about the out-of-plane axis). Operating in the 2 dimensions space, the beam elements consist of a straight line of length L (span) that connects two nodes. Hence, each elements integrate a total of 4 DoFs (2 per node).

Two theories can be considered when dealing with beam elements: the Euler-Bernoulli theory where shear deformation is negligible and the the Timoshenko theory for which the shear deformation is accounted.

A.2 Description of the multi-layer shell elements

Shell elements can be viewed as generalizations of beam elements to curved surfaces in three-dimensional space. They can be used to easily model thin structures whereas too many solid elements would be needed to obtain a reasonable solution [2].

A shell element with 6 DoFs per node is a 2D surface finite element where each node presents the three translations and the three rotations. A quadrangular shell element

exhibits consequently a total of 24 DoFs. Two theories can be considered when dealing with shell elements: the Kirchhoff–Love theory (thin shells, no transverse shear), and the Mindlin–Reissner theory (thick shells, where transverse shear is considered).

The multilayer shell elements

One of the valuable feature of SDT is that it integrates the modelling of the different layers of a piezoelectric patch, which was initially developed in [3]. It allows a complex structure (such as a MFC patch, which is illustrated in Figure A.1) to be broken down into a collection of layers. This collection then forms a laminate based on the bounding of all the layers (the bond between two layers is assumed to be perfect to ensure the continuousness of the displacement).

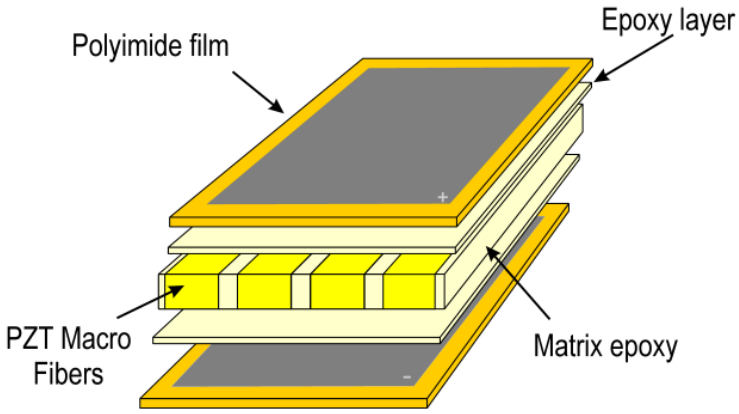

Figure A.1: General layout of a MFC d_{31} patch [4].

To illustrate how the multilayer elements are built in SDT, a beam with a collocated pair of MFC patches can be considered (mounted on the top and bottom of the beam). In addition, a PZT can be added on the top surface, as done in Section 2.3. The illustration of such structure can be found in Figure A.2 and, as it can be seen, the number of layers varies depending on the longitudinal position on the beam. When no piezoelectric patch is mounted, the model only considers one single layer (the beam and its related properties). At the location where the PZT patch is mounted, two layers are considered (the beam, and the active PZT layer). Once at the location of the MFC collocated pair, a total of 7 layers are implemented: the three layers for the bottom MFC, the beam layer and finally the three layers for the top MFC where each layer is defined according to its related properties.

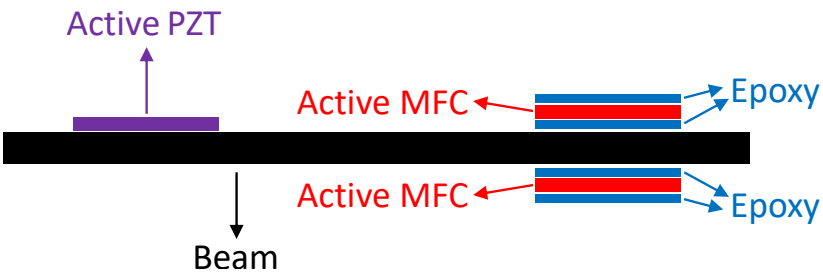

Figure A.2: Illustration of the multilayer principle in SDT. Depending on the location, the model is built with 1 layer, 2 layers or 7 layers.

A.3 On the use of shell elements for piezoelectric patch modelling

A piezoelectric patch is a two-dimensional surface bonded to the host structure, and its electromechanical behaviour depends on both in-plane strains (membrane effects) and out-of-plane bending deformations (see Section 5.4.2 for the general constitutive equations of piezoelectric patches). Two significant phenomena occur when a piezoelectric patch is actuated: a set of self-equilibrating forces is generated [5], and transverse strains appear [6]. Such self-equilibrating forces leads to a localised deformation of the beam in the vicinity of the piezoelectric patch as illustrated in Figure A.3, where the induced transverse strains are shown as well. The basic kinematic of the beam does not adequately represent those type of deformations because of the assumption that it cannot be deformed within its plane. This is therefore the reason why shell elements should be considered when modelling piezoelectric patches.

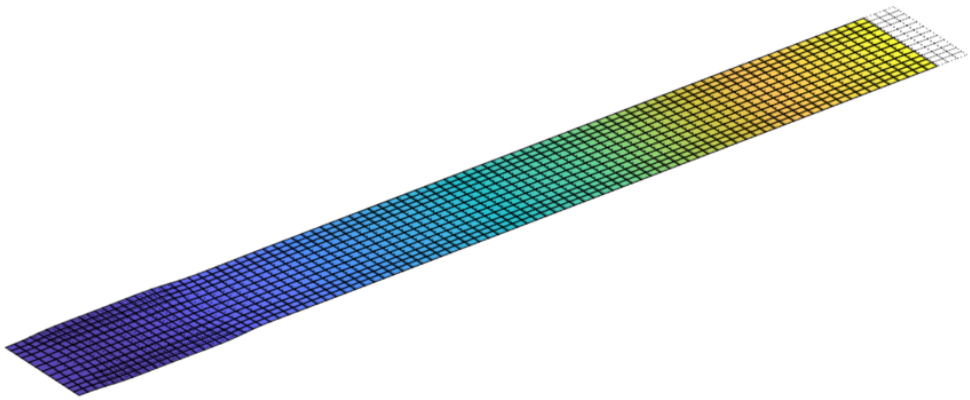

Figure A.3: Static response that illustrates the localised deformation in the vicinity of a piezoelectric patch when actuated and the induced transverse strains.

References

[1] E. Balmes. *Structural Dynamics Toolbox 7.3 (for use with MATLAB)*. 1991. URL: https://www.sdtools.com.

[2] J. Fish and T. Belytschko. *A first course in finite elements*. Vol. 1. Wiley New York, 2007.

[3] V. Piefort. "Finite element modelling of piezoelectric active structures". PhD thesis. Université Libre de Bruxelles, Faculté des sciences appliquées, 2001.

[4] E. Balmes and A. Deraemaeker. *Modeling structures with piezoelectric materials: full, reduced order, and state-space models*. SDTool. 2025.

[5] A. Deraemaeker, G. Tondreau, and F. Bourgeois. "Equivalent loads for two-dimensional distributed anisotropic piezoelectric transducers with arbitrary shapes attached to thin plate structures". In: *The Journal of the Acoustical Society of America* 129.2 (2011), pp. 681–690. DOI: 10.1121/1.3523338.

[6] A. Preumont, A. François, P. De Man, and V. Piefort. "Spatial filters in structural control". In: *Journal of sound and vibration* 265.1 (2003), pp. 61–79.

Appendix B

Analysis of the search algorithms

B.1 Analysis of the Genetic algorithm from Matlab

This section provides insights on the evolutionary GA available within the Global Optimization Toolbox of Matlab, which is called by the *'ga'* function. This function is indeed used in Section 4.3.1 where the proposed strategy introduced in this thesis is numerically illustrated on a cantilever beam.

The implementation of such available GA in Matlab follows the working mechanisms of general GAs that have been exhaustively described in Section 4.2. More specifically, starting from a random initial population, a new generation is created at each iteration where children are obtained based on elite, crossover and mutation processes.

List of the optimization parameter values

Table 4.1, which is recalled here below in Table B.1, provides the value of several parameters used to configure the GA in Section 4.3.1. Although those parameters have a direct impact on the GA performance when configuring the Matlab *'ga'* function, other important ones were not mentioned in the manuscript for the sake of conciseness. The value of all the remaining tuned parameters are therefore provided in Table B.2, where *MaxStallGenerations* and *FunctionTolerance* are both related to the stopping criteria. The convergence is indeed intended to be stopped when the maximum defined number of generations is reached. Yet, those two parameters allow to prematurely stop the convergence when the algorithm does not find an improvement of *FunctionTolerance* in the objective function over *MaxStallGenerations* generations.

The remaining parameters from the Matlab *'ga'* function that are not available in the two provided tables have been kept according to the predefined standard values from the toolbox. The complete list can found within the Matlab documentation [1] and their corresponding values can be sighted with the { } identifier.

[1] Available within the Mathworks Help Center at the address: `https://www.mathworks.com/help/gads/ga.html/` (last accessed:August 2025)

Table B.1: Initial parameter settings used for the implementation of the GA.

Parameters	Settings
Design variables	$\mathbf{x}$, g
Optimization objective	Maximize $\tilde{J}(\mathbf{x}, g)$
Population size	50
Mutation probability	Gaussian distribution
Crossover probability	0.8
Elite children per generation	Minimum 2

Table B.2: Remaining parameter settings used for the implementation of the GA.

Parameters	Mode	Settings
Variable type x	All	Integer
Variable type g	All	Continuous
Bounds on x	All	0 <x <L
	Mode 1	5000
Bounds on g	Mode 2	1e5
	Mode 3	2e5
FunctionTolerance	All	0.001
	Mode 1	6
MaxStallGenerations	Mode 2	7
	Mode 3	12

As mentioned, a GA always starts with the creation of a random population. Because of such a stochastic essence, the probability to recover the exact similar results that are shown in Section 4.3.1 tends to zero, even if all the provided parameter values are implemented. Nonetheless, the general trends should be preserved, i.e. the number of evaluations of the cost function to converge and the optimal modal damping values should be in the same range.

B.2 Analysis of the *'fminsearch'* algorithm from Matlab

This section analyses the *'fminsearch'* function available in Matlab within the Global Optimization Toolbox. This optimization routine is indeed used throughout Chapters 4 and 5 when performing the numerical validations of the proposed method. The *'fminsearch'* function provides a non-evolutionary method, as it relies on a direct search method, i.e. a search strategy that evaluates a set of points in the vicinity of the current parameter values. As direct search algorithms do not compute any gradient nor derivative of the cost function but only rely on its evaluation, they are often called derivative-free optimization algorithms [1]. Direct search algorithms are consequently particularly useful when gradients are unavailable (e.g. the cost function is not differentiable and/or not continuous), expensive to compute or unreliable (e.g. the cost function shows high level of noise).

The Matlab *'fminsearch'* algorithm specifically relies on a simplex search approach introduced in [2], which is a refinement of the original Nelder-Mead method presented by John Nelder and Roger Mead in [3]. Heuristic in nature, the Nelder-Mead algorithm is widely used in optimization problems because of its simplicity and robustness but also because it shows good efficiency for low-dimensional problems.

Working principle of the *'fminsearch'* algorithm

As mentioned, the *'fminsearch'* algorithm is built upon a more sophisticated version of the original Nelder-Mead method. This section aims to describe how *'fminsearch'* operates to reach the optimal solution.

Similarly to the gradient descent described in Section 4.2, the convergence of the *'fminsearch'* algorithm is initiated by the definition of the starting value(s) of the parameter(s) to optimise. The optimal solution obtained after convergence is consequently bounded by such selection of the initial starting value(s), leading to the possible retention of a local optimum rather than a global one [1].

From the initial starting value(s) provided to the *'fminsearch'* function $\{x_0\} \in \mathbb{R}^n$, the algorithm builds a simplex in n dimension(s) where n is the number of variable(s) to optimize. Such a simplex in n dimension(s) is the simplest possible polytope that is made from the minimum number of points (called vertex) to span that space, i.e. $(n+1)$ vertices[2] [4]. As only one initial starting vertex is provided to *'fminsearch'*, the algorithm first creates the remaining n vertices by adding 5% of each component of $\{x_0\}$ as follows:

$$[x_{0,full}] = \begin{bmatrix} x_{0,1} & x_{0,1} * 1.05 & x_{0,1} & \dots & x_{0,1} \\ x_{0,2} & x_{0,2} & x_{0,2} * 1.05 & \dots & x_{0,2} \\ \vdots & \vdots & \vdots & \ddots & \vdots \\ x_{0,n} & x_{0,n} & x_{0,n} & \dots & x_{0,n} * 1.05 \end{bmatrix} \tag{B.1}$$

where $[x_{0,full}] \in \mathbb{R}^{n\times(n+1)}$. The method used in the *'fminsearch'* algorithm consists of modifying the simplex at each iteration by replacing the vertex that presents the worst function value. The repeatedly creation of each new simplex is based on the following procedure, where the current simplex is defined by $[x] = [\{x_1\}\,\{x_2\} \dots \{x_n\}\,\{x_{n+1}\}]$ and f is the cost function to minimize. For the sake of simplicity, matrix and vector notations are not explicitly included in the following text. Nevertheless, it should be understood that the formulations inherently remain of a vectorial and matrix nature, which should be kept in mind throughout the discussion.

Sort
The $(n+1)$ vertices are sorted from the lowest evaluation of the cost function $(f(x_1))$ to the highest one $(f(x_{n+1})$. From this identification, the algorithm attempts to modify the vertex x_{n+1} that presents the worst performance by applying a geometric transformation. The first one to be tested is the reflect mechanism.

Reflect
The point x_{n+1} is reflected (flipped) through the centroid formed by the other vertices, leading to a new vertex called r. If $f(x_1) \leq f(r) < f(x_n)$, the new point r is kept and replaces x_{n+1}. The new simplex is built and the iteration stops.

Expand
If $f(x_r) < f(x_1)$ (i.e. the new vertex provides better performance than the entire vertices from the current simplex), the algorithm expands the point r a second time using the same centroid, leading to point s. If $f(s) < f(r)$, s is kept and replaces

[2]The polytope is a more general shape that can have more vertices and faces but is still made of flat surfaces. For example: a simplex in 1 dimension is a line segment while the related polytope can be a line segment, or a union of line segments. In 2 dimensions, the simplex is a triangle while the related polytope can be a triangle, a square, a hexagon,... .

x_{n+1}. The new simplex is built and the iteration stops. On the contrary, if r still presents better performance than s (i.e. if $f(r) \leq f(s)$), s is discarded and r is kept to replace x_{n+1}. The new simplex is built and the iteration stops.

Contract

The initial reflection performed to obtain the vertex r can also lead to a reduction in performance, i.e. $f(r) \geq f(x_n)$. If applicable, a new point m is created at the centroid defined in the reflect mechanism (i.e. the centroid formed by all the vertices except x_{n+1}).

- If $f(r) < f(x_{n+1})$ (i.e. r is still better than x_{n+1}), a new point c is built at the centroid of m and r (contract outside) and the cost function is evaluated. If $f(c) < f(r)$, c is kept and replaces x_{n+1}. The new simplex is built and the iteration stops.
- If $f(r) \geq f(n+1)$ (i.e. r presents worst performance compared to all the original vertices), a new point cc is built at the centroid of m and x_{n+1} (contract inside) and the cost function is evaluated. If $f(cc) < f(x_{n+1})$, cc is kept and replaces x_{n+1}. The new simplex is built and the iteration stops.

Shrink

If contracting outside or inside does not provide a better result (i.e. $f(c) \geq f(r)$ or $f(cc) \geq f(x_{n+1})$, respectively), all the vertices are pulled closer to the best one x_1 which reduces the simplex size. More specifically, the new shrunk simplex contains the following vertices: $x_{shrunk} = \left[x_1\ x_2^{shrunk} \ldots x_n^{shrunk}\ x_{n+1}^{shrunk}\right]$ where the shrunk vertices are obtained as follows:

$$x_i^{shrunk} = x_1 + \Big(x_i - x_1)/2\Big) \quad (i = 2, ..., n+1) \tag{B.2}$$

Once all the new vertices have been computed according to Equation B.2, their performance is evaluated with the cost function f (i.e. the cost function is evaluated n times). Then, the new simplex is built and the iteration stops.

Check of the stopping conditions

After the creation of each new simplex (i.e. after each iteration), the *'fminsearch'* algorithm analyses if one of the stopping criteria is met. If applicable, the convergence is stopped and the vertex x_1 of the latest simplex that minimises the function f is provided as the optimal solution. The *'fminsearch'* algorithm provides three stopping criteria that can stop the convergence:

- The maximum number of function evaluations has been reached.
- The maximum number of iterations has been reached.
- The norm between the new vertex and x_{x+1} is smaller than a defined tolerance **and** the change in the value of the objective function obtained between the new vertex and x_{x+1} is smaller than a defined tolerance.

By applying those different mechanisms, the algorithm adapts the shape of the simple as well as its position, progressively approaching regions of lower cost function values. Interestingly, it can be concluded based on the described method that for each iteration the cost function f is evaluated at minimum $(n+3)$ times (sort, reflect and expand) and at maximum $(2n+4)$ times (sort, reflect, expand, contract, shrink). It therefore reassures the efficiency of the direct search algorithms compared to the GAs, where each individual of the the entire population is evaluated per iteration. For a sake of clarity, an illustration of the reflect, expand, contract and shrink mechanism is provided in Figure B.1.

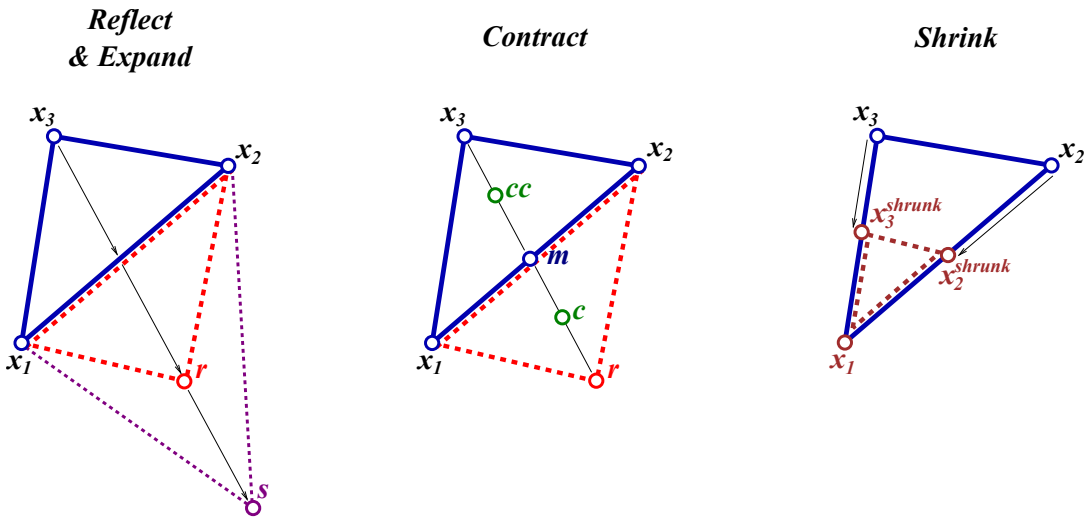

Figure B.1: Visual illustration of the mechanisms to update the simplex.

List of the optimization parameter values

The *'fminsearch'* function has been used throughout Chapters 4 and 5. This section consequently aims to provided the value of the employed tuned parameters to allow the recovery of the obtained results.

More specifically, mainly two parameters linked to the stopping criteria have been used: *TolX* and *TolFun*. Those two parameters are linked together, as both must be satisfied to stop the convergence process. While *TolX* analyses if the change in the input variables between iterations is smaller than the defined threshold, *TolFun* controls whether the change in the cost function value is smaller than the other defined threshold (more insight about the working principle are provided in the operational principles of the *'fminsearch'* algorithm detailed here above). Table B.3 refers to the cantilever beam from Section 4.3.1, Table B.4 to the wing of the Boeing 777-200ER in Section 5.2 and Table B.5 to the wafer gripper in Section 5.3.

Table B.3: Parameter settings implemented in the *'fminsearch'* algorithm for the validation of the proposed method on the cantilever beam

Parameters	Settings
TolX	0.05
TolFun	0.05

Table B.4: Parameter settings implemented in the *'fminsearch'* algorithm for the validation of the proposed method on the wing of the Boeing 777-200ER

Parameters	Settings
TolX	0.0144
TolFun	1

Table B.5: Parameter settings implemented in the *'fminsearch'* algorithm for the validation of the proposed method on the wafer gripper

Parameters	Settings
TolX	0.0175
TolFun	1

References

[1] C. Audet and W. Hare. *Derivative-Free and Blackbox Optimization*. First Edition. Springer Series in Operations Research and Financial Engineering. Springer Nature, 2017.

[2] J. C. Lagarias, J. A. Reeds, M. H. Wright, and P. E. Wright. "Convergence properties of the Nelder–Mead simplex method in low dimensions". In: *SIAM Journal on optimization* 9.1 (1998), pp. 112–147. DOI: 10.1137/S1052623496303470.

[3] J. A. Nelder and R. Mead. "A simplex method for function minimization". In: *The computer journal* 7.4 (1965), pp. 308–313.

[4] A. Brondsted. *An introduction to convex polytopes*. Vol. 90. Springer Science & Business Media, 2012.